



Ultrafast Spectroscopy Studies on Charge Transfer Process in Avian Cryptochrome 4 Proteins

Von der Fakultät für Mathematik und
Naturwissenschaften der Carl von Ossietzky Universität
Oldenburg zur Erlangung des Grades und Titels eines
Doktors der Naturwissenschaften (Dr.rer.nat) im Fach
Physik
angenommene Dissertation

Von
Frau M.Sc. Anitta Rose Thomas
geboren am 04. November 1989
in Nedumkandam, Kerala, India

Gutachter

: Prof. Dr. Christoph Lienau

Carl von Ossietzky Universität Oldenburg

Weitere Gutachter: Prof. Dr. Mathias Wollenhaupt

Carl von Ossietzky Universität Oldenburg

: Prof. Dr. Karl-Wilhelm Koch

Carl von Ossietzky Universität Oldenburg

Tag der Disputation : 07.03.2024

Abstract

Migratory birds possess very accurate magnetic compasses for their long-range navigation. However, the primary mechanism for their magnetic sensitivity and corresponding sensor molecule is still unknown. Later it was recognized that the radical-pair mechanism in cryptochrome photoreceptor molecules is possibly responsible for the magnetic sensitivity in migratory birds. The cryptochrome 4 molecule, found in the retina of migratory birds, form long-lived radical-pairs by the photoexcitation of the chromophore flavin adenine dinucleotide (FAD), which is accompanied by consecutive electron transfer from four tryptophan amino acid chains. In this thesis, ultrafast spectroscopic studies on purified cryptochrome 4 molecules from the night migratory bird European robin (*Erithacus rubecula*) (ErCry4) and its four mutants are discussed. In the mutant samples, tryptophan molecules involved in the electron transfer process in the cryptochrome are selectively replaced with redox-inactive phenylalanines. Through these experiments, the photophysical properties of the ErCry4 protein and the effects of the protein environment on the dynamics and yield of the charge separation process in the ErCry4 molecule were investigated. This thesis explores the advantages of fluorescence and transient absorption spectroscopy with picosecond to femtosecond time resolution for exploring the photophysical properties of ErCry4. A time-resolved excitation-emission spectrometer has been developed for fluorescence spectroscopic studies. With the spectrometer, it was possible to distinguish and fully separate coherent and incoherent emissions from the samples. It was also possible to monitor the photophysics and changes in the redox state of the protein sample, using the developed spectrometer. The dynamics and yield of the first three electron transfers through the tryptophan chain were observed through ultrafast transient absorption spectroscopy. It was noted that the presence of the fourth tryptophan in the chain increased the concentration of the long-lived radical-pairs in the protein sample compared to the mutants. A microscopic insight into the charge separation process along the tryptophan chain in ErCry4 has been obtained by comparing these experimental results with those of the semi-empirical density-functional tight binding method (DFTB) based real-time quantum mechanical/molecular (QM/MM) electron transfer simulations. These approaches provide a path for understanding spin transport and dynamical spin correlation in flavoprotein radical-pairs.

Keywords

Cryptochrome proteins, Mutagenesis, Tryptophan, Flavin adenine dinucleotide(FAD), Radical-pair formation, Fourier transform spectroscopy, Time-resolved-excitation-emission spectroscopy, Coherent and incoherent emission, Electron transfer, Ultrafast spectroscopy, Transient absorption spectroscopy.

Kurzfassung

Die Zugvögel verfügen über sehr genaue Magnetkompassse für ihre Langstreckennavigation. Der primäre Mechanismus für ihre magnetische Empfindlichkeit und das entsprechende Sensormolekül ist immer noch unbekannt. Es wird vermutet, dass der Radikalpaar-Mechanismus in Cryptochrom-Photorezeptormolekülen für die magnetische Empfindlichkeit von Zugvögeln verantwortlich ist. Das Cryptochrom-4-Molekül, das in der Netzhaut von Zugvögeln vorkommt, bildet langlebige Radikalpaare durch die Photoanregung des Chromophors Flavin-Adenin-Dinukleotid (FAD), die von einem konsekutiven Elektronentransfer von vier Tryptophan-Aminosäureketten begleitet wird. In dieser Arbeit werden ultraschnelle spektroskopische Untersuchungen an gereinigten Cryptochrom-4-Molekülen des Nachtzugvogels Rotkehlchen (*Erithacus rubecula*) (ErCry4) und seiner vier Mutanten diskutiert. In den mutierten Proben ist Tryptophan, das am Elektronentransferprozess im Cryptochrom beteiligt ist, selektiv durch redox-inaktives Phenylalanin ersetzt. Durch diese Experimente wurden die photophysikalischen Eigenschaften des ErCry4-Proteins und die Auswirkungen der Proteinumgebung auf die Dynamik und die Ausbeute des Ladungstrennungsprozesses im ErCry4-Molekül untersucht. In dieser Arbeit werden die Vorteile der Fluoreszenz- und transienten Absorptionsspektroskopie mit einer Zeitauflösung von Pikosekunden bis Femtosekunden zur Aufklärung der photophysikalischen Eigenschaften von ErCry4. Für die fluoreszenzspektroskopischen Untersuchungen wurde ein zeitaufgelöstes Anregungs-Emissionsspektrometer entwickelt. Mit dem Spektrometer war es möglich, kohärente und inkohärente Emissionen der Proben zu unterscheiden und vollständig zu trennen. Mit dem entwickelten Spektrometer war es auch möglich, die Photophysik und die Veränderungen im Redoxzustand der Proteinprobe zu überwachen. Die Dynamik und die Ausbeute der ersten drei Elektronentransfers durch die Tryptophankette wurden durch ultraschnelle transiente Absorptionsspektroskopie beobachtet. Es wurde festgestellt, dass die Anwesenheit des vierten Tryptophans in der Kette die Konzentration der langlebigen Radikalpaare in der Proteinprobe im Vergleich zu den Mutanten erhöhte. Ein mikroskopischer Einblick in den Ladungstrennungsprozess entlang der Tryptophankette in ErCry4 wurde durch den Vergleich dieser experimentellen Ergebnisse mit denen der semi-empirischen Dichtefunktionalen Tight-Binding-Methode (DFTB) auf der Grundlage von Echtzeit-Quantenmechanik-/Molekular (QM/MM) Elektronentransfersimulationen gewonnen. Diese Ansätze bieten einen Weg zum Verständnis des Spintransports und der dynamischen Spin-Korrelation in Flavoprotein-Radikalpaaren.

Schlagwörter

Cryptochrom-Proteine, Mutagenese, Tryptophan, Flavin-Adenin-Dinukleotid (FAD), Radikalpaarbildung, Fourier-Transformations-Spektroskopie, Zeitaufgelöste Anregungs-Emissionsspektroskopie, Kohärente und inkohärente Emission, Elektronentransfer, Ultraschnelle Spektroskopie, Transiente Absorptionsspektroskopie.

Contents

Chapter I1

The Long-Range Navigation and Magnetoreception in Migratory Birds 1

I.1 Bird Navigation 1

I.2 Different Hypotheses Based on Magnetoreception Mechanisms 3

I.3 Cryptochrome Proteins 9

I.4 Summary 22

I.5 Outline of the Thesis 25

Chapter II29

Fourier Transform-Based Time-Resolved Excitation-Emission Spectrometer
..... 29

II.1 Introduction 29

II.2 Experimental Section 31

II.3 Distinguishing Between Coherent and Incoherent Signals in Excitation-Emission
Spectroscopy 34

II.4 Time-Resolved Excitation Emission Spectroscopy 46

II.5 Summary and Conclusions 51

Chapter III53

Time-Resolved Excitation-Emission Spectroscopic Studies on Cryptochrome 4
Molecules 53

III.1 Introduction 53

III.2 Experimental Section 55

III.3 Results and Discussion 57

III.4 Summary and Conclusions 80

Chapter IV83

Ultrafast Transient Absorption Spectroscopy Studies on Cryptochrome 4 Molecules.....83

IV.1 Introduction83

IV.2 Experimental Section and Methods85

IV.3 Results90

IV.4 Discussion.....104

IV.5 Summary and Outlook.....106

Chapter V 107

V.1 Summary and Conclusion.....107

V.2 Outlook110

Appendix-A.....113

A.II.....113

A.II.1 TWINS Interferometer.....113

A.II.1.1 TWINS113

A.II.1.2 TWINS Calibration.....118

A.II.1.3 TWINS Spectrometer.....123

A.II.2 BI-TWINS.....125

A.II.2.1 BI-TWINS Signal125

A.II.2.2 Separation Method128

A.III.....133

A.III.1 ErCry4 Protein Sample Preparation Protocol for Spectroscopic Experiments 133

A.III.1.1 Protocol for washing BME from ErCry 4 sample.....133

A.III.1.2 Protocol for concentrating ErCry 4 sample.....133

A.III.1.3	Protocol for oxidizing ErCry 4 sample	134
A.III.2	Undersampling	135
A.IV	137
A.IV.1	Linearity and Sample Stability.....	137
A.IV.2	Potassium Ferricyanide Oxidizer	138
A.IV.3	FAD in Buffer	139
A.IV.4	Data Preparation and Analysis.....	140
A.IV.5	Additional Simulation Data	145
References	I
Publication Related to This Thesis	XIX
Acknowledgment	XXI
Declaration of Independence	XXIII

Chapter I

The Long-Range Navigation and Magnetoreception in Migratory Birds

I.1 Bird Navigation

Humans have always been fascinated by different things seen in nature ever since they began to observe their surroundings. One of the exciting things they have always wondered about is the appearance of some birds in summer and their disappearance in winter in different regions of the world. In the beginning, people thought the birds were resting at the bottom of the river during wintertime. But later, these misconceptions changed when communication and traveling between the different continents improved. Then it was realized that these lovely and small birds migrate to the tropical and subtropical regions of the earth during freezing and mild weather in their breeding areas. Bar-tailed godwits (*Limosa lapponica*) migrate from Alaska to New Zealand, traveling more than 7,000 km in 7 to 9 days and nights without a single stopover [3, 9, 24]. Arctic terns (*Sterna paradisaea*) which breed around the North Pole, migrates to the South Pole during winter flying ~80,000 km per year [20, 25]. Sea birds fly more than 100,000 km per year to return to islands in the middle of vast oceans to breed [26]. But these findings raise more questions about the long-range journey of birds. How do these birds navigate with a precision of centimeters over a distance of 5,000 km or more? How do they find their way at night? How do the young and first migrating birds navigate without contact with elder and experienced ones? [3, 25, 27-29]

Plenty of studies have shown that even insects migrate over unbelievable distances. Monarch butterflies (*Danaus plexippus*) travel around 3,000 km during autumn from the USA to Canada to specific trees [30]. A similar pattern is observed in Bogong moths (*Agrotis infusa*) in migrating over 1,000 km at night between their breeding sites and aestivation caves in the Snowy Mountain [31]. In marine life, organism such as coral reef fish, [32] salmonid fish, [33] and sea turtles [34] also migrate over thousands of kilometers [3, 27].

For the long migrating journey of organisms, they have developed a wide variety of sensory cues, which enable highly efficient navigation are integrated with their nervous system [27, 35]. However, for accurate navigation, migrating animals first must determine their location (position on the map). Then they have to orient according to their destination (compass). Therefore, they need map and

compass information for long-range navigation. For a directional sense, a reference compass is necessary. The easily available, weather-independent reference compass is the geomagnetic field. The geomagnetic field is universal, but its intensity and inclination angle (the angle between the geomagnetic field lines and the earth surface) gradually increase from the South to North Poles [27, 35, 36].

The behavioral experiment results have shown that migrating insects, animals, and birds use the inclination angle of the geomagnetic field to orient in the desired direction [35]. Migratory birds, European robin (*Erithacus rubecula*), silvereyes (*Zosterops lateralis*), and Eurasian blackcaps (*Sylvia atricapilla*) are sensitive to changes in the inclination angle of the earth magnetic field. They either reverse their heading direction or disorient while changing the inclination angle [3, 37-39]. In addition to the geomagnetic field and inclination angle, migrating birds such as European robin (*Erithacus rubecula*) and garden warblers (*Sylvia borin*) are sensitive to the geomagnetic intensity [3, 38, 40]. Interestingly, these migrating birds are only sensitive to the geomagnetic inclination angle but not magnetic polarity [38]. The migratory birds can grab position information from total geomagnetic intensity, inclination, and declination angle (angular deviation between magnetic and geographical North) [27, 35, 41]. The geomagnetic declination angle is the best way to determine the east-west position [42].

Another specialty of the avian magnetic compass is its light wavelength dependence. Behavioral experiments have proved that migratory birds are oriented in the wavelength range from 370 to 565 nm towards their specific traveling direction, and they are disoriented for any other wavelength outside this window [37, 43]. So this suggests that migratory birds possess a light-dependent magnetic compass.

However, there is a difference in migrating cues used by first or one-time and experienced navigators. The first and one-time migrants have orientation information imprinted in their inherited genes or already learned before starting their journey. They do not have a detailed map of their migration route but have a basic idea about the destination, which is also inherited. Experienced migrants can use cue gradients and maps that they have already acquired to correct the unknown location during their travel [28, 34-36, 41].

During navigation that involve thousands of kilometers, migrating animals use different gradients of cues and inherited and acquired map. In the case of experienced long-distance migrants, there are at least three phases in their navigation 1) a long-distance phase, 2) a homing phase, and 3) the goal phase [27]. Each of these navigational phases is different, but universal for various organisms. The first one, the long-distance phase, is the long-range navigation which is far from their home. In this phase, animals and birds mainly use celestial and magnetic cues. Inexperienced first-time travelers can use only the inherited compass-based orientation [28-30, 36]. Experienced ones uses the compass orientation and

information from the learned map from their prior journeys, such as the position of coastlines, and mountains [29, 36]. In the homing phase, they narrow their destination to a near a familiar home range. They use learned local gradient maps that rely on different senses and environmental cues (rivers, mountain ranges, forest borders, roads, and so on) [27, 35, 44, 45]. The goal phase is identifying and reaching their final points, such as a cave entrance, a specific tree, or a lake for a nest hole or sleeping perch. At this stage, the migrating organisms should remember specific visual landmarks and/or the smell of the particular locations from its previous experiences [45-48].

Effective navigation includes all three phases stated above. However, here we focus only on the first phase of navigation, the long-distance migration of birds using the geomagnetic field.

I.2 Different Hypotheses Based on Magnetoreception

Mechanisms

The behavioral experiments have proved that migrating birds could orient and make long-range navigation using geomagnetic field intensity, inclination, and declination angle [37-40] at a specific wavelength of light [37, 43]. But it is still unclear and under debate how these birds sense the earth's magnetic field (magnetoreception) with these parameters. Currently, there are three prominent magnetoreception hypotheses under discussion. 1) electromagnetic induction, 2) magnetic-particle-based magnetoreception, and 3) radical-pair-based magnetoreception [3, 27]. A short description of the first two hypotheses is given in sections I.2.1 and I.2.2 . Here, the main focus is on radical-pair-based magnetoreception, and a detailed description of the hypothesis is given in section I.2.3 .

I.2.1 Electromagnetic Induction

An electric potential is generated in a conductor when it moves through a magnetic field, Faraday's law of induction. Elasmobranch fishes like sharks, skates, and rays have a conductive canal inside their ampullas, and the inner end of these ampullas has electroreceptors. The geomagnetic field induces voltage changes in these conductive canals and alters nerve activities when they move. Hence the animals are sensitive to these voltage changes and changing magnetic field intensity. The evidence for this hypothesis is available for sharks [49-51] and birds [52-54]. Birds have a semicircular conductive canal in their heads with sodium, potassium chloride, and calcium ion, which is sensitive to the magnetic field.

There are several pieces of evidence that fish and birds can detect the geomagnetic field through electromagnetic induction. But the proof of this hypothesis is ambiguous. This hypothesis is still in the proposed stage, and no direct evidence has been obtained yet [3].

I.2.2 Magnetic-Particle-Based Magnetoreception

Ferromagnetic material, especially iron oxide (Fe_3O_4) clusters, is present in the cell membrane of almost every animal, which is essential for various functions in organisms. According to the magnetic-particle-based magnetoreception hypothesis, these iron clusters act as compass sensors in the organisms [55, 56]. Blakemore, R reported that magnetotactic bacteria could produce an intercellular chain of magnetite crystals that can act as a magnetic compass [57]. This was the beginning of magnetic-particle-based magnetoreception theory. An external magnetic field can induce a torque on the cell membrane with magnetite crystals leading to the opening of ion channels in the cell membrane. These processes generate a membrane potential that can cause neuronal activation in the brain and lead to magnetoreception [58, 59].

A magnetic-particle-based magnetoreceptor candidate structures can be found in the olfactory epithelium of fish [60] and the ophthalmic branch of the trigeminal nerve (responsible for sensation in the face and its motor functions), which is in the upper beak and frontal face of the birds [61]. An experiment with a strong directed magnetic pulse disoriented experienced migratory bobolink (*Dolichonyx oryzivorus*) birds [62]. A strong directed magnetic pulse can re-magnetize ferromagnetic material, which may disorder the magnetic-particle-based magnetoreception [63]. But this is not affecting the inexperienced, juvenile birds [64]. These observations indicate that magnetic particles may be correlated to the magnetic map sense of experienced migrants. In addition, it is also observed that the lesioning of the trigeminal nerve causes loss of map sense in adult birds but does not affect their magnetic compass orientation ability [58, 65]. The behavioral experiments support the magnetite-based magnetoreception mechanism in the magnetic map sense of birds. However, the presence of magnetite-based receptors has not yet been confirmed. The main challenge for finding such receptors is identifying ferromagnetic crystals in consistent and specific locations in many individuals of the same species associated with the nervous system [3, 20, 27].

I.2.3 Radical-Pair Based Magnetoreception

Schulten et al.(1978) [66] proposed the possible involvement of the radical-pair mechanism in the magnetic-compass sense of migratory birds. Radical-pair mechanism is an exciting quantum physics phenomenon, but its effects on magnetoreception were unconvincing at the proposed time. Because the geomagnetic field has only a strength ranging from 24 to 66 μT depending on the location on earth [67], which is a million times smaller than the thermal energy $k_b T$ of a single molecule in migrating animals under physiological conditions. Later, it was discovered that radical-pairs are sensitive to the magnetic field and have a critical role not only in magnetoreception [20] but also in various other biochemical reactions [68-75].

Molecules with an odd number of electrons in the outer shell are called radicals. Radicals are magnetically sensitive due to the inherent quantum property of electrons called spin angular momentum. Spin is the quantum property of elementary particles. The spin of an elementary particle can be described using spin quantum number s and spin projection quantum number m_s . The elementary particles such as electrons, protons, and neutrons have a spin quantum number $s = \frac{1}{2}$, fermions. Since these particles have angular momentum characteristics, the spin of the particles can interact with the external magnetic field and the spin of other particles in their vicinity. The spin axis of the electron precesses around either parallel or antiparallel direction to the external magnetic field with projections $m_s = \pm \frac{1}{2}$. This kind of coupling between two fermions results in a total spin with a quantum number $S = 0, M_s = 0$, called singlet ($\{S\}$) or $S = 1, M_s = 0, \pm 1$, triplet ($\{T\}$) states. Usually, the radical-pairs are formed by breaking a bond between the molecules, $\{A D\} \rightarrow \{A^\bullet D^\bullet\}$, or an electron is transferred from D to A and forms $\{A^{\bullet-} D^{\bullet+}\}$. The formed radical-pair will either be in $\{S\}$ or be in $\{T\}$ state, depending on the spin of the parent molecules $\{A D\}$, i.e., spin is conserved. Then the radical-pair recombination is only possible when the formed radicals stay in the initial state [20, 74, 76-79].

In radical-pair, the spins of the unpaired electrons are coupled to each other. Similarly, these spins of unpaired electrons can interact with the spin of the atomic nucleus which also has spin due to the nuclear particles, protons, and neutrons. The atomic nuclei isotopes with an odd number of protons, neutrons, or both have magnetic moments, hence spin. The most common magnetic isotopes in organic radicals are 1H ($I=1/2$) and ^{14}N (seven protons and seven neutrons) ($I=1$). The unpaired electrons in the radical-pair interact with themselves and several surrounding nuclei since the electron cloud in the molecule is delocalized. This is called hyperfine interactions. The hyperfine interaction is anisotropic when the radicals are aligned and partially or fully immobilized [80, 81]. The radical-pairs are also sensitive to the external magnetic field. The spins of the unpaired electrons in the radicals interacting with the external magnetic field are called Zeeman interaction. The atomic spin of the radical-pair can also interact with the external magnetic field, but it is negligible [20, 74, 78, 82].

The magnetic moments of the radical-pair also cause dipolar interaction between them. These dipolar interactions can affect the hyperfine and Zeeman interaction in the radical-pairs [20, 83]. In addition to dipolar interactions, spin-orbit coupling, and exchange interaction are also present in the radical-pairs. The spin-orbit coupling is the interaction between the electric dipole of radicals, its orbital motion, and the electrostatic force of the nucleus. Due to the spin-orbit interaction, the atomic energy level of electrons always shifts and causes non-radiative transitions between the two electronic states [84, 85]. The electrons in the radical-pair are considered identical and indistinguishable. This indistinguishability arises from the exchange interaction. The exchange interaction also unfavorably affects the hyperfine

and Zeeman effect in the radical-pair. The results of dipolar interactions, spin-orbit coupling, and exchange interactions can weaken with increase in the separation of radical-pair [20, 74, 86].

Usually, the radical-pair is in {S} or {T} state while it is forming, if the spin-orbit coupling in the system is negligible. The exchange interaction in the radical pair keeps them oriented with respect to each other. After a certain time, the radical pair in the initial state undergoes intersystem crossing and forms the other spin state, spin mixing. Then, there will be an interconversion between {S} and {T} state due to hyperfine interaction. This process can be understood easily using a vector model spin mixing in radical pair [87, 88]. The spin and nuclear angular momentum of each radical couple each other, and they precess around their resultant in the angular frequency $\omega_p = \frac{g_i \mu_B B_{eff,i}}{\hbar}$. In this equation,

g_i is g -factor characterize the three magnetic moments (spin, orbit and total angular momentum) of an electron in radical i , μ_B is Bohr magneton, magnetic moment of an electron caused by spin or orbital angular momentum. $\mu_B = \frac{e\hbar}{2m_e}$, e charge of electron, m_e is electron mass, and \hbar is reduced plank constant. Here $B_{eff,i} = B_{hyp,i} + B$ is effective magnetic field at the electron in the radical i due to the hyperfine interaction ($B_{hyp,i}$) and external magnetic field (B). Even in the absence of B , each radical experiences different B_{hyp} in the pair due to difference in the hyperfine coupling. B_{hyp} in the radical can be calculated using the equation $B_{hyp} = \sqrt{\sum_k (a_k / |\gamma|)^2 I_k (I_k + 1)}$ [81, 89-91]. Here in the equation,

the sum is over all of the nuclear spins in the radical i , a_k is the isotropic hyperfine constant associated with nuclear spin k , I_k is its spin quantum number, and γ is the gyromagnetic ratio (ratio of magnetic moment to the angular momentum) of the electron in radical i . γ is related to the g as $g = \pm \frac{\gamma\hbar}{\mu}$. So, the differences in B_{hyp} in the radical cause different precession rate around different axes in pair. This will eventually change the initial relative orientation of the spin of electrons in the radical pair, hence the spin state of the radical pair. If g_i and $B_{hyp,i}$ is same for each radical in pair, they keep coherent precession and a constant 180° phase difference between the spins as they precess. But g_i and $B_{hyp,i}$ are different in both radical, then these differences will eventually leads to {S}-{T} state conversion. [87, 88, 92]. Then the frequency of this conversion is determined by difference in B_{hyp} and g_i values of the two electrons in the radical-pair [20, 74, 81, 88-90].

The radical-pair can undergo interconversion between {S} and {T} states in the presence of an external magnetic field, B called quantum beating, if they are spatially separated well enough, and both spin

states have the same energy. This is Zeeman interaction. In presence of B the spin and nuclear magnetic momentum of each radical in pair also continues their precession around their resultant. But now, the resultant magnetic moment precess around the direction of B . This causes the inversion of electron spin one radical with respect to B and to the other electron in the second radical [87, 92]. The interconversion between {S} and {T} state in radical pair is a coherent process, since the spin mixing in the radical-pair is driven by a constant magnetic field B_{eff} . The electrons in the radical-pair is coupling with different magnetic field through applied external field B , g -factor difference in radicals in the pair or hyperfine interaction. Then the radical-pair oscillate between {S} and {T} state. These oscillation is only damped once the radicals are removed by other reactions [88, 92]. The oscillation caused by B between {S} and {T} is slow compared with hyperfine oscillation, and its frequency (Larmor frequency) depends on the strength of B . The hyperfine oscillations are superimposed with external magnetic field oscillation in this case. For example, if we apply an external magnetic field of $\sim 50 \mu\text{T}$, corresponding to the average earth magnetic field, then the Larmor frequency is 1.4 MHz which has a modulation period of $\sim 700 \text{ ns}$ [20]. More importantly, since the hyperfine interaction is anisotropic, the oscillation between {S} and {T} states in the presence of an external magnetic field depends on its direction with respect to the radical-pairs. These oscillations between {S} and {T} states dramatically change when the direction of the external magnetic field switches [20, 74].

There are also different incoherent relaxation processes in radical-pair that affect coherent spin conversion processes. The spin-dephasing process is induced by diffusional fluctuation of exchange and dipolar interactions. The exchange and dipolar interactions are highly depend on inter-radical distance. So, they highly fluctuate during the re-encounter process of radical-pair. The time scale for the spin-dephasing is comparable with the coherent spin mixing process. This process randomly flips the spin of radical. Another incoherent process seen in radical-pair is longitudinal spin relaxation which arising from the local magnetic field fluctuations at the electron due to its random motion. The local magnetic field arises mainly from anisotropic hyperfine interaction. The magnetic field from this interaction may vary in time because of the random motion of radicals relative to B . If this random motion is slow, then it will affect the re-orientation of electron spin in B . This eventually changes the relative phase of the component of the spins of two electrons in perpendicular direction. The time scale of spin relaxation is in several hundreds of nanoseconds. If the incoherent processes are faster than coherent one, then the external magnetic field cannot alter the spin state of radical-pair. So, it is very crucial to have coherent process lifetime equal or greater than radical-pair life time [20, 87, 88, 92-94].

The radical-pair $\{A^{\bullet-} D^{\bullet+}\}$ initially formed either in {S} or in {T} state. Once the oscillations are established from the initial spin state to the other, the fates of both spin states differ. There is always a back reaction from the initial radical spin state to the parent molecule $\{A B\}$ with rate constant k_S . The back reaction from the other radical spin state to the parent molecule is spin forbidden. There is another

reaction with rate constant k_c from {S} and {T} radical states to product state {C}. The rate of back reaction and production of {C} state depend not only on the reaction rate constants k_s and k_c , but also on the extent and frequency of {S} to {T} interconversion. If there is enough external magnetic field and its frequency is equal to or greater than the Larmor frequency, more radical-pairs will be converted to the second spin state. Then, they are converted to the product, provided both reaction rates and relaxation process are slow so that radical-pairs can interact with a weak external magnetic field. So ideally, the yield of product {C} depends entirely on the direction and the strength of the external magnetic field B and lifetime of radical-pairs. So, the final yield of product state {C} consists of information about the direction of the external magnetic field B . Hence, the radical-pair mechanism can give exact compass information, “a quantum needle” to the avian magnetic compass [20, 74, 95].

The radical- pair-based magnetoreception is the only hypothesis that explains all the essential features observed by the behavioral experiments of migratory birds. The behavioral experiments show that birds have a magnetic inclination compass, which is used to identify equatorward and poleward directions. But not the north and south pole directions [37-40]. We have already seen that the oscillation between {S} and {T} states and the yield of the second spin state depends on the orientation of the radical-pair and the direction of the external magnetic field [11]. Ritz et al. [11] suggest that the product of the radical-pair mechanism affects the photoreceptor sensitivity and thus modulates the visual sense of the birds, resulting in brighter and darker regions in their visual fields [11, 96, 97]. When the birds look parallel or antiparallel to the magnetic field vector, they should see identical patterns generated from the product state {C} of the radical-pair mechanism. These patterns can only provide axial information. So it is clear that the avian compass cannot respond to the polarity of the magnetic field. The magnetic field intensity dependence of the avian magnetic compass can also explain using the visual patterns generated from the radical-pair mechanism. The field intensity can affect the contrast of brightness and shape of the visual modulation patterns created by {C}. So, birds could not orient to a sudden magnetic field intensity change outside a narrow functional window [3, 98-100].

Ritz et al. (2000) proposed blue-light sensitive cryptochrome protein as the photo-induced magnetoreceptor molecule for the first time [11]. This is because cryptochrome proteins were the only known photoreceptor molecule that could form radical-pairs upon photon excitation in vertebrates. Even after 22 years, there is no promising candidate other than cryptochrome protein molecules for light-induced magnetoreception in birds [27, 101, 102].

In the next section I.3 ,the structure of cryptochrome proteins, their functions, and the radical-pair mechanism in cryptochrome are briefly described.

I.3 Cryptochrome Proteins

Proteins are biological macromolecules, the primary building blocks of living cells. They are composed of one or more long chains of amino acid residues. The carboxyl group ($-COOH$) in the amino acid is attached to the amino group ($-NH_2$) of another amino acid by a covalent bond. This is known as a peptide bond. The amino acid in the peptide bond is called the residue. Usually, protein molecules consist of more than 20-30 peptide bonds. All the peptide has two ends, amino-terminal (N terminus) and carboxyl-terminal (C terminus). The N and C terminus residues in the proteins play a crucial role in the peptide chain. There are almost 20 different amino acids, which can combine and form different kinds of proteins. Each protein molecule has its unique three-dimensional structure, determined by the sequence of amino acids involved. The protein molecules have a variety of functions in the living cells, such as functioning like antibodies, enzymes, signaling, transportation, and structural components [103-107].

Cryptochrome proteins (Cry) are photoactive protein molecules that can be found throughout the biological kingdom, from bacteria to mammals. Cry was first identified in a plant, *Arabidopsis thaliana* functioning as blue-light and UV photoreceptors [14, 108]. The name cryptochrome originated from the two words, chromatic and cryptogamic. The first word indicates the nature of this photoactive molecule, which is sensitive to blue light. The second word is the name of specific plants used for many blue-light studies [109, 110]. Cry proteins are similar to photolyase in structure and photoactive domain and have similar chromophore cofactors. Photolyase proteins are known for their abilities for the light-dependent repair of UV-damaged DNA. Cry proteins are thought to evolved from photolyase without or with less ability for DNA repair but with signaling capability [111].

I.3.1 Structure of Cryptochrome Protein

The crystal structures of different types of Cry are available today. These structures show that cryptochrome proteins have a globular structure [112, 113]. The crystal structure of cryptochrome 4 from the pigeon (*Columba livia*) (protein bank, PDB 6PU0) is shown in Figure I. 1. Photolyase and Cry have identical three-dimensional structures in the amino-terminal photolyase homology region (PHR), characterized by a N – terminal α / β domain (Figure I. 1, blue cartoon) and a C – terminal α – helical domain (Figure I. 1, green cartoon). The N – and C – terminals are connected by an inter-segment region (Figure I. 1, gray cartoon). The plant and animal Cry have attained an additional extension of C – terminal that plays a crucial role in their several specific functions [8, 114-116].

Like photolyase, Cry also accommodates two chromophores that are non-covalently bound to the protein structure. The α – helical domain shelters the flavin adenine dinucleotide (FAD) cofactor

(Figure I. 1, magenta color structure). The crystal structures of different Cry indicate that the α/β domain binds a second chromophore, either 5,10-methenyl-5,6,7,8-tetrahydrofolate (MTHF) or 8-hydroxy-5-deazaflavin (8-HDF) [111, 114, 117]. In photolyase and some cryptochrome, the chromophore in the N -terminal α/β domain act as a light-harvesting antenna that absorbs near-UV range. After absorption, the excitation energy is transferred to the FAD cofactor through Förster resonance energy transfer [117] since there is a spectral overlap between the emission and absorption of light-harvesting antenna and FAD molecules [118]. The efficiency of these types of energy transfer dramatically depends on the distance between the two chromophores, which is in the range of 15-18 Å [14]. But in most of the Cry, the second chromophore is not significant for its signaling functioning [114, 119].



Figure I. 1 Structure of cryptochrome. Illustration of cryptochrome based on the crystal structure of pigeon cryptochrome 4 (Cry4) (protein bank-PDB 6PU0). The photolyase homology region (PHR) has an N -terminal α/β domain (blue cartoon) and C -terminal α -helical domain (green cartoon) connected by an extensive inter-region segment (grey cartoon). The C -terminal of cryptochrome consist flavin adenine dinucleotide (FAD) (magenta structure) as a chromophore. The four tryptophan residues involved in the photoinduced electron transfer in Cry4 are shown in red [3, 8, 9].

I.3.2 Cryptochrome Classifications and Their Functions

Blue light mediates numerous functions in organisms through Cry protein. There are mainly three types of Cry proteins, plant, animal, and DASH (Drosophila, Arabidopsis, Synechocystis, Homo). All these Cry evolved from different subfamilies of photolyase protein. Here the plant and animal Cry have lost their DNA repair activity during evolution but have other signaling functions in numerous plant and animal systems. But the DASH Cry retains its DNA repair activity [120], and its role in signaling is not

yet confirmed [14, 121]. Recent studies also indicate that the DASH Cry can also function as a transcriptional regulator (conversion of DNA to RNA) [122, 123] and participate in circadian input pathways [114, 124].

As pointed out earlier, Cry was first identified in a plant, *Arabidopsis thaliana*, for its role in inhibiting hypocotyl elongation [14, 108]. Then it was identified in numerous other plants, based on its DNA sequences. There are mainly two types of plant Cry, Cry1 and Cry2. Cry1 protein controls anthocyanin production and chalcone synthase gene expression [125]. Cry2, which is also more sensitive to low blue-light irradiances, is responsible for the photoperiodic initiation of flowering [126]. Cry1 and Cry2 have some identical functions in plant growth and development, such as clock function-entrainment of the plant circadian clock and shortening of the period length in the light, hypocotyl growth inhibition, blue light-dependent random hypocotyl-bending, regulation of the flowering time, regulation of stomatal opening (CO_2 intake), enhancement of phototropism (growth in response with light) under low fluence rate blue light, and primary root elongation [14, 114, 125]. Recently five types of plant Cry were identified (Cry1, Cry2, Cry3, Cry4, and Cry5) in fern *Adiantum capillus-veneris* which all have general functioning of Cry protein. The more specific roles of these Cry are under investigation [125].

In addition to plants, Cry is also present in animals. The animal type Cry can be classified into three categories, type I, type II, and type IV. Type I Cry is found in insects [8]. The best studied type I Cry is from insects, especially *Drosophila*. The studies disclosed that type I Cry is a circadian photoreceptor involved in light-mediated entrainment of the circadian clock [127]. In vertebrates exist the type II Cry. Type II Cry is generally considered a light-independent transcriptional regulator of the clock [14, 128]. But their roles are still under debate [129]. Different sub-divisions of type II Cry, Cry1a, Cry1b, Cry2a, and Cry2b are found in other vertebrates also [8, 14, 100, 130-134]. Here “a” and “b” represent different isoforms, long or short slicing variants of Cry. The Cry2 in the birds may have an active role in the light-independent circadian clock. The exact function of Cry1b is not determined yet [3, 100]. The Cry1 and Cry2 from mouse models show that they control circadian oscillator rather than circadian photoreceptors in mammals [135].

The last type of animal Cry, type IV called Cry4, has been found in birds, frogs, sea turtles, and fish. Cry4 is thought to have an essential role in the long-range navigation of birds, amphibians, and fish, using the earth magnetic field [33, 35, 41, 136-140]. Two types of Cry4 are found in European robins, Cry4a and Cry4b. They are found in the retina of migratory birds. Unlike Cry4a, Cry4b exhibits 24-hour mRNA circadian expression patterns, which shows that it has a function in circadian rhythm regulation [114, 141, 142].

There are different types of Cry, and their subcategories are present in plants and animals. Each subcategory of Cry has various functions, some of which need to be further investigated.

I.3.3 Cryptochrome Signaling and Photoactivation

The different functions of various types of Cry were explained in the previous section. All these are signaling functions. Evidence for light-initiated conformational changes in the photoreceptor domains of Cry has already been reported during the functioning of proteins. These conformational changes allow the signaling functioning of proteins [115]. In cryptochrome, as well as in photolyase, the chromophore in the α -helical domain, FAD, plays a significant role in its functioning. For example, in the DNA repair mechanism in the photolyase protein, an electron transfer occurs between photo excited fully reduced FAD (FADH^-) to UV-damaged DNA. But there are no DNA repair functions in the case of plant and animal Cry. However, in the photolyase and Cry proteins, an electron is transferred to the excited FAD through a chain of amino acids, called tryptophan (or tyrosine residue), from the protein surface, after blue light excitation. This is called photoactivation. Since in most of the Cry, the intramolecular electron transfers through the tryptophan (Trp) residues (Figure I. 1, red color structure) are conserved, this photoactivation process is thought to be important in its signaling process [14, 143, 144]. During these photoactivation processes, different oxidation and redox states of FAD and Trp are involved in various signaling stages.

I.3.3.a Flavin Adenine Dinucleotide

Flavin adenine dinucleotide (FAD) is a vital chromophore molecule in different proteins such as DNA-photolyase [111], phototropins [145], BLUF proteins [146], and as well in cryptochromes [108]. Due to their exciting response to blue light and participation in photo-induced biological processes, the photophysical properties of FAD have already undergone numerous spectroscopic and structural studies [10, 19, 22, 147-149]. The chemical structure of the FAD molecule is shown in Figure I. 2 (a). In FAD, an isoalloxazine moiety $\text{C}_{10}\text{H}_6\text{N}_4\text{O}_2$, also called flavin (Figure I. 2, blue structure), determines the fundamental properties of molecules. Different flavin groups can be formed by varying the side chains to isoalloxazine moiety. Lumiflavin, Riboflavin, Flavin Mononucleotide (FMN), and FAD are common flavin groups [10, 149].

In FAD, an isoalloxazine ($\text{C}_{10}\text{H}_6\text{N}_4\text{O}_2$) moiety (Figure I. 2 (a), blue structure) is attached to an adenine moiety (Figure I. 2 (a), red structure) through a D-ribitol ($\text{C}_5\text{H}_{12}\text{O}_5$), Pyrophosphate ($\text{P}_2\text{O}_7^{4-}$), and D-Ribose ($\text{C}_5\text{H}_{10}\text{O}_5$) chain (Figure I. 2 (a) metallic black structure). The adenine and isoalloxazine moieties in the FAD molecule can be oriented at a different distance apart and form different conformers of FAD molecules. There are mainly three FAD conformers in the solution in the pH range 3-12, stacked or closed (Figure I. 2 (b)), un-stacked or open (Figure I. 2 (c)), and semi-stacked (Figure I. 2 (d)). These conformers form by varying the orientation distance between adenine and isoalloxazine moieties. The distance between adenine and isoalloxazine rings in the stacked conformer is below 5-6 Å. So there will

be a fast electron transfer from adenine to isoalloxazine ring within 5 ps after the photoexcitation of the isoalloxazine moiety [16, 22]. As a result, the fluorescence emission of the FAD molecule is quenched within this time frame in the stacked conformer. The adenine and isoalloxazine rings are separated between 6 to 10 Å in the semi-stacked form. By varying these distances, different semi-stacked conformers can be formed by the FAD molecules. All these semi-stacked conformers have a fluorescence lifetime between 2 to 2.5 ns. The unstacked conformer of FAD has a long fluorescence lifetime of 4 ns. In the unstacked form, the isoalloxazine and adenine are greater than 10 Å apart. The fast electron transfers between adenine and excited isoalloxazine are nearly impossible in this case. In a solution, the concentration of stacked conformers is dominant in the pH range of 5 to 10. So the FAD molecule has only a low fluorescence quantum yield (0.03) in this pH range [19, 149]. The open conformer of FAD can also undergo an irreversible transformation to closed conformers through photoisomerization (light-induced isomerization) in the excited state of FAD molecules [149].

Unlike solutions, Cry only consists of the stacked conformer of FAD molecule in the photoactive domain of proteins that actively participate in the signaling functions through intramolecular electron transfer through Trp chains [150, 151]. In Crys, an ultrafast electron transfer occurs to the excited isoalloxazine moiety in the FAD from the nearest Trp residue [16, 152, 153]. This charge separation is possible in Cry proteins since there are Trp residues in the closer vicinity of the isoalloxazine ring than the adenine moiety, less than 4 Å (see Figure I. 7 (b)) [16, 154]. Moreover, the ionization potential of the Trp residue is less than that of adenine moiety, which makes Trp an ideal electron donor for excited FAD in Cry rather than the adenine moiety [155, 156].

Usually, there are different oxidized and reduced states of the FAD chromophore participating in the signaling functions in the protein molecules. They are quinones (fully oxidized FAD), semiquinones (semi reduced, one electron reduced from quinones), and hydroquinones (fully reduced, two electrons reduced from quinones) (see Figure I. 3) [157]. Depending on the pH of the solution, each of these redox states of FAD can exist in cationic, neutral, and anionic forms. The structure of these forms is shown in Figure I. 3 for different redox states of FAD. In Figure I. 3, the 'R' in the chemical structures represent D-ribitol ($C_5H_{12}O_5$), pyrophosphate ($P_2O_7^{4-}$), D-ribose ($C_5H_{10}O_5$), and adenine moiety ($C_5H_5N_5$) part in the FAD molecule (Figure I. 2 (a), metallic black and red structures) in the FAD molecules.

In a solution with a pH range of 3-10, the FAD molecule could exist in its fully reduced neutral form FAD_{ox} . But in flavoproteins, different neutral and anionic redox states of FAD molecules participate in their photoactivation process, see Figure I. 4. For example, in photolyase, FAD exists as the semi reduced neutral radical, $FADH^\bullet$. Then the photo excited $FADH^\bullet$ ($FADH^{\bullet*}$) is reduced to $FADH^-$ through the three tryptophan residues conserved in the surface of the protein (Figure I. 4, dashed square

parts) [12, 158, 159] within hundreds of femtosecond (fs) [12, 160]. In the case of Cry, FAD exists in its fully oxidized neutral form FAD_{ox} . It is considered the most stable form of FAD molecule in Cry. FAD_{ox} has a broadband absorption band ranging from 300 to 500 nm with absorption peaks at 375 and 450 nm (solid blue line, Figure I. 5(a)). Blue light excitation brings the FAD_{ox} to its excited state FAD^*_{ox} (see Figure I. 4). Then electron transfer from the nearest Trp residue to the FAD_{ox} , creating a FAD anion radical, $\text{FAD}^{\bullet-}$ in ~ 0.4 picoseconds (ps) [153, 161, 162]. $\text{FAD}^{\bullet-}$ is also sensitive to blue light with a broad absorption spectrum (solid blue line, Figure I. 5 (b)). The excited state of $\text{FAD}^{\bullet-}$ ($\text{FAD}^{\bullet-*}$) can emit yellow light (440 to 650 nm) and go back to its ground state $\text{FAD}^{\bullet-}$ within a 140 ps time scale. Once the anion radical is formed, either charge recombination with Trp brings the ground state of FAD_{ox}

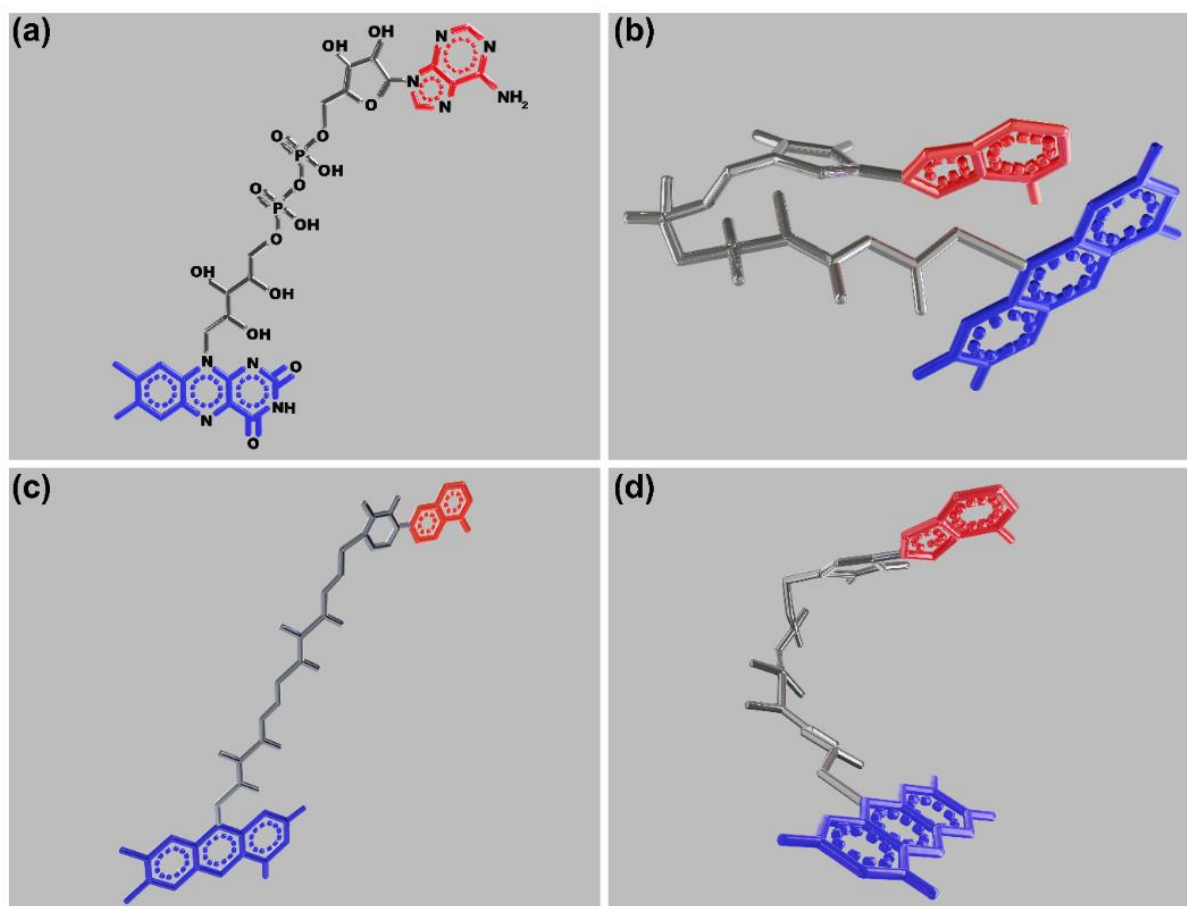


Figure I. 2 Structure and different conformations of flavin adenine dinucleotide (FAD). (a) Structure of FAD molecule. An isoalloxazine moiety ($\text{C}_{10}\text{H}_6\text{N}_4\text{O}_2$) (blue) is connected to the adenine moiety ($\text{C}_5\text{H}_5\text{N}_5$) (red) through a D-ribitol ($\text{C}_5\text{H}_{12}\text{O}_5$), pyrophosphate ($\text{P}_2\text{O}_7^{4-}$), and D-ribose ($\text{C}_5\text{H}_{10}\text{O}_5$) chain (metallic black). By varying the orientation distance between isoalloxazine and adenine moiety, different conformations of FAD molecules, (b) stacked or closed ($< 5\text{-}6 \text{ \AA}$), (c) un-stacked or open ($> 10 \text{ \AA}$), and (d) semi-stacked ($6\text{-}10 \text{ \AA}$) can be formed [18, 19]. These conformers are present in a solution with pH range 3-12.

within 20-80 ps or FAD anion radical, $\text{FAD}^{\bullet-}$ undergoes further consecutive electron transfer reaction from the Trp chains in the protein surface. In the presence of oxygen, $\text{FAD}^{\bullet-}$ also can slowly reoxidize

to FAD_{ox} within a minute. The protonation (H^+) of $\text{FAD}^{\bullet-}$ causes the generation of FAD neutral radical,

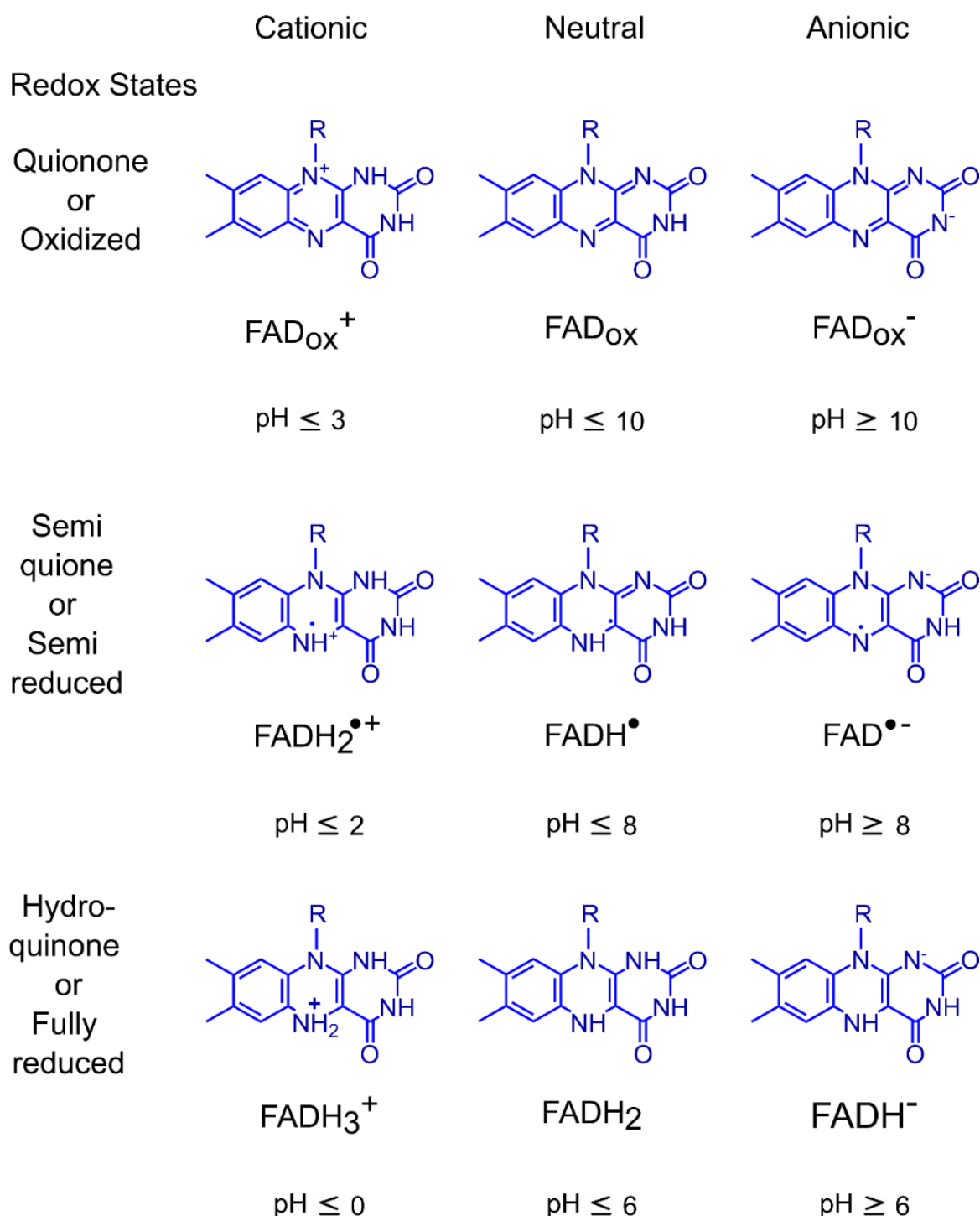


Figure I. 3 Different redox and acid-base moieties of flavin adenine dinucleotide (FAD). FAD can exist different redox state in solution and flavoproteins. Each redox state can be existing in different cationic, neutral and anionic states depends on the pH of medium [10]. The 'R' representation in the figure indicates D-ribitol ($\text{C}_5\text{H}_{12}\text{O}_5$), pyrophosphate ($\text{P}_2\text{O}_7^{4-}$), and D-ribose ($\text{C}_5\text{H}_{10}\text{O}_5$) and adenine moiety ($\text{C}_5\text{H}_5\text{N}_5$) part in the FAD molecule (Figure I. 2 (a), metallic black and red structures).

FADH^\bullet . However, this is a very slow process, that happens in hundreds of milliseconds (ms) time scales in Crys. FADH^\bullet has a broad absorption band ranging from 300 to 700 nm (Figure I. 5 (c), solid blue line). Blue or green light excitation again photo reduces the FADH^\bullet to FADH^- within 20 ps. FADH^- can be further excited by blue light (300 to 500 nm, Figure I. 5 (c)). FADH^- can also undergo charge recombination and return to FADH^\bullet . In another case, FADH^- can reoxidize to FADH^\bullet as a slow process under aerobic conditions. Similar to $\text{FAD}^{\bullet-}$, the FADH^- can also participate in consecutive electron transfer reactions with Trp in the photolyase protein [2, 12, 153, 162-164].

Ultraviolet-visible (UV) (300 to 700 nm) absorption spectra of different redox states of FAD molecules are shown in Figure I. 5 in a solid blue line. These spectra are reported in Kao et al. for insect type cryptochrome and photolyase proteins [2]. The electronic transitions from the highest occupied molecular orbital (HOMO) to the lowest occupied molecular orbital (LUMO) create the absorption spectrum of the molecules. The absorption spectra of FAD in the visible range (400-700 nm) are from

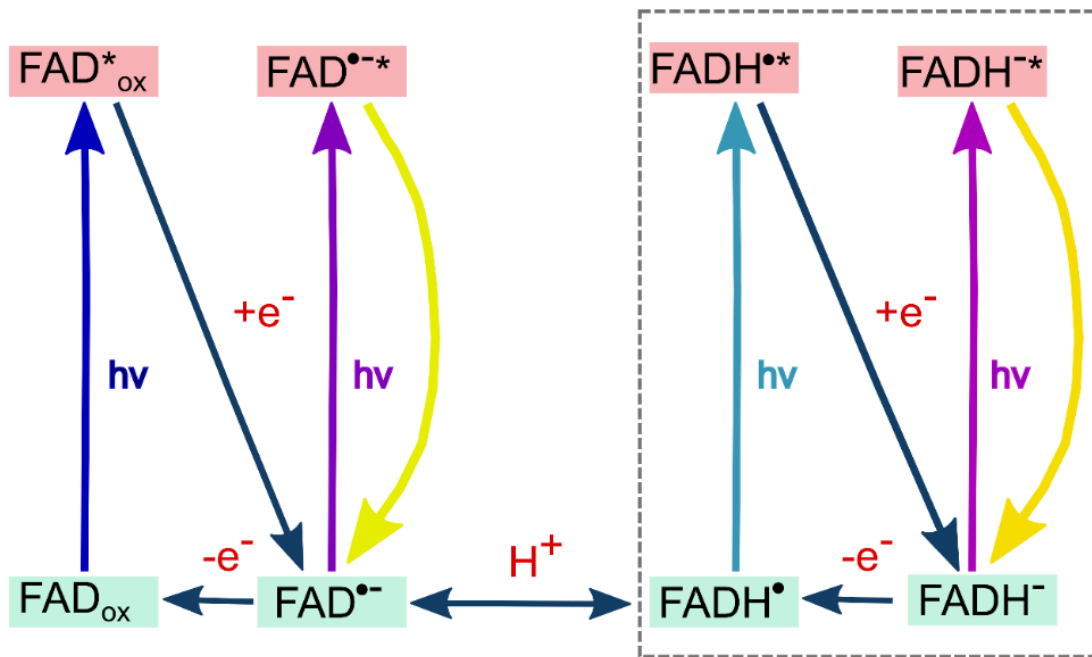


Figure I. 4 Photoactivation of flavin adenine dinucleotide (FAD) in cryptochrome and photolyase (right dashed square) protein. The photocycle of cryptochrome is starting from fully oxidized neutral FAD (FAD_{ox}). Blue light excitation on FAD_{ox} creates its excited state FAD^*_{ox} . Then an electron (e^-) from the tryptophan residue is transfer to FAD^*_{ox} and form the semi reduced anionic FAD radical ($\text{FAD}^{\bullet-}$). $\text{FAD}^{\bullet-}$ can further excited by UV-A (315 to 400 nm) to blue light and form $\text{FAD}^{\bullet--*}$ and then de-excited to $\text{FAD}^{\bullet-}$. Semi neutral radical of FAD, FADH^\bullet is formed by the protonation (H^+) of $\text{FAD}^{\bullet-}$. In the photolyase protein the photocycle starts from FADH^\bullet and it has a broad absorption band from 300 to 700 nm. An electron is transferred from tryptophan to FADH^{\bullet} creating fully reduced anionic FAD, FADH^- . UV-A light can create the $\text{FADH}^{\bullet-}$ state which will be de-excited to FADH^- by yellow light emission (500-600 nm). The interconversion from each redox state is slow, but possible from the ground state under aerobic condition [2, 12-14].

the electronic transition in the molecular orbitals of the isoalloxazine ring of FAD (Figure I. 2 (a), blue structure) molecules. The electronic transition in the adenine ring of FAD molecules causes an

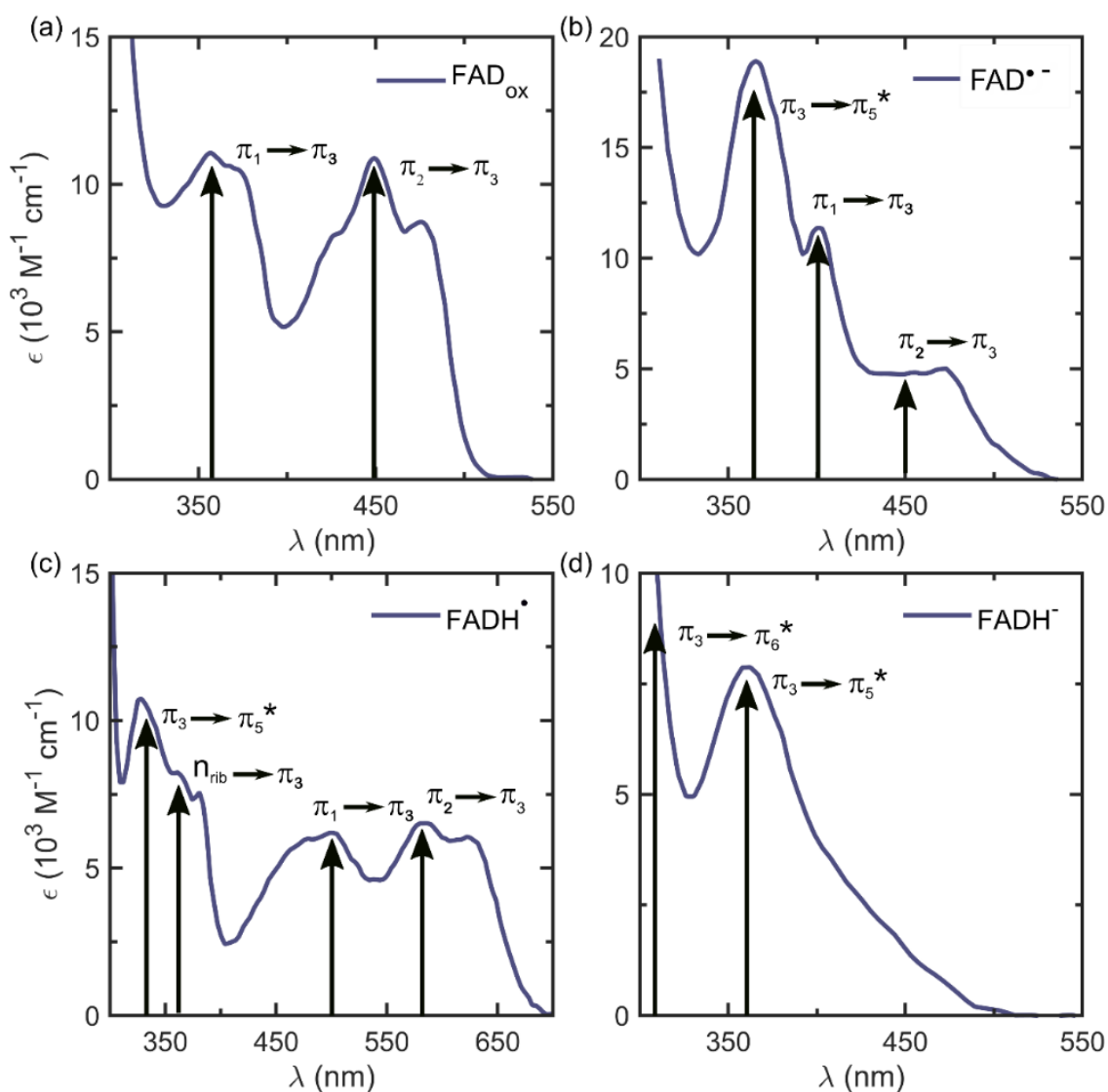


Figure I. 5 Ultraviolet-Visible absorption spectrum (solid blue line) and associated molecular orbitals of different redox state of flavin adenine dinucleotide (FAD) molecules [1-3]. The fine structures in the absorption spectrum represents the vibrational transition in the molecular orbitals. Absorption spectrum of (a) fully oxidized FAD (FAD_{ox}), (b) semi reduced anion radical, (c) semi reduced neutral radical, and (d) fully reduced anion FAD. In the case of FAD_{ox} π_3 is the lowest occupied molecular orbital (LUMO). For the neutral and anion radical forms π_3 is a singly occupied molecular orbital (SOMO). In the fully reduced forms π_3 is highly occupied molecular orbital (HOMO).

absorption band in the ultraviolet region [10, 154, 157, 165]. Usually, the UV region absorption spectra of molecules correspond to the electron transitions in the π molecular orbital or non-bonding (n) orbital. In different redox states of FAD molecules, the π_3 molecular orbital plays a vital role in its absorption spectra. In FAD_{ox} , the π_3 orbital is the LUMO. The peaks at 375 and 450 nm in the absorption spectrum of FAD_{ox} represent $\pi_1 \rightarrow \pi_3$ and $\pi_2 \rightarrow \pi_3$ electronic excitation, respectively. The π_3 orbital also accepts electrons from the lower-lying π orbitals and oxygen lone-pairs on the phosphate (n_{phos}) and the ribitol (n_{rib}) chain. These transitions are dark and overlap with the $\pi_1 \rightarrow \pi_3$

transition. The fine structure around these prominent peaks (at 350, 375, 430, and 475 nm) indicates vibronic transitions between different electronic levels. After the photoexcitation of FAD_{ox} inside the Cry protein, an electron is transferred to the π_2 molecular orbital and forms $\text{FAD}^{\bullet-}$. Then the π_3 orbital becomes singly occupied molecular orbital (SOMO) for the FAD anion radical. The most intense electronic transition for $\text{FAD}^{\bullet-}$ is from SOMO π_3 to LUMO π_5^* (365 nm). Similar to FAD_{ox} in $\text{FAD}^{\bullet-}$ also, the $\pi_2 \rightarrow \pi_3$ transition is observed at 450 nm (Figure I. 5, (b)). The $\pi_1 \rightarrow \pi_3$ transition of $\text{FAD}^{\bullet-}$ observed at 400 nm is slightly red-shifted compared to FAD_{ox} . The molecular transitions observed in $\text{FAD}^{\bullet-}$ are also present in the absorbance spectra of FADH^{\bullet} . However, the most intense transition $\pi_3 \rightarrow \pi_5^*$ is blue shifted to 325 nm for FADH^{\bullet} . The other molecular transitions $\pi_1 \rightarrow \pi_3$ (450 nm) and $\pi_2 \rightarrow \pi_3$ (600 nm) are red-shifted from $\text{FAD}^{\bullet-}$. These blue and red shifts in the transitions are due to an increase and decrease in the energy gap between the respective molecular orbitals. An additional absorption peak at 360 nm appears for FADH^{\bullet} , which indicates $n_{\text{rib}} \rightarrow \pi_3$ molecular transition. Further addition of an electron to the FADH^{\bullet} creates fully reduced neutral FAD, FADH^- . This reduction process converts the π_3 SOMO into HOMO. Then the intense transition in the absorption spectrum of FADH^- is $\pi_3 \rightarrow \pi_5^*$ at 360 nm. For FADH^- , another transition between the $\pi_3 \rightarrow \pi_6^*$ molecular orbital appears below 300 nm [1, 2].

I.3.4 Cryptochrome as a Magnetoreceptor Molecules

Cryptochrome-mediated magnetic-field dependent effects are reported for the plant, *Arabidopsis thaliana* [166] and fruit-fly *Drosophila melanogaster* [167]. Studies on *Arabidopsis thaliana* have shown that applying a weak magnetic field on its seedlings creates an enhanced cryptochrome response. At the same time, applying a weak magnetic field on the plants causes inhibition of hypocotyl elongation and anthocyanin accumulation as its response to higher-intensity blue light [168]. In the fruit-fly (*Drosophila melanogaster*), the application of a weak magnetic-field shortens the period of the circadian clock. Nevertheless, the absence of the fields lengthens the circadian clock period [167, 169]. In addition to circadian activity, low intensity magnetic fields alter locomotor activity [169], binary choices in T-mazes [170], geotaxis [171], orientation towards food sources [172], and seizure responses in fruit-flies[173]. These strands of evidences suggest that cryptochrome proteins have magnetic responses on weak fields, but they do not prove that Cry has magnetic sensitivity.

Cry molecules were first recommended as a probable magnetoreceptor by Ritz et al. in 2000 [11] due to their ability to form radical-pairs by electron hopping through the Trp chain conserved in the protein surface after the photoexcitation of the chromophore molecule FAD. Cry is the only photoreceptor protein molecule in magneto sensitive animals that can form radical-pairs upon photoexcitation [101, 102, 114]. Evidence for the magnetic field effects on the quantum yield and reaction kinetics of radical-pairs forming in Cry was first reported for *Escherichia. coli photolyase* (*E. coli photolyase*) [174]. Then further studies in Cry in *Drosophila melanogaster* [175] and *Arabidopsis thaliana* [21] proved the same magnetic field effects on radical-pairs observed in *E. coli photolyase*. Furthermore, the DASH-type Cry from *Xenopus laevis* (African clawed frog) behaves similarly to plant and fruit-fly cryptochrome [17]. But *Drosophila melanogaster* possesses a fourth Trp residue in the photoreduction of FAD chromophore different from those of *E. coli photolyase*, *Arabidopsis thaliana*, and *Xenopus laevis* [163]. From all these studies, a general radical-pair scheme in Cry is proposed and shown in Figure I.

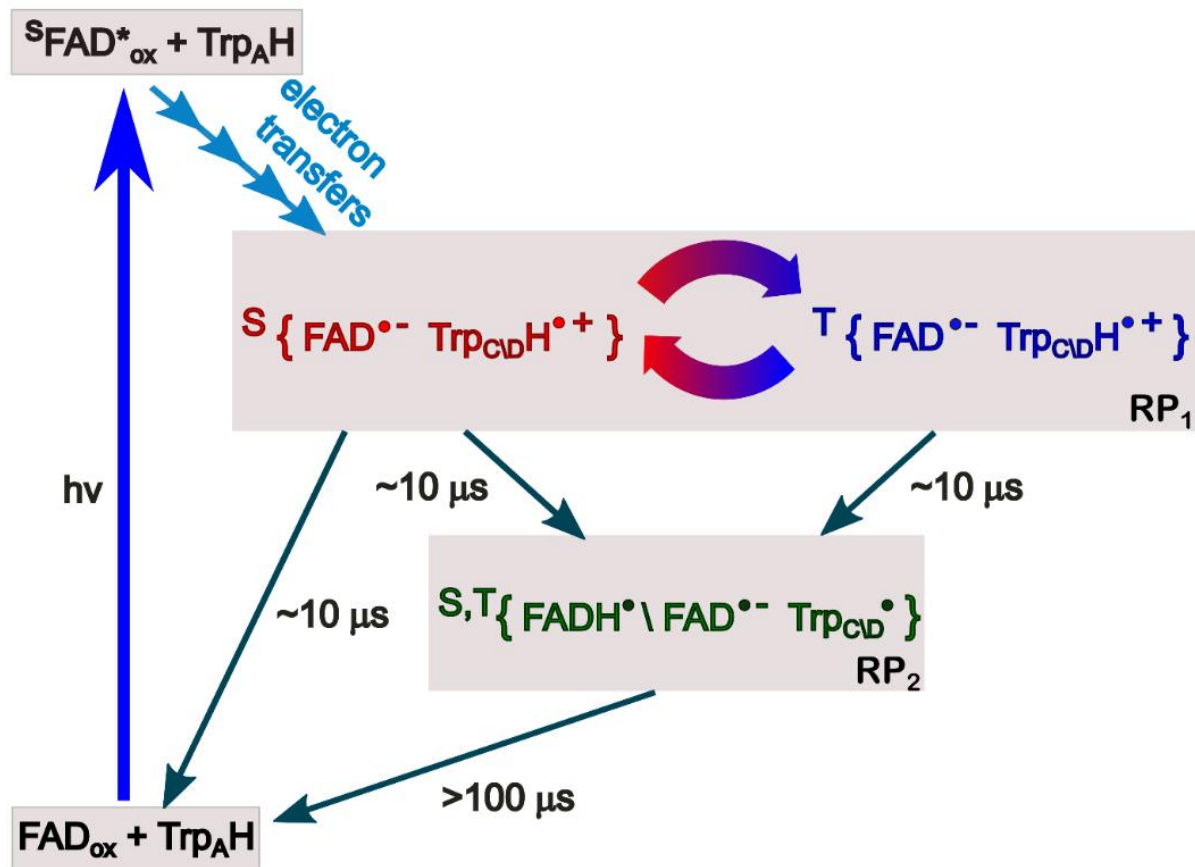


Figure I. 6 The currently proposed light-induced radical-pair mechanism in the cryptochrome protein molecule [11]. The first radical-pair $\text{RP}_1 \{ \text{FAD}^{\bullet-} \text{Trp}_{\text{CD}}\text{H}^{\bullet+} \}$ is formed in a singlet state by the spin-conserving transfer of an electron along the tryptophan triad or tetrad (Trp_{A} , Trp_{B} , Trp_{C} or Trp_{D}) to the photo-excited singlet state of the FAD_{ox} (FAD^*_{ox}) on an ultrafast time scale. Then singlet to triplet interconversion (curly arrows) happens in the presence of external magnetic field. This process follows either by spin-selective charge recombination within the singlet state, which reproduce the ground state of the cryptochrome protein or else by a spin-independent change in the protonation state of one or both radicals to form a secondary radical-pair (RP_2) within $10 \mu\text{s}$. The RP_2 acts either as signaling state or as its forerunner. The life time of RP_2 is $\sim 100 \mu\text{s}$ [3, 18-21].

6 [11, 20, 21, 174]. According to the current proposal, the radical-pair mechanism in Cry protein starts from the ground state of FAD_{ox} and the Trp_H state of the nearest tryptophan (Trp_A) to FAD (FAD-Trp_A , ~ 0.4 nm) (see Figure I. 7 (b)) [154]. Behavioral experiments have shown that migratory birds could orient to the traveling direction under the light with a wavelength range of 370 to 565 nm (blue light). These spectral ranges matches the absorption band of FAD_{ox} [37, 43]. Blue light excitation brings the FAD_{ox} to its excited state, FAD_{ox}^* . Then the FAD_{ox}^* is photo reduced to $\text{FAD}^{\bullet-}$ by the ultrafast electron transfer from the Trp_A and forming $\{\text{FAD}^{\bullet-} \text{Trp}_\text{A}\text{H}^{\bullet+}\}$. There will be another two or three consecutive spin-conserving electron transfers between the associated Trp chains (Trp_B , Trp_C , and Trp_D), $\text{Trp}_\text{A} \rightarrow \text{Trp}_\text{B}$, and $\text{Trp}_\text{B} \rightarrow \text{Trp}_\text{C}$; if a fourth Trp is involved in this transfer reaction, then $\text{Trp}_\text{C} \rightarrow \text{Trp}_\text{D}$. This will generate radical-pair $\{\text{FAD}^{\bullet-} \text{Trp}_{\text{C/D}}\text{H}^{\bullet+}\}$ (RP_1) in a singlet $\{S\}$ state [11, 20]. The spin-correlated RP_1 has a microsecond lifetime and can interconvert between singlet and triplet $\{T\}$ states by hyperfine and Zeeman effects. The RP_1 has two proceeding pathways; it can revert to the ground state or generate a long-lived second radical-pair (RP_2). Due to the spin conservation, only from the singlet state of RP_1 can recombine and form the ground state. Both the singlet and triplet states of RP_1 can create RP_2 ($\{\text{FAD}^{\bullet-}/\text{FADH}^{\bullet} \text{Trp}_{\text{C/D}}\bullet\}$) by spin independent deprotonating of the $\text{Trp}_{\text{C/D}}\text{H}^{\bullet+}$ radical [21, 174, 176]. In *Arabidopsis thaliana*, the protonation of the $\text{FAD}^{\bullet-}$ radical is also observed [21] for RP_2 . RP_2 has a lifetime of 1 to 10 ms [101]. Since the spin correlations of RP_1 relax when RP_2 is recombined, then RP_2 is magnetically insensitive. The time-dependent probability of the singlet and triplet state of RP_1 can be altered using the external magnetic field. So the amount of RP_2 created in this radical-pair mechanism, once all the RP_1 has disappeared entirely, depends on the strength and direction of the external magnetic field [176]. The long-lived RP_2 is considered the signaling state or a forerunner for magnetoreception. This proposed light-dependent radical-pair mechanism fits the cryptochrome protein molecule as a magnetoreceptor [3].

As discussed in section I.1 , the behavioral studies on migratory birds pointed out that their magnetic compass is light dependent. According to the current proposal, the product of light-induced radical-pair magnetoreception alters the visual patterns of migratory birds and animals [11, 96, 97]. So, the magnetoreceptor molecule should be in an easily light receivable position. Several pieces of experimental evidence indicate that cryptochrome proteins are in the retina of night-migratory birds [100, 177]. In the retina of birds, Cry molecules are found in ganglion cells (retinal cells that communicate information from the eye to the brain), large, displaced ganglion cells (ganglion cells that are not part of the ganglion cell layer but in the inner nuclear layer) and in photoreceptor cells. Usually, the retina of birds has seven photoreceptor cells, a rod, double cones, and four types of single cones. When considering the cell anatomy, the membrane structure of the outer segment disc of photoreceptor cells and its associated structures or the inner segment provides an oriented cylindrical structure which will be an ideal location for the radical-pair based magnetoreception process. In addition, restricted mobility of radical-pairs is necessary for the directional magnetic-field effect. If the radical-pairs are

tumbled inside the protein molecule, the directional effect of the magnetic field will be averaged to zero [20, 114, 178, 179]. Another essential thing is that cryptochrome molecules should follow an aligned pattern in the retinal cells to have a correlated magnetic field response. All these immobility and alignment conditions are satisfactory for the Cry molecule found in the aforementioned retinal cells. So the cryptochrome protein molecule position in the photoreceptor cells is an ideal candidate for magnetoreceptor [20, 114, 178, 179].

The consecutive electron transfer reaction and radical-pair formation in the Cry molecule involve three or four Trp residues (Trp_A, Trp_B, Trp_C, and Trp_D) [20, 154]. In these sequential electron transfer reactions, the distance between each species (FAD→Trp_A, Trp_A→Trp_B, Trp_B→Trp_C, Trp_C→Trp_D) is almost 0.4 nm [154], and this allows a very rapid separation of electron spin. Finally, the radicals FAD^{•-} and Trp_{C/D}H^{•+} are separated for a distance of 1.5 to 2 nm once the electron transfer process is completed. This 2 nm separation ensures that the spin exchange and dipolar interactions cancel and allows {S}→{T} interconversion by the weak earth magnetic field and hyperfine interaction. If the radicals are separated by more than 2 nm, the radical formation cannot compete with other molecular processes in the protein, such as fluorescence and intersystem crossing. So the structural and kinetic aspects of the Cry molecule make it an excellent candidate for magnetoreception [20, 83, 180].

I.3.4.a Cryptochrome 4 as a Potential Candidate for Magnetoreceptor

Section I.3.2 explains different types of Crys and their function in detail. Six different animal types of cryptochromes have been identified in migratory birds. They are Cry1a, Cry1b, Cry2a, Cry2b, Cry4a, and Cry4b. Here a and b represent different isoforms, long or short slicing variants of Crys [8, 100, 141, 142, 177]. In the beginning, Cry1a, expressing and localizing in the UV cones, was considered the magnetoreceptor molecule since it can form light-induced radical-pairs and conformational changes. However further studies failed to show the signs of light-dependent activation of Cry1a [131]. The exact function of Cry1b, located in the retinal ganglion cells, displaced ganglion cells, and in the inner segment of the photoreceptor, has to be studied. Cry2a and Cry 2b avian cryptochrome are expressed in the retinal cells and have a light-independent role in the circadian clock.

After considering different types of Cry and its subcategories, type IV Crys are identified as magnetoreceptor molecules, especially Cry4a [33, 35, 41, 136-140]. There is no evidence for their magnetic field sensing in Mammals lacking Cry4 [114]. The other isoform, Cry4b, exhibits a 24-hour mRNA circadian expression pattern. So, it is evident that Cry4b has a role in circadian rhythm regulation [141, 142], and not as a magnetoreceptor. Interestingly Cry4a exhibits no significant circadian oscillation in its expression. In addition, the expression of Cry4a proteins is ~ 2.5 times higher in night migratory birds during their migratory season than in the non-migratory months. On the other hand, in the domestic chicken, Cry4a mRNA levels do not fluctuate in any season [3, 141, 142].

Other important aspects of the current radical-pair mechanism are that the protein should fix a relative alignment and distance between FAD and Trp triads to have a directional magnetic-field effect. The directional effect would average to zero if the radicals are rotated around without a fixed direction. So it is relevant to have FAD protein binding in cryptochrome if it is a magnetoreceptor molecule [20]. In purified Cry4 from chicken [181], pigeon [182], European robin [154], and zebra fish [181] has been found protein-bound FAD. However, in contrast, Kutta et al. [183] recently claimed that type II animal cryptochrome has a magnetoreception function but does not bind to FAD strongly. More importantly, the location of the Cry4 expression in night-migratory European robins is found in the outer segment of the double-cone and long-wavelength single-cone photoreceptor cells [141]. This is an ideal location for a light-dependent magnetoreceptor. So these different properties of Cry4a suggest that its function may differ from other types of Crys [8] and is a potential candidate for light-dependent magnetoreceptor [3].

I.3.4.b Possibility of Light Independent Radical-Pairs in Cryptochrome

The flavin and Trp based light-induced radical-pair mechanism is the currently existing and widely accepted magnetoreception in migratory animals and birds [11]. Different redox states of FAD, FAD_{ox}, FAD^{•-}, FADH[•], and FADH⁻ participate in this model. Each redox state has different photophysics and photochemistry and has various biological activities in other proteins. Recently Pooam and coworkers [184] proposed a light-independent re-oxidation step for magnetic sensitivity. Wiltshcko et al. proposed that another radical-pair {FADH[•] Z^{•-}} [185] forms in the darkness and is responsible for the orientation of European robins under the dark condition after light exposure. Now the identity of the Z[•] radical is proposed as superoxide (O₂^{•-}) [11, 74, 186]. But this radical-pair cannot explain the behavioral experiment results in European robin cryptochrome. These experiments proved that birds could not orient in yellow light (above 590 nm) [37]. If the radical {FADH[•] O₂^{•-}} plays a crucial role in magnetoreception in birds, they should also orient above 590 nm, since FADH[•] has a wide absorption spectral range from 300 to 700 nm (see Figure I. 5 (c)). So the cryptochrome based light-induced radical-pair mechanism is the most convincing magnetoreception in birds and animals [3].

I.4 Summary

Every year many birds travel during winter more than thousands of kilometers with centimeter accuracy from mild weather area to tropical or subtropical regions with their “tiny birds” brain. For precise navigation, they have map and compass information and use the geomagnetic field for sensing the details. However, the long-range navigation is different in the case of first time and experienced migrants. Young birds use the inherited information coded in their genes and the acquired knowledge before the journey; mostly, they only have compass senses. Adult migrants use their previous

experience as well as inherited information. They have a compass and positional information [3, 24, 25, 27-30, 34-36, 41].

The behavioral experiment results show that migratory birds possess a light-dependent magnetic compass. They orient for a short wavelength window of 390 to 565 nm. The magnetic compass of migratory birds is also sensitive to the earth magnetic field intensity, inclination (the angle between the geomagnetic field lines and the earth surface), and declination angle (angular deviation between magnetic and geographical North). These birds obtain positional and compass information using these geomagnetic field parameters [20, 27, 35, 37, 41, 45]. This received information is integrated with their sensory systems, altering their visual patterns [100]. So, these indicate that the primary sensory molecules should be in an easily light receivable position, like the retina of the birds [20, 100, 101, 177].

By considering all the properties of the magnetic compass in migratory birds, Schulten et al. (1978) proposed a light-induced radical-pair formation as the geomagnetic field sensing mechanism [20, 66], and Ritz et al. (2000) suggested that cryptochrome protein as the primary magnetic field detecting molecule [11]. The cryptochromes proteins are photoactive molecules that evolved from the photolyase protein without or with less ability of DNA repairing but with signaling capabilities [111].

The flavin adenine dinucleotide (FAD), a chromophore molecule non-covalently bounded to the cryptochrome, bridges the protein surface through a chain of three or four tryptophan amino acid residues. The fully oxidized FAD (FAD_{ox}), in its stacked conformer form [150, 151], is excited by the light wavelength range from 300 to 550 nm. The absorption spectral range of FAD_{ox} matches the orientation wavelengths of migratory birds. Then successive ultrafast electron transfers from the nearest three or four tryptophan chains (Trp_A , Trp_B , Trp_C or Trp_D) to the excited FAD_{ox} form the first radical-pair (RP_1) $\{FAD^{\bullet-} Trp_{H_{C/D}}^{\bullet+}\}$. Initially, the RP_1 is in the singlet state. Then the combined effects of hyperfine (spin coupling between electron and nuclear particles) and Zeeman effects (coupling between electron spin and external magnetic field) coherently oscillate the spin of the RP_1 between singlet and triplet states. The singlet to triplet interconversion ensues in the nanosecond (ns) to microsecond (μs) time scale. The oscillation frequency of these interconversion processes and yield of the triplet state of RP_1 depend on the direction of the external magnetic field, and the orientation of radical-pair, which give an inclination angle sensitivity to magnetic compass in migratory birds rather than its polarity. The fate of radical-pair in the singlet and triplet states are different. Either the singlet RP_1 can undergo a recombination process and generate the ground state of a molecule with reaction rate k_s or both singlet and triplet states of RP_1 generate a second radical-pair (RP_2) by spin-independent deprotonation or protonation of one or both radicals $\{FAD^{\bullet-} Trp_{C/D}^{\bullet}/ FADH^{\bullet} Trp_{C/D}^{\bullet}\}$ with rate constant k_c . The RP_2 act as the signaling or a precursor state and possibly alter the visual patterns of the migratory birds. The

intensity of the external magnetic field can change the contrast of the visual patterns generated by RP_2 . Thus, migrating birds are sensitive to external magnetic field intensity. RP_2 has a lifetime of ~10 milliseconds (ms). The yield of the RP_2 once all the RP_1 has disappeared completely depends on the presence and the direction of the external magnetic field. This is the origin of magnetic-field sensitivity in migratory birds according to the radical-pair based mechanism. The proposed radical-pair mechanism in cryptochrome could explain all the observed features of the avian magnetic compass [3, 20, 74, 76-81, 98, 99].

The cryptochrome proteins are classified into three categories, DASH (Drosophila, Arabidopsis, Synechocystis, Homo), plant, and animal types. Among them, animal cryptochrome, type IV cryptochrome, Cry4 is considered a magnetoreceptor [60 90, 112-116]. This is because 1) birds, amphibians, and fish that are sensitive to the magnetic field have Cry4. Mammals are insensitive to the magnetic field and lack Cry4 [114]. 2) The Cry4 protein purified from chicken, pigeon, European robin, and zebrafish are significantly bound FAD to protein, protein chromophore binding is essential for the directional effect of a magnetic field [20]. 3) Cry4 protein, especially the Cry4a isoform, shows much weaker circadian oscillations than other types of cryptochrome found in European robins. 4) Compared to non-migratory birds, the expression levels of Cry4a protein during the migratory season in European robin is highly elevating [3, 141, 142]. 5) The position of Cry4a, which is in the outer segment of the double-cone and long-wavelength single-cone photoreceptor cells, is an ideal location for the light-dependent magnetoreceptor [141]. So the distinctive properties of Cry4, particularly Cry4a, indicate an ideal magnetoreceptor candidate [33, 35, 41, 114, 136-140].

Even though the light-induced radical-pair mechanisms are widely accepted, the light-independent radical-pair mechanism for magnetic sensitivity of birds through different re-oxidation state FAD has also recently been recently proposed [184]. The evidence for these types of radical-pairs is still required. Another radical-pair $\{FADH^\bullet \ O_2^{\bullet-}\}$, between semi reduced neutral FAD radical ($FADH^\bullet$) and super oxidant radical $O_2^{\bullet-}$ formed in the dark has also been proposed as the radical-pairs responsible for the orientation of the European robin in the dark [11, 74, 185, 186]. However, the disorientation of the birds above 590 nm wavelength light is not in correlation with this proposal, since $FADH^\bullet$ has a broad range of absorption from 300 to 700 nm [37].

Migratory birds use the earth magnetic field as the primary sensory cue for long-range navigation. They receive the magnetic field sensitivity through the radical-pair mechanism using cryptochrome protein as detector molecules. In the cryptochrome, the formation of long-lived radical-pairs is triggered by blue light excitation of bound FAD chromophore and consecutive electron transfer along three or four tryptophan chains. Among different types of cryptochrome, cryptochrome 4, especially cryptochrome 4a in European robins, is thought to be responsible for geomagnetic sensitivity in migratory birds.

I.5 Outline of the Thesis

In the above sections, the long-range navigation of migratory birds using magnetoreception through the formation of light-induced radical-pairs in cryptochrome protein molecules was briefly described. Various behavioral experiments on migratory birds show that they have a very accurate and sensitive magnetic compass [3, 28, 34-39, 41], and studies on purified cryptochrome proteins provided evidence for magnetic sensitivity and radical-pair formation [101, 102, 114]. These experimental results are promising. However, these findings only answer some questions related to the long-range navigation and the magnetic sensitivity of migratory birds. In addition, it raises several other questions, such as how light-induced electron transfer processes in cryptochromes result in the efficient formation of magnetically sensitive radical-pairs? What factors make cryptochrome fit for such purposes as a magnetoreceptor? When this doctoral study was started, this was the state and facts of magnetoreception through radical-pair mechanism theory in birds. However, answering all the puzzles related to this magnetoreception process is impossible during a doctoral thesis. So, it was decided to approach this problem from its beginning phase.

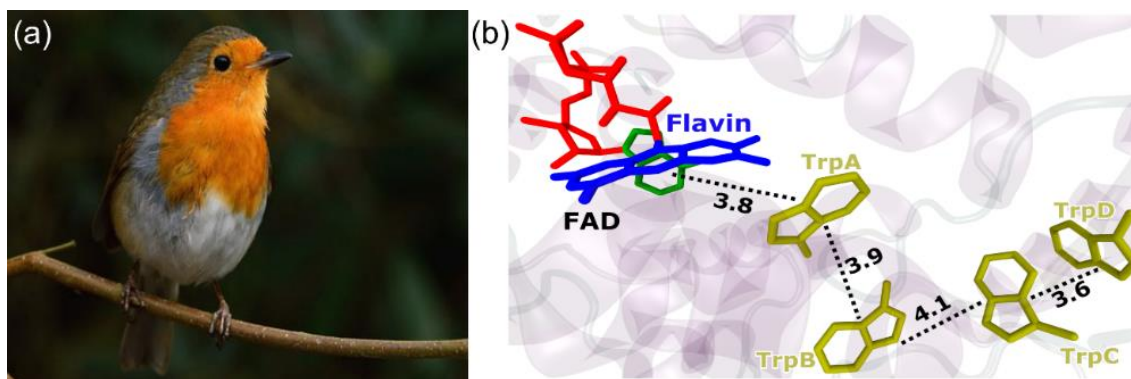


Figure I. 7 (a) Photograph of European robin bird (*Erithacus rubecula*) [7]. (b) Structure of European robin cryptochrome 4 (ErCry4) [16]. In ErCry4 flavin adenine dinucleotide (FAD) chromophore and four tryptophan W395 (Trp_A), W372 (Trp_B), W318 (Trp_C), and W369 (Trp_D) are involved in the photoactivation of protein [9]. The edge-to-edge distances between FAD and four tryptophan in ErCry4 are shown in Angstrom (Å) [20, 21].

An important aspect of the proposed radical-pair based magnetoreception is light-induced charge separation through flavin adenine dinucleotide (FAD) chromophore and tryptophan (Trp) chains of the cryptochrome protein molecules and the formation of radical-pairs. This charge separation and radical-pair formation is a very fast process in the fs time regime. When this thesis study was started on cryptochrome, the exact dynamics and quantum yield of the radical-pair formation, and the effects of protein environment in charge separation and radical-pair formation were unknown.

Another significant property of the magnetic compass in migratory birds is its directional effect. Migratory birds easily detect the directional changes of external magnetic fields. According to the proposed radical-pair mechanism, this is possible only by maintaining a fixed alignment and distance

between the formed radical-pair and protein molecules. So, the chromophore molecule FAD should bind with protein molecules rather than tumbling around in the protein environment. But Kutta et al. (2017) showed that type II animal cryptochrome does not bind FAD strongly, but still has magnetoreceptor function [183]. So, an investigation on chromophore protein binding in magnetoreception candidate Cry4 is another crucial question to be answered through this study.

In 2017, the Neurosensory/Animal Navigation working group at the University of Oldenburg successfully purified Cry4a protein from the European robin (*Erithacus rubecula*) [3, 154], a night-migratory bird (Figure I. 7 (a)) seen all over Europe. In European robins, two isoforms of Cry4 are present in the retina, ErCry4a and ErCry4b. Among them, ErCry4a is considered as the magnetoreceptor candidate (see section I.3.4.a). In this thesis, the ErCry4a protein is represented as “ErCry4”. The ErCry4 has not yet been crystallized, so the atomistic structure of the protein has not been known yet experimentally. However, the Gene sequencing [141] and computational modeling [141, 154] suggest that the protein structure is identical to that of pigeon (*Columba livia*) Cry4 (protein bank, PDB 6PU0). Similar to pigeon Cry4, ErCry4 also involved four tryptophan, namely Trp_A (W395), Trp_B (W372), Trp_C (W318), and Trp_D (W369) (Figure I. 7 (b)), in the photoactivation process [9, 16, 154].

The successful purification of ErCry4 (WT ErCry4) gives us a chance to characterize the structural, kinetic, and dynamic factors of a migratory bird cryptochrome with femtosecond (fs) resolution without the magnetic sensing function for this doctoral study, in which the photophysical properties, protein chromophore environmental features, efficiency, and timescales of the photo-induced charge separation process in ErCry4 were investigated by analyzing the early phases of the photocycle of WT ErCry4 and its four mutants (four tryptophan involved in the photoactivation process are selectively replaced with inactive phenylalanine) using spectrally and timely resolved fluorescence [4] and ultrafast pump-probe [16, 187, 188] spectroscopic techniques with ps to fs time-resolution.

The methods and results of the studies are structured in the following chapters of the thesis:

Chapter II describes and demonstrates the development of a Fourier transform-based excitation-emission (EE) spectrometer using two passively phase-stabilized common path interferometers (BI-TWINS). The developed EE spectrometer is capable of recording the polarization-resolved, time-resolved EE data of the samples. Also developed was a method for separating coherent light scattering and incoherent photoluminescence contributions from the time-integrated and time-resolved EE data recorded using the BI-TWINS spectrometer. The developed method successfully applied to the recorded EE data of highly fluorescence sample Coumarin 6 (C6) in ethylene glycol and weakly emissive flavin adenine dinucleotide (FAD) chromophore both free in solution and inside the protein in the European robin cryptochrome 4 (ErCry4). The results derived from the ErCry4 sample indicated protein-chromophore binding.

Chapter III explains the results of photophysical property studies of molecular FAD, WT ErCry4, and its four mutant samples using the developed time-resolved excitation emission spectrometer. The four tryptophans (Trp_A, Trp_B, Trp_C, and Trp_D, see Figure I. 7 (b)) involved in the electron transfer reactions in ErCry4 are selectively replaced with phenylalanine and then created the mutants. These studies demonstrated the presence of different conformers of FAD in protein samples. The results also indicate that the protein only binds to the stacked conformer of FAD, and there is an effective electron transfer between bounded FAD and Trp_A in ErCry4. The experiments also confirm the stability of protein samples during 12 hours of optical excitation.

Chapter IV illustrates the ultrafast transient absorption spectroscopy results of ErCry4 and its four mutants. The electron transfer time along the first three tryptophan and the quantum yield of the formed radical-pairs are calculated from the ultrafast measurements. The experimental results are evaluated and compared with the results from real-time QM/MM electron transfer simulation based on the DFTB (Density-Functional based Tight-Binding) approach. A comparison of results provides a clear understanding of the successional electron transfer through the tryptophan chain. More importantly, these studies open up a new path for spin transport and dynamical spin correlation in radical-pairs in molecules.

Chapter V presents the summary and outlook of the results presented in this thesis.

Chapter II

Fourier Transform-Based Time-Resolved Excitation-Emission Spectrometer

Section II.1 II.2 II.3 in this chapter was published in [4]

Daniel C. Lünemann*, **Anitta R. Thomas***, Jingjing Xu, Rabea Bartölke, Henrik Mouritsen, Antonietta De Sio, and Christoph Lienau

Distinguishing Between Coherent and Incoherent Signals in Excitation-Emission Spectroscopy

<https://doi.org/10.1364/OE.428850>.

* Both authors contributed equally to this chapter. A.R.T and D.C.L planned, performed and analyzed the experiments. A.R.T. prepared the samples for the experiments.

II.1 Introduction

Light-matter interaction is always an excellent and efficient tool for analyzing and understanding the structural and chemical properties of matter. When light interacts with an atomic or molecular system, it gets absorb and emits light according to the properties of the interacting system. The emitted light from the photoexcited sample may be phase-correlated with the interacting light, as in the case of Rayleigh and simulated Raman Scattering, or it may be entirely incoherent with excitation light, such as in photoluminescence and spontaneous Raman Scattering [189]. Usually, a measurement of the degree of coherence, the first-order correlation of the incident and emitted light, distinguishes between these processes [189, 190]. The differentiation of both components helps to understand the optical properties of the various system such as single ions [191], carbon nanotubes [192], gold nanostructures [193], or semiconductor quantum wells [194-197]. In the coherent anti-Stokes Raman Scattering [198], stimulated Raman Scattering [199, 200], or in second harmonic microscopy [201], incoherent emissions are background signals, and identification of both emissions is the only way to suppress the background. On the other hand, in excitation-emission (EE) matrix spectroscopy, coherent scattering creates a background signal, and a posteriori data interpolation or exclusion is commonly done to remove the background [202-206]. So it is necessary to distinguish between coherent and incoherent emissions.

In EE spectroscopy, the spectrally resolved intensity of emitted light for various excitation wavelengths is recorded, and thus it provides a two-dimensional (2D) data map. In the case of narrowband excitation, spectral filtering using bandpasses [207, 208], monochromators [209], or acousto-optical modulators [210] has been successfully employed to separate coherent scattering from incoherent emission. This, however, masks information about the emission process in the spectral vicinity of the excitation. To some extent, the inconvenience of narrowband excitations is overcome by broadband spectroscopy. But in broadband spectroscopy distinguishing between coherent scattering and incoherent emission is more challenging, requiring to record a phase-stable interferogram between the emission and replica of the excitation light, acting as a local oscillator [211, 212]. Quite often, sophisticated nonlinear optical spectroscopies, such as fluorescence up-conversion [213], are used to separate these emissions in the time domain, as demonstrated, e.g., by separating resonant Rayleigh scattering and incoherent luminescence from semiconductor quantum well [196, 197, 212]. Also, in nonlinear optics, coherent and incoherent emission channels are readily distinguished by using similar interferometry techniques [214].

The latest crucial development in spectral interferometry was the invention of the Translating-Wedge Based Identical Pulses eNcoding System (TWINS). TWINS are extremely stable common-path interferometers. They have already simplified the interferometric experiments in the ultraviolet to the near-infrared spectral range. In TWINS, birefringent wedges are used to introduce variable time delays between orthogonally polarized replicas of the incident light [215, 216] (see section A.II.1). Recently TWINS interferometers are established in different linear and nonlinear experiments such as in Fourier transform (FT)-based absorbance [6], EE [208, 217], or time-and frequency-resolved fluorescence spectroscopy [218], hyper-spectral imaging [219], pump-probe [220] and two-dimensional electronic spectroscopy [221-223], and in stimulated Raman Scattering microscopy [224].

The emitted light from optically excited samples carries spectral and temporal information. There are many time-resolved emission measurements available now to obtain the dynamical properties of the samples. Fluorescence up-conversion [213, 225], and gating [226, 227], fluorescence spectrum recording using streak cameras [228, 229] are some of the important methods. But they are complicated, expensive, delicate, and only have reduced sensitivity. Another simple and sensitive time-resolved emission measurement is time-correlated single photon counting (TCSPC) [230]. It is simple and has a time resolution of up to 20 ps. In TCSPC, a single-photon avalanche diode (SPAD) or photomultiplier (PMT) detects the arrival time of emitted photons with respect to the excitation using suitable electronics. It creates a histogram of photon arrival times, obtaining fluorescence time traces from the histogram. TCSPC is a well-established straightforward technique but only provides spectrally integrated emission data.

Here a FT-based broadband, white light excitation-emission (EE) spectrometer has been developed using TWINS interferometers in both the excitation and detection path (BI-TWINS). Using the SPAD detector and TCSPC electronics, the BI-TWINS spectrometer recorded the photon arrival histogram at each delay introduced by the two TWINS interferometers, hence recording a time-resolved EE spectrum of the sample. Using this BI-TWINS spectrometer, we could distinguish and fully separate coherent and incoherent emissions in linear scattering spectroscopy. In the first part of this chapter is demonstrated the approach for the suppression of the Rayleigh scattering signal from the highly fluorescence emission of Coumarin 6 dye (C6) and the weak fluorescence emission of the flavin adenine dinucleotide (FAD) chromophore in isolation and when it is bound inside the cryptochrome 4 protein from European robin (*Erithacus rubecula*) (ErCry4) [141, 154] (see Chapter I). This part is published in [4]. In the second part of the chapter, the lifetime associated with the coherent and incoherent emissions is analyzed. The time-resolved data also allow us to calculate the rotational reorientation time of chromophore molecules in free solution and protein-bound cases. The signs of FAD-ErCry4 protein binding were seen in this our study.

II.2 Experimental Section

II.2.1 Experimental Setup

A schematic representation of a time-resolved EE spectrometer based on FT spectroscopy and combining two TWINS (BI-TWINS) is shown in Figure II. 1. Picosecond laser pulses with a spectral range from 400 to 2400 nm are delivered from a white light source (Fianium SC400). The pulses are then filtered using two short pass filters (DM, Thorlabs DMSP805R, and DMSP650) to the spectral range of 400 to 680 nm to match the EE spectral range of the samples. The excitation power of the pulses could be controlled using the neutral density filter (NDF). The laser pulses are first passed through the excitation TWINS (“ex”) interferometer, a passively stabilized common path interferometer [215, 216] that creates two phase-locked pulse pairs with time delay τ_{ex} . A detailed description of the TWINS interferometer is given in Appendix A.II.1. The polarization of the pulse pairs from the excitation TWINS is controlled using the polarizer P_3 . A small fraction of the output light from the excitation TWINS had been given to the photodiode PD_1 using a beam splitter (BS). Then the photodiode records the field autocorrelation of excitation pulses as a function of excitation TWINS wedge position x_{ex} . The spectrum of the excitation field could be retrieved from the FT of the recorded field autocorrelation [4, 215] (Appendix A.II.1.3 TWINS Spectrometer). The excitation pulses were then focused on the sample (S) using a microscope objective (O_1 , 0.35 NA). The photodiode PD_2 records the autocorrelation signal of the transmitted light through the sample as a function of x_{ex} simultaneously with PD_1 . Then the recorded signals in the PD_1 and PD_2 were used to retrieve the absorption spectrum of the sample [6]. The emitted coherent and incoherent light from the sample was then collected using

another objective (O_2 , 0.3 NA). The polarization of the collected signal could be determined using a Polarizer (P_4). Then the collected signal passes through the detection TWINS (“det”), and the spatial coherence of the signal increases using the two irises (I_1 and I_2). The two-pulse replica of the emitted light created by the detection TWINS focused on the single-photon avalanche photodiode (SPAD, Micro Photon Device PDM, 100 μm active sensing area diameter, 60 ps resolution at 550 nm). These pulse replicas interfere at the detector. The arrival time of each photon with respect to the excitation was entered using a time-correlated single photon counting unit (TCSPC, Pico Quant PicoHarp 300). A light intensity map of emitted light as a function of photon arrival time, and TWINS wedge positions x_{ex} and x_{det} is recorded.

To record a single light intensity map, each TWINS was scanned in a range of 3 mm with a step size of 10 μm . This scan range is chosen to give a spectral resolution of ~ 6.5 nm to the excitation and the detection TWINS in the specified spectral range [6]. At the same time, the step size is set to fulfill the Nyquist theorem by recording at least 2 data points per spatial oscillation period, resulting in a BI-TWINS map with 300×300 pixels. To get a reasonable signal-to-noise ratio, an average of 10^5 photons per excitation and detection position are accumulated by setting the integration time to 200 ms per pixel.

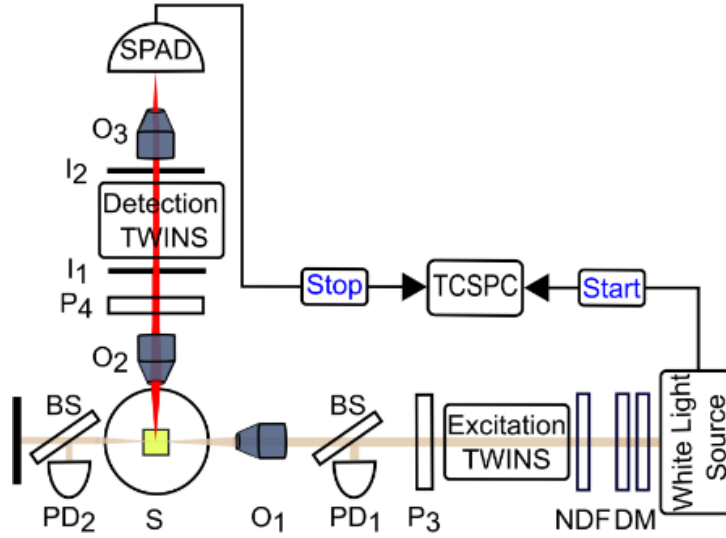


Figure II. 1 The experimental setup used for Fourier transform excitation emission spectroscopy using two passively stabilized common-path interferometers (BI-TWINS) [4]. The spectrally (DM, Dichroic filter) and power (NDF, neutral density filter) filtered light from a super continuum white light source is passed through excitation TWINS and creates phase locked pulse pair of picosecond pulses with time delay τ_1 . The pulses are then focused into sample S using an objective O_1 . The coherent and incoherent emission from the sample collected using the objective O_2 and the emitted light then passes through the detection TWINS. The phase locked pulse pairs created by the Detection TWINS focused into the single-photon avalanche photodiode (SPAD) and the pulse pairs interfere then at the SPAD. The arrival time of each photon with respect to the excitation is marked in a time correlated single-photon counting (TCSPC) unit. A light intensity map recorded as a function of arrival time of the photon and wedge positions x_{ex} and x_{det} of the excitation and detection TWINS. A detailed schematic representation of the TWINS is given in Figure A. II. 1 in Appendix A.II.1.

In this way, the pile-up effect is avoided by keeping the count rate below 10^6 photons per second. The excitation power for the EE studies of the C6 dye is limited to $10 \mu\text{W}$, and for molecular FAD, it was $25 \mu\text{W}$. In the case of ErCry4 protein, we have used $50 \mu\text{W}$ to achieve a good signal-to-noise ratio and to avoid protein degradation [4].

In the BI-TWINS spectrometer, the polarization of the excitation and detecting light can be selected using the polarizer P_3 and P_4 as mentioned earlier (Figure II. 1). For every EE measurement, P_3 had been chosen in the vertically polarized direction (V), perpendicular to the laser beam in the detector plane. The polarization of the emitted light can be chosen to be either parallel (V), perpendicular (H), or at magical angle (M, $\theta = 54.7^\circ$) polarized with respect to the laser polarization direction. The experimentally recorded EE data shown in the case of coherent and incoherent separation were recorded in VM polarization configuration. Here in section II.3 , for the separation of coherent and incoherent light, time-resolved EE data are not used but time-integrated data.

II.2.2 Sample Preparation and Handling

To check out the efficiency of the BI-TWINS spectrometer, we have used C6 dye, FAD, weakly emissive cryptochrome 4 protein from the retina of night migratory songbird European robin (ErCry4)

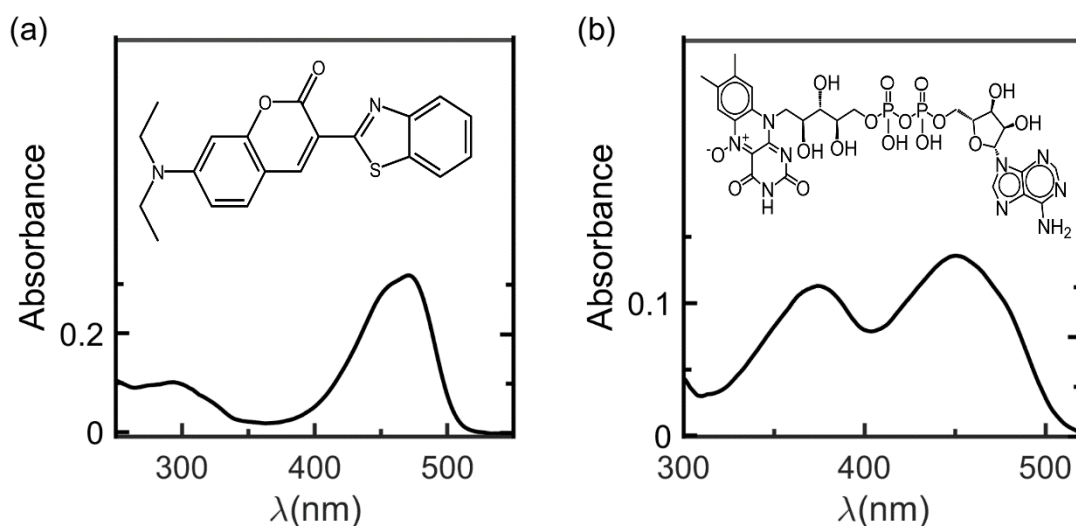


Figure II. 2 Absorbance spectrum of (a) $40 \mu\text{M}$ Coumarin 6 (C6) in ethylene glycol, and (b) $80 \mu\text{M}$ flavin adenine dinucleotide (FAD) in a buffer solution (pH 8) [4]. The chemical structure of both molecules are shown in the inset of respective spectra.

[20, 27, 141, 154] as samples. C6 dye belongs to the 7-diethylaminocoumarin series and has numerous applications in the biological field [231]. C6 is one of the highest quantum yield fluorescence dyes

[232], dissolved in ethylene glycol at a concentration of 40 μM . Here, the emission signal from C6 dye is used to optimize the BI-TWINS spectrometer.

FAD molecules are blue light sensitive, functioning as a chromophore in ErCry4 protein. Blue light excitation of FAD initiates a series of ultrafast electron transfers inside the protein through the tryptophan chains, generating sensitive radical-pairs [154]. This is considered as the key mechanism in the magnetic field compass in migratory birds [20, 27] (See Chapter I). Initially, free FAD without a protein background is investigated. For that, molecular FAD (Sigma Aldrich F6625) with 80 μM concentration in buffer solution (20 mM tris(hydroxymethyl)aminomethane, 250 mM NaCl in 80% water, and 20% glycerol).

The chemical structure and absorbance spectrum of C6 dye and molecular FAD are shown in Figure II. 2 (a), and (b), respectively. ErCry4 protein synthesis and purification method reported and described previously [154]. Here the protein sample is concentrated for a FAD concentration of 80 μM before the measurement (see more details in A.III.1.2), the same concentration used for molecular FAD in the buffer. The protein sample and molecular FAD measurements are carried out at a temperature of 0° C, at pH 8 and this ensured a similar acid-base balance to that in the bird's eye at 40-43° C and pH 7.3 [233]. The protein sample is centrifuged for one hour in a temperature-controlled environment before the measurement to filter out any previously aggregated protein, which induces coherent scattering. The C6 measurements were at room temperature. All the measurements were carried out in a low-volume cuvette with a 0.15 cm optical path length (Hellma, 105-252-15-40) [4].

II.3 Distinguishing Between Coherent and Incoherent Signals in Excitation-Emission Spectroscopy

II.3.1 Method Concept

Here a FT-based EE spectrometer is used for distinguishing and separating coherent and incoherent emissions (Figure II. 1). Picosecond laser pulses from a white light source are discrete into two phase-locked pulses with a variable time delay τ_1 using the interferometer 1. This pulse pair optically excites the sample under investigation, as shown in Figure II. 3. The sample molecule can either coherently scatter the interacting light and/or it can emit incoherent PL. The coherent light scattered from the sample will emit a secondary phase-locked pulse pair that is delayed by τ_1 (Figure II. 3, blue pulses). In opposition to the coherent emission, incoherent PL is an emission of intensity bursts of light; these are also delayed by τ_1 (Figure II. 3, red). Both coherent and incoherent emissions are allowed to pass through the second interferometer and generate another set of pulse replicas of the emitted light with a

new variable time delay τ_2 . The output signals from interferometer 2 are given to a time integration photodiode. Then the photodiode records the intensity of incident light as a function of both time delays τ_1 and τ_2 . To understand the situation more clearly, the EE interference map is simulated as a function of τ_1 and τ_2 for coherent and incoherent emission (Figure II. 4 (c) and (d)). A broadband excitation

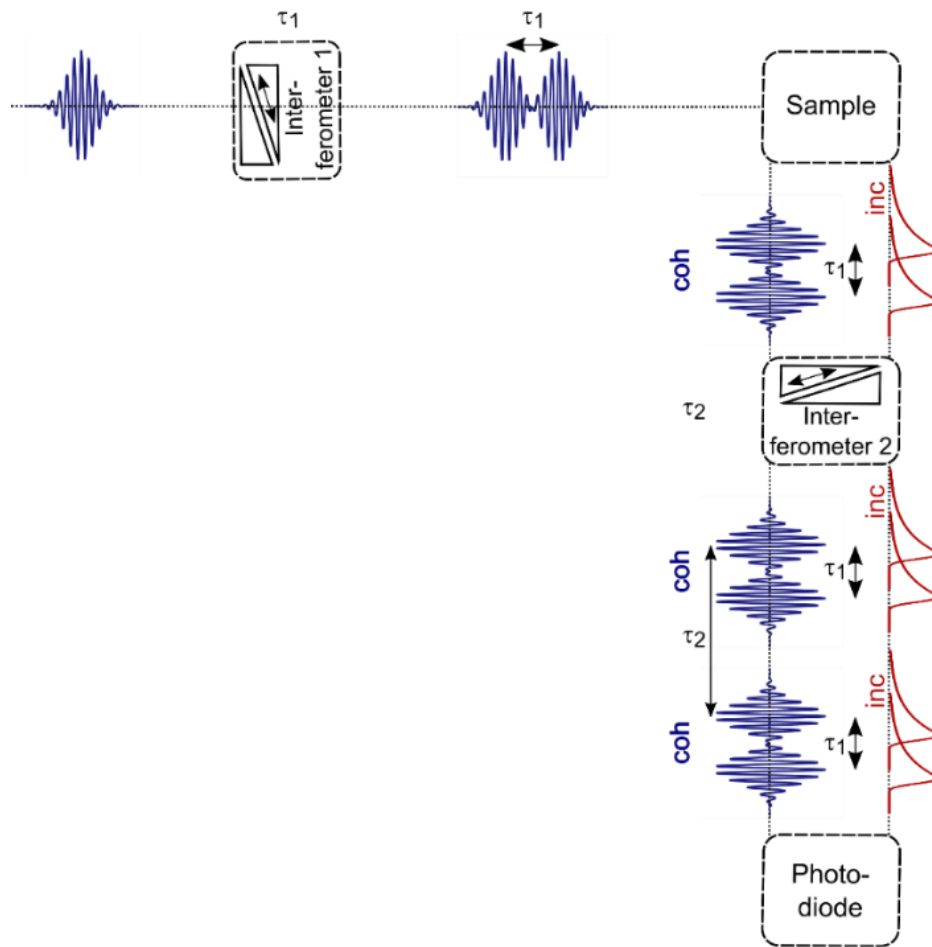


Figure II. 3 Coherent and incoherent emissions in Fourier transform excitation–emission spectroscopy using two interferometers [4]. The interferometer 1 generates a phase locked pulse pair with relative time delay τ_1 . This pulse pair excite the sample and coherently scatter excitation light (blue) and /or emit incoherent photoluminescence (red). Both emitted light passes through the second interferometer and generate phase locked pulse replicas of both emission with time delay τ_2 . Finally the time delayed replicas interfere at the photodiode that records light intensity as function of τ_1 and τ_2 [3, 4].

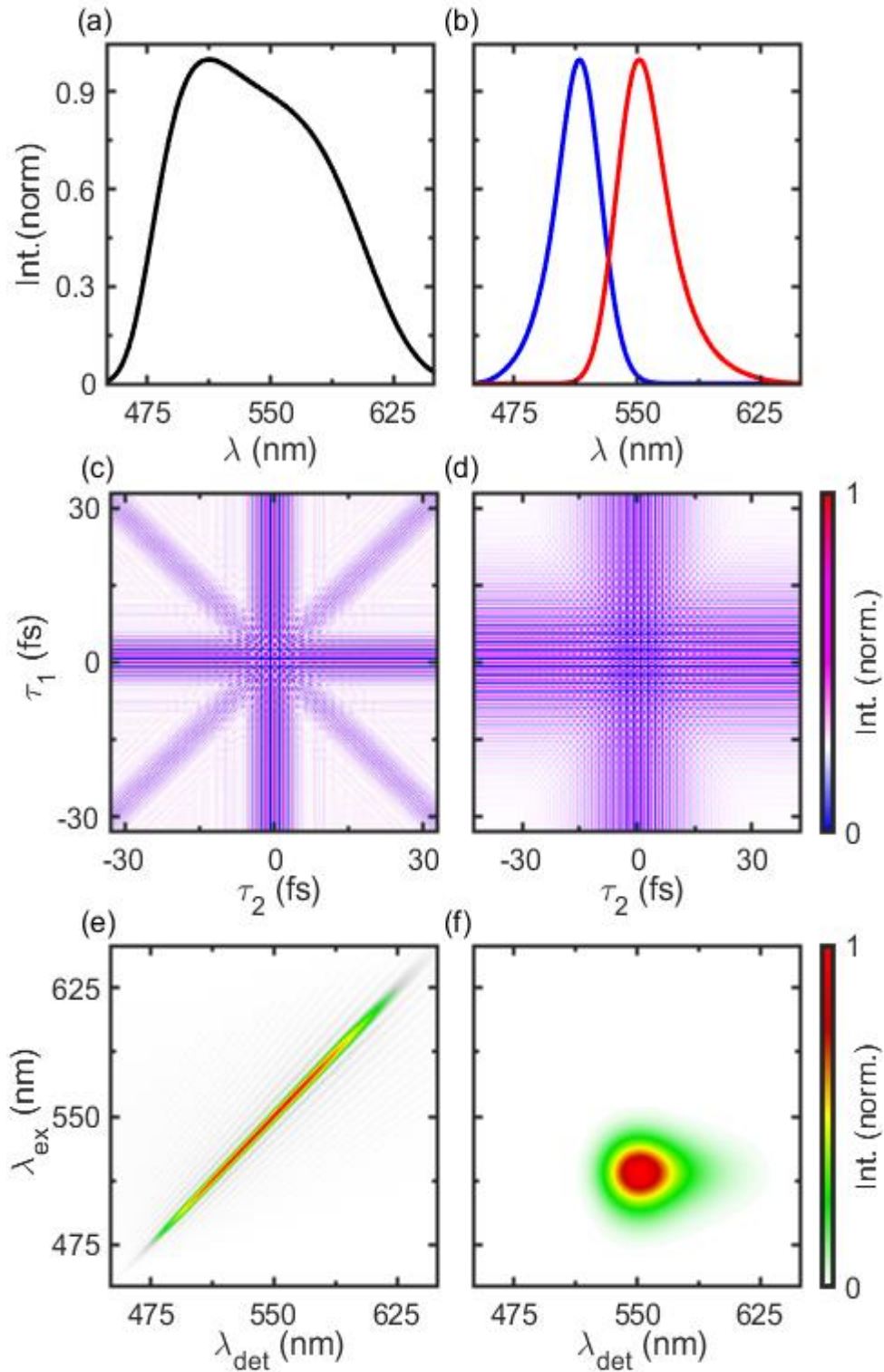


Figure II. 4 Simulation for distinguishing between coherent scattering and incoherent emission in Fourier transform excitation-emission spectroscopy using two interferometers. [4]. (a) The assumed broadband excitation light source $I_0(\lambda)$ given to the first interferometer in Figure II. 3. (b) Absorption (solid blue line) and emission (solid red line) spectra of presume sample used for simulation. (c), (d) Simulated excitation-emission interferograms of a sample that scatters coherently (c) and emits incoherent photoluminescence (d). The diagonal patterns in (c) are a distinct signature of coherent light scattering in these two-dimensional maps which allow for their isolation. (e), (f) Excitation-emission spectra of coherent scattering (c) and incoherent emission (d) as a function of excitation λ_{ex} and detection λ_{det} wavelength.

light $I_0(\lambda)$ (Figure II. 4 (a)) is assumed to be given to the first interferometer, and the sample that

absorbs light to have an absorption spectrum $\alpha(\lambda)$ (blue) and emission spectrum $I_{FL}(\lambda)$ (red), as shown in Figure II. 4 (b). In these simulations, it was also assumed that the scattering and fluorescence contribute equally to the signal. The intensity correlation traces for coherent and incoherent scattering are different; the incoherent emission featured vertical and horizontal stripes (Figure II. 4 (d)). While the coherent emission (Figure II. 4 (c)) has an additional trace along the diagonal direction in the EE interferogram. Since the stripes along the diagonal are the unique feature of coherent scattering, it is then used to identify and separate coherent emission from incoherent emission contributions.

Here in our experiment, we have used two TWINS as excitation and detection interferometers (BI-TWINS). The structural difference in Figure II. 4 (c) and (d) can be understood by analyzing the light propagation through BI-TWINS. Light propagation through a single TWINS is discussed and described in Appendix A.II.1.1. The excitation TWINS creates a pair of phase-locked pulses (P_1 and P_2) with relative delay τ_1 and interact with the sample. For the coherent scattering process, the sample interaction results in the emission of the secondary pulse pair with the same relative phase relation and time delay. This pulse pair then passes through the detection TWINS and split into two pairs again (P_{11}/P_{12} , P_{21}/P_{22}) with relative time delay τ_2 . The different features in the coherent map (Figure II. 4 (c)) are the result of interference of these pulses as the function of relative time delays τ_1 and τ_2 . These four pulses can create six distinct interference patterns in the coherence map (Figure II. 4 (c)). Here only those pulses that are not separated much more than the coherence time of each can contribute to the interferogram. So at $\tau_2 \approx 0$, mainly the interference between P_{11} with P_{12} and P_{21} with P_{22} contributes to the interferogram. In this case, the interference has no dependency on τ_1 so the resulting interference patterns appear as vertical stripes on the map (Figure II. 4 (c)). Additionally, around $\tau_1 \approx 0$ the inference of P_{11} with P_{21} and P_{12} with P_{22} takes place, and that will contribute to the horizontal stripes in the coherent map (Figure II. 4 (c)), which is independent of τ_2 . The diagonal structure in the coherent map (Figure II. 4 (c)) arises when $\tau_1 \approx \tau_2$ (interference of P_{12} with P_{21}) and $\tau_1 \approx -\tau_2$ (interference of P_{11} with P_{22}). All the above interference patterns will overlap for $\tau_1 \approx \tau_2 \approx 0$. The non-interfering pulses yield a constant background on the map.

Vacuum field fluctuations create the incoherent PL emissions. The sample absorbs the excitation pulse pair and emits PL light (FL_1 and FL_2) in the incoherent emission process. The phase coherence of the excitation pulses is absorbed in the excitation process of the sample, and it is lost in the PL emission. The PL light also split in the detection TWINS and interferes in three different ways as the function of τ_1 and τ_2 . The variation of τ_1 modulates the intensity of excitation light, which changes the number of photons absorbed by the sample and thus also the number of photons emitted by the sample. So this causes a modulation along the excitation axis, but it does not change the emitted spectrum and is

independent of τ_2 . This creates a horizontal stripe in the incoherent map (Figure II. 4 (d)). A FT of the horizontal interferogram along τ_1 gave the photoluminescence excitation (PLE) spectrum of the sample. Similarly, the variation of τ_2 modulates the interference between the two replicas of fluorescence emission, created by the detection TWINS. This resulting in vertical stripes in the incoherent map (Figure II. 4 (d)). In the case $\tau_1 \approx \tau_2 \approx 0$, the excitation light has maximum intensity, and PL emission is also high intensity, there will be interference between two emitted PL pulses. This creates checker-board-like patterns in the center of the EE interferogram map (Figure II. 4 (c)). So the incoherent interference map is the product of the resulting interference patterns along the excitation and detection axes (Figure II. 4 (d)). A detailed analysis of these four components is reported in Appendix A.II.2.

Interestingly the incoherently emitted fluorescence does not interfere with the coherently scattered light. As such, the total map for a coherently and incoherently scattering sample in the time domain arises from the superposition of the coherent and incoherent contribution (Figure A. II. 8 (a)).

II.3.2 Data Analysis

To analyze the experimental data, first the horizontal and vertical patterns were removed from the interferogram, since these are included in the map for both coherent and incoherent contributions (Figure II. 4 (c) and (d)). Second, it was realized that the autocorrelation traces recorded with the TWINS interferometer did not perfectly match those of an ideal, dispersion-free interferometer and that the two TWINS interferometers were not identical. This mainly results from the wavelength-dependent time delay introduced when moving the $\alpha - BBO$ wedges, and from manufacturing tolerances. This was corrected in the second step of the data analysis, the interferograms to those that would be obtained with two identical interferometers. This correction is described in detail in Appendix A.II.2.2. In the next step, diagonals were used in the correlation maps to isolate the coherent scattering from incoherent PL emission. For this, the correlation signals were extrapolated in the region that is not overlapping with the PL correlation to the entire map. For both diagonals, the cross-sections were determined by a weighted average along the diagonals. Here, the weights were chosen in a way that the center of the interferogram, which is influenced by the PL contribution, is suppressed. Based on these cross-sections the diagonal patterns were reconstructed. This allows to isolate the coherent contribution to the EE map and to subtract it, leaving only the PL contribution. In the final step a two-dimensional FT of the separated interferograms was performed and the resulting frequency axes was converted to wavelengths. This results in EE spectra that plot the emitted intensity as a function of excitation and detection wavelength (Figure II. 4 (e) and (f)). A detailed description of this transformation is given in Appendix A.II.2.2. Briefly, the axis transformation requires to measure a calibration curve for each TWINS. To this end, the broadband whitelight spectrum was passed through the respective TWINS and

a spectrometer was used to record an interferogram at each TWINS motor position $x_{ex/det}$. From the FT of this interferogram along $x_{ex/det}$ we were then relate every color $\lambda_{ex/det}$ of the incident spectrum to the corresponding modulation wave number $k_{ex/det}^0$ of the TWINS. This measured relation yielded the calibration curve $k_{ex/det}^c(\lambda)$. The TWINS calibration method has been described in detail earlier [215, 216, 221, 234] and is summarized in Appendix A.II.1.2.

II.3.3 Results and Discussion

Figure II. 5 (a) plots a BI-TWINS map of the time-integrated intensity of the emission from molecular FAD as a function of wedge positions of both the excitation (x_{ex}) and the detection (x_{det}) TWINS. It appears that the interferogram contains mainly vertical and horizontal interference patterns induced by varying either excitation or detection delays. The crosscuts of the intensity map along x_{ex} and x_{det} are shown in Figure II. 5 (b), to see these patterns more clearly. The upper crosscut, taken along the horizontal x_{det} axis at the position marked by a horizontal black dashed line in Figure II. 5 (a), represents a field autocorrelation of the light that is emitted from the sample after the excitation with a pulse pair. The lower crosscut is taken along the vertical black dashed line in Figure II. 5 (a) and shows a field autocorrelation of the excitation pulses that interact with the sample. The fringe spacing in the detection crosscut (upper, Figure II. 5 (b)) is larger than that in the cross-section along the detection axis. This reflects the Stokes shift between the absorbed light and the light that is emitted from the sample. The fringe contrast in Figure II. 5 (b) is significantly lower than the ideal 100% contrast. This is mainly due to the reduced spatial coherence of the light emitted from the focal volume of the excitation beam in the cuvette. As the spectrum of the whitelight source used to excite the sample is highly structured (Figure A. II. 9 (b) in Appendix A.II.2.2), the oscillation along the x_{ex} axis decay much slower than along x_{det} as can be seen in the bottom crosscut of Figure II. 5 (b). Both crosscuts are highly asymmetric around $x_{ex/det} = 0$. This asymmetry arises from the pronounced color (λ) dependence of the phase shift $\Delta\varphi(x, \lambda) = \Delta\varphi_0(\lambda) + k^0(\lambda)x$ that is introduced in each interferometer. Here, $k^0(\lambda) = 2\pi\Delta n(\lambda)\sin(\vartheta) / \lambda$ is the modulation wavenumber introduced by refractive indices of $\alpha - BBO$, denotes the birefringence introduced by the wedge pair W ; ϑ is the opening angle of each wedge and $\Delta\varphi_0(\lambda)$ is a position-independent phase offset introduced by the TWINS. For a quantitative analysis of the interference fringes, the one-dimensional cross sections in Figure II. 5 (b) needs to be Fourier transformed. Afterward, both resulting wave number axes need to be transformed to the corresponding wavelength axes according to the respective calibration curve $k_{ex/det}^c(\lambda)$ of each TWINS. The one-dimensional cross

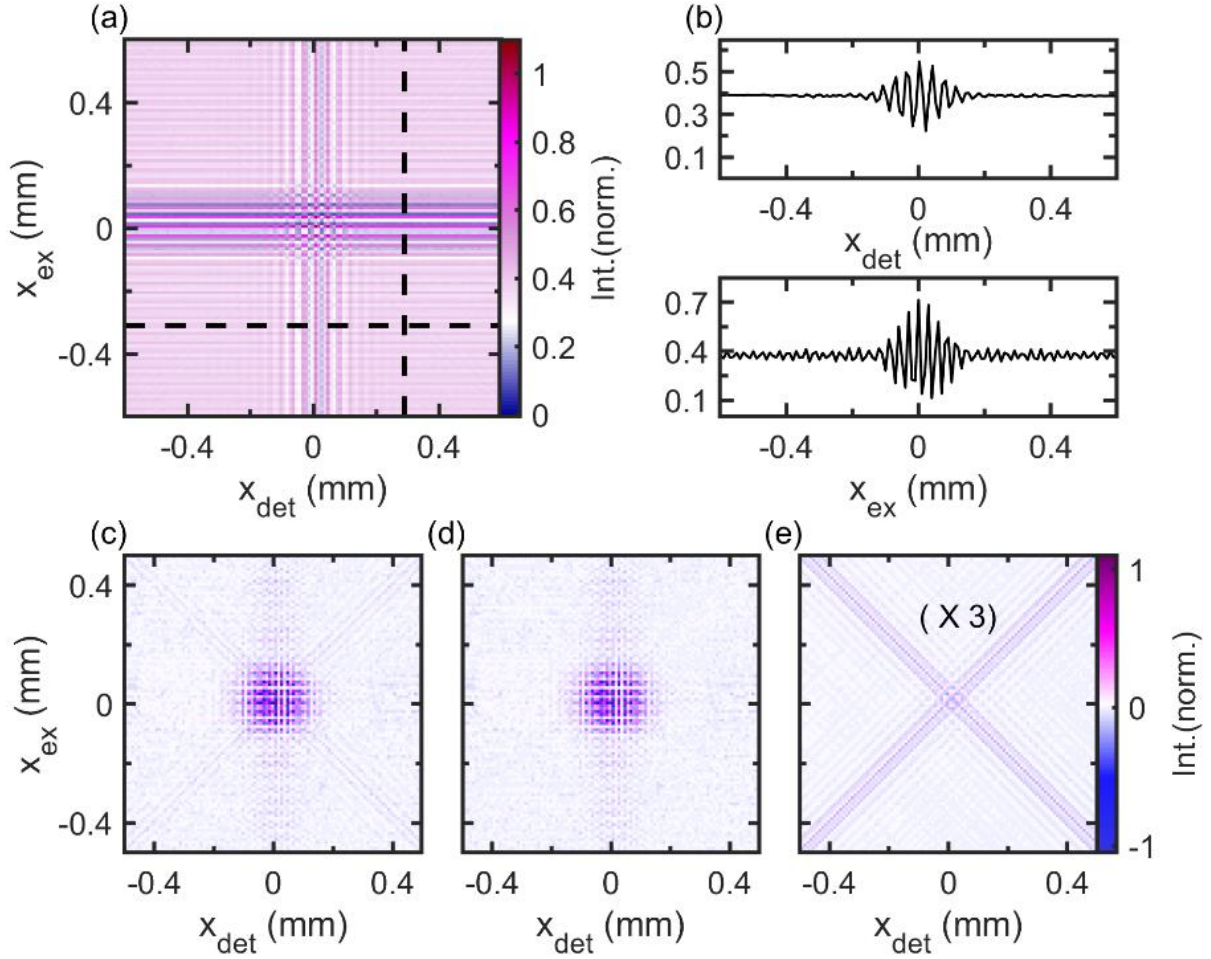


Figure II. 5 Distinguishing between incoherent fluorescence and coherent light scattering from molecular flavin adenine dinucleotide (FAD) in buffer solution (pH8) by BI-TWINS excitation-emission spectroscopy. (a) Measured interferogram (center part) of the temporally integrated FAD emission as a function of excitation (x_{ex}) and detection (x_{det}) wedge positions. (b) Cross sections along the horizontal (top) and vertical (bottom) black dashed lines in (a), showing characteristic interference structures recorded by the excitation and detection TWINS. (c) Interferogram from (a) after subtraction of the background signals and axis equalization. (d) Incoherent contribution of (c) after subtraction of the diagonal structures. (e) Coherent contribution to (c), magnified by factor 3 [4, 5].

sections in Figure II. 5 (b) provide the spectra of the light that excites the sample and of the light that is emitted by the sample. These signals have been analyzed before [208, 217, 218] and briefly discussed in Appendix A.II.1.3. However, they cannot distinguish between the sample's coherent scattering and incoherent emission. They can be measured separately by putting a single TWINS either in the excitation or in the detection path, as known from earlier work [4, 208, 218].

Since these signals do not contribute directly to the EE spectrum of interest here, they were subtracted from the raw data in Figure II. 5 (a). As the signals are constant along one of the coordinate axes, they are readily obtained by averaging along the TWINS position axes. After the subtraction, the background-free EE interferogram $\mathcal{I}_d^{\%}(x_{ex}, x_{det})$, shown in Figure II. 5 (c) results. It consists of two

distinct structures: a checkerboard-like pattern in the center originating solely from incoherent emission (Figure II. 5 (d)) and two diagonals that contain the information on the coherent scattering contribution (Figure II. 5 (e)). The diagonal structures are very feeble Figure II. 5 (c). Separating these two structures makes it possible to distinguish between coherent and incoherent emission components [4].

The difference between the two structures can be understood intuitively. For an incoherent EE spectrum, excitation and emission color are uncorrelated, and the spectrum is the product of the absorption and emission (PL) spectra (see Appendix A.II.2.1). Since both spectra have a finite

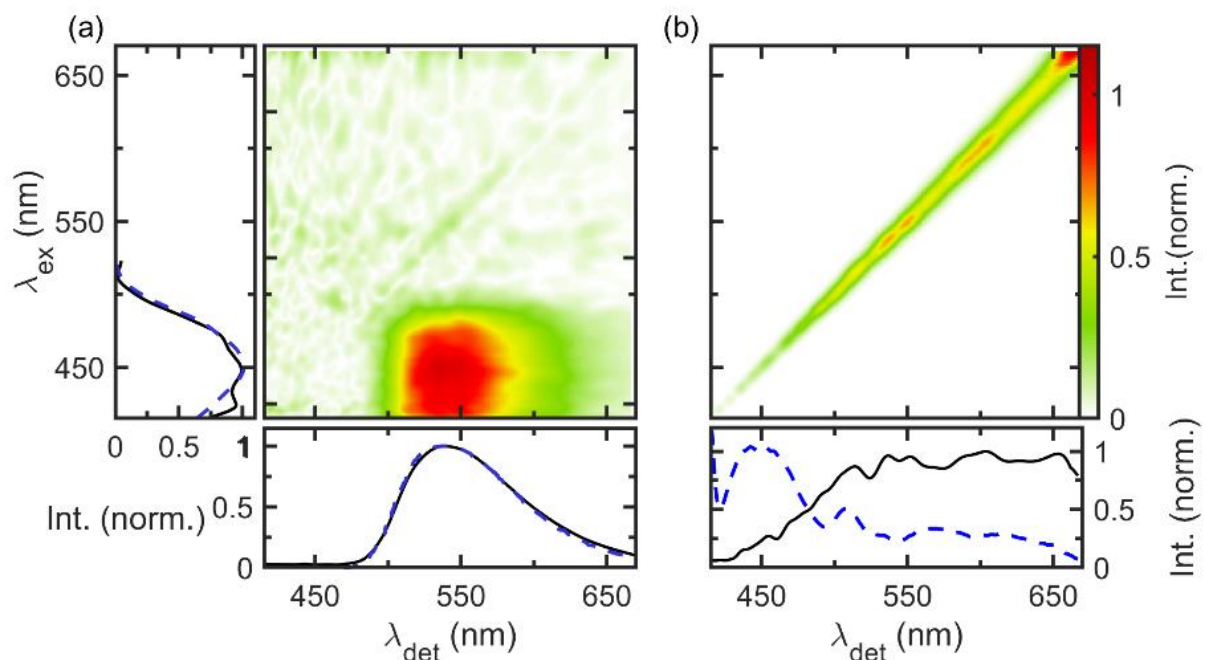


Figure II. 6 Separation of incoherent and coherent light scattering from the excitation-emission spectra of molecular flavin adenine dinucleotide (FAD) [4]. Excitation-emission spectra of (a) incoherent photoluminescence and (b) coherent light scattering from molecular FAD, deduced from the interference map in Figure II. 5 (a). (a) Spectrally averaged excitation and emission spectrum of FAD are displayed at the left and bottom side of the diagram (black solid line). The excitation and emission spectra well agree with earlier reported spectrum (blue dashed line) of fully oxidized FAD [2, 3]. (b) Bottom: Light scattering spectrum, normalized to the excitation light spectrum (black) and the excitation spectrum itself (dashed blue line).

bandwidth, the signal will inevitably vanish for sufficiently large wedge positions $x_{ex,det}$. In contrast, excitation and emission colors are strictly the same in the case of coherent light scattering. Hence, finite correlations exist along the diagonals of the EE interferogram even for arbitrarily large wedge displacements. A detailed discussion of these two signal components is given in Appendix A.II.2 [4].

To isolate coherent and incoherent EE interferograms, a two-dimensional FT technique is applied (Appendix A.II.2.2). This method is based on the calibration of the two TWINS. Briefly, the data are

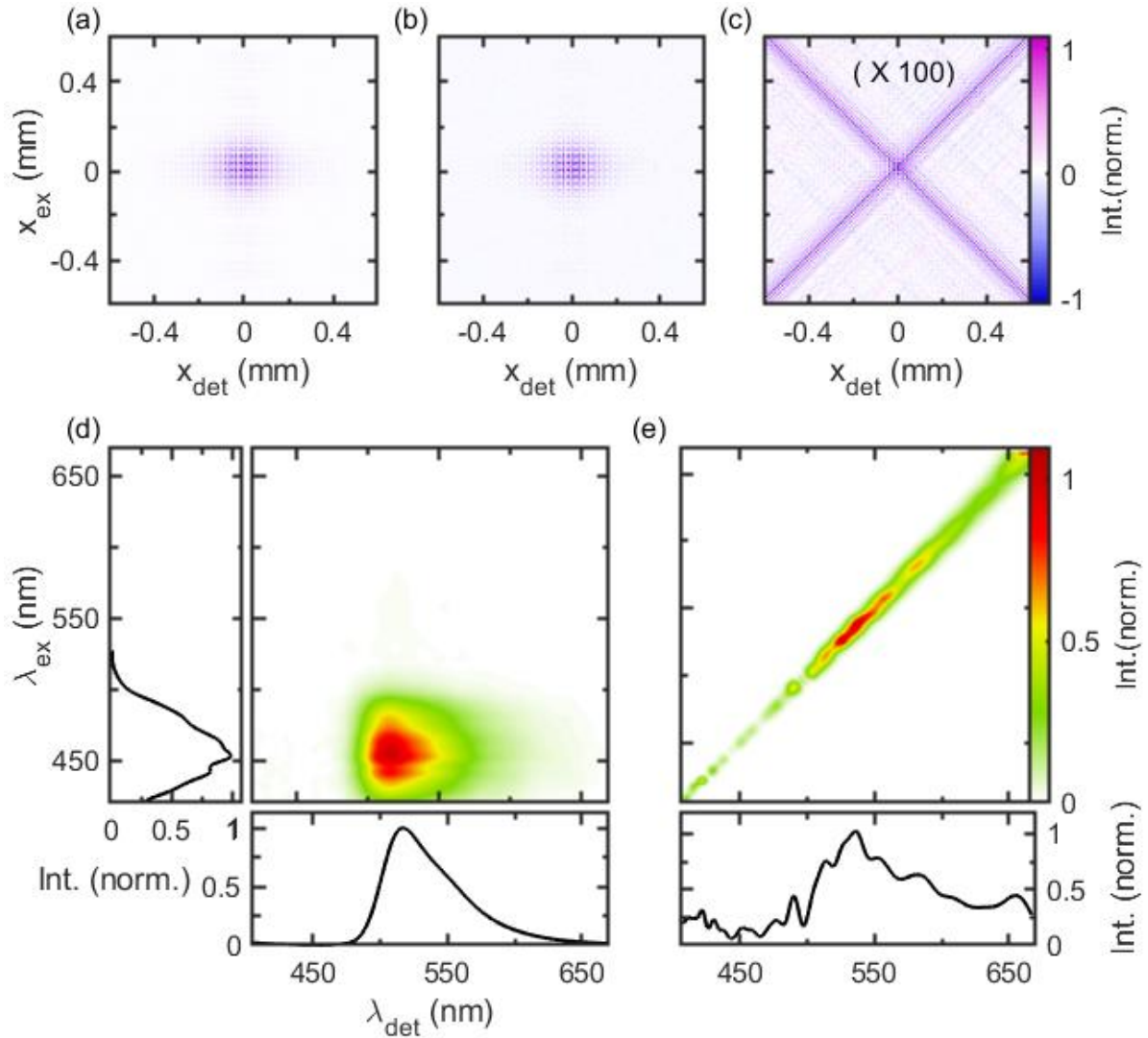


Figure II. 7 Distinguishing between incoherent photoluminescence and coherent light scattering from Coumarin 6 (C6) in ethylene glycol by BI-TWINS excitation-emission spectroscopy. (a) Measured interferogram after subtraction of the background signal and axis equalization as a function of excitation (x_{ex}) and detection (x_{det}) wedge positions. (b) Incoherent contribution of (a) after subtraction of the diagonal structures. (c) Coherent contribution to (a). Excitation-emission spectra of (d) incoherent photoluminescence and (e) coherent light scattering from C6 dye, deduced from the interference map in (a). (d) Spectrally averaged excitation and emission spectra of C6 dye are displayed at the left and bottom side of the diagram. The excitation spectrum is normalized with the laser excitation spectrum. (e) Bottom: Light scattering spectrum, normalized to the excitation light spectrum.

first transformed to a new excitation axis \hat{x}_{ex} that has the same frequency-dependent modulation wave number (calibration curve) $k_d^c(\lambda)$ as the detection axis. Then, the contribution of the incoherent emission to the signal along the diagonals is suppressed by applying an appropriately chosen windowing function, providing the coherent scattering interferogram $\hat{I}^{sc}(\hat{x}_{\text{ex}}, x_{\text{det}})$ Figure II. 5 (e)). Subtraction from the full interferogram gives the incoherent EE interferogram $\hat{I}^n(\hat{x}_{\text{ex}}, x_{\text{det}})$ (Figure II. 5 (d)). These

interferograms are then transformed into wavelength axes, using the calibration curve of the detection TWINS, $k_d^c(\lambda)$ [4].

Figure II. 6 (a) shows the incoherent EE spectrum $I_0^f(\lambda_{ex}, \lambda_d)$, of the molecular FAD in the buffer solution that results from this analysis. The EE spectrum in Figure II. 6 (a) is normalized to the excitation spectrum from the whitelight source. The inset in Figure II. 6 (a) display the retrieved absorption (left) and emission spectra (bottom) that are in excellent agreement with the previously

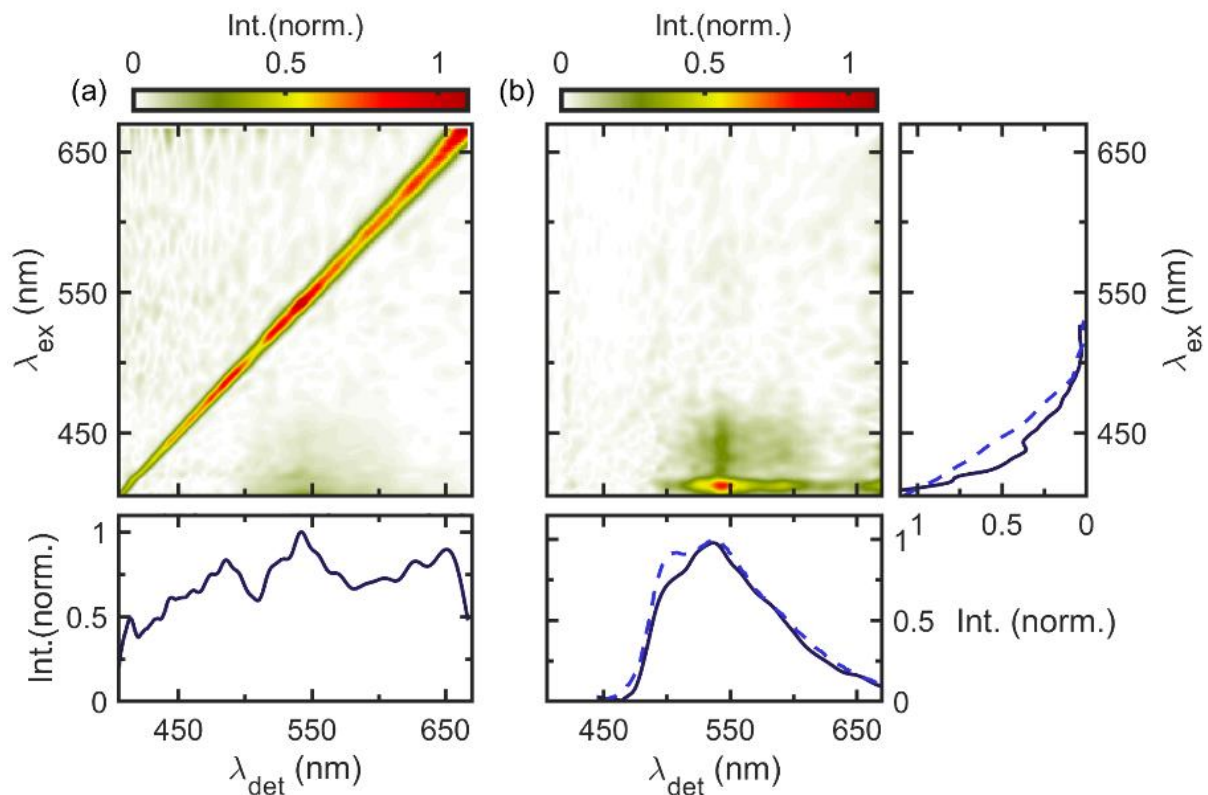


Figure II. 8 Suppression of light scattering from the excitation-emission spectra of the weakly emissive FAD chromophore inside the European robin Cryptochrome 4 (ErCry4) protein [4, 5]. (a) Excitation-emission spectrum recorded using BI-TWINS showing both fluorescence emission and coherent scattering. (b) Isolated incoherent excitation-emission spectrum. (b) Absorption and incoherent (photoluminescence) spectrum of chromophore FAD in ErCry4 are displayed in right and bottom panel respectively. The obtained spectra are compared to absorption and emission spectra of FAD chromophore in its fully reduced state ($FADH^-$) in a Photolyase protein [2, 5] (blue dashed line). All data set have been normalized to the excitation light spectrum.

reported spectra of fully oxidized FAD (FAD_{ox}) in another buffer solution (blue dashed line Figure II. 6 (a)) [2]. Figure II. 6 (b) displays the coherent scattering contribution to the measured signal with the FT of the cross section of the diagonal structures showing the scattered spectrum (bottom). This map is obtained from the interferogram in Figure II. 5 (e). FAD molecules only have a fluorescence quantum yield of 0.03 in pH 8 [19, 149]. The scattering contributions in Figure II. 6 (b) mainly arise from the 20% glycerol fraction in the buffer solution. A comparison of the two maps in Figure II. 6 (a) and (b)

confirms the successful separation of coherent and incoherent components to the EE spectra of molecular FAD [4].

Now the separation approach is applied to separate coherent and incoherent emissions from C6 dye, which is dissolved in ethylene glycol. C6 has large fluorescence quantum efficiency [232] compared to molecular FAD. Figure II. 7 (a) shows the background subtracted EE interferogram $I(x_{ex}, x_{det})$ of C6 dye. The EE interferogram contains a checker-board like pattern in the center contributed exclusively by incoherent emission. The diagonal structures from coherent emission are invisible for C6. The coherent and incoherent contributions are discrete from the EE interferogram by applying the separation procedure described earlier in the case of molecular FAD. Completely separated incoherent and coherent contribution from C6 dye is shown in Figure II. 7 (c) and (b), respectively. The readable donation in C6 is extremely faint, and the interferogram in Figure II. 7 (c) is 100 times magnified. The absorption and emission spectra of C6 derived from the EE spectrum are displayed in the left and bottom panel Figure II. 7 (a). These spectra match with already reported data of C6 in ethylene glycol [5]. Thus the emission from C6 is an example of a completely incoherent emission. Even though, coherent and incoherent separation method was used, it was possible to separate extremely feeble coherent scattering from the C6 dye.

The coherent and incoherent scattering separation method was applied to a weakly-emissive sample containing the chromophore FAD embedded in the ErCry4 protein. When the photophysical process of FAD inside the protein sample was considered, the fast electron transfer process quickly repopulates the ground state of FAD after the optical excitation [153, 235, 236]. Thus it obviously quenches the photoluminescence from the protein molecule. Then the emission from the protein sample is very weak and superimposed by spurious light scattering from, e.g., aggregated proteins in the solution or the solvent itself, and they again mask the weak PL. In the investigated protein sample, the fluorescence yield was reduced by a factor of about 30 in comparison with that of free FAD in buffer solution. Besides, FAD can exist in different redox state while inside the protein, oxidized (FAD_{ox}), semiquinone (one-electron reduced, $FAD^{\bullet-}/FADH^{\bullet}$), and hydroquinone (fully reduced, $FADH^-$), and each have definite absorption and emission properties [2, 12, 21, 154]. So it is essential to distinguish the PL from the scattering background signal [4].

Figure II. 8 (a) shows the complete EE spectrum of the ErCry4 protein sample retrieved from the BI-TWINS map using the separation method described above. It contains coherent light scattering (diagonal line) and PL (bottom) contributions with a lower magnitude than coherent contribution. The isolated incoherent EE spectrum in Figure II. 8 (b) mainly shows a single emission component with an absorption spectrum (Figure II. 8 (b), right panel (solid black line)), whereas the scattering component spectrum (Figure II. 8 (a), bottom panel) is efficiently suppressed. The PL emission spectrum (Figure

II. 8 (b), bottom panel (solid black line)) is structured with peaks at 530 and 550 nm and extended up to about 650 nm [4].

When a chromophore molecule is optically excited, there will be transitions between the ground state to Franck-Condon allowed vibronic levels of the higher excited electronic states. Then the excited chromophore molecule from the higher excited electronic states, quickly relaxes to the lower vibrational level of the higher excited state, according to Kasha's rule. Then the molecules decays to Franck-Condon allowing vibronic levels of ground state by emitting photons. In absorption and emission, the transition between vibronic levels of different electronic states is very sharp, and each transition has its own dephasing time. For free chromophore molecules in a solution, the dephasing time of each transition gets large due to the interaction of surrounding solvent molecules. Consequently, single vibronic transitions are invisible, and there will occur an inhomogeneous broadening of transition thus resulting in the unstructured broadened absorption (emission) spectra of the molecules. But if the chromophore molecules are isolated from the surroundings, the vibronic transitions can appear in the absorption (emission) spectra. This is the scenario in the FAD chromophore inside the ErCry4 protein molecule. The FAD molecules, situated in the protein cage of ErCry4 molecules, only have limited or no access to the surrounding solvent solution. So the vibronic transitions in the emission process appears as the structured peaks at 530 and 550 nm in the emission spectra (Figure II. 8 (b), lower panel) of the FAD chromophore attached to the ErCry4 protein [237, 238].

Both the excitation and emission spectra (Figure II. 8 (b), right and bottom panel) are in good agreement with the one reported for the FAD chromophore in its anionic, fully reduced (hydroquinone) form (FADH^-) in Photolyase protein [2]. For comparison absorption and emission spectra of FADH^- in Photolyase flavoprotein are shown in Figure II. 8 (b), right and bottom panels as blue dashed line [2]. It is conclude from the retrieved absorption and emission spectra Figure II. 8 (b) that the PL in the investigated ErCry4 sample is dominated by emission from the FAD chromophore in its hydroquinone redox form (FADH^-). No sign of emission from the FAD_{ox} chromophore forms is found. Since the redox equilibrium between the different redox states can readily be controlled by adding suitable oxidizing agents to the buffer solution, such EE spectra provide a quantitative means for monitoring the redox state. Moreover, the structured emission spectra give the signs of protein chromophore binding [17, 235, 239] in ErCry4 protein [4].

It had been shown here that using the BI-TWINS spectrometer, the intensity map of sample emission is recorded as a function of the arrival time of photons, and excitation (x_{ex}) and detection (x_{det}) wedge positions. The temporally integrated emission map creates an interferogram as a function of x_{ex} and x_{det} . From the interferogram it was possible to distinguish and isolate patterns generated by coherent and incoherent emissions using the separation procedure described earlier. The method, developed for

distinguishing and separating of coherent and incoherent scattering contributions from the EE map is extremely effective, simple and useful. Even immeasurable faint incoherent (coherent) emission was differentiated and isolated from coherent (incoherent) scattering [4].

II.4 Time-Resolved Excitation Emission Spectroscopy

II.4.1 Results and Discussion

As mentioned earlier, in the BI-TWINS spectrometer, SPAD was used as a detector and it records the histogram of photons arrival time as a function of excitation (x_{ex}) and detection (x_{det}) wedge positions using TCSPC electronics. So the spectral and dynamical characteristics of each emitted photon are recorded in the BI-TWINS intensity map. So far, the generation of coherent and incoherent EE spectra from the time-integrated interferogram of the BI-TWINS intensity map has been discussed. But it is possible to apply the same separation method to TCSPC time-resolved intensity map recorded by the BI-TWINS spectrometer. This allows us to separate coherent and incoherent contribution from the time-resolved three-dimensional (3D) data set. The FT of BI-TWINS intensity map along x_{ex} and x_{det} leads to an EE spectrum at each TCSPC time point [219]. Then a Matlab-based toolbox [202] is used to globally analyze the 3D data set, decomposing it into independent sets of EE spectra and dynamics. Figure II. 9 shows the decomposed time-resolved coherent (solid blue line) and incoherent (solid black line) decay dynamics from the 3D data set for (a) C6 dye in ethylene glycol, (b) molecular FAD in buffer solution, and (c) FAD chromophore inside the ErCry4 protein recorded for vertically (V) polarized excitation and magic angle (M) detection. The decay dynamics of all three samples exhibit long fluorescence decay and fast decaying coherent dynamics. A model function $A(t)$ is fitted to these time-resolved decay dynamics by neglecting the finite response time of the TCSPC detector and the finite pulse duration of excitation light. The $A(t)$ can be described as,

$$A(t) = A_1 \Theta(t - t_1) \exp\left(-\frac{t - t_1}{\tau_{c/F}}\right). \quad (\text{II.1})$$

Here A_1 is the initial amplitude of the exponential function, Θ represents the Heaviside function, and $\tau_{c/F}$ is the coherent/fluorescence decay time. The function $A(t)$ is fitted to the decay for $t > t_1$ (red dash line in Figure II. 9 (a)). The value of t_1 is selected in such a way that avoids the initial rise in the decay curves. The fitting procedures provide the decay time τ_c as 0.26, 0.25, and 0.109 ns and τ_F as 2.37,

3.9, and 4.49 ns for C6, molecular FAD, and chromophore FAD inside the ErCry4 protein, respectively. The coherent decay times τ_c represent the instrument response time (IRF) of the setup.

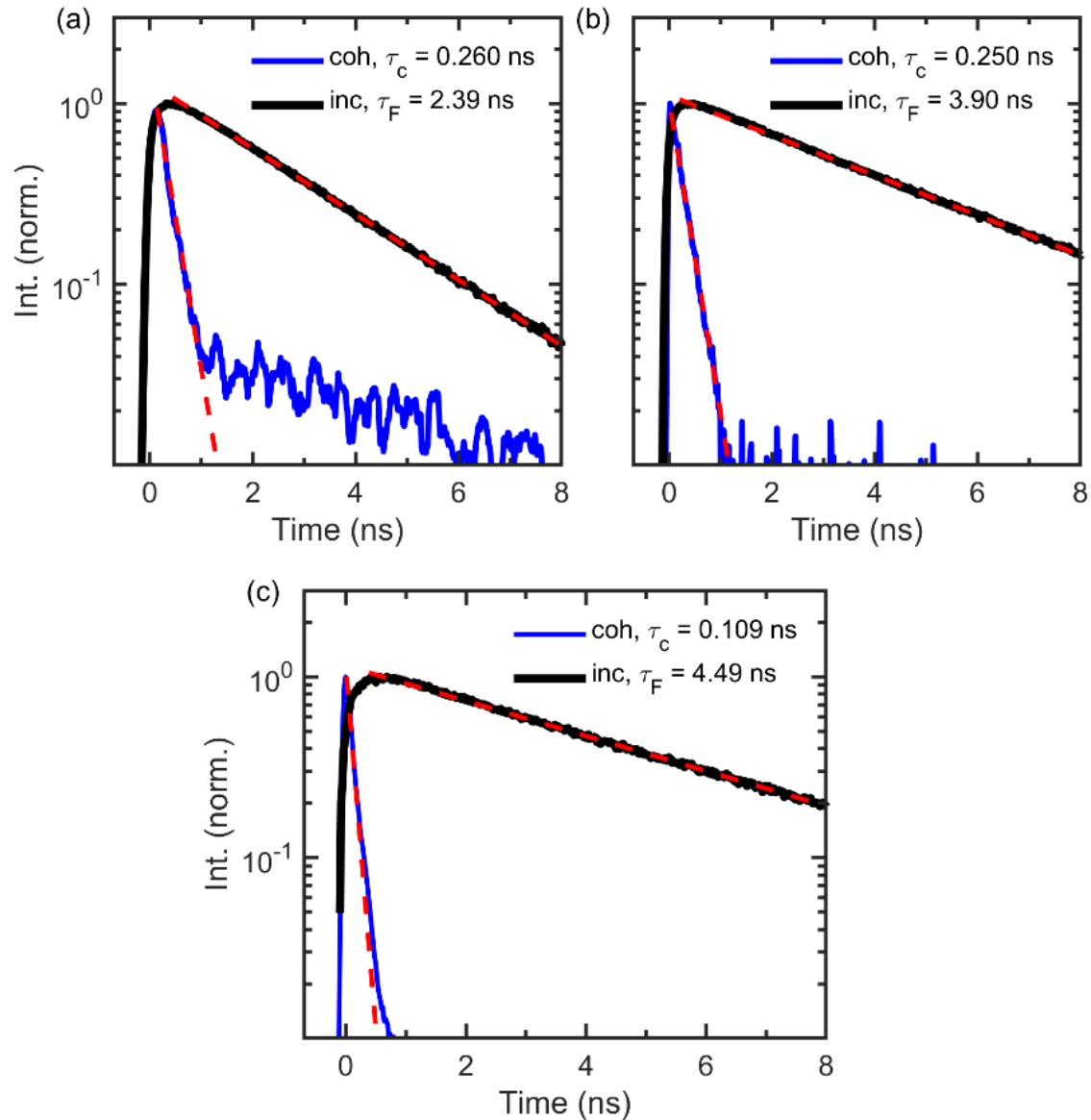


Figure II. 9 Time-resolved coherent (blue solid line) and incoherent (black solid line) decay dynamics of (a) Coumarin 6 (C6) in ethylene glycol (b) flavin adenine dinucleotide (FAD) in buffer solution (c) FAD chromophore inside the European robin (*Erithacus rubecula*) cryptochrome 4 (ErCry4). These decay dynamics are recorded using our BI-TWINS spectrometer (Figure II. 1) for vertically (V) polarized excitation and magic angle (M) detection. A model function, $A(t) = A_1 \Theta(t-t_1) \exp\left(-\frac{t-t_1}{\tau_{c/F}}\right)$ is fitted (red dashed line) to these fluorescence decay dynamics and obtained $\tau_{c/F}$ value indicated in the inset of corresponding figure. The fluorescence decay dynamics of (a) C6 dye and (b) molecular FAD have decay time (τ_F) of 2.37 and 3.90 ns respectively, equivalent to already reported literature values [5, 10]. (c) The chromophore FAD in the ErCry4 protein sample exhibit long fluorescence decay with $\tau_F = 4.49$ ns. The long decay time matches the protein-bound fully reduced flavin dynamics [3, 19-21, 23]. The coherent time τ_c indicates the instrument response time of the setup.

The spectral and dynamical behavior of C6 dye in ethylene glycol was reported earlier and obtained results Figure II. 7 (a) and Figure II. 9 (a)) match well with the literature [5]. The spectral behavior of molecular FAD in buffer solution is equivalent to FAD_{ox} (Figure II. 6 (a)). The decay time constant $\tau_F = 3.9$ ns associated with the decay dynamics of molecular FAD also confirms the existence of FAD_{ox}

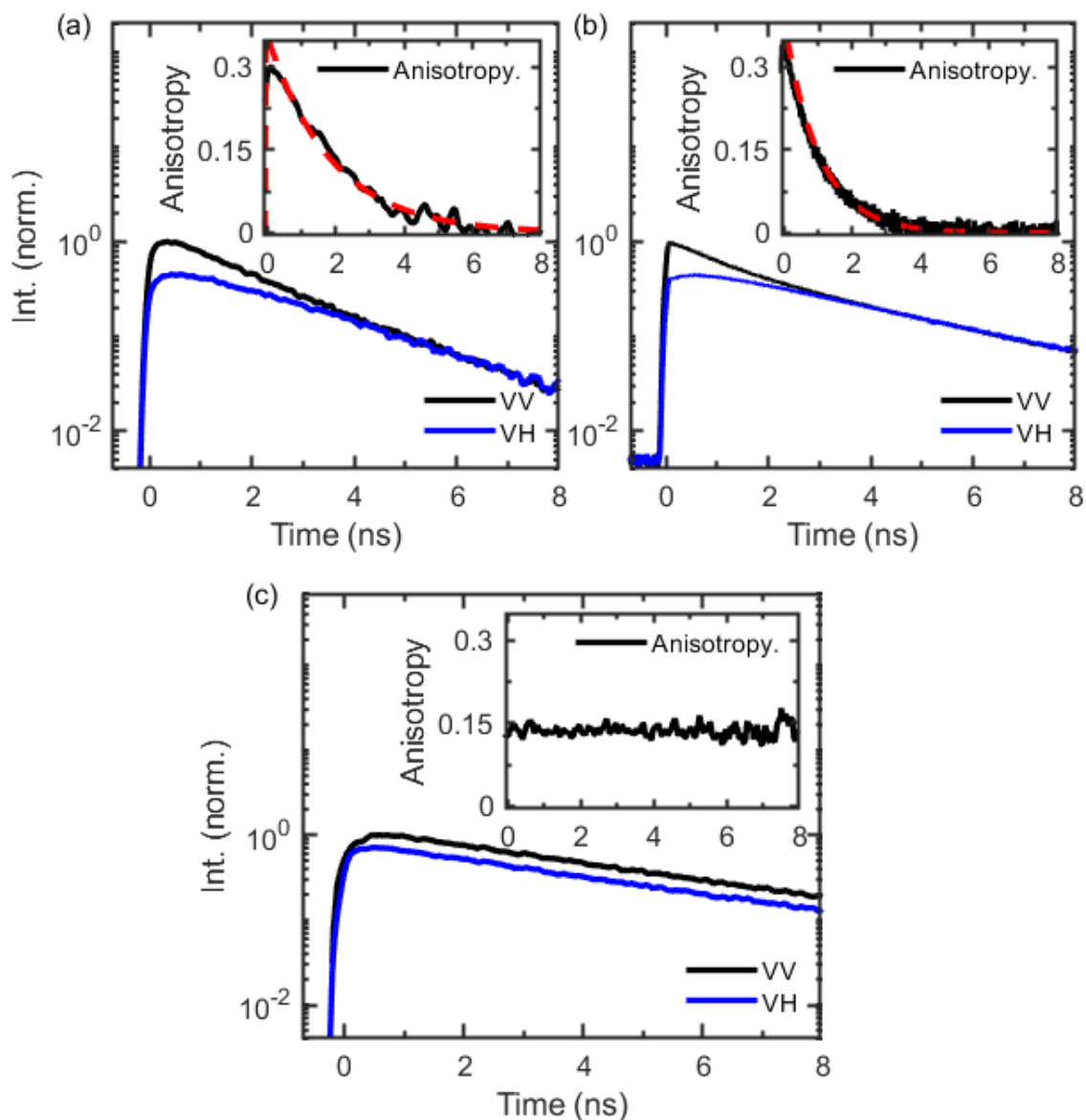


Figure II. 10 VV (black solid line) and VH (blue solid line) polarized fluorescence decay dynamics and calculated anisotropy (inset, black solid line) decay of (a) Coumarin 6 in ethylene glycol (b) Molecular FAD in buffer (c) FAD chromophore inside the European robin (*Erithacus rubecula*) cryptochrome 4 (ErCry4) protein. (a) The VV and VH polarized decay dynamics of Coumarin 6 and molecular FAD are identical at long time (~ 3 ns) after excitation. (Inset) The anisotropy decay of Coumarin 6 decays to zero with rotational relaxation time $\tau_r = 1.91$ ns (red dashed line) matches well with literature [5]. (b, inset) For molecular FAD the anisotropy decay has $\tau_r = 1.02$ ns. (c) The VV and VH polarized decay dynamics of chromophore FAD inside ErCry4 are not identical at long time after excitation. The anisotropy decay (c, inset) of FAD chromophore has a pronounced residual anisotropy of ~ 0.15 and persists for time delays up to 8 ns. This proves that dominant fraction of FAD chromophore is bound to the ErCry4 protein.

[2, 10, 149] in its open conformer [2, 10, 12, 18, 19, 148] in the buffer solution. The FAD chromophore inside the ErCry4 sample possess long fluorescence decay dynamics with $\tau_f = 4.49$ ns (Figure II. 9 (c), black solid line). The excitation emission spectra in Figure II. 8 (b) proved the existence of hydroquinone redox form (FADH⁻) inside the ErCry4 sample. Leenders et al [23] reported that the protein attached fully reduced FAD have long fluorescence decay dynamics. So the result in Figure II. 9 (c) is matching with those of earlier reported studies.

The BI-TWINS spectrometer can record polarization-resolved fluorescence decay dynamics (VV and VH) by changing the orientation of P₃ and P₄ polarizers. A polarization-resolved fluorescence decay dynamics is always a way to monitor molecular reorientational motions in solution. When we initially excite the sample molecule with V polarized light, there will be an enhancement of fluorescence emission for the V polarized detection and suppression of light along H polarized due to the fixed transition dipole moment of the molecules. But at a later time, the thermally induced diffusive rotational motion of the molecule leads to the loss of dipole alignment and thus to equilibration of the emitted light for both polarization configurations. Probing the rotational anisotropy of the sample as a function of the arrival time of the photons thus provide an understanding of the rotational motion of the emissive molecules in the sample solution. The time-dependent anisotropy decay $r(t)$ of the sample molecules can then be calculated from the fluorescence intensity (I_{VV} and I_{VH}) of VV and VH polarized decay components.

$$r(t) = \frac{I_{VV}(t) - I_{VH}(t)}{I_{VV}(t) + 2I_{VH}(t)} \quad (\text{II.2})$$

Here $I_{VV}(t) = e^{-t/\tau_f} (1 + 2r_0 e^{-t/\tau_r})$ and $I_{VH}(t) = e^{-t/\tau_f} (1 - r_0 e^{-t/\tau_r})$. Here r_0 is initial anisotropy, $r_0 = 1/5(3\cos^2 \delta - 1)$, where δ is the angle between absorption and emission dipoles. Usually $\delta = 0$ for fluorescence emission, and $r_0 = 0.4$. The τ_r is the rotational relaxation time [240].

Then the Equation (II.2) becomes,

$$r(t) = r_0 e^{-t/\tau_r}. \quad (\text{II.3})$$

VV and VH polarized fluorescence decay dynamics were recorded for three samples, Coumarin 6, molecular FAD, and chromophore FAD in the ErCry4 protein environment. These fluorescence decay curves have effects of polarization orientation in their intensity and decay time. So, a correction factor G is calculated and applied to the polarization-resolved curves to avoid its impact. There are so many methods available for G factor correction [230]. Here the tail-matching method was followed [230] to

Coumarin 6 data and G was calculated as 1.26 for our BI-TWINS spectrometer. Then the Equation (II.3) becomes,

$$r(t) = \frac{I_{VV}(t) - GI_{VH}(t)}{I_{VV}(t) + 2GI_{VH}(t)}. \quad (\text{II.4})$$

Figure II. 10 (a) shows VV (solid black line) and the G factor corrected VH (solid blue line) polarized fluorescence decay curves of Coumarin 6 in ethylene glycol. It is evident from the figure that the polarization-resolved fluorescence decay curves of Coumarin 6 become identical after ~ 3 ns due to the loss of dipole orientation of molecules at a longer time. The time-dependent anisotropy curve $r(t)$ is calculated for Coumarin 6 using the Equation (II.4) shown in Figure II. 10 (a), inset. A model function according to the Equation (II.4) is fitted to the anisotropy decay (Equation (II.4), red dashed line) and finds that the time-resolved anisotropy has an initial value $r_0 = 0.31$ and decays to zero within 3.5 ns. The rotational relaxation time τ_r associated with the time dependent $r(t)$ of C6 is calculated as 1.91 ns. The calculated τ_r value is equivalent to the literature reports for Coumarin 6 in ethylene glycol [5]. The VV and VH polarized fluorescence decay dynamics and anisotropy decay for molecular FAD in buffer solution are shown in Figure II. 10 (b) and its inset. The anisotropy decay curve has τ_r value of 1.02 ns. The calculated τ_r value for molecular FAD in buffer solution is higher than in water [19]. The presence of glycerol in the buffer solution makes the solvent more viscous (η) and causes an increase in τ_r ($\tau_r = \frac{4\pi a^3 \eta}{3kT}$) [241, 242]. The initially observed anisotropy for C6 and molecular FAD decays after 3 and 2 ns, respectively, are expected to be similar to those for free chromophore molecules in solutions.

The VV (solid black line) and VH (solid blue line) polarized fluorescence decay curves for the FAD chromophore inside the ErCry4 are shown in Figure II. 10 (c). Unlike the cases of free molecules in solution, VV and VH curves of chromophore FAD in the ErCry4 protein do not become equal even at 8 ns, they remain separated. The anisotropy decay $r(t)$ (Figure II. 10 (c), inset) is persistently fixed at a higher residual value ~ 0.15 for the entire measurement time. This is more than 35% of the maximum anisotropy value 0.4, sign of a perfectly aligned protein-bound chromophore [239]. When a chromophore molecule is attached to a protein cage, its rotational motion is partially or fully restricted by the protein cage. The loss of anisotropy of the chromophore molecules inside the protein is only possible by reorientation of the entire protein cage [243-245]. Therefore the constant anisotropy residual value of FAD inside the ErCry4 prove that the cryptochrome 4 protein cage essentially locks the alignment of the optically excited transition dipole of chromophore FAD and effectively suppresses its rotational relaxation. The rotational relaxation time of a protein of the size ErCry4 in water at room

temperature was calculated to be more than 50 ns [246]. So that the rotational relaxation is absent for ErCry4 protein on the time scale of the measurement in this study.

The time- and polarisation-resolved fluorescence study of Coumarin 6, molecular FAD, and FAD chromophore inside the ErCry4 protein samples was done in this chapter. The fluorescence decay time τ_F of C6 and molecular FAD is already reported [4, 5, 10, 19, 22, 149] and the derived values from this study match the reported values in literatures. The absorption and emission spectra (Figure II. 8) of FAD chromophore in the ErCry4 protein environment demonstrate that inside the ErCry4 protein, FAD is in its fully reduced form (FADH^-). The τ_F value calculated from the time-resolved fluorescence decays of chromophore FAD proves the existence of FADH^- inside the protein and protein-chromophore binding [23]. The anisotropy studies estimated the rotational relaxation time of C6 in ethylene glycol and molecular FAD in buffer solution. The anisotropy decay of the FAD chromophore inside the ErCry4 protein assured the protein chromophore binding [239, 243-246].

As discussed earlier, the BI-TWINS spectrometer records the intensity map of the investigating sample as a function of the arrival time of photons, excitation (x_{ex}) and detection (x_{det}) TWINS wedge positions. The excitation and detection TWINS had been moved for 3 mm with a step size of 25 μm during the recording of single BI-TWINS intensity map. The SPAD detector in the spectrometer had set for an integration time of 200 ms. So it takes almost 700 minutes to record a single BI-TWINS intensity map in this measurement conditions. But exploiting the symmetry properties of the BI-TWINS map, it is possible to reduce the data size of the recording intensity map by a factor of four. However, the number of pixels per axis in the data map can be substantially reduced without degradation of resolution and signal-to-noise ratio by following the undersampling condition (see Appendix A.III.2) [4, 224].

II.5 Summary and Conclusions

In this chapter, a Fourier transform (FT)-based approach described and demonstrated for the acquisition of time-resolved excitation-emission (EE) spectra using two passively phase-stabilized common-path interferometers (BI-TWINS). By introducing one interferometer in the excitation and one in the detection path, it was possible to distinguish and efficiently separate coherent light scattering and incoherent photoluminescence contributions to the EE spectra. For this, the intrinsically different time structure of these two emission components in the measured interferograms in the time domain are exploited. This separation is demonstrated for the time-integrated EE data of highly fluorescent and poorly scattering Coumarin 6 in ethylene glycol and weakly emissive flavin chromophore (FAD) both free in solution and inside the protein European robin Cryptochrome 4 (ErCry4). The optical excitation of this FAD chromophore is the primary step in the formation of radical-pairs inside the protein. The radical-pairs are long-lived intermediate with reaction dynamics that are believed to be sensitive to

weak geomagnetic fields [20, 154]. The time-domain interferometric acquisition of the EE maps allows us to unambiguously isolate the partly spectrally overlapping incoherent fluorescence and coherent scattering components. Since, inside proteins, this fluorescence depends on the redox state of flavin, the obtained EE spectra can monitor the redox state of the chromophore by unambiguously determining its EE spectrum. The derived EE spectra of flavin chromophore inside the ErCry4 prove that flavin is in its hydroquinone redox form (FADH^-). The vibronically structured emission spectrum also confirms chromophore protein bonding in the ErCry4 protein [237, 238].

For the demonstration of the separation method, time-integrated EE maps are analyzed in the first part of study. In the second part of study, the same separation approach was straightly applied to TCSPC time-resolved spectra [218]. This approach is useful for life-time analysis of weakly emissive and/or highly scattering samples. Through the analysis the time dynamics of FAD chromophore inside the ErCry4 protein shows the presence of FADH^- with long-lived fluorescence. The developed BI-TWINS spectrometer can also record the polarization-resolved time-resolved EE spectra. The polarization-resolved time dynamics analysis gives insight about the rotational reorientation time of sample molecules. The persisting high residual value of anisotropy decay of FAD chromophore in the ErCry4 protein once again justifies the chromophore-protein binding [243-245].

The FT-based time-resolved EE spectrometer is a wonderful method for spectral and dynamical analysis of investigating sample molecules. The scanning time and size of the data recorded by the spectrometer can be reduced by exploiting the symmetry properties of the BI-TWINS map and undersampling condition. The integration time per pixel in the spectrometer is limited by the specific type of detector, to enable time-resolved measurements. The integration time could be again reduced, by using time-integrating photodiodes and lock-in detection if we do not need the time-resolved measurements [4].

The presented interferometric time-resolved EE scheme based on the BI-TWINS may be helpful for another technique where scattering suppression is critical, such as hyperspectral imaging [201], coherent Anti-Stokes Raman Scattering [198], or stimulated Raman Scattering [199, 200]. Further miniaturization of the setup, e.g., by replacing free-space propagation of the excitation and collected light beams by optical fibers, will facilitate the design of portable spectrometers for simultaneous absorbance and time-resolved EE measurements [247]. Other interesting applications of the demonstrated method lie in probing the (nonclassical) statistics of the emitted light [4].

Chapter III

Time-Resolved Excitation-Emission Spectroscopic Studies on Cryptochrome 4 Molecules.

Some of the results in this chapter are published in [16].

Daniel Timmer, Anders Frederiksen, Daniel C. Lünemann, **Anitta R. Thomas**, Jingjing Xu, Rabea Bartölke, Jessica Schmidt, Antonietta De Sio, Ilia A. Solovyov, Henrik Mouritsen, and Christoph Lienau

Tracking the Electron Transfer Cascade in European Robin Cryptochrome 4 Mutants

[ja-2023-00442v.R1](#)

A.R.T and D.C.L performed and analyzed the experiments. A.R.T prepared samples for the experiments.

III.1 Introduction

Optical spectroscopy is an essential tool for investigating the elementary properties of materials by analyzing the interaction of light with matter. The structural, dynamic, and chemical properties of the system can be figured out by using absorption, emission, scattering, and rotation of the light field by atoms or molecules with non-compatible time resolution. The most common and straightforward optical spectroscopy studies are linear absorption and emission measurements of the system. These measurements provide the primary photophysical properties of the samples. Unlike linear absorption and emission studies, excitation-emission (EE) spectroscopy records the intensity of the emitted light at various excitation wavelengths and provides a two-dimensional data map. This two-dimensional data map includes information about energy transfer in the systems [248], coherent and incoherent emission [4], and the source and concentration of the emitting species [249]. So these EE spectroscopy studies have a wide variety of applications in biological and medical systems [205], water and food quality control [250-253], electronic transitions in the gas phase [249, 254], and condensed phase systems [255-257], fluorescence microscopy [258] and reaction dynamics [259].

The EE measurements require a longer acquisition time due to the narrow band excitation and recording of the corresponding emitted light from the samples. In addition, EE setups were always bulk and expensive in earlier days, using excitation and emission monochromators. But these drawbacks are

overpowered by broadband spectral interferometric techniques [258, 260, 261]. The recent invention of intrinsically stable common-path interferometers, called TWINS [215, 216], made broadband spectral interferometry in the ultraviolet to near-infrared spectral range more accessible and has already been established in EE spectroscopy [4, 217].

Here the Fourier transform-based BI-TWINS spectrometer (see Chapter II) was used to perform three-dimensional (3-D) EE spectroscopy experiments. TWINS interferometers were used in the excitation and emission arms of the setup. The excitation TWINS generates two time-delayed (τ_1) replicas of the excitation light. These pulse replicas interact with the sample and emit light with a time delay (τ_1). The emitted light again passes through the detection TWINS and creates another pair of transmitted light with delay τ_2 . Then, a single photon avalanche photodiode records a histogram of the emitted light by time-correlated single-photon counting (TCSPC) electronics as a function of τ_1 and τ_2 . This provides a 3-D data map of the emitted light as a function of excitation (τ_1), emission (τ_2) delay, and arrival time photon. A two-dimensional Fourier transform of the data map yields a time-resolved EE map of the sample under investigation. The additional time axis in the data map provides information about the dynamics of different species in the samples [4, 16, 218].

The time-resolved EE spectroscopic studies were carried out on cryptochrome 4 protein molecules. Cryptochrome 4 proteins consist of blue light-sensitive flavin adenine dinucleotide (FAD) as a chromophore. The Cryptochrome 4 (ErCry4) proteins are located in the retina of the European robin (*Erithacus rubecula*) and have a non-covalently bound FAD chromophore that bridges the protein surface through a chain of four tryptophan (Trp) amino acid residues, namely Trp_A (W395), Trp_B (W372), Trp_C (W318), and Trp_D (W369). Blue light excitation of the FAD molecules triggers consecutive electron transfer through these Trp chains and causes magnetically sensitive radical-pair formation [154]. This photoinduced electron transfer and formation of magnetically sensitive radical-pairs are thought to be the reason for the sensitive magnetic field compass mechanism in night migratory birds (See Chapter I). Here we have tried to identify the signature of electron transfer reactions in ErCry4 protein and the different species involved in the reaction using time-resolved EE spectroscopy. In this study, we have used molecular FAD, synthesized ErCry4 protein (WT ErCry4), and its four mutants (W_AF, W_BF, W_CF & W_DF), in which Trp involved in cryptochrome activation has been site-selectively replaced by a redox-inactive phenylalanine (Phe) [16]. Our spectroscopic studies confirm the electron transfer through the Trp chains and protein-chromophore binding in ErCry4 protein.

III.2 Experimental Section

III.2.1 Experimental Implementation

The time-resolved EE studies of molecular FAD, ErCry4, and its four mutants (W_{AF} , W_{BF} , W_{CF} , and W_{DF}) are done using our BI-TWINS spectrometer (Figure II. 1, Chapter II, [4]). The excitation TWINS in the BI-TWINS spectrometer generates phase-locked pulse pair of picosecond pulses from a supercontinuum whitelight source (SC 400, 40 MHz repetition rate, Fianium). The laser spectrum is

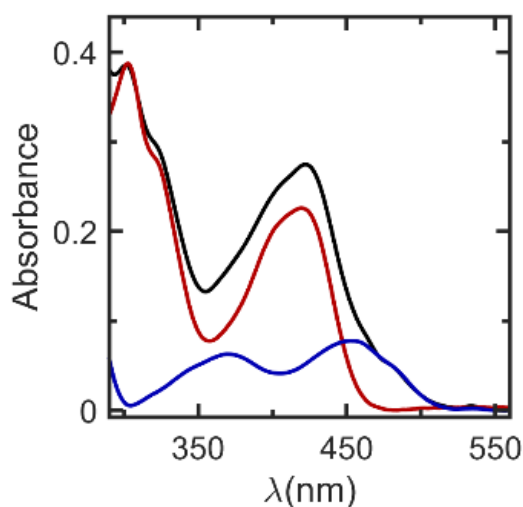


Figure III. 1 Absorbance spectrum of free molecular flavin adenine dinucleotide (FAD) in 1.5 mM potassium ferricyanide (PFC) and buffer solution (pH 8.0). (solid black line) Combined absorbance spectrum of 46 μM molecular FAD and 1.25 mM PFC in buffer solution. (solid red line) The absorbance spectrum of 1.25 mM PFC in buffer solution has an absorption maximum at 420 nm. (solid blue line) The absorbance spectrum of molecular FAD at a concentration of 40 μM is obtained by subtracting the PFC absorbance (solid red line) from the combined absorbance spectrum (solid black line).

filtered to a 400-680 nm spectral range with an average power of 50 μW . The excitation spectral range is selected according to the absorption and emission band of the samples. The average excitation power of 50 μW is chosen to avoid degradation of the sample molecules. The polarization of the excitation pulse is selected to the vertical direction (V), perpendicular to the laser beam in the detector plane, using the polarizer P_3 in the BI-TWINS spectrometer (Figure II. 1, Chapter II, [4]). Then the polarization-resolved time-delayed pulse pair from the excitation TWINS is focused on the sample. As the result of their interaction with the sample, coherent or incoherent light is emitted. The emitted light from the sample is collected at a 90° angle with respect to the excitation path. The polarization of the emitted light can be selected either parallel (V), perpendicular (H), or magical angle (M, $\theta = 54.7^\circ$) polarization with respect to the laser polarization direction using the polarizer P_4 in the BI-TWINS spectrometer

(Figure II. 1, Chapter II , [4]). The emitted light passes through the detection TWINS, creating phase-locked pulse pairs. These pulse pairs are then focused onto a single-photon avalanche photodiode (SPAD). The arrival time of each emitted photon in the SPAD detector with respect to excitation is recorded using a TCSPC unit. Thus, the BI-TWINS spectrometer records an intensity map as a function of arrival time and excitation (x_{ex}) and detection (x_{det}) TWINS wedge positions. For a single EE map, here the excitation and detection TWINS are scanned over 3 mm with a step of 25 μ m. The scan range is chosen so that the spectral resolution reaches 6.5 nm, and the step size is selected to satisfy the under-sampling condition [224]. Here the SPAD integration time was set to 200 ms to get a good signal-to-noise ratio and avoid the pileup condition. This will result in a BI-TWINS map of size 121 x 121 pixels within a measurement time of 70 minutes (Figure II. 1, Chapter II , [4]).

III.2.2 Sample Preparation

For the time-resolved EE spectral studies of the FAD sample, molecular FAD (Sigma-Aldrich F6625) is dissolved in a buffer and 1.25 mM potassium ferricyanide (PFC) solution at a concentration of 46 μ M. The absorbance spectrum of the sample is shown in Figure III. 1 (solid black line). The buffer solution is used to synthesize ErCry4 protein samples, and it consists of 20 mM tris(hydroxymethyl)aminomethane and 250 mM NaCl in 80% water and 20% glycerol. The PFC is added as the oxidizing agent in cryptochrome protein samples to prevent photoreduction of the samples during the measurements. Figure III. 1 shows the linear absorbance spectrum of 1.25 mM PFC in buffer solution (Figure III. 1 solid red line). The main absorption band of PFC is around ~420 nm, [262] and it overlaps with the absorption band of molecular FAD at 450 nm (Figure III. 1, solid blue line).

Wild-type (WT) ErCry4 (GenBank: KX890129.1) and its four mutants (W_{AF} , W_{BF} , W_{CF} , and W_{DF}) protein samples were cloned, expressed, and purified according to the protocol described by Xu et al [154]. Briefly, the ErCry4 protein mutants are generated by replacing the DNA codon for tryptophan (TGG) at amino acid position 395 (W_{AF}), 372 (W_{BF}), 318 (W_{CF}), or 369 (W_{DF}) in the ErCry4 protein gene by a phenylalanine codon (TTT) in a PCR using the Q5 site-directed mutagenesis kit (New England Biolabs). Plasmids were confirmed by Sanger sequencing (LGC Genomics). Proteins were expressed in BL21(DE3) *Escherichia. coli* (*E. coli*) cells in the dark and purified by Ni-NTA agarose columns, followed by anion exchange chromatography. Purified protein samples were concentrated to 5-6 mg/mL in the aqueous buffer solution. In total 10 mM of 2-mercaptoethanol (BME) is added to the concentrated sample to prevent the dimerization of the proteins. Samples are snap-frozen in liquid nitrogen and stored at -80° C for 3-5 days until the measurements [16]. The added BME in the protein sample is a reducing agent, which will bring the FAD molecules in the protein to different redox states such as FAD neutral radical ($FADH^\bullet$) and fully reduced state ($FADH^-$). Since the photocycle of ErCry4 starts from the fully oxidized FAD (FAD_{ox}) [20], it is necessary to remove the BME and oxidize the

sample before the measurements. In total, 400 μL of low concentrated stored proteins were used to prepare highly concentrated samples for the measurements. To remove the BME reducing agent from the protein, the sample was shifted to an Amicon Ultra-0.5 centrifugal filter unit. The sample is centrifuged at 4° C, 14000 rpm, until it reaches 200 μL . Then, a 200 μL volume of BME-free buffer solution is added to the filter unit and the sample is centrifuged in the same condition until the volume again reaches 200 μL . The addition of BME-free buffer solution and centrifugation is repeated another nine times. After the washing process, only $\sim 10 \mu\text{M}$ BME will be present in the protein samples. To bring the protein samples to the desired concentration, the BME-free sample was centrifuged again until it reached a volume of $\sim 75 \mu\text{L}$. Then the exact concentration of the FAD molecules in the sample was determined by checking the absorbance at the wavelength of 393 nm. At this wavelength, FAD_{ox} , FADH^{\bullet} , and FADH^- all have a molar absorption coefficient of $6,000 \text{ cm}^{-1}\text{M}^{-1}$ [2, 12]. The FAD concentration in the WT-ErCry4 and its mutant samples is regulated between 85 to 95 μM . Finally, to completely oxidize the FAD in the protein, 1.5 mM PFC is added to the samples, which are then followed by one-hour centrifugation. The addition of PFC and centrifugation of the sample continued until the FAD in the protein samples was fully oxidized, which conformed through the absorbance measurements. It was ensured that a PFC concentration of 1 to 1.5 mM was present in the protein samples during the EE measurement to avoid photoreduction. The PFC corrected absorbance (Figure III. 1) was used to determine the final concentration of FAD molecules in the protein samples using the molar extinction coefficient of FAD_{ox} [16]. A detailed description of protein sample preparation for spectroscopic studies are given in the section A.III.1.

All the measurements were carried out at 0° C in a low-volume cuvette with an optical path length of 0.15 cm (Hellma, 105-252-15-40).

III.3 Results and Discussion

III.3.1 Excitation-Emission studies on Molecular FAD

The spectral and fluorescence dynamical features of ErCry4 and its four mutants were studied using our BI-TWINS spectrometer. As a reference for the EE studies, firstly free molecular FAD without the surroundings of protein molecules was investigated. The BI-TWINS spectrometer records the time-resolved fluorescence decay of the sample as a function of wedge positions of excitation (x_{ex}) and detection (x_{det}) TWINS. The decay dynamics of molecular FAD are recorded for vertically (V) polarized excitation and magic angle (M) polarized detection. The background signal of the decays is calculated by averaging the counts before the arrival of the excitation pulse (before 0 ns), and subtracted from the corresponding decay curve. Figure III. 2 shows a background-free fluorescence decay of molecular FAD in buffer and 1.25 mM PFC solution (solid black line) recorded at zero delay positions

of both TWINS. By neglecting the finite response time of the TCSPC detector and the finite pulse duration of the excitation laser, the fluorescence decay dynamics can be described as,

$$A(t) = A_1 \Theta(t - t_1) \exp\left(-\frac{t - t_1}{\tau}\right), \quad (\text{III.1})$$

where A_1 is the initial amplitude of the exponential function, Θ the Heaviside function with $t_1 = 0.3 \text{ ns}$

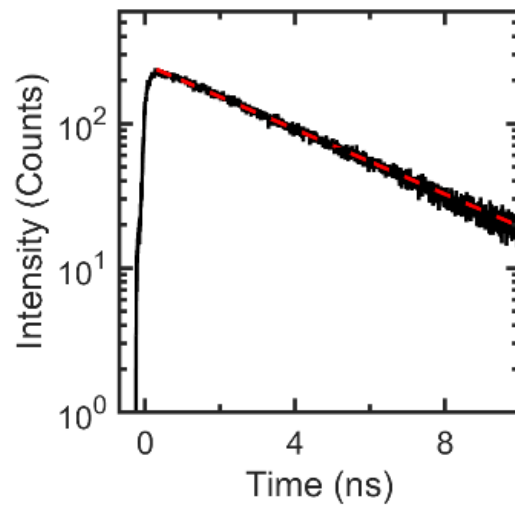


Figure III. 2 Time-resolved fluorescence decay dynamics of free molecular flavin adenine dinucleotide (FAD) in 1.5 mM potassium ferricyanide (PFC) and buffer solution (pH 8.0) at a concentration of 46 μM . The decay dynamics is recorded using our BI-TWINS spectrometer setup (Figure II. 1) for vertically polarized excitation (V) and magic angle (M) detection in under-sampling condition (See details in Chapter II) [4]. The BI-TWINS spectrometer records an intensity map as a function of the arrival time of the photon and wedge positions of excitation (x_{ex}) and detection (x_{det}) TWINS. The decay dynamics (solid black line) shown here are recorded when excitation and detection TWINS are at their zero delay positions. A model function, $A(t) = A_1 \Theta(t - t_1) \exp\left(-\frac{t - t_1}{\tau}\right)$, $t_1 = 0.3 \text{ ns}$ with $A_1 = 256$ counts and $\tau = 3.9 \text{ ns}$ is fitted (red dashed line) to the fluorescence decay. The long fluorescence decay ($\tau = 3.9 \text{ ns}$) is a characteristic of free FAD molecules in their open conformation.

ns, and τ is the fluorescence decay time. The function $A(t)$ is fitted to the fluorescence decay for $t > t_1 = 0.3 \text{ ns}$ (red dotted line in Figure III. 2). The value of t_1 is selected in such a way that avoids the initial rise in the decay curve. This fluorescence dynamics exhibit a monoexponential decay with $A_1 = 260$ counts and $\tau = 3.7 \text{ ns}$. The long fluorescence decay value can be assigned directly to the open conformer of optically excited fully oxidized FAD molecules (FAD_{ox}) [10, 18, 19, 148]. The fluorescence decay time of the optically excited stacked conformer of FAD_{ox} molecules is around 6.6 ps [16, 22], which cannot resolve within the instrument resolution ($>100 \text{ ps}$) used in this study. The

function in the Equation (III.1) is fitted to all other time-resolved fluorescence decay curves (for $t > t_1$) recorded at different excitation and detection TWINS wedge positions. The initial amplitude A_1 and the fluorescence decay time τ of all fit functions are collected and plotted as a function of excitation and detection TWINS wedge positions, shown in Figure III. 3 (a) and (b), respectively. The A_1 map is an interferogram with incoherent scattering contribution [4]. It has vertical and horizontal interference patterns created by changing excitation and detection TWINS delays. There are no diagonal stripes on the A_1 map, only photoluminescence (PL) contributions are detected. Cross-cuts of the A_1 map along the x_{ex} and x_{det} positions are shown in Figure III. 3 (a) left and bottom panels, respectively. The positions of cross-cuts in the map are marked as a dash-dotted line. The cross-cut along the x_{ex} position

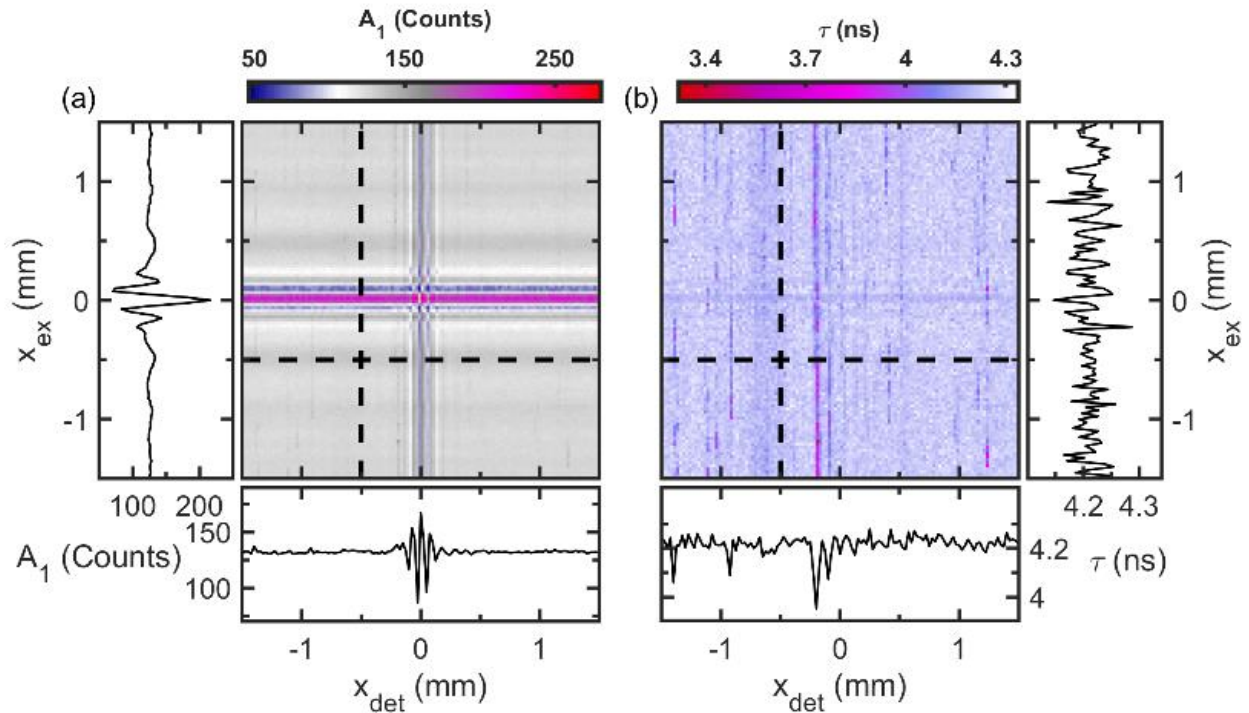


Figure III. 3 The initial amplitude counts A_1 (a) and decay time τ (b) maps of free molecular FAD in buffer solution. As shown in Figure 1, a model function $A(t)$ is fitted to all the fluorescence decay of free molecular FAD recorded by the BI-TWINS spectrometer. The initial amplitude counts A_1 and decay time τ of all fit functions are collected and plotted as a function of excitation (x_{ex}) and detection (x_{det}) TWINS wedge positions. The A_1 map has the characteristic feature of an incoherent excitation-emission interferogram, horizontal, and vertical stripes. The vertical and horizontal stripes in the τ map is not as prominent as in the A_1 map. A cross-section (black dashed line) of the A_1 and τ maps along the horizontal ((a) and (b) bottom panel) and vertical ((a) left panel and (b) right panel), are shown here. The cross cuts of the A_1 map have the characteristic features of an interference (under-sampled) structure recorded by excitation ((a) left panel) and detection ((a) bottom panel) TWINS.

represents a field autocorrelation of a fraction of the excitation light interacting with the sample in under-sampling condition. The horizontal cross-cut of the A_1 map (Figure III. 3 (a) bottom panel) gives the field autocorrelation of the fluorescence light emitted from the sample after excitation with the phase-locked pulse pair. The τ map, Figure III. 3 (b)), does not show any visible interference pattern at first glance along the excitation and detection TWINS positions. But a careful observation indicates

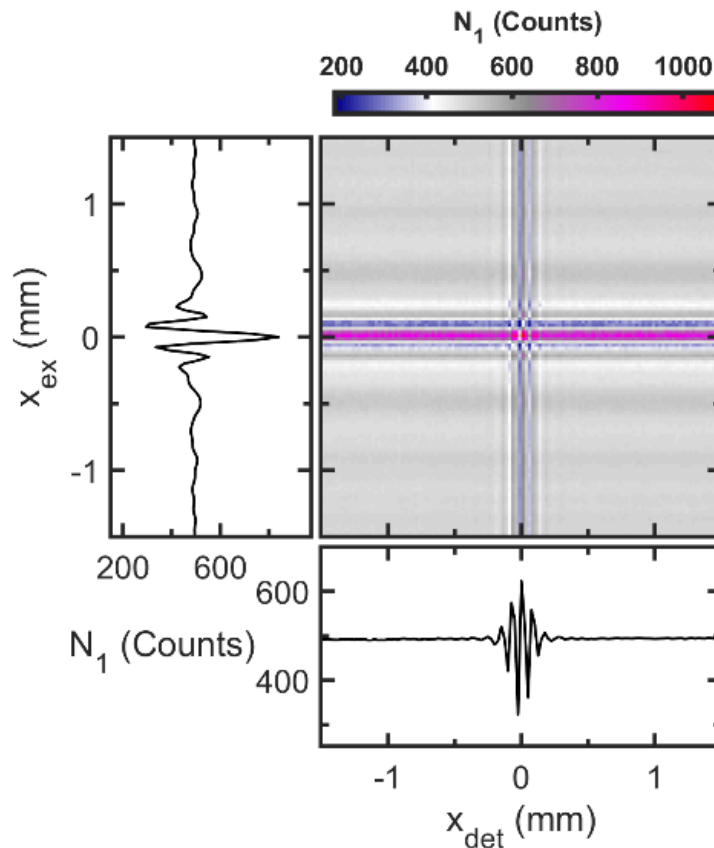


Figure III. 4 The total photons (N_1) map of free molecular FAD in buffer solution. The total number of photons N_1 that are detected during the time-resolved fluorescence decay can be calculated from A_1 and τ values

$$\left(N_1 = \int_{t_1}^{\infty} A_1 \exp\left(-\frac{t_1}{\tau_1}\right) dt = A_1 \tau_1 \exp\left(-\frac{t_1}{\tau_1}\right) \right).$$

The N_1 map was calculated from the A_1 and τ maps in Figure III. 3.

This is an excitation-emission interferogram with incoherent contribution. The averaged value of the interferogram along excitation (left panel) and detection (bottom panel) TWINS wedge positions shows a field autocorrelation of a fraction of the excitation pulse that interacts with the sample (left panel) and of the fluorescence emission from the sample (bottom panel), respectively.

fade interference stripes along the direction of x_{det} . The τ map has a mean value of 4.2 ns which matches the fluorescence lifetime of the FAD_{ox} open conformer [19, 22, 149]. Cross-cuts (dashed black line) of the τ map along the x_{ex} and x_{det} (Figure III. 3 (b) bottom and right panel) show decay times

that are randomly distributed over a mean value of 4.2 ns. The A_1 and τ values can be used to calculate the total number of photons (N_1) detected with the time-resolved fluorescence decay (for $t > t_1$),

$$N_1 = \int_{t_1}^{\infty} A_1 \exp\left(-\frac{t}{\tau}\right) dt = A_1 \tau \exp\left(-\frac{t_1}{\tau}\right). \quad (\text{III.2})$$

Using this Equation (III.2), the total number of photons (N_1) detected during the fluorescence decay in Figure III. 2 is calculated as 948 counts. In this manner, N_1 detected at different x_{ex} and x_{det} positions are calculated and plotted as a map Figure III. 4. The N_1 map also shows vertical and horizontal interference patterns along the x_{ex} and x_{det} positions same as the A_1 map (Figure III. 3 (a)). Again the diagonal patterns are invisible on the N_1 map, a EE incoherent interferogram [4]. The N_1 map is averaged along the vertical and horizontal direction and obtained characteristics interference patterns are recorded using excitation and detection TWINS, respectively (Figure III. 4 left and bottom panel). These interference patterns can be recorded separately by placing a single TWINS either in excitation or in detection path. The photoluminescence excitation (PLE) and emission spectrum of the sample (Chapter II , [4]) can be obtained from the left and bottom panel interference patterns [1, 4]. But before

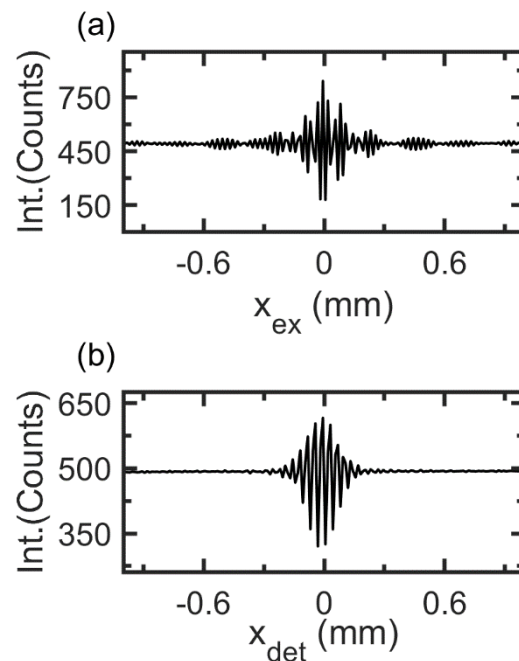


Figure III. 5 A field autocorrelation (a) of the fraction of the excitation light that interacts with the sample and (b) of the emitted light from the sample. The autocorrelation signals in Figure 3 (left and bottom panel) are recorded using under-sampling, and they converted to Nyquist sampling to obtain the plots shown in (a) and (b). Since the white light source spectrum used to excite the sample is highly spectrally structured, the field autocorrelation along the x_{ex} axis (a) oscillates more rapidly than along x_{det} (b) and shows superimposed slower oscillations of its envelope. Moreover, (a) is blue-shifted with respect to the emitted light from the sample (b).

calculating the corresponding spectra, the interference patterns recorded in under-sampled conditions are changed to Nyquist sampling conditions. The details of changing to Nyquist sampling conditions are explained in Appendix A.III.2. The conversion from under-sampling to Nyquist sampling condition is required since there is a mismatch between actual and expected wedge positions of both TWINS during the measurement scan. This mismatch in wedge positions creates frequency modulation that appears as side peaks in the Fourier transform of the intensity autocorrelations. To overcome this situation, these interference patterns are converted to Nyquist sampling conditions, and position corrections that have already been measured during the calibration of the TWINS interferometer (Appendix A.II.1) are applied. This detailed analysis procedure gave Figure III. 5 (a) and (b). The field autocorrelation of the excitation light, which is afterward absorbed by the sample molecule, is shown in Figure III. 5 (a). This oscillates more rapidly than the field autocorrelation along x_{det} (Figure III. 5 (b)), because the spectrum of the whitelight used to excite the sample is highly spectrally structured. Additionally, in Figure III. 5 (a), superimposed minor oscillations of the excitation light envelope can be observed. The fringe spacing of the field autocorrelation along the x_{det} (Figure III. 5 (b)) is larger than that along the x_{ex} axis. This indicates a redshift for the emitted light from the sample compared to the absorbed light. Figure III. 5 (b) shows a significantly lower fringe contrast than Figure III. 5 (a).

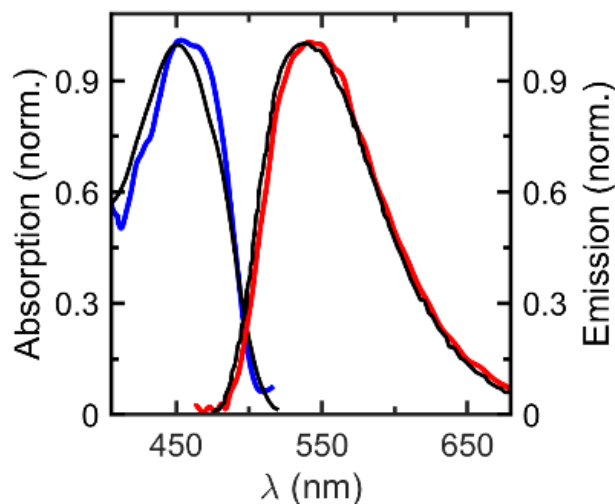


Figure III. 6 Absorption and emission spectra of free molecular FAD in buffer solution. The excitation and emission (solid red line) spectra of FAD molecules can be obtained from the Fourier transform of Figures 4 (a) and (b), respectively [2, 4, 6]. The absorption spectrum (solid blue line) of the sample is derived by normalizing the excitation spectrum with the white light source spectrum used to excite the sample. Both absorption and emission spectra agree well with the reported spectrum in the literature (solid black line).

This is due to the reduced spatial coherence of the emitted light from the focal volume of the excitation beam in the cuvette. Another noticeable thing is, that the autocorrelations in Figure III. 5 (a) and (b) are

highly asymmetric around $x_{ex/d} = 0$. This asymmetry is the evidence for the color (λ) dependence of the phase shift $\Delta\varphi(x, \lambda) = \Delta\tilde{\varphi}(\lambda) + \tilde{k}(\lambda)x$ introduced by each TWINS interferometer (see Appendix A.II.1) [4]. Fourier transform of Figure III. 5 (a) and (b) can give a more quantitative analysis of the interference fringes. Then, the resulting wave number axes need to be transformed into excitation and detection wavelength axes using the respective calibration curve of each TWINS. These procedures provide the excitation (PLE) and emission spectra of the sample (Figure III. 6 (solid red line)). The normalization of the PLE spectrum with the spectrum of the laser light used to excite the sample provides an absorption spectrum Figure III. 6 (solid blue line) of the sample. The whitelight spectrum of the laser source is recorded during the measurement using the photodiode PD₁ in the BI-TWINS spectrometer setup (Figure A. II. 9 (b) in Appendix A.II.2.2 [4]). The calculated absorption spectrum has a peak at 450 nm. The emission spectrum peaks at 530 nm and extends to about 700 nm. Both excitation and emission spectrum agree with the ones reported for molecular FAD in its fully oxidized form (FAD_{ox}) [2, 12]. For comparison, an absorption and emission spectra of molecular FAD_{ox} in another buffer solution reported in Kao et al. (2008) [2] is plotted as a solid black line in Figure III. 6.

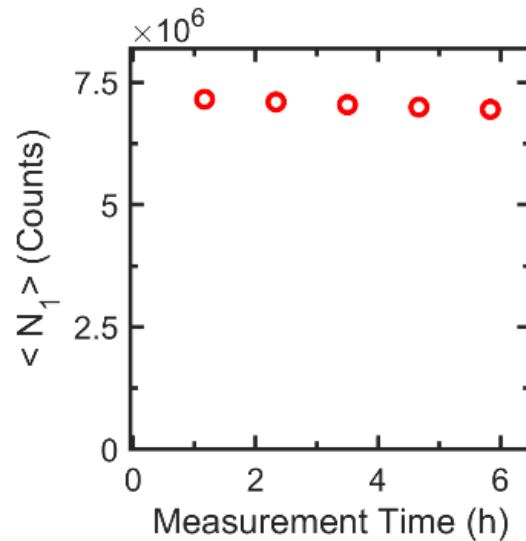


Figure III. 7 The total photon counts $\langle N_1 \rangle$ of free molecular FAD in buffer solution as a function of measurement time. The total number of photons detected for the sample was calculated by summing up the total photons (N_1) map (Figure III. 4) of different measurements. The total photon counts of the FAD sample are almost constant during the entire measurement.

The total number of photons ($\langle N_1 \rangle$) detected during a single measurement scan can be found by summing up the total number of photon (N_1) map of the corresponding measurement. The N_1 map in Figure III. 4 detects a total of 6.5×10^6 counts. In the same way, the $\langle N_1 \rangle$ detected in the other four

consecutive measurement scans are calculated and plotted as a function of the measurement time in Figure III. 7. The total incoherent photons emitted from the molecular FAD in buffer solution are almost constant during measurement. No drastic changes could be observed in $\langle N_1 \rangle$ counts, which suggests that in buffer solution, the molecular FAD is stable. It can be concluded that molecular FAD exists in open conformer in its fully oxidized form (FAD_{ox}) in buffer solution. Any sign of emission from the added oxidizing agent, PFC, any other conformer of FAD_{ox}, and different redox states of molecular FAD could not be found.

The absorption and emission properties of molecular FAD have been studied and reported earlier. The derived fluorescence decay time $\tau = 4.2 \text{ ns}$, and the absorption and emission spectra from the EE measurements agree with the studies reported earlier [1, 2, 12, 18, 19, 149]. Even though no new information was observed on molecular FAD, a new method was developed to analyze and understand the time-resolved EE studies of ErCry4 protein and its mutant samples.

III.3.2 Excitation-Emission studies on WT ErCry4

As described earlier, ErCry4 proteins are blue light-sensitive [27, 141, 154]. The Blue light absorption of FAD chromophore inside the protein samples triggers a series of ultrafast electron transfers across the Trp chains. These sequential electron transfers form a pair of FAD/tryptophan radicals. These

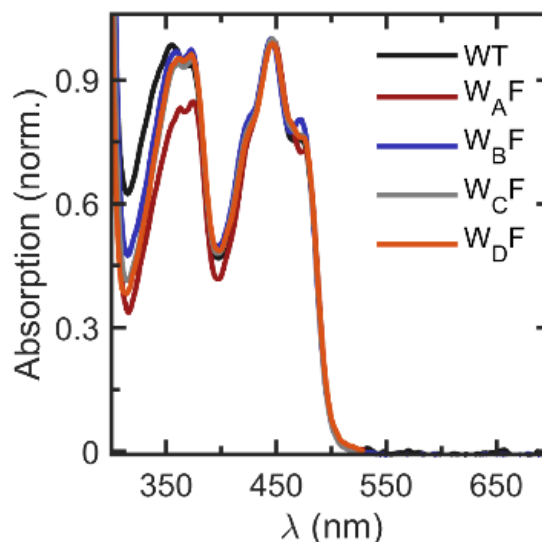


Figure III. 8 Normalized absorption spectrum of fully oxidized cryptochrome 4 protein (WT ErCry4, solid black line) and its four mutants W_XF (X = A, B, C, D) from European robin (*Erithacus rubecula*). In ErCry4 mutants, W_XF (X = A, B, C, D) one of the four tryptophan that involved in the light induced electron transfer reaction has been site-selectively replaced by a redox-inactive phenylalanine (F), to block the electron transfer at different positions in the protein structure. The absorption behavior of WT ErCry4 and its four mutants are similar. The pronounced vibronic structure around 450 nm indicates FAD binding in the protein samples. The absorption spectra of each sample is calculated by subtracting the concentration of remaining oxidizing agent (PFC) in the fully oxidized protein samples

photoinduced electron transfers and the resulting radical-pair generation are currently discussed as key mechanisms underlying the magnetic field compass in migratory songbirds [4, 20, 27, 141, 154]. The electron transfer reaction quickly repopulates the ground state of FAD_{ox} molecules after the photoexcitation of the chromophore. Moreover, during the electron transfer reactions and radical-pair formations, different redox states of FAD, fully oxidized (FAD_{ox}), one-electron reduced semiquinone (FAD^{•-}/FADH[•]), or fully reduced hydroquinone (FADH⁻) can exist in the protein [20]. Different redox states of FAD have distinct absorption and emission spectra and decay dynamics [2, 20]. Recent successful expression and purification of ErCry4 (WT ErCry4) and its mutants, W_AF, W_BF, W_CF, and W_DF [154], allows us to do a time-resolved EE study on them to identify optical spectral and dynamic properties of the different redox state of chromophore FAD involved in the radical-pair mechanism. The synthesized and stored protein samples contain different redox states of the FAD chromophore. But the photocycle of ErCry4 proteins starts from FAD_{ox}. So it was necessary to completely oxidize the FAD in the protein samples prior to the measurements. For that, an oxidizing agent, PFC, is added to the protein samples. A detailed description of protein sample preparation and oxidization procedures is

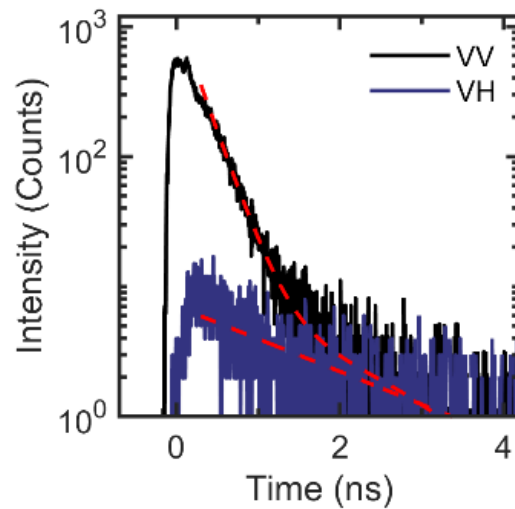


Figure III. 9 Time resolved fluorescence decay dynamics of wild type European robin cryptochrome 4 (WT ErCry4). The protein sample has 88 μ M FAD concentration. The fluorescence decay dynamics shown above are recorded using the BI-TWINS spectrometer setup (Figure II. 1) when excitation (x_{ex}) and detection (x_{det}) TWINS are at their zero delay positions. Using the setup, time-resolved fluorescence decays were recorded for vertically (V) polarized excitation and V- polarized detection (solid black), and horizontally (H) polarized detection (solid blue). A biexponential decay function

$$A(t) = \Theta(t - t_1) \left(A_1 \exp\left(-\frac{t - t_1}{\tau_1}\right) + A_2 \exp\left(-\frac{t - t_1}{\tau_2}\right) \right), t_1 = 0.5 \text{ ns} \text{ with } A_1 = 1211 \text{ counts}, \tau_1 = 0.27 \text{ ns}, A_2 = 10$$

counts, and $\tau_2 = 2.6 \text{ ns}$ is fitted (red dotted line) to the VV polarized fluorescence decay (solid black line). The τ_1 value indicates the instrument response function (IRF) of the setup. The second decay dynamics τ_2 attributed to long fluorescence decay. The VH polarized fluorescence decay (solid blue line) is very weak and it shows a monoexponential decay with an initial amplitude $A_2 = 7$ counts and a decay time $\tau_2 = 2 \text{ ns}$.

given in Appendix A.III.1. The normalized linear absorption spectrum of wild-type ErCry4 (WT) and its four mutants are shown in Figure III. 8. The absorbance behavior of WT protein and its four mutant samples are very similar. The protein samples have the main absorption peak around 450 nm with well-resolved vibronic structures. This vibronic structure is a prominent feature of chromophore binding to the protein, which will fade away in molecular FAD in solution [10, 16]. By considering recent hybrid quantum/classical modeling studies [1, 16] and vibronic coupling to nuclear vibrations, the substructure around the main peak at 450 nm is assigned to $\pi \rightarrow \pi^*$ transition from the π_2 to π_3 orbitals localized on the isoalloxazine moiety of the FAD cofactor inside the cryptochrome [16, 263]. The structured peak around 370 nm arises from the $\pi_1 \rightarrow \pi_3$ transitions of FAD [1, 16]. The absorption spectra in Figure III. 8 are calculated by carefully subtracting the remaining concentration of PFC from the completely oxidized protein samples [16].

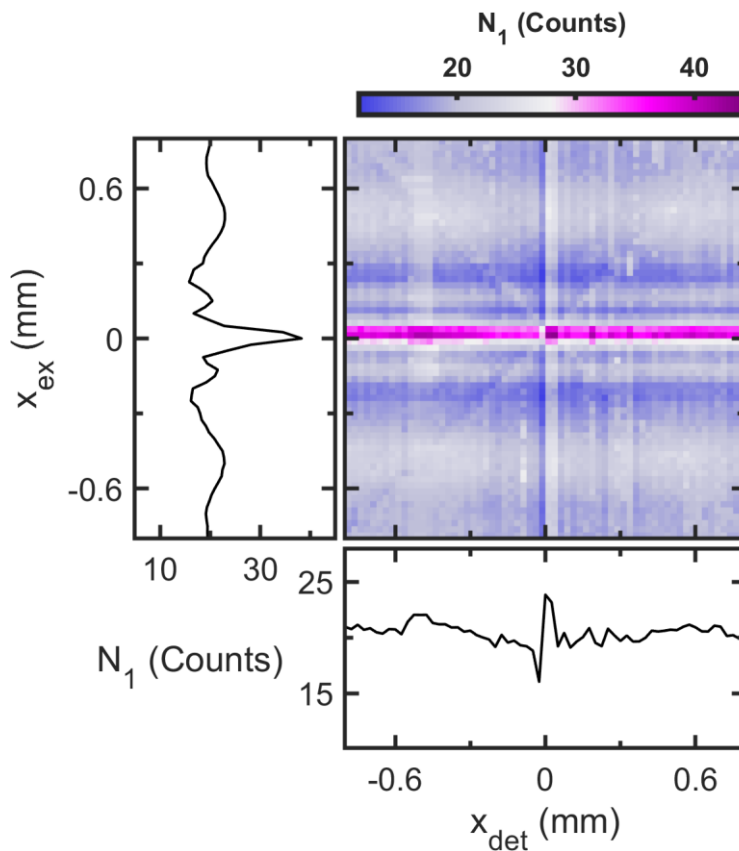


Figure III. 10 The total photons (N_1) map of wild-type European robin cryptochrome 4 (WT ErCry4). The initial amplitude A_1 and the decay time τ_1 associated with the fit function (Equation (III.3)) for all the VV polarized time-resolved fluorescence decay in the intensity map recorded by BI-TWINS spectrometer were collected and calculated the N_1 map (Equation (III.2)). The N_1 map has vertical, horizontal and very weak diagonal stripes, coherent excitation-emission interferogram. The averaged value of the N_1 map along excitation and detection TWINS wedge positions are shown in left and bottom panel s respectively. The left panel has characteristic features of an interference structure recorded by excitation TWINS. The interference patterns in the bottom panel are not prominent.

The time-resolved EE measurements of ErCry4 protein and its four mutant samples are also carried out. The measurement conditions such as excitation power, excitation spectral range, TWINS scan range, and measurement temperature are the same as for the molecular FAD measurements. For the protein samples, the BI-TWINS spectrometer records time-resolved fluorescence decay dynamics in VV and VH polarization configuration as a function of x_{ex} and x_{det} . The background signals for each fluorescence decay dynamics are calculated and subtracted as described for molecular FAD measurements. The VV (solid black line) and VH (solid blue line) polarized, background-free fluorescence decay dynamics of the wild-type (WT) ErCry4 protein sample recorded at zero delay positions of excitation and detection TWINS are shown in Figure III. 9. The VV polarized decay dynamics of WT ErCry4 can be described as,

$$A_{VV}(t) = \Theta(t-t_1) \left(A_1 \exp\left(-\frac{t-t_1}{\tau_1}\right) + A_2 \exp\left(-\frac{t-t_1}{\tau_2}\right) \right), \quad (\text{III.3})$$

with $t_1 = 0.5 \text{ ns}$. The VV polarized decay dynamics of WT is a biexponential decay function with $A_1 = 1211$ counts, $\tau_1 = 0.27 \text{ ns}$, $A_2 = 10$ counts and $\tau_2 = 2.6 \text{ ns}$. The first decay time τ_1 is limited by the instrument response function (IRF $\sim 0.24 \text{ ns}$) of the setup. The value of τ_1 may either be the result of coherent scattering from the sample, or be a very fast fluorescence decay components resulting from the ultrafast electron transfer in the WT protein sample. However, it is unfeasible to distinguish whether

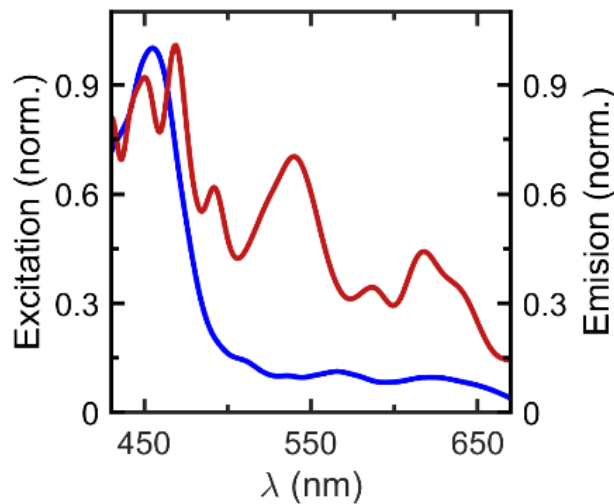


Figure III. 11 The excitation (blue solid line) and emission (red solid line) spectra of WT ErCry4 protein sample from the N_1 map (Figure III. 10). The excitation and emission spectra are calculated using the autocorrelation function along the excitation (x_{ex}) and detection (x_{det}) TWINS position respectively from the N_1 map (Figure III. 10, left and right panels). The emission spectrum shows the coherently scattered light from the protein sample (red solid line).

it is a coherent or incoherent emission at this point. The second decay time $\tau_2 = 2.6$ ns with initial amplitude $A_2 = 10$ counts is long, and can be attributed to incoherent fluorescence emission. The decay time τ_2 is similar to that of molecular FAD. The VH fluorescence decay dynamics of the WT sample in Figure III. 9 (solid blue line) exhibit a monoexponential decay,

$$A_{VH}(t) = \Theta(t - t_1) A_2 \exp\left(-\frac{t - t_1}{\tau_2}\right), \quad (\text{III.4})$$

with an initial amplitude $A_2 = 7$ counts and decay time $\tau_2 = 2$ ns. The VH curve does not show any fast decay component like VV, but it possesses long incoherent fluorescence decay dynamics. The absence of a fast component in VH fluorescence decay indicates that the decay component τ_1 in VV

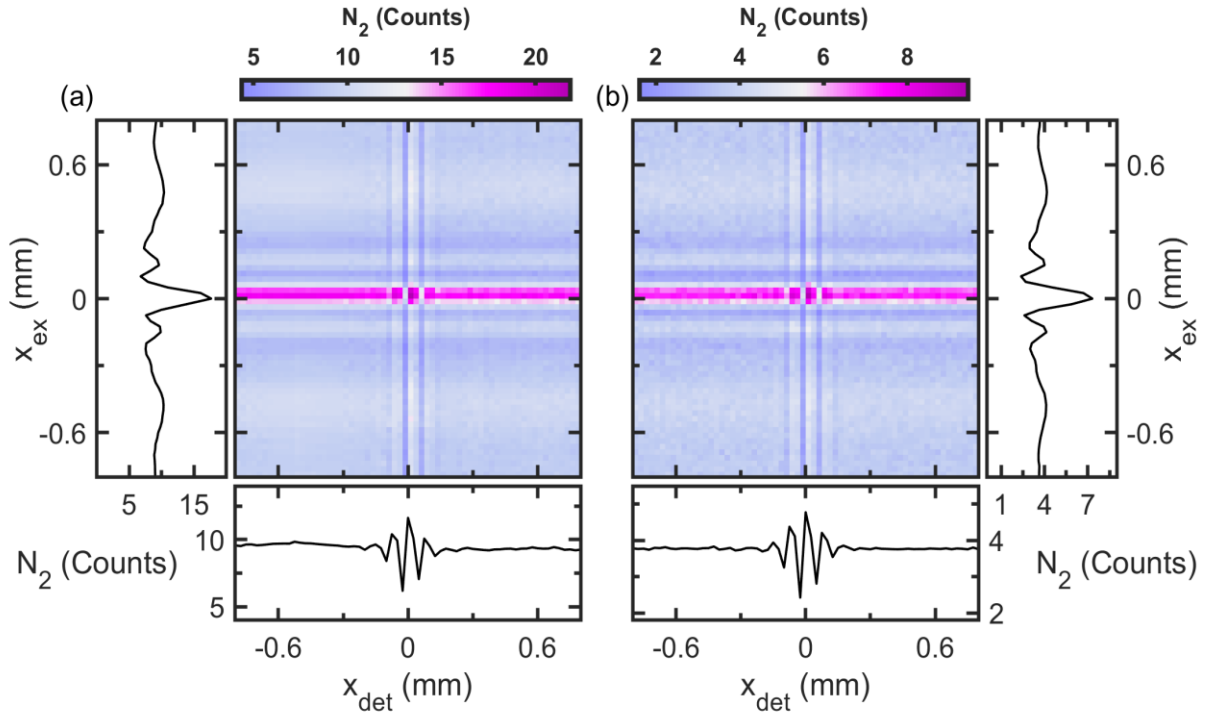


Figure III. 12 The total photons (N_2) map of wild-type European robin cryptochrome 4 (WT ErCry4) for VV (a) and VH (b) polarization. The total photon counts, N_2 are calculated from the initial amplitude A_2 and the decay time τ_2 of fit function for the time resolved fluorescence decay in VV and VH polarized BI-TWINS map,

$$\left(N_2 = \int_{t_1}^{\infty} A_2 \exp\left(-\frac{t - t_1}{\tau_2}\right) dt = A_2 \tau_2 \exp\left(-\frac{t_1}{\tau_2}\right) \right).$$

The N_2 maps have vertical and horizontal stripes, the diagonal patterns are absent, incoherent excitation-emission interferogram. The VV (a) and VH (b) N_2 maps are very similar in their interference pattern along the excitation (x_{ex}) and detection (x_{det}) TWINS wedge positions. The averaged value of the N_2 map along the excitation (x_{ex}) and detection (x_{det}) TWINS wedge positions ((a), left and bottom panels, (b) right and bottom panel respectively) showing characteristics interference structures recorded by the excitation and detection TWINS.

may be associated with the spurious light scattering by the protein sample while it does not contribute to the VH decay dynamics. Equation (III.3) is fitted to all the VV fluorescence decay curves recorded for the entire scan range of x_{ex} and x_{det} . The τ_n and $A_n, n=1,2$, values are collected as was done in the case of molecular FAD. These procedures will generate a τ_n and A_n maps. The τ_1 map has a mean value of 0.28 ns, and the A_1 map has a mean value of 450 counts. The fluorescence decay map τ_2 has a mean value of 2.36 ns and its initial amplitude map A_2 has a mean value of 6 counts. Using Equation (III.4), the total counts N_1 associated with the first decay component τ_1 , can be calculated from the τ_1 , and the A_1 values. In this way, a N_1 map (Figure III. 10) as a function of x_{ex} and x_{det} is calculated from A_1 and τ_1 maps. The total photon counts N_2 associated with τ_2 decay time for the case of VV and VH polarization fluorescence decay curves can be calculated by placing A_2 and τ_2 in the Equation (III.2).

The N_1 map of WT ErCry4 in Figure III. 10 is an EE interferogram. Very feeble diagonal patterns are present on the map. This is the contribution from the coherent emission as discussed in Chapter II [4]. In addition, vertical and horizontal stripes along excitation and detection TWINS delays are also present in Figure III. 10. A careful examination of the N_1 map indicates that the vertical and horizontal stripes

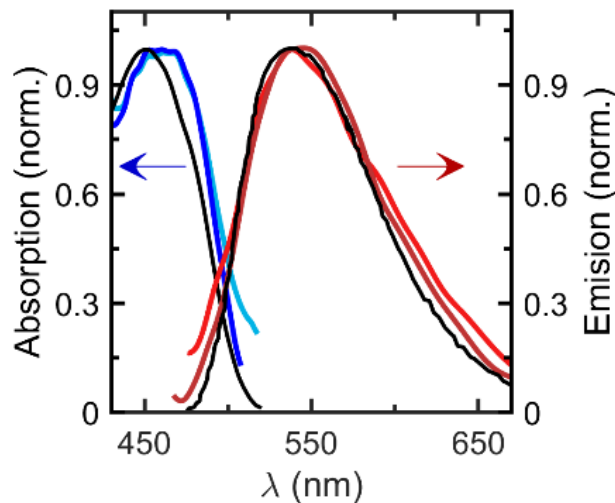


Figure III. 13 Absorption and incoherent emission spectrum of wild-type European robin cryptochrome 4 (WT ErCry4) protein sample. The excitation and emission (dark and light red solid line) spectra can be derived by applying a spectrum retrieval process on the autocorrelation signals along excitation (x_{ex}) and detection (x_{det}) TWINS positions from the VV and VH N_2 maps (Figure III. 12 (a) and (b)). The dark and light solid line absorption and emission spectra are derived from the VV and VH polarization autocorrelation functions in the N_2 maps respectively. The spectra match the absorption and emission spectra of the molecular FAD in its fully oxidized form (solid black line).

are narrower than the N_1 map of molecular FAD (Figure III. 4). Some data points with strongly enhanced signal intensity are observed in the N_1 map of WT ErCry4. This is due to the random light scattering from the buffer solution and aggregated proteins during measurements. The protein sample is usually centrifuged before measurement to resolve the aggregation and reduce the random scattering. Even though, a finite amount of aggregated proteins remain in the sample, which cause random motion through the sample solution during the measurement and creates outliers, as seen in Figure III. 10. These outliers destroy the interference patterns in the autocorrelation functions along the x_{det} (Figure III. 10, bottom panel), fast scanning axes. The data points which showed the strong outliers are removed and replaced with the average value of the neighboring points. The mean value of the N_1 map along the x_{ex} shows the autocorrelation function that was recorded using the excitation TWINS (Figure III. 10, left panel). An excitation and emission spectrum can be derived from the autocorrelation functions along x_{ex} and x_{det} . The spectrum retrieval procedures from the autocorrelation functions are explained in the case of molecular FAD. We followed the same spectral retrieval procedures here in the case of the ErCry4 protein samples. The solid blue line in Figure III. 11 displays the PLE spectrum of the sample. The emission spectrum (solid red line in Figure III. 11) is broad in the spectral range of the excitation light, without any spectral shape. So this is clearly exhibiting coherent light scattering as revealed from the decay time constant.

The total photon map, N_2 , associated with the fluorescence decay time τ_2 is shown in Figure III. 12 for VV (a) and VH (b) polarization configuration measurements. The VV (a) and VH (b) polarized N_2 maps are equal except for the intensity counts. The intensity counts in the VV polarized N_2 map are ~ 2.5 times higher than on the VH polarized map. These N_2 maps are EE incoherent interferograms. They have clear vertical and horizontal patterns along x_{det} and x_{ex} direction. The diagonal patterns are absent in both N_2 maps. So these maps are only generated by fluorescence emissions. The left (a) and right (b) panel of Figure III. 12 shows the mean value of N_2 maps along x_{ex} . The bottom panel (Figure III. 12 (a) and (b)) is the field autocorrelation of fluorescence light emitted from the WT protein sample.

The calculated absorption spectrum from the autocorrelation function along x_{ex} for the VV and the VH polarization configuration is shown in solid light and dark blue lines (Figure III. 13). The absorption spectra of the WT protein samples peak at 450 nm with unresolved vibronic structure. This absorption spectrum is very similar to the absorption of molecular FAD in buffer solution (Figure III. 13, solid black line). The emission spectrum in Figure III. 13 (solid light and dark red line) peaks at 550 nm. It also shows an unstructured emission spectrum similar to emission from molecular FAD in buffer solution (Figure III. 13, solid black line). The absorption and emission spectra of WT protein derived from the N_2 maps are similar to those of free molecular FAD in buffer solution rather than protein-

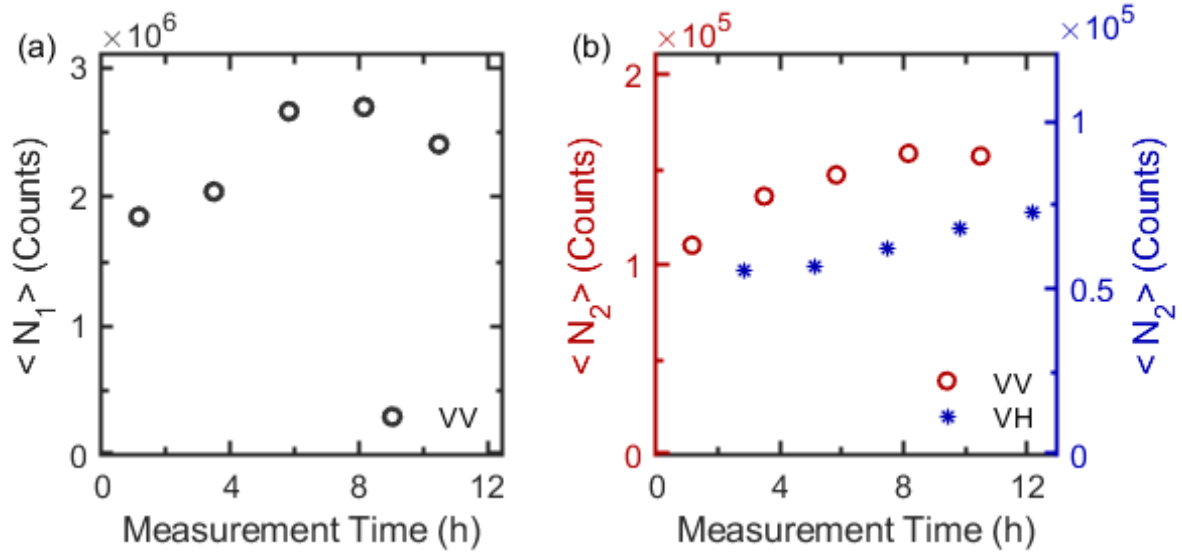


Figure III. 14 Total (a) coherent ($\langle N_1 \rangle$), and (b) incoherent ($\langle N_2 \rangle$) photons counts detected during the polarization resolved EE measurements of wild type (WT) ErCry4 protein sample as a function of measurement time. (a) Total number of coherent photons counts ($\langle N_1 \rangle$) are calculated by summing up the N_1 map of five consecutive EE measurement on VV polarization configuration. (b) The total incoherent photon counts ($\langle N_2 \rangle$) are calculated for VV (red “o” symbol) and VH (blue “*” symbol) polarization configuration. The $\langle N_1 \rangle$ and $\langle N_2 \rangle$ counts are increasing over the measurement time regardless of the polarization configuration.

bound chromophore FAD. The fluorescence decay time associated with the N_2 map shows that the free molecular FAD present in the WT ErCry4 sample is in semi-stacked conformer form [19]. So our EE studies on the WT protein sample reveal the spectral and dynamical properties of free molecular FAD in buffer solution. No measurable spectral signatures were obtained from the protein-bound FAD in the time-resolved EE studies on the WT ErCry4 protein.

The total number of coherent ($\langle N_1 \rangle$) and incoherent photons ($\langle N_2 \rangle$) detected during the EE measurements of the WT protein sample can be calculated from the N_1 (Figure III. 10) and N_2 (Figure III. 12 (a) and (b)) maps. As discussed earlier, the N_1 map was calculated for the VV polarization configuration. The coherent N_1 map detects a total of 1.85×10^6 photons during the first seventy minutes of the measurement. In the same way, the $\langle N_1 \rangle$ counts for five consecutive VV polarized EE measurements were calculated and plotted in Figure III. 14 (a). The $\langle N_1 \rangle$ counts rise with the measurement time, by an $\sim 30\%$ within twelve hours. That means that the concentration of coherent emission sources gradually increases over the measurement time. As discussed earlier, the buffer solution and the minimal amount of aggregated proteins present in the sample, even after careful preparation, may also be the source of coherent scattering. As the measurement time increase, more

proteins accumulate together further and become the source of coherent scattering. The first N_2 map in VV polarization detects a total of 1.77×10^5 photons and the first N_2 map from VH polarisation detects a total of 5.53×10^4 photons. As done for the $\langle N_1 \rangle$, $\langle N_2 \rangle$ counts for five consecutive polarization-resolved EE measurements scans were calculated and plotted in Figure III. 14 (b). The red ‘o’ symbol in Figure III. 14 represents the $\langle N_2 \rangle$ counts for VV polarisation and the blue ‘*’ sign for VH polarization. There is an increase of ~40 and 30% in total photon counts for both polarization configurations. Since the incoherent emission spectrum of WT ErCry4 protein (Figure III. 13) reveals unstructured molecular FAD fluorescence, the source of increased incoherent total photon count is free FAD molecules in the protein sample. Controlled centrifugation of the protein sample in the filter unit before the measurements usually removes free FAD from the sample. But it does not remove free FAD entirely from the sample. Therefore, the remaining small concentration of free FAD in the protein sample can be optically excited and emit fluorescence light during the EE measurements. Furthermore, the continuous optical excitation during the measurement scan causes a further gradual release of chromophore FAD from its protein pockets, leading to an increase in the $\langle N_2 \rangle$ counts over the measurement time.

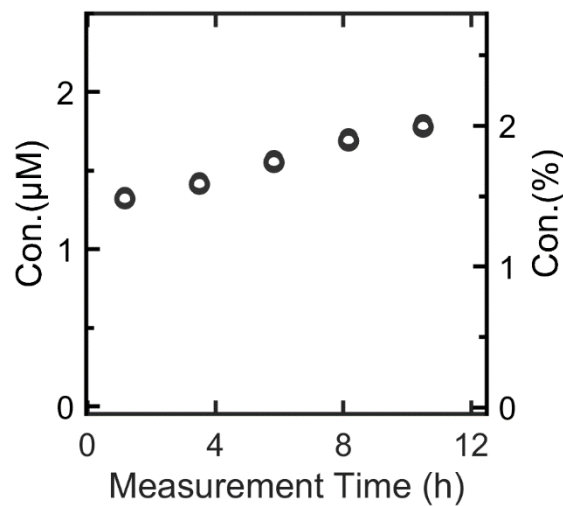


Figure III. 15 Increase in free molecular FAD concentration in wild type European robin cryptochrome 4 (WT ErCry4) protein as a function the measurement time. The free molecular FAD concentration in WT ErCry4 protein samples is calculated by comparing the total incoherent photon counts for free FAD in buffer solution ($\langle N_1 \rangle$) and WT protein ($\langle N_2 \rangle$) sample (Equation (III.2)). The left axis shows the increasing concentration of free FAD in molar units. The right axis indicates the percentage of free FAD with respect to the total FAD concentration in the protein sample (88 μM). There is only a maximum of ~2% increase in free FAD concentration during 12-hour measurement time.

The concentration of free FAD in the protein sample ($C_{FAD,WT}$) over the measurement time can be calculated by considering the total photon counts detected for free molecular FAD in buffer solution ($\langle N_1 \rangle$, Figure III. 7) and WT protein sample ($\langle N_2 \rangle$, Figure III. 14 (b)).

$$C_{FAD,WT}(n) = C_{FAD} \frac{P_{FAD}}{P_{WT}} \cdot \frac{\langle N_2 \rangle_{M,WT}(n)}{\langle N_1 \rangle_{M,FAD}} \frac{\eta_{FAD}}{\eta_{WT}} \quad (\text{III.5})$$

The concentration of molecular FAD in buffer solution (C_{FAD}) for the EE measurement was 46 μM . The excitation power (P) is set to be identical for both samples, 50 μW . The EE measurement of free molecular FAD and WT protein samples is carried out in different polarization configurations, VM and VV, and VH, respectively. So it is necessary to consider the polarization effects on the total photon counts while comparing them. The polarization-independent total photon counts ($\langle N_2 \rangle_{M,WT}$) for the WT protein sample can be calculated by considering the total counts of all of the two subsequent measurements (VV and VH) scans as,

$$\langle N_2 \rangle_{VM,WT} = \frac{\langle N_2 \rangle_{VV,WT}(2n-1) + 2g \langle N_2 \rangle_{VH,WT}(2n)}{2g+1}.$$

Here n is the number of the measurement scan pairs. The correction factor g for the setup has already been calculated for molecular FAD as 1.26. $\langle N_2 \rangle_{VM,WT}$ is calculated for the first scan pair as 1.11×10^5 counts by taking this into account. The $\langle N_1 \rangle_{M,FAD}$ value is taken from Figure III. 12, 7×10^6 counts. The efficiency η of the setup in the Equation (III.5) always depends on the orientation of the detection polarizer (θ) with respect to the first polarizer at the detection TWINS which is oriented to 45° . If a constant efficiency η_0 is assumed for the setup despite the polarization angle orientation, then the efficiency for molecular FAD measurement in the case of VM polarization configuration is $\eta_{FAD} = \eta_0 \cos^2(54.7^\circ - 45^\circ) = 0.97\eta_0$. Then the efficiency for the WT protein sample measurements is calculated for VV and VH polarization configuration as $\eta_{WT} = \eta_0 \cos^2(90^\circ - 45^\circ) = \eta_0 \cos^2(0^\circ - 45^\circ) = 0.5\eta_0$. Using all these values, the concentration of free FAD in the WT protein sample during the first VV and VH measurements can be calculated as, $C_{FAD,WT}(1) = 1.3 \mu\text{M}$. This is only $\sim 1.5\%$ of the total FAD chromophore concentration (88 μM) in the WT ErCry4 sample. The remaining FAD molecules are attached to the WT ErCry4 protein during the first pair of scans. The increase in free FAD concentration in the WT ErCry4 sample during the measurement time is shown in Figure III. 15. The left axis of the figure shows the free FAD concentration in the molar unit, and the right axis displays the amount of free FAD compared to the

total concentration of FAD chromophore in the WT ErCry4 protein sample. There is only a maximum of ~2% increase in the free FAD concentration during the 12 hour measurements. This indicates that the remaining >97% FAD molecules are bound to the ErCry4 protein sample during our long time-resolved EE measurement scans.

III.3.3 Excitation-Emission studies on ErCry4 Mutants

Here the time-resolved EE studies were continued on ErCry4 mutants, W_{AF} , W_{BF} , W_{CF} , and W_{DF} ,

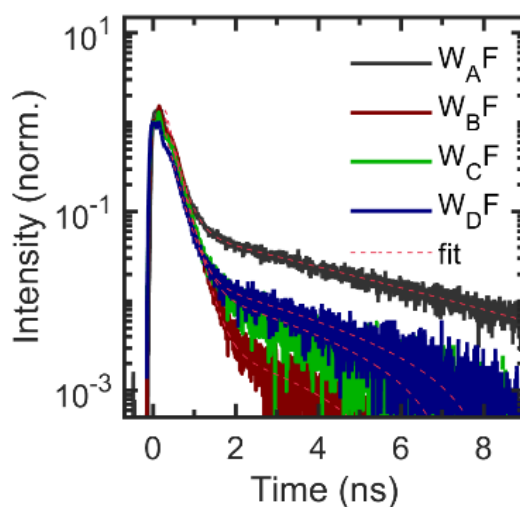


Figure III. 16 Time-resolved fluorescence decay dynamics of four mutants (W_{AF} , W_{BF} , W_{CF} , and W_{DF}) of European robin cryptochrome 4 (ErCry4). The decay dynamics are recorded using our BI-TWINS spectrometer setup for excitation and detection TWINS at their zero delay position in VV polarization configuration. A biexponential decay function (Equation (III.3)) is fitted (red dotted line) to all the fluorescence decay curves with $\tau_1 = 0.24$ ns, and $\tau_2 \approx 4$ ns.

following the same sample preparation procedures, measurement conditions, and data analysis methods as WT protein for four mutant samples. The FAD concentration in the mutant samples was between 90 to 95 μM . For the mutant samples also the BI-TWINS spectrometer recorded the time-resolved fluorescence decay curves as a function of x_{ex} and x_{det} for VV and VH polarization configuration. The normalized time-resolved fluorescence decay curves in VV polarization configuration were recorded for four mutants, W_{AF} , W_{BF} , W_{CF} , and W_{DF} of ErCry4 at the zero delay positions of excitation and detection TWINS and shown in Figure III. 16. All the four decay curves exhibit biexponential decay dynamics, a very fast and a long decay component. The long-lived fluorescence decay is evident in the case of W_{AF} mutant (Figure III. 16, solid black line). So a biexponential decay function (Equation (III.3))

) with $\tau_1 = 0.24 \text{ ns}$ and $\tau_2 = \sim 4 \text{ ns}$ is fitted to the time-resolved fluorescence curves that are recorded

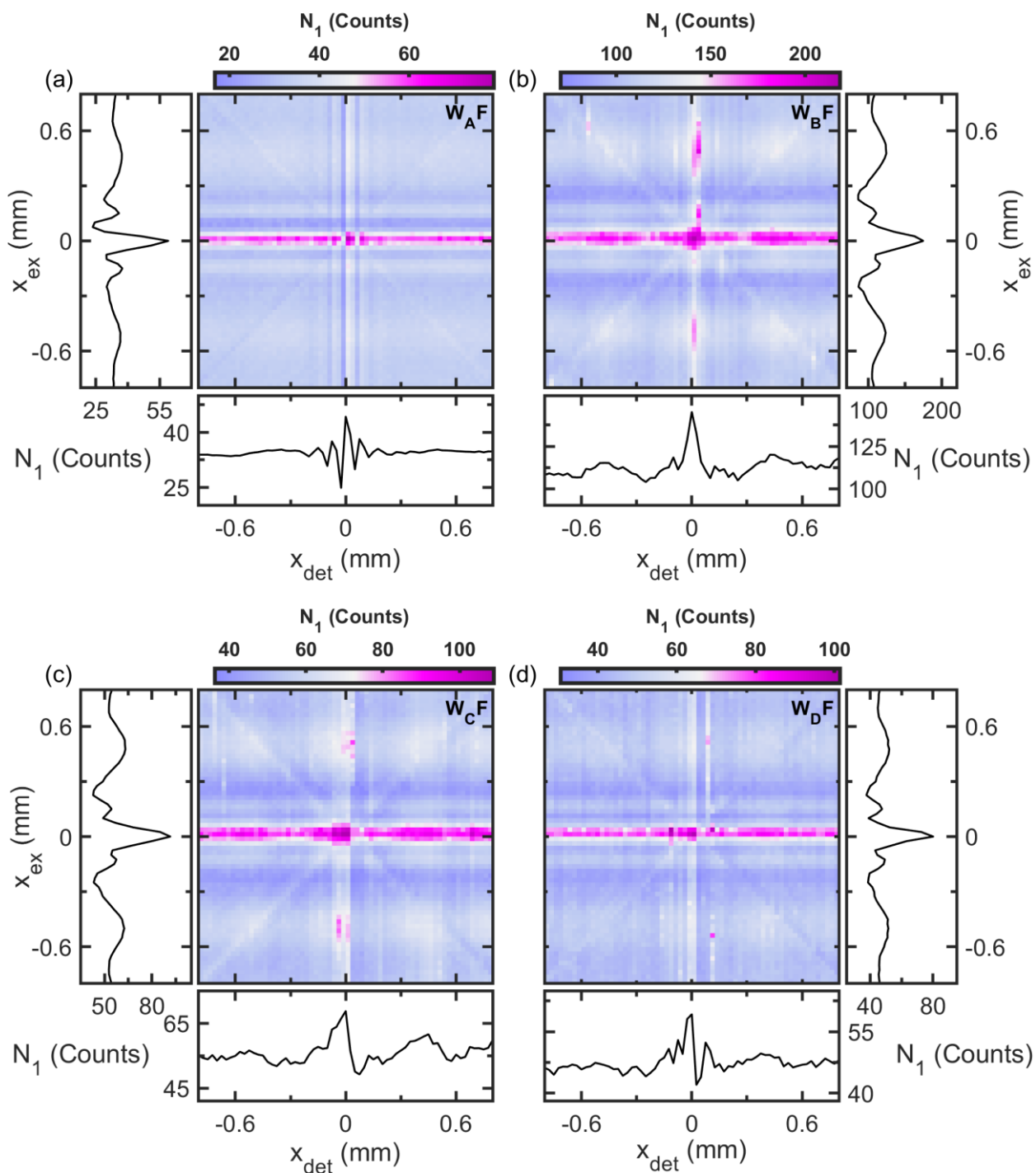


Figure III. 17 The total photon N_1 map of European robin (*Erithacus rubecula*) cryptochrome 4 (WT ErCry4) mutants, (a) W_AF, (b) W_BF, (c) W_CF and (d) W_DF. All the N_1 maps have diagonal patterns (coherent scattering contribution) and vertical and horizontal stripes. The mean value of N_1 maps along x_{ex} and x_{det} direction given in the left ((a) and (c))/ right ((b) and (d)) and bottom panels respectively shows interference pattern recorded using excitation TWINS. The autocorrelation along x_{ex} for all mutant samples have the same interference patterns. In the case of W_AF (a) the interference pattern along detection (x_{det}) direction ((a) bottom panel) has a stock shift compared to that along x_{ex} .

in the entire scan range of the mutant samples measurements. Through the fitting procedures, the initial amplitudes A_1 and A_2 maps, and the decay time τ_1 and τ_2 maps were created. Then, the total number

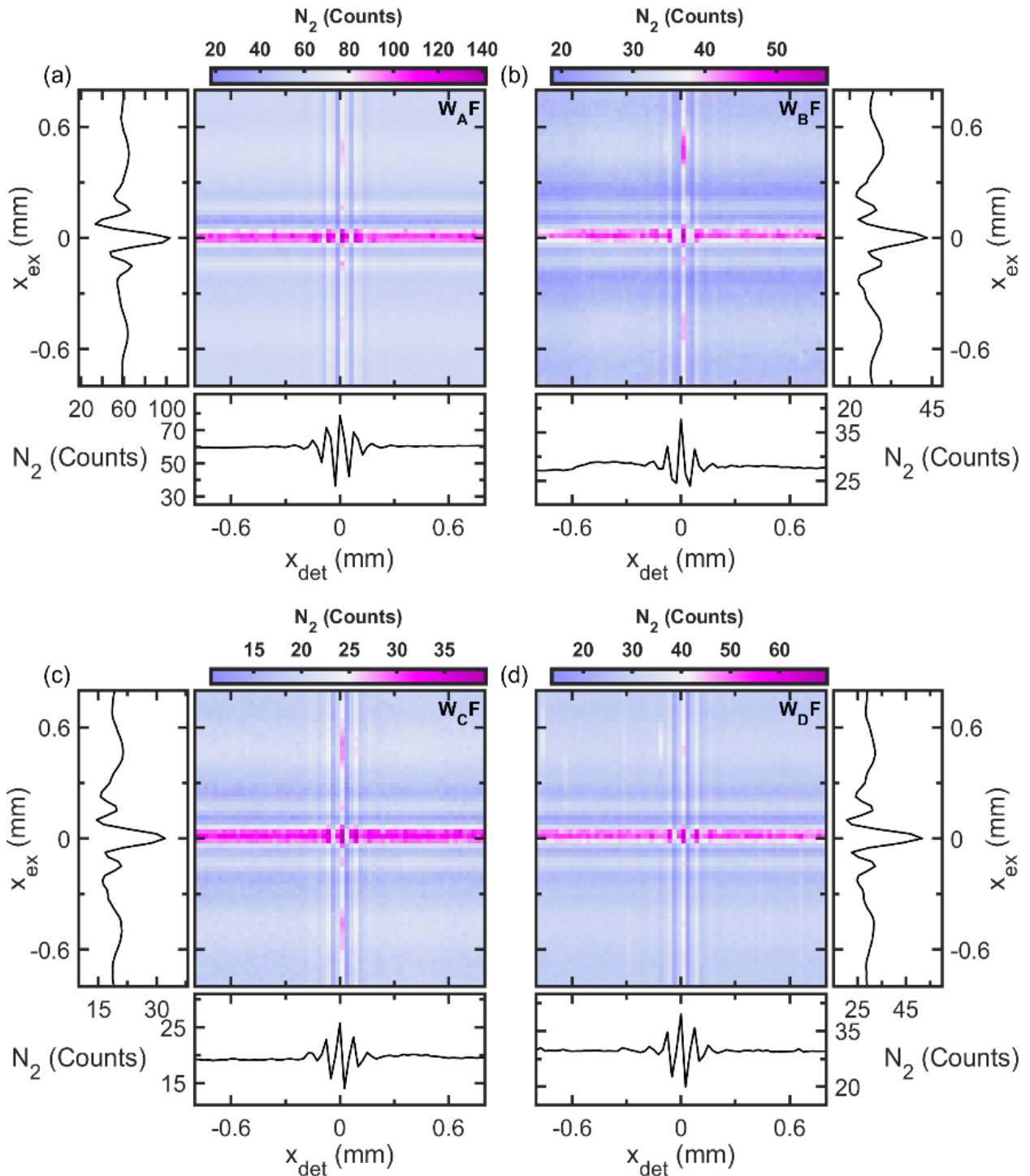


Figure III. 18 The total photon N_2 maps of mutants of (a) W_{AF} , (b) W_{BF} , (c) W_{CF} and (d) W_{DF} European robin cryptochrome 4 (ErCry4). The N_2 maps are excitation-emission incoherent interferogram, vertical and horizontal stripes only. The mean value of N_2 maps along x_{ex} and x_{det} displayed in left (a and c)/right (b and d) and bottom panels respectively. The autocorrelations along x_{det} is red shifted compared with the interference pattern along x_{ex} .

of photons maps N_1 and N_2 detected for τ_1 and τ_2 maps were calculated using the Equation (III.2). The N_1 and N_2 maps for ErCry4 mutant samples are displayed in Figure III. 17 and Figure III. 18, respectively. VH polarized time-resolved fluorescence decay curves of mutant samples exhibit a monoexponential decay with $\tau_2 = 4 \text{ ns}$. The VH polarized N_2 maps of mutant samples are comparable with the VH polarized map of the WT sample, which is not shown here.

At first glance, all the N_1 maps of the mutant samples (Figure III. 17) have diagonal, vertical, and horizontal stripes. So these N_1 maps may have contributions from coherent and incoherent emissions. The horizontal patterns present on all the N_1 maps are identical. The mean value of N_1 maps along the x_{ex} is also similar (Figure III. 17 (a) and (c) left panel, (b) and (d) right panel), again they are the autocorrelation function of the PLE spectrum of the samples. The vertical patterns in the N_1 map of W_{AF} show characteristic features of interference structures recorded using detection TWINS. The mean value of N_1 map of W_{AF} along x_{det} (Figure III. 17 (a) bottom panel) is broad and red-shifted compared to the interference pattern along x_{ex} (Figure III. 17 (a) left panel). All other N_1 maps of mutant samples, W_{BF}, W_{CF}, and W_{DF} display similar interference structures along x_{det} . Identical to WT samples, the random scattering overlaps the interference patterns in Figure III. 17 ((b), (c), and (d) bottom panel) and causes outliers in the N_1 maps. Excitation and emission spectra (Figure III. 19 (a) and (b)) can be obtained from the mean values of N_1 maps along x_{ex} and x_{det} . The PLE spectrum of the samples is identical for all the mutant samples (Figure III. 19 (a)). The emission spectrum of W_{AF} broadened from 400 to 750 nm and has a peak at 530 nm. This peak and its shape indicate the emission spectrum of FAD_{ox} with a contribution from coherent scattering (below 480 nm). The other mutant samples, W_{BF}, W_{CF}, and W_{DF}, emit broadly in the wavelength region of excitation light without any specific shape and peaks. So these W_{BF}, W_{CF}, and W_{DF} samples emit coherently.

The N_2 maps of W_{AF}, W_{BF}, W_{CF}, and W_{DF} (Figure III. 18 (a)-(d)) are incoherent interferogram and exhibit identical interference patterns along x_{ex} as well x_{det} . These N_2 maps only differ by their intensity counts. All other features are similar. The mean value of N_2 maps along x_{ex} direction (Figure III. 18 (a) and (c) left and (b) and (d) right panel) shows interference patterns of the excitation light that interacts with the mutant samples. These interference patterns are comparable to the patterns along x_{ex} from the N_1 map. The autocorrelation function of fluorescence emission from the mutant samples is shown in the bottom panels of Figure III. 18 (a)-(d). The absorption and emission spectra of four mutant samples derived from these autocorrelation functions are shown in Figure III. 20 (a) and (b), respectively. All the absorption spectra exhibits an unstructured peak at 450 nm and extended up to 520 nm, characteristics absorption features of free molecular FAD_{ox} (Figure III. 20 (a) black solid line).

The emission spectra are extended from 500 to 750 nm, with a peak at 530 nm. The emission peaks are unstructured and are identical to fluorescence emission from molecular FAD_{ox} (Figure III. 20 (b) solid black line). The EE N_2 map of ErCry4 mutant samples specifies the presence of free molecular FAD_{ox} in the samples. Similar to the WT ErCry4, the W_{BF} , W_{CF} , and W_{DF} mutant samples did not show any glimpse of protein-bound FAD and any other redox state of FAD in the protein samples.

In contrast to other mutants, the N_1 map of the W_{AF} shows fluorescence emission (Figure III. 19 (b), solid black line). The spectral range of the fluorescence light matches the emission from the FAD_{ox} . But the spectral shape does not exactly match the free molecular FAD_{ox} emission (Figure III. 19 (b), dashed-dotted line). We can observe vibronic features at 540, 560, and 590 nm in the emission spectrum of W_{AF} . The fluorescence emission molecules are always an energy transition from the lower vibrational level of the first excited electronic state to the vibrational wave function overlapped levels of the ground electronic state. The spectral width of these transition depends on the dephasing time of each transition, and these transitions are very sharp in gas molecules. But in the case of liquids and solids, the dephasing time will be larger due to the solvent and surrounding environment inducing inhomogeneous line broadening. This will eventually make the single vibronic transitions vanish in the emission spectra of molecules and resulting broad emission spectra, as in the case of molecular FAD. But in the case of chromophore FAD which is bound inside the protein pockets of ErCry4, there is only a restricted

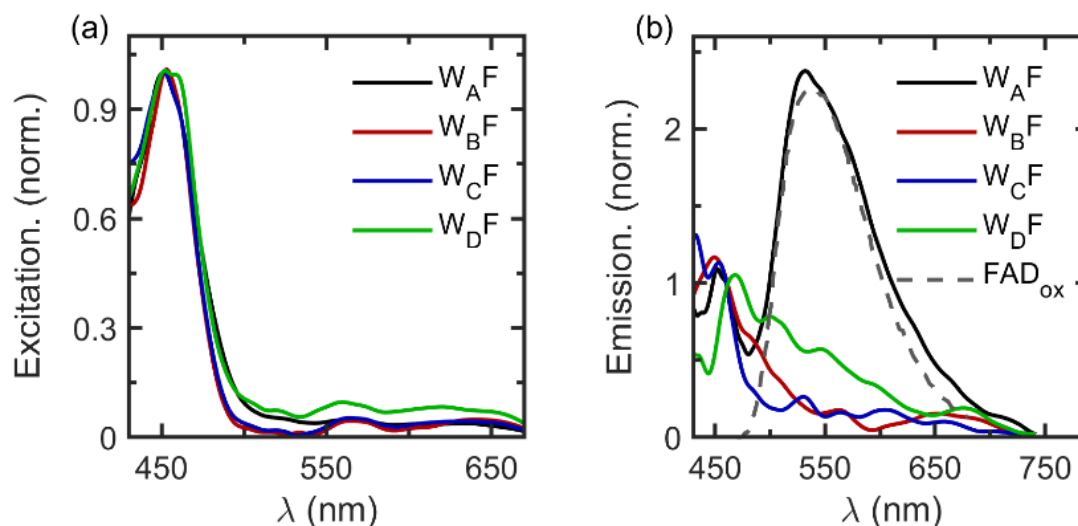


Figure III. 19 (a) Excitation and (b) emission spectrum of mutants of (W_{AF} , W_{BF} , W_{CF} & W_{DF}) European robin cryptochrome 4 (ErCry4) from the N_1 map. The excitation spectra derived from the autocorrelation functions along x_{ex} (Figure III. 17) are identical. The emission spectrum of W_{AF} (black solid line) has identical spectral ranges like FAD_{ox} (black dash-dotted), but has vibronic structures at 540 nm, 560 nm and 590 nm. The mutants W_{BF} , W_{CF} and W_{DF} are randomly emitting over the excitation spectral range (coherent scattering).

interaction to the surrounding environment. This causes the appearance of vibronic structures as observed in the emission spectra of the W_{AF} mutant (Figure III. 20 (b), solid black line) [237, 238].

In the W_{AF} mutant, the Trp_A is substituted by the Phe, and this is expected to create a barrier for the first electron transfer in ErCry4 protein. Therefore for the W_{AF} mutant should be considered as FAD molecules that are tied in the ErCry4 protein pocket. The optical excitation of W_{AF} brings the ground state of FAD_{ox} in the protein samples to excited state FAD_{ox}^* . Since the electron source is replaced with an inactive Phe molecule in W_{AF} , there is no immediate electron transfer to the ground state of FAD_{ox} . So the optically excited FAD_{ox}^* in W_{AF} is long-lived and its fluorescence emission is not completely quenched by the inter molecular electron transfer. As a result, W_{AF} emit in the spectral region of FAD_{ox} with vibronic structures (Figure III. 19 (b), solid black line). But in WT protein and other mutants (W_{BF} ,

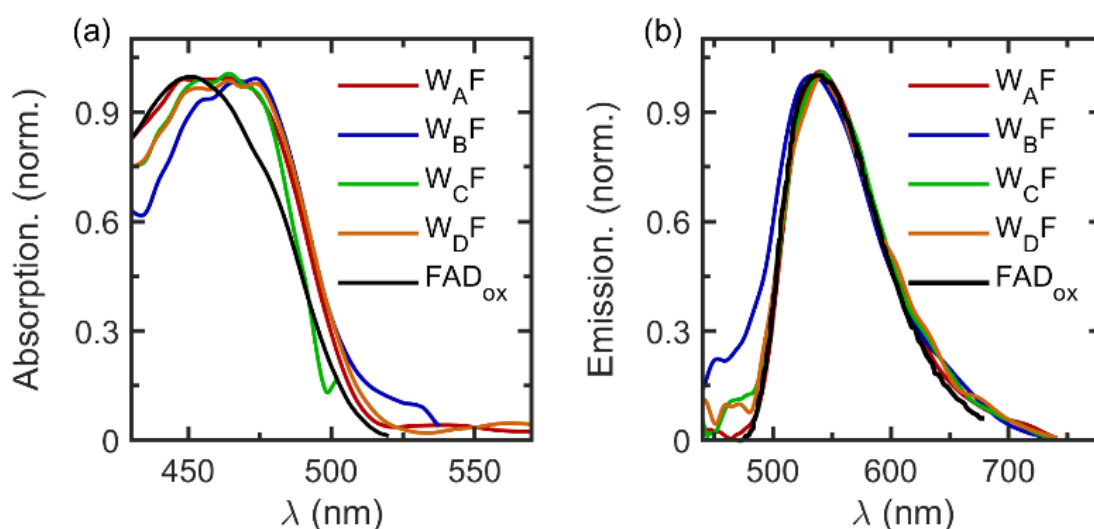


Figure III. 20 (a) Absorption and (b) emission spectrum of mutants (W_{AF} , W_{BF} , W_{CF} , and W_{DF}) of European robin cryptochrome 4 (ErCry4) from the N_2 map. (a) The absorption spectra derived from the autocorrelation function of N_2 (Figure III. 18) map are almost identical and have unstructured peaks at 450 nm. (b) The emission spectra have an unstructured peak at 550 nm. Both absorption and emission spectra agree well with the reported spectra of completely oxidized molecular FAD in the literature (solid black line).

W_{CF} , and W_{DF}) samples, the Trp_A is available as an electron donor and this will effectively quench the PL emission from FAD_{ox} . This leads to no detectable fluorescence emission from protein-bound FAD molecules. The decay time constant associated with the N_1 map of W_{AF} is 0.24 ns. This decay time is limited with the instrument's response function of the setup. The decay time constant confirms that the stacked conformer of FAD_{ox} [18, 19, 22, 147] is present in the protein-pockets of ErCry4 [17, 235]. The other conformers of FAD molecules, semi-stacked, and open forms, existing in the protein samples have a long fluorescence decay time [18, 19]. These conformers are not attached to the

protein samples; consequently, they do not participate in electron transfer reactions in ErCry4 protein through the Trp chains.[16, 17].

III.4 Summary and Conclusions

Fourier transform-based time-resolved excitation-emission (EE) studies were carried out using our BI-TWINS spectrometer with 0.24 ns time resolution on molecular Flavin adenine dinucleotide (FAD), purified cryptochrome 4 from the night-migratory European robin (WT ErCry4) and its four mutants (W_{AF} , W_{BF} , W_{CF} and W_{DF}). FAD molecules act as a chromophore in ErCry4 proteins. Optical excitation of FAD chromophore in the ErCry4 protein triggers consecutive electron transfer reactions from the nearest four tryptophans (Trp), Trp_A , Trp_B , Trp_C , and Trp_D and this eventually leads to the formation of radical-pairs between different redox states of FAD and Trp. These long-lived intermediate radical-pairs are sensitive to weak geomagnetic fields [20, 141]. The four mutants of ErCry4 proteins are generated by site-selectively replacing one of the Trp involved in cryptochrome 4 activation by a redox-inactive phenylalanine (Phe) [154]. In time-resolved EE studies, the BI-TWINS spectrometer records the time-resolved fluorescence decay dynamics of sample molecules as a function of wedge positions of excitation and detection TWINS [4]. Using the fluorescence decay time and the initial amplitude of decay dynamics in each excitation and detection TWINS position, we could create a total number of photon maps and then can derive the absorption and emission spectra of the samples.

The time-resolved EE studies of the molecular FAD reveal the presence of fully oxidized FAD (FAD_{ox}) in its open conformer. The linear spectral behavior and its fluorescence decay dynamics (~ 4 ns) derived using the measurements adopted in this study agree well with previously reported studies for molecular FAD [2, 18, 22]. The experimental results do not show the presence of any other conformers and redox state of FAD molecules in the sample. The EE studies of molecular FAD gave the basis for the EE studies on ErCry4 protein and its four mutant samples. A biexponential, fast (~ 0.24 ns), and long ($\sim 2.4/4$ ns) fluorescence decay dynamics are associated with WT ErCry4 and its four mutant protein samples. The fast decay dynamics (~ 0.24 ns) from WT ErCry4 and its mutants, W_{BF} , W_{CF} , and W_{DF} , are associated with the coherent light scattering from the protein aggregation and buffer solution. Unlike WT ErCry4 and other mutants, W_{AF} exhibits short-lived fluorescence in which Trp_A ($W395$) close to the FAD chromophore is replaced with Phe. By replacing Trp_A from the ErCry4 protein, the rapid electron transfers from the Trp_A to the FAD chromophore are cut off, and then the W_{AF} mutant can consider as a protein-bound FAD molecule. Thus, optically excited FAD_{ox} in W_{AF} can be long-lived, and the fluorescence emission may not be quenched by the electron transfer from the nearest Trp_A . The derived vibronically structured emission spectrum of W_{AF} from the short fluorescence dynamics proved this protein-chromophore binding and non-quenched fluorescence. The short fluorescence decay observed in W_{AF} is associated with the stacked conformer [18, 19, 147] of protein-bound FAD. The

instrument response function of the setup of this study limits the measured fast decay time for W_{AF} . The long fluorescence decay ($\sim 2.4/4$ ns) exhibited by ErCry4 and its four mutant samples is from free molecular FAD present in the protein sample. The unstructured absorption and emission spectra obtained from the long-lived time-resolved decay curves proved this is very clearly. The excitation spectra associated with all protein samples are similar and independent of emission energy. The detected fluorescence intensities from the free molecular FAD in the protein samples are shallow ($\sim 7\%$) compared to the fluorescence light from free molecular FAD in buffer solution. It was possible to estimate the minute amount of free molecular FAD present in the protein samples as $\sim 1.5\%$ of the total FAD concentration in the protein sample. There is only a maximum of $\sim 2\%$ increase in free FAD concentration in the protein during the 12 hours of measurement. This ensures that more than 97% of FAD molecules are inside the protein pockets for all as-prepared samples.

Through these time-resolved EE measurement studies, it was possible to study the photophysical properties of the ErCry4 protein and its four mutants. These studies show that photo-excited ultrafast electron transfer along FAD and Trp chains naturally quenches the weak fluorescence from FAD molecules, and it could not be detected within a time resolution of 0.24 ns. So, the measurements only could detect the free FAD molecules in WT ErCry4 and its mutants W_{BF} , W_{CF} , and W_{DF} . But in the W_{AF} mutant, no electron transfer to chromophore FAD has a long-lived fluorescence, showing emission spectrum with protein-bound signatures. These results confirmed that there is an efficient electron transfer from Trp_A to chromophore FAD in ErCry4 and only protein-bound FAD molecules participate in the electron transfer reaction and radical-pair formation in the protein. Moreover, the results showed, that the protein-bound FAD molecules exist in their stacked conformer form in the ErCry4 protein pockets. Importantly the studies proved that even though there is a minute ($\sim 2\%$) release of FAD chromophore from protein pockets, the protein samples are entirely stable and safe during the controlled optical excitation measurements. These findings are definitely relevant for further studies of ultrafast charge transfer dynamics of the cryptochrome 4 protein complex and its mutants and thus the formation of the magnetically sensitive radical-pairs.

Chapter IV

Ultrafast Transient Absorption Spectroscopy Studies on Cryptochrome 4 Molecules.

This chapter was published in [16].

Daniel Timmer, Anders Frederiksen, Daniel C. Lünemann, **Anitta R. Thomas**, Jingjing Xu, Rabea Bartölke, Jessica Schmidt, Antonietta De Sio, Ilia A. Solovyov, Henrik Mouritsen, and Christoph Lienau

Tracking the Electron Transfer Cascade in European Robin Cryptochrome 4 Mutants

[ja-2023-00442v.R1](#)

A.R.T. and D.C.L performed and analyzed the photoluminescence experiments. A.R.T prepared the samples for the experiments.

IV.1 Introduction

Ultrafast science has intra-disciplinary applications and it has its own roles in the development of modern physics, chemistry, and biology fields. The development of frequency tunable, and stable ultra-short laser pulses in combination with time-resolved non-linear spectroscopy causes the advancement of versatile ultrafast spectroscopy techniques such as pump-probe spectroscopy [220, 264, 265], two-dimensional (2D) spectroscopy [222, 223, 266], and ultrafast structural dynamics [267, 268]. These ultrafast techniques provide information about photo-induced dynamical processes in atoms, molecules, nanostructures, and semiconductor systems [188, 222, 223, 269-276].

When a sequence of ultrashort pulses is interacting with samples, it generates a third-order optical response in the interacting system [277]. Generally, in ultrafast spectroscopy, three time delayed and synchronized ultrashort pulses are interacting with the investigating system. The electric field of the first pulse creates polarization in the system. The second pulse will change the population of the system after a time t_1 . Then the third pulse that is delayed by time t_2 generates a third-order polarization in the sample. This causes the generation of a light field that is proportional to the created nonlinear polarization in the interacting system [278, 279].

Pump-probe spectroscopy is a so developed ultrafast technique, very sensitive, and has broad spectral coverage and high temporal resolution from few femtoseconds to attosecond. The pump-probe

spectroscopy, also known as transient-absorption (TA) spectroscopy was first used by Abraham (1899) and Lemoine [264]. In TA spectroscopy, the first pulse, known as pump, creates a polarization in the system and also changes the population of the system. After a time interval t_2 another pulse, probe which is non-collinear with the pump creates nonlinear field in the direction of probe pulse. The arrival time of the probe pulse t_2 can be varied to follow the real-time population dynamics in the investigating system. In TA experiments the pump pulse can periodically on and off and hence a differential absorption spectrum (ΔA) is recorded. Using a tunable pump pulse and broadband probe pulse in TA experiments, one could resonantly excite the different transitions in the system and extract the maximum amount of information about system dynamics [278, 280].

Cryptochrome proteins (Cry) are blue-light-sensitive flavo proteins that have a variety of functions in animal and plants [14, 130, 281-287]. These flavo-proteins become more interesting due to their involvement in long-range navigations in migratory song birds by sensing the Earth's magnetic field [20, 27, 154, 288, 289]. Cryptochrome proteins from some species [9, 154, 183] internally bind a flavin adenine dinucleotide (FAD) chromophore non-covalently that bridges the protein surface through a chain of aromatic amino acid residues of approximately 25 Å. In plant Cry, the chain consists of three tryptophans (Trp) [288, 290], whereas animal and animal-like Cryptochrome typically have a chain of four Trps [154, 291]. Blue light absorption via a $\pi \rightarrow \pi^*$ transition in the isoalloxazine moiety of the FAD cofactor in its fully oxidized ground state (FAD_{ox}) triggers a series of sequential electron transfers across the Trp chain and results in the formation of a pair of flavin/tryptophan radicals {FAD^{•-}TrpH^{•+}} in a spin-correlated singlet state [12, 154, 292]. The lifetime of this radical-pair state (^SRP₁), which is typically in the μ s range [20, 154, 293], is expected to be long enough for a weak magnetic field to affect the quantum yield for intersystem crossing to its triplet state (^TRP₁) [11, 66, 288, 294]. RP₁ is expected to be sensitive to the direction of the external magnetic field and, therefore, is a likely candidate for the magnetically sensitive radical-pair in birds [154] (see Chapter I).

Consequently, the ultrafast light-induced electron transfer across the Trp chain forms the primary step in the photochemical cycle of Crys. The ultrafast dynamics of flavins and flavoproteins have been the subject of numerous experimental studies during the past two decades [2, 9, 12, 22, 111, 143, 147, 153, 236, 295]. In particular, for FAD in aqueous solution, an intramolecular electron transfer from the adenine to the isoalloxazine moiety occurs in stacked conformation with a time constant of 5 ps, followed by charge recombination on a faster time scale [22]. In open conformation, a much longer, ns lifetime has been measured [22]. For protein-bound FAD, a fast electron transfer from a nearby tryptophan has been observed that forms a [FAD^{•-}TrpH^{•+}] radical-pair within ~1 ps in animal type I Cry [12, 235, 236] and with sub-picosecond time constants in plant Cry and photolyases [153, 161, 296-298]. Dynamics on longer time scales are mostly interpreted in terms of the sequential electron transfer steps along the Trp chain. It remains difficult, however, to unambiguously assign rate constants to

individual steps of the charge migration since competing nonequilibrium dynamics such as vibrational cooling [236] may affect the TA spectra.

Very recently, it became possible to recombinantly express and purify [182] wild type cryptochrome 4 from the night-migratory European robin [154] (ErCry4) with internally bound FAD chromophores with high yield (>97%) [154]. TA spectra of wild-type ErCry4 and four mutants, in which one of the Trp involved in Cry activation has been site-selectively replaced by a redox-inactive phenylalanine (Phe), have been studied with sub-ns time resolution [154]. The study gave evidence for the creation of light-induced radicals with lifetimes exceeding 100 ns in the wild-type protein and in the mutant in which the terminal Trp has been substituted by the Phe residue. The experiments also showed sizable changes in the TA by up to 15% for magnetic field strengths of ~10 mT. Due to time resolution limitations, the sequential charge transfer rates could not be resolved experimentally but were estimated computationally based on molecular dynamics (MD) simulations and empirical Moser-Dutton theory. Since those rates are critical for understanding the magnetic sensitivity of ErCry4, establishing them from independent ultrafast spectroscopic experiments is urgently needed. Such experiments would open new frontiers for probing intraprotein charge and spin transfer dynamics [299] and important horizons for experiment/theory comparison [154, 162, 163, 291].

In the present chapter provided a comparative ultrafast optical study of the electron transfer cascade along a tetradic amino acid chain in wild-type ErCry4 and in its four mutants, where one of the four tryptophans in the chain has been site-selectively replaced with a phenylalanine residue. This approach allows to isolate the dynamics and yields of the first three sequential electron transfers across the chain in ErCry4. This provides a benchmark for modeling radical-pair formation in cryptochromes, as explored here by a direct comparison to hybrid quantum-mechanics/molecular mechanics simulation. The emerging synergy between experiment and simulations provides a first step towards quantitative modeling of electron transport in ErCry4a and forms a basis for the investigation of spin transport and correlations in magnetically sensitive flavin-tryptophan radical-pairs.

IV.2 Experimental Section and Methods

IV.2.1 Sample Preparation and Handling

Wild-type (GenBank: KX890129.1) and its four mutants W_XF ($X = A-D$) were cloned, expressed, and purified according to the protocol described by Xu et al [154]. Detailed sample preparation is given in Chapter III, section III.2.2. Briefly, the tryptophan mutants were generated by replacing the DNA codon for tryptophan (TGG) at amino acid position 395 (W_{AF}), 372 (W_{BF}), 318 (W_{CF}), or 369 (W_{DF}) in the *ErCry4* gene by a phenylalanine codon (TTT) in a PCR using the Q5 site-directed mutagenesis kit (New England Biolabs). Plasmids were confirmed by Sanger sequencing (LGC Genomics). Proteins

were expressed in BL21(DE3) *Escherichia. coli* cells in the dark and purified by Ni-NTA agarose columns, followed by anion exchange chromatography. Purified protein samples were concentrated to 5-6 mg/mL in an aqueous buffer solution (20 mM Tris, 250 mM NaCl, and 20% glycerol) along with 10 mM of the reducing agent 2-mercaptoethanol (BME) to avoid dimerization of the protein. Samples were snap frozen in liquid nitrogen and stored at -80° C for 3 to 5 days until the measurements. Since the photocycle starts from the fully oxidized state FAD_{ox}, the reducing agent was removed and the sample was fully oxidized prior to the optical measurements. For this, the protein sample was washed with BME-free buffer solution in a Millipore centrifugation filter (Amicon Ultra, 30 kDa) using a temperature-controlled microcentrifuge (4° C, 14,000 rpm). This step would also remove free FAD from the sample. Addition of 1.5 mM potassium ferricyanide (PFC), followed by centrifugation for one hour to remove aggregated proteins, was repeated until the sample was fully oxidized as confirmed by absorbance measurements. A remaining concentration of ~1.7-2.6 mM PFC prevented photoreduction during the optical experiments. The PFC-corrected absorbance was used to determine the final concentration of the samples to be ~120-220 μM using the molar extinction of FAD_{ox} [22]. During the preparation the samples were always kept at ~4° C and measurements were performed at 1° C. A detailed description of protein sample preparation for spectroscopic studies are given in the section A.III.1 .

Transient absorption measurements on a buffer solution containing 1 mM PFC showed only very weak nonlinear signal with a few-ps lifetime when pumped at 450 nm (see Figure A. IV. 3, in Appendix A.IV.2) and no detectable photoluminescence was observed.

IV.2.2 Transient Absorption (TA) Experiment

The TA measurements were performed using ~28 fs pump pulses at 450 nm on a 15 μl volume of the sample in a quartz microcuvette (Hellma). A schematic representation of experimental setup is shown in Figure IV. 1. A 10 kHz, 1 mJ regenerative Titanium Sapphire (Ti:Sa) amplifier (Legend Elite, Coherent) provides pulses with ~25 fs duration centered around 800 nm (Figure IV. 1, red solid line). The laser is pumping a tunable optical parametric amplifier (TOPAS, Light Conversion) generating 450 nm pulses with a bandwidth of 15 nm (Figure IV. 1, blue solid line). A pair of chirped mirrors (DCM 12, Laser Quantum) is used for chirp compensation (CMP) of setup dispersion. A home-built Transient Grating Frequency Resolved Optical Gating (TG-FROG) setup [300] provides a measured pulse duration of ~28 fs.

A fraction of the fundamental Ti:Sa light is focused into a 3 mm thick calcium fluoride (CaF₂) plate (Eksma Optics), which is continuously moved by two motorized translation stages to avoid photo-induced damage of the crystal over time. The emitted white light spans from ~320 to 750 nm (Figure

IV. 1, green solid line) and is collimated with an off-axis parabolic mirror. The remaining fundamental laser light is attenuated with a colored glass filter (F, FGS580M, Thorlabs).

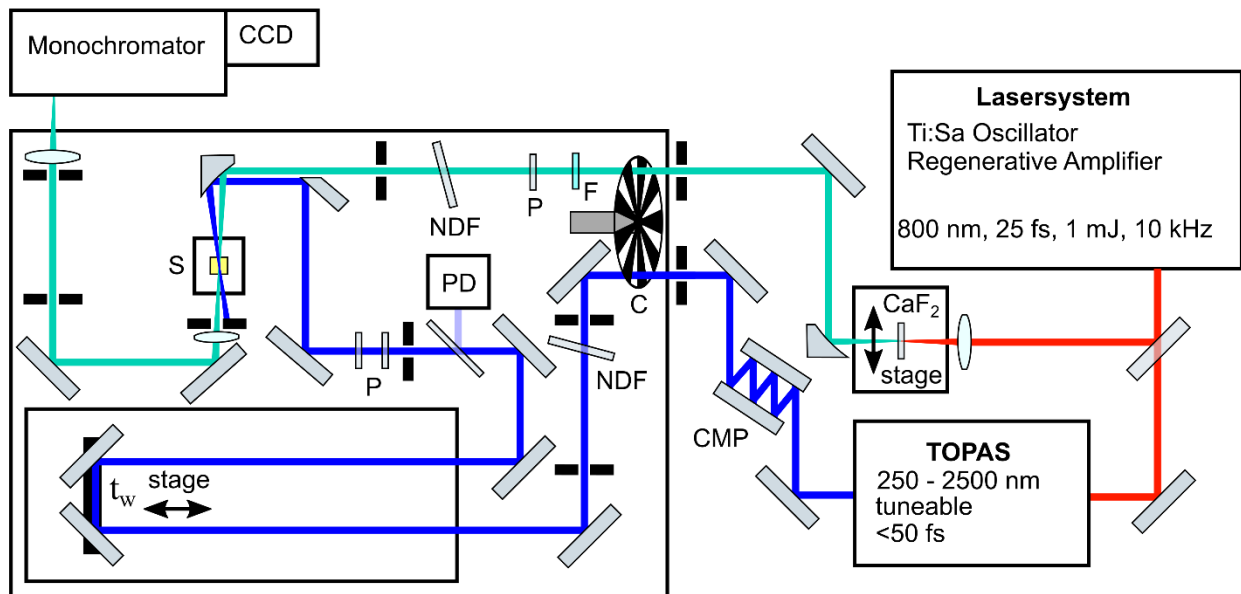


Figure IV. 1 A schematic representation of transient absorption (TA) experimental setup. A regenerative Titanium Sapphire (Ti: Sa) amplifier centered around 800nm (red solid line) is pumping a tunable optical parametric amplifier (TOPAS) and generating 450 nm pulses (blue solid line). A pair of chirped mirror (CMP) is using for chirp compensation of setup dispersion. A fraction of fundamental light from Ti: Sa is focused into a calcium fluoride (CaF_2) and emit whitelight ranges from ~ 320 to 750 nm (green solid line). The CaF_2 plate is continuously moved by two motorized translation stage to avoid photo-induced damage of the crystal over time. The emitted whitelight is collimated with an off-axis parabolic mirror and the remaining fundamental laser light is attenuated with colored glass filter (F). Pump (blue solid line) and probe (green solid line) beams are both simultaneously chopped with 2:1 duty cycle chopper wheel (C) on a single shot basis for data acquisition. The chopping generates a sequence of pump-on/probe-on, pump-off/probe-on, and pump-on/probe-off spectra that is used for evaluating differential transmission spectra. The waiting time delays τ_w between pump and probe are varying with a linear transition stage. The pump and probe beams are focused into the sample (S) under a small angle of $\sim 4^\circ$ by use of an off-axis parabolic mirror. The sample is kept in a temperature-controlled sample chamber at 1°C and is continuously moving to minimize the effects of photoreduction. Finally, the transmitted light from the sample focused onto a fast and sensitive low noise line camera (CCD), mounted to a monochromator. The CCD records 1000 single short spectra for each time delay t_w . From this individual spectra differential transmission spectra

$\frac{\Delta T}{T}(\lambda, t_w)$. The polarization of pump and probe signal controlled using the polarizers (P). the polarization of the probe is parallel to the optical table and the pump has a polarization of 45° . The polarization of the pump can turn using a motorized rotation stage and that allowing for parallel and crossed polarization between pump and probe.

Pump and probe beams are both simultaneously chopped (MC2000, Thorlabs) with a 2:1 duty cycle chopper (C) wheel on a single shot basis for data acquisition. This generates a sequence of pump-on/probe-on $S_{p_{on}, p_{on}}(\lambda, t_w)$ for delay times pump-off/probe-on $S_{p_{off}, p_{on}}(\lambda)$, and pump-on/probe-off $S_{p_{on}, p_{off}}(\lambda)$ transmitted spectra that are then used for evaluating differential transmission spectra $\Delta T / T(\lambda, t_w)$ as a function of probe wavelength λ and waiting time delay t_w .

$$\frac{\Delta T(\lambda, t_w)}{T} = \frac{S_{p^{u_{on}}, p^{r_{on}}}(\lambda, t_w) - S_{p^{u_{off}}, p^{r_{on}}}(\lambda)}{S_{p^{u_{off}}, p^{r_{on}}}(\lambda)} \quad (\text{IV.1})$$

The waiting time delays t_w between pump and probe are changed with a linear translation stage (M531.5IM, Physik Instrumente). A series of delay scans are performed and averaged afterwards.

The sample (S) is kept in temperature-controlled sample chamber, set to 1° C, and is continuously moved to minimize effects of photoreduction. The pump and probe beam are focused into the sample under a small angle of ~4° by use of an off-axis parabolic mirror. The transmitted light from the sample is focused onto a fast and sensitive low noise line camera (CCD, Aviiiva EM4, e2v), mounted to a 150 mm grating monochromator (Acton SP-2150, Princeton Instruments, 150 l/mm grating blazed for 500 nm) records 1,000 single shot spectra for each pulse delay t_w .

From these individual, scattering-corrected differential transmission spectra

$$\frac{\Delta T}{T}(\lambda, t_w) = \frac{S_{p^{u_{on}}, p^{r_{on}}}(\lambda, t_w) - S_{p^{u_{on}}, p^{r_{off}}}(\lambda) - S_{p^{u_{off}}, p^{r_{on}}}(\lambda)}{S_{p^{u_{off}}, p^{r_{on}}}(\lambda)} \quad (\text{IV.2})$$

are calculated and then averaged. The subtraction of the $S_{p^{u_{on}}, p^{r_{off}}}(\lambda)$ spectrum ensures that weak and spurious light scattering contributions on the detector that are induced by the pump pulse are efficiently suppressed.

TA measurements are performed with 20 nJ pump and ~1 nJ probe pulses at 10 kHz laser repetition rate. The pump pulses are focused to a spot size of ~50×50 μm², giving an excitation fluence of 1 mJ/cm². The polarization of the probe is parallel to the optical table, while the pump has a polarization of 45°. A polarizer (P) mounted on a motorized rotation stage can turn the pump polarization, allowing for parallel and crossed polarization between pump and probe without affecting the pump power.

Experimental data are acquired in crossed and parallel polarization of the pump and probe beams for each scan, from which isotropic differential transmission spectra at magic angle (MA) are calculated as

$$\frac{\Delta T}{T}_{MA} = \frac{1}{3} \left(\frac{\Delta T}{T}_{parallel} + 2 \frac{\Delta T}{T}_{crossed} \right) \quad (\text{IV.3})$$

These MA spectra are displayed in this chapter and used for further analysis.

IV.2.3 Data Analysis

TA scans recorded with parallel and crossed pump and probe polarizations were averaged and isotropic, MA spectra were calculated. The few-ps chirp of the probe continuum was corrected by extracting the wavelength-dependent time delay zero ($t_w(\lambda) = 0$) from the cross-phase modulation artifact of a TA measurement of plain buffer solution. The first 200 fs of the corrected dynamics were discarded due to residual coherent signal contributions from the solvent. The datasets were subjected to a global analysis using a multi-exponential decay model [301]. This decomposes the data into a set of n decay associated difference spectra ($DADS_i$) with corresponding decay times τ_i , $\Delta T / T(\lambda, t_w) = \sum_{i=1}^n DADS_i(\lambda) e^{-t_w/\tau_i}$. The lowest number of decays necessary to simultaneously reproduce the data at all wavelengths was taken. For more details, see Appendix. The DADS spectra were then used to obtain evolution associated difference spectra $EADS_k(\lambda) = \sum_{i=k}^n DADS_i(\lambda)$.

IV.2.4 Molecular Dynamics Simulations

The structure of ErCry4 in its dark state was adapted from earlier studies [141, 154, 302], where it was simulated in a $94 \text{ \AA} \times 106 \text{ \AA} \times 102 \text{ \AA}$ water box neutralized with 0.15 M NaCl, resulting in a total of 100,518 atoms. The structure was minimized for 500 conjugate gradient steps using the steepest descent minimization algorithm, followed by a second, 2 ns equilibration using the leap-frog integrator with a temperature of 300 K, kept constant by a Berendsen thermostat. The equilibration was followed by a 100 ns dynamic equilibration and 100 ns production simulation. Both equilibration and production simulations utilized a 2 fs timestep and the LINCS algorithm [303] was used to keep the lengths of bonds involving hydrogen atoms fixed at their equilibrium values. Periodic boundary conditions were adopted for all stages, and the particle-mesh-Ewald summation method was employed for evaluating the Coulomb forces. Van der Waals forces were calculated using a smooth cut-off of 12 \AA with a switching distance of 10 \AA . All calculations were carried out utilizing the GROMACS package [304, 305]. The MD calculation utilized the Amber99SB forcefields for proteins [306, 307] with earlier parametrized forcefields for the FAD cofactor [298, 308].

IV.2.5 Non-Adiabatic Simulation of Electron Transfer

The method for the real-time electron transfer has been carried out using a hybrid real-time quantum mechanical/molecular mechanical (QM/MM) simulations semi-empirical density-functional tight binding method (DFTB) protocol from two earlier studies on frog and plant cryptochromes [298, 304]. The protocol employed molecular fragments participating in the electron transfer as a defined segment of the system that was subjected to the quantum mechanical description (QM region), with the rest of

the system being described using classical molecular mechanics force fields (MM region). The computational scheme utilizes a separation of frontier orbitals similar to the Hückel and Pariser–Parr–Pople models [309, 310] although in this case the orbitals are based on molecular fragments instead of a atoms. For the DFTB calculations a total of 100 structures (snapshots) were sampled from the production MD simulation, each of the snapshots was taken at a 1 ns time interval. The QM region was for all QM/MM simulations selected as the four tryptophans. In this region, Trp_AH^{•+} was assumed to have a missing electron as the initial structure and FAD was assumed to have an extra electron, i.e., being in its FAD^{•-} state. The snapshots were each simulated for 1 ns using a time step of 1 fs, though due to computational limitations only 50 of the snapshots completed the 1 ns calculation while the other 50 calculations resulted in a simulation length of 630 ps. The MM region was simulated using the Amber99SB forcefields for proteins [306, 307] with earlier parameterized forcefields for the FAD cofactor [298, 304], while the QM region and electron transfer was estimated using earlier parameters [311, 312].

IV.3 Results

IV.3.1 Transient Absorption Spectra of ErCry4 Mutants

Ultrafast spectroscopic studies were performed on wild type ErCry4 and four mutants expressed and purified as described earlier [154]. The atomistic structure of the wild type ErCry4 protein has not been obtained experimentally, as it has not been crystallized yet. Gene sequencing [141] and computational modeling [141, 154] suggest that it is overall similar to that of pigeon (*Columba livia*, Cl) Cry4, also with four Trps involved in the activation, namely Trp_A (W395), Trp_B (W372), Trp_C (W318), and Trp_D (W369) [9]. The structure of the FAD chromophore and the Trp tetrad, as obtained from such simulations, is schematically depicted in Figure I. 7 (b) (Chapter I). Site-specific mutagenesis [154] has been used to express four mutants, W_XF (X=A, B, C, D), in which one of the four Trp (W) has been selectively replaced with phenylalanine (F) to block the electron transfer at different positions in the ErCry4 structure, as illustrated in Figure IV. 2 a)-d).

The linear absorption spectra of wild-type ErCry4 and its four mutants are found to be very similar (Figure III. 8, Chapter III), featuring a main peak around 450 nm with well-resolved vibronic substructure. Recent hybrid quantum/classical modeling [1], taking vibronic couplings to nuclear vibrations explicitly into account, successfully described the substructure of these spectra and assigned the peak to a $\pi \rightarrow \pi^*$ transition from the π_2 to π_3 orbitals localized on the isoalloxazine moiety of the FAD cofactor inside Cry [263]. The vibronic substructure is a distinct sign of chromophore binding to the protein and vanishes for FAD in solution. The structured peak around 370 nm arises from the $\pi_1 \rightarrow \pi_3$ transition of FAD [1].

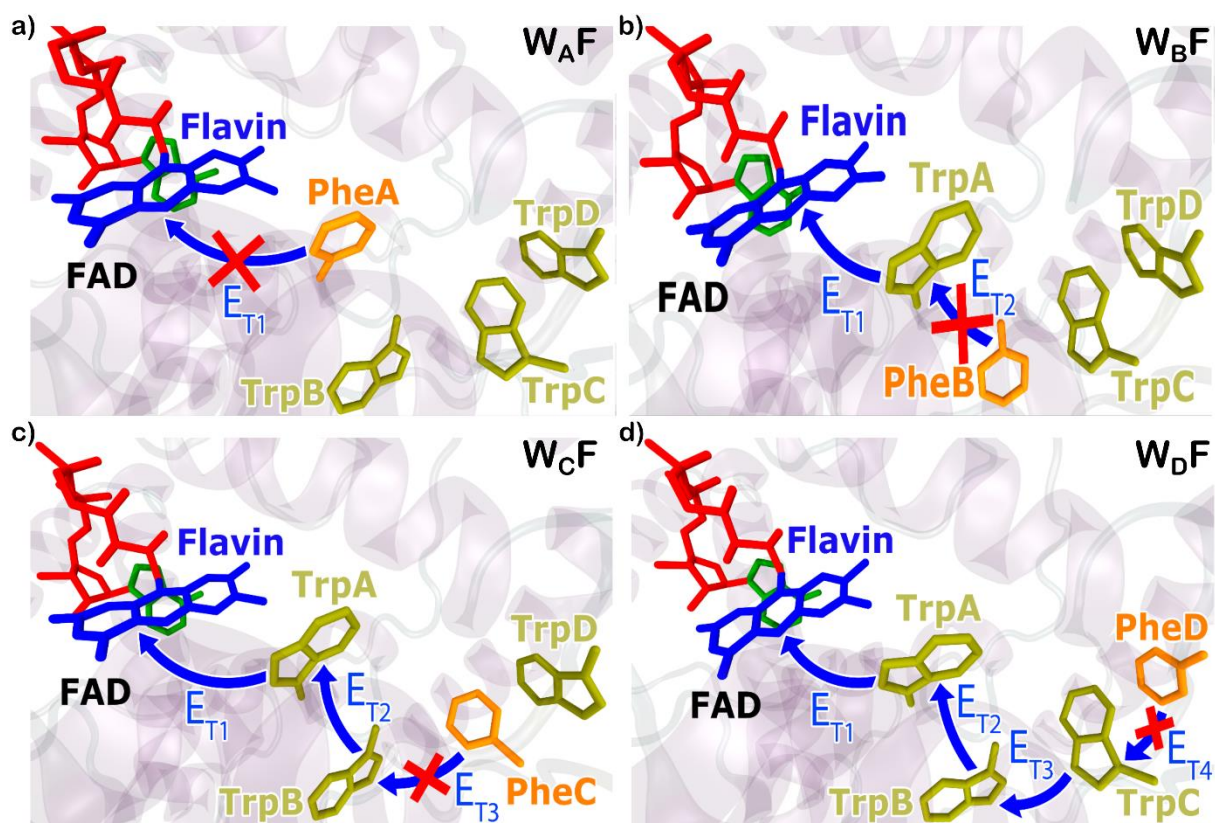


Figure IV. 2 Visualization of the principal electron transfer route in the European robin cryptochrome 4 (ErCry4) protein and the effect of single amino acid mutations on blocking the electron transfer process at different stages. a-d) Electron transfer in ErCry4 mutants involving Trp→Phe substitutions with W395 (Trp_A), W372 (Trp_B), W318 (Trp_C), and W369 (Trp_D). The arrows illustrate the electron transfer paths while the crossed arrows represent the electron transfers that are blocked, as suggested by the experimental data in this study.

The photoluminescence (PL) study results of wild-type ErCry4 and four mutants samples are summarized in Chapter IV A. A comparison of the PL emission intensities of the mutant samples with that of molecular FAD in buffer solution indicates that, in all protein samples, >97% of all FAD molecules are bound and there is a small amount of unbound FAD which will show weak residual PL. This observation is confirmed by time-resolved PL studies showing for all mutants, except for W_AF, a 4 ns mono-exponential decay matching that of molecular FAD in buffer. The W_AF mutant reveals an additional fast, resolution-limited emission component and vibronically structured emission spectrum. In this mutant, Trp_A, which is close to the FAD chromophore, is replaced with Phe, making a rapid electron transfer from Trp_A to FAD impossible. Therefore, the optically excited FAD_{ox}* in W_AF may be longer lived and its emission is not completely quenched by the presence of a nearby Trp_A. In all other mutants, instead, the Trp_A electron donor is present, resulting in efficient PL quenching and thus no emission from FAD_{ox}*. This observation already points to an efficient electron transfer from Trp_A to FAD (Chapter III).

Differential transmission $\Delta T / T$ spectra were recorded under comparable experimental conditions for wild-type ErCry4 and the four considered mutants. Linearly polarized pump pulses with 30 fs duration

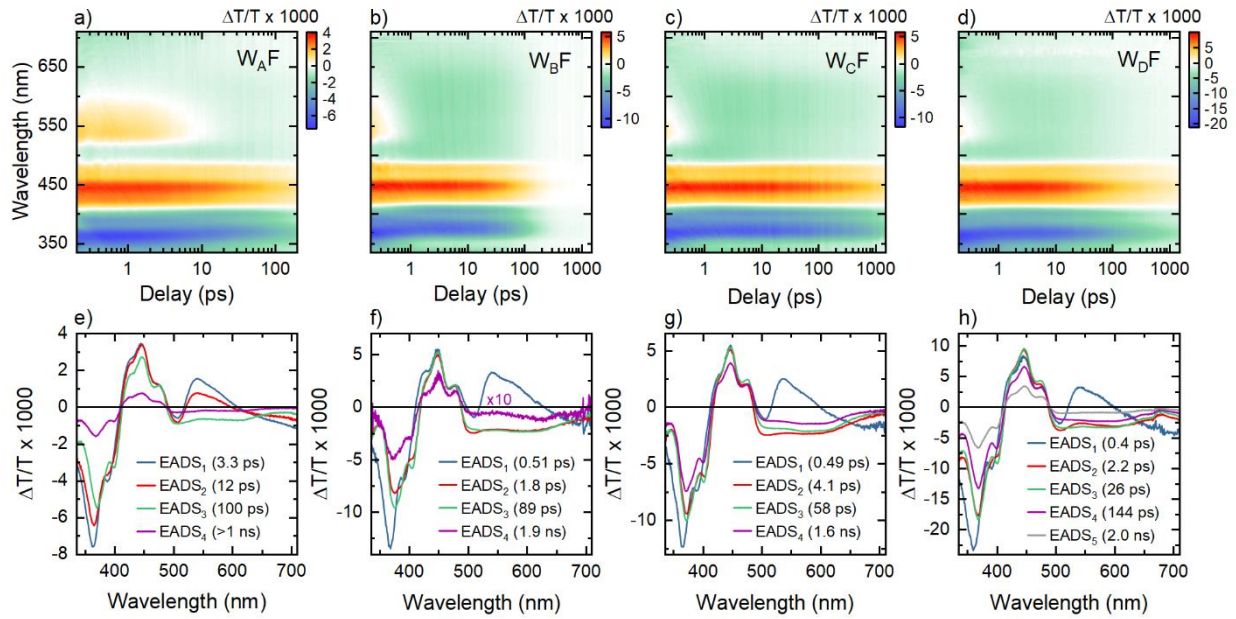


Figure IV. 3 Transient absorption spectroscopy of European robin cryptochrome 4 (ErCry4) mutants. a)-d) Differential transmission $\Delta T / T$ spectra of the mutants W_{AF} to W_{DF} for delays between 0.2 ps and 2 ns (logarithmic time axis). e)-h) Corresponding evolution associated difference spectra ($EADS$) for each mutant resulting from a global analysis. e) The W_{AF} mutant does not show a sub-ps decay component since the electron transfer from Trp_A to FAD is suppressed. f)-h) The 0.5 ps decay component in the $EADS$ spectra, giving evidence for the second and third electron transfer chain in ErCry4. A 2-4 ps decay component in all four mutants is assigned to vibrational cooling of the optically create radical-pairs. The slowest component in all mutants reflect radical -pair recombination on a ns time scale.

centered at 450 nm were used to resonantly excite the $\pi_2 \rightarrow \pi_3$ transition of the FAD chromophore inside ErCry4. Pump-induced changes in the transmission of the sample were probed using a broadband white light continuum. $\Delta T / T$ spectra for MA polarization between pump and probe are shown in Figure IV. 3 a)-d) for the four mutants for delay times t_w between the pulses of up to 1.5 ns. All datasets are subjected to a global data analysis and can be readily explained through a multi-exponential decay model, including a minimal set of decay associated difference spectra ($DADS$) [313]. Each $DADS$ spectrum (Figure A. IV. 6) describes components of $\Delta T / T$ that decay or rise with an associated time constant. Since such spectra are sometimes somewhat difficult to interpret, we also have calculated evolution associated difference spectra ($EADS$ [313], see section IV.2.3). Here, $EADS_1$ represents the $\Delta T / T$ spectra before the onset of incoherent consecutive relaxation steps in the sample while $EADS_n, n > 1$ reflects, in simplified terms, the shape of the $\Delta T / T$ spectrum after the $(n-1)$ th relaxation process has been completed. The resulting $EADS$ spectra are presented in Figure IV. 3 e)-h).

IV.3.1.a Transient Absorption Spectra of ErCry4 WBF

We first consider the W_{BF} mutant (Figure IV. 3 b) and Figure IV. 3. f), where the conceptually simplest, sub-ps electron transfer dynamics from Trp_A to FAD is expected. The distinct signature of this electron transfer is the vanishing of the stimulated emission (SE) band around 550 nm in Figure IV. 3 b) on a 0.5 ps scale. The $\Delta T / T$ spectra in Figure IV. 3. b) at early time delays, represented by the first *EADS* spectrum (*EADS*₁) in Figure IV. 3 f), are recorded before this electron transfer sets in. These $\Delta T / T$ spectra thus show pump-induced changes in the spectrum of the oxidized species, FAD_{ox}, only. The spectra are therefore not yet affected by the formation of radicals in the sample. Indeed, *EADS*₁ (blue line in Figure IV. 3 f)) can well be understood on the basis of the known optical transitions of FAD_{ox} (Figure IV. 4 a)). The pump excitation promotes electrons to vibrationally excited states of π_3 and this gives rise to a positive ($\Delta T > 0$) ground state bleaching (GSB) contribution to the differential transmission with a spectrum matching the linear absorption of FAD_{ox} (blue line in Figure IV. 4 a)). The pronounced vibronic substructure around 450 nm is evident in *EADS*₁ and is a distinct marker for the concentration of optically excited FAD_{ox}* chromophores [236]. Rapid vibrational relaxation within π_3 , complete within 200 fs, gives rise to a strongly red-shifted stimulated emission ($\Delta T > 0$) band ($\pi_3 \rightarrow \pi_2$) around 550 nm (see red line in Figure IV. 4 a) and Figure A. IV. 7 in Appendix). GSB below 400 nm is covered by a pronounced excited state absorption (ESA, $\Delta T < 0$) around 360 nm (with slight substructure around 390 nm) from the $\pi_3 \rightarrow \pi_5$ transition [1] (red lines in Figure IV. 4 a), c)). In addition, the $\Delta T / T$ spectra suggest broadband ESA of FAD_{ox}*, spanning the range from 500 nm to 700 nm and a spectrally almost flat ESA between 400 and 470 nm that is more difficult to assign since ESA of FAD_{ox}* has not yet been modeled with high accuracy (red lines in Figure IV. 4 a), c)). Similar experimental ESA spectra have also been recorded by Kutta et al. but could not yet be well reproduced by quantum chemical calculations [236].

Importantly, the overall shape of *EADS*₁ in Figure IV. 3 e)-h) is very similar in all investigated ErCry4 mutants and also the relative amplitude of the different contributions remains basically unchanged. Since mutation alters the Trp chain with little effect on the FAD chromophore, this provides further support for the assignment of *EADS*₁ to the $\Delta T / T$ spectrum of the FAD chromophore in its oxidized form. The most obvious dynamic feature of the $\Delta T / T$ map for the W_{BF} mutant (Figure IV. 3 b)) is the complete vanishing of the $\pi_3 \rightarrow \pi_2$ SE band around 550 nm with a decay time of 0.5 ps, while the amplitude of the GSB bands remains unchanged. This indicates that the decay of the excited state π_3 population is not due to the refilling of the FAD_{ox} ground state π_2 but reflects the formation of the negatively charged FAD^{•-} radical, most likely due to the transfer of an electron from Trp_A. The map in

Figure IV. 3b) also shows more subtle features. After the first electron transfer has been completed, the $\Delta T / T$ spectrum, now given by $EADS_2$ in Figure IV. 3f, has changed substantially. Not only the characteristic SE band around 550 nm has disappeared completely, but also the sharp peak in the FAD_{ox}^* absorption around 360 nm and the broad ESA tail (red line in Figure IV. 3 f)) has vanished in $EADS_2$. While the GSB and ESA around 450 nm do not change when switching from $EADS_1$ to $EADS_2$, a new narrow ESA band around 370 nm with a side peak at 400 nm and a broad ESA band in the 500 to 700 nm range emerge in $EADS_2$. After subtracting the GSB contribution from $EADS_2$ a $\Delta T / T$ spectrum is obtained that quantitatively matches the sum of the absorption spectra of the $FAD^{\bullet-}$

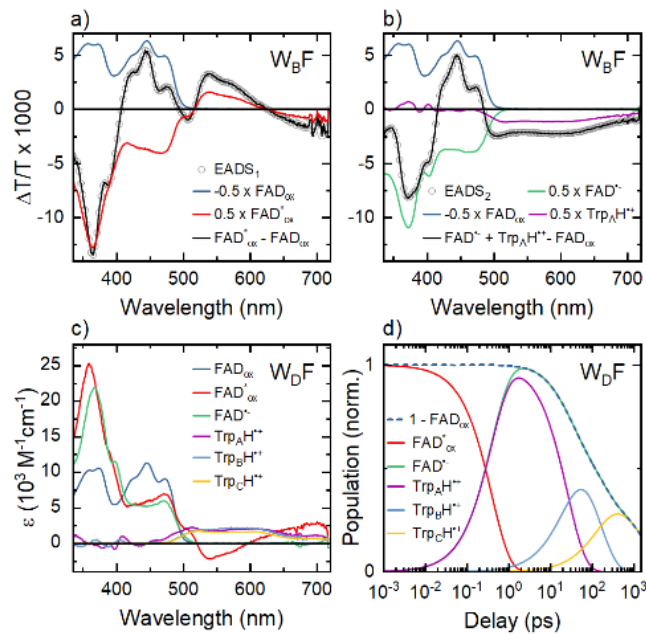


Figure IV. 4 Analysis of the different transmission $\Delta T / T$ spectra of ErCry4 mutants. a) $EADS_1$ spectrum of mutant W_{BF} with 0.51 ps decay time (open circles) and decomposition into the $\Delta T / T$ spectra of FAD_{ox} and FAD_{ox}^* (solid lines). b) $EADS_2$ spectrum of mutant W_{BF} with 1.8 ps decay time (open circles) and decomposition into the $\Delta T / T$ spectra of FAD_{ox} , and $FAD^{\bullet-}$, and $Trp_A H^{\bullet+}$ (solid lines). c) Differential transmission $\Delta T / T$ spectra of the different neutral and charged radical components in the ErCry4 protein as deduced from the analysis of mutant W_{BF} . d) Population dynamics of the different neutral and charged radical states in mutant W_{BF} .

radical anion and the $TrpH^{\bullet+}$ radical cation known from the literature [162, 236]. The corresponding spectra deduced from $EADS_2$ are shown as solid lines in Figure IV. 4 b). The signatures of the spectrum of the Trp radical cation (purple line in Figure IV. 4 c) are the broad absorption centered around 560 nm and a tail of a UV absorption band at 335 nm that is at the edge of the probe window [161, 236, 314]. Theoretical studies of the $FAD^{\bullet-}$ absorption spectrum show a strong transition from the singly occupied π_3 to the unoccupied π_5 orbital [1], which are seen experimentally in the strong absorption peak in Figure IV. 4 b) (circles) at 370 nm, red-shifted by ca. 10 nm with respect to the corresponding transition

in FAD_{ox} . Based on this theoretical analysis [1], we assign a weak peak at 400 nm in $EADS_2$ to the transition from $\pi_1 \rightarrow \pi_3$ and a broad resonance between 400 and 470 nm (green line in Figure IV. 4 b)) to the $\pi_2 \rightarrow \pi_3$ transition. Since the shape of the latter resonance is virtually identical to that seen in the ESA from FAD_{ox} , it is natural to assume that also in FAD_{ox} this ESA peak reflects a two-quantum excitation of $\pi_1 \rightarrow \pi_3$. The decomposed spectra are in convincing agreement with those reported for other types of Cry, suggesting that the disappearance of FAD_{ox}^* leads to the formation of the $\{FAD^{\bullet-} Trp_A H^{\bullet+}\}$ radical-pair. The associated decay time of $t_w \square \tau_r \tau_1 = 1/k_1 = 0.51 ps$ thus appears to be the time constant for the first electron transfer in ErCry4 activation, corresponding to the $\{FAD_{ox}^* Trp_A H\} \xrightarrow{k_1} \{FAD^{\bullet-} Trp_A H^{\bullet+}\}$ process. Since, within our measurement precision, the characteristic markers for FAD_{ox}^* , i.e., the SE emission band around 550 nm and the ESA peak around 360 nm, are completely absent in $EADS_2$, we conclude that the yield for this first electron transfer η_1 is close to unity.

Our data analysis reveals some dynamics associated with a second time constant of $\tau_2 = 1.8 ps$. These dynamics processes, however, have only a minor effect on the $\Delta T / T$ spectra. The $EADS_3$ (green line in Figure IV. 3 f)), monitoring $\Delta T / T$ after the completed relaxation process, shows overall the same spectral structure and amplitude as $EADS_2$ (red line in Figure IV. 3 f)). Close inspection reveals a slight narrowing of the $TrpH^{\bullet+}$ band around 560 nm and a minor reshaping of the $FAD^{\bullet-}$ peaks at 370 and 400 nm. Some authors have recently associated this spectral evolution with vibrational cooling of the optically formed radicals [236] while others have assigned it to a second electron transfer across the Trp chain [162]. The residual $\Delta T / T$ signal decays almost entirely with a time constant of $\tau_r = 89 ps$. This decay monitors the decay of the optically created radical-pairs and the refilling of ground state FAD_{ox} . It is thus associated with the geminate recombination of the radical-pairs. The residual, faint $EADS_4$ spectrum in Figure IV. 3 f), with a shape matching that of $EADS_3$ yet with 20 times smaller amplitude, suggests that a small concentration of radical-pairs is still possible for $t_w \square \tau_r$. Importantly, the $\Delta T / T$ spectra of W_{BF} show no clear signatures of other electron transfer processes except for k_1 .

IV.3.1.b Transient Absorption Spectra of ErCry4 WAF

Ideally, one expects the first electron transfer in ErCry4 activation to be efficiently blocked by substituting Trp_A with Phe, as is done in the W_{AF} mutant. Initially, the $\Delta T / T$ spectra in Figure IV. 3 a) ($EADS_1$, blue line in Figure IV. 3 e)) are very similar to those in the W_{BF} mutant. The fast dynamics

on the sub-ps scale, however, are no longer observed, which directly confirms the assignment of the first electron transfer in the dynamics of the W_BF mutant. The fastest electron transfer dynamics in the case of the W_AF mutant occurs with a time constant of 3.3 ps and results ($EADS_2$, red line in Figure IV. 3 e)) in a partial reduction of SE and ESA from FAD_{ox}*. Since intermolecular electron transfer processes involving TrpA cannot be the origin of this decay, the observed dynamics is most likely of intramolecular nature. Indeed, intramolecular photo-induced electron transfers from the adenine to isoalloxazine moiety of the FAD cofactor is known to occur in solution on a 5 ps time scale for the stacked FAD conformation [2, 22]. Even though the exact time scale for the back electron transfer to adenine is somewhat debated for molecular FAD in solution [2, 22], it is generally thought to happen on a similar time scale as the forward transfer, forming an equilibrium between neutral and charge-separated species. The existence of such an equilibrium for the intramolecular electron transfer in the W_AF mutant may be the reason why the recorded data show only a partial decay of FAD_{ox}* with a 3.3 ps time constant. More surprising is the $\Delta T / T$ dynamics with a larger 12 ps time constant. After its completion, the resulting $EADS_3$ (green line in Figure IV. 3 a)) matches that seen in the W_BF mutant, indicating the formation of a {FAD^{•-} Trp_xH^{•+}} radical-pair. Molecular dynamics simulations of the protein structure (Figure IV. 6 a)) indicate that two additional Trp residues, Trp290 and Trp350, are present at an edge-to-edge distance of 4 Å from the adenine and 7.5 Å from the flavin moiety, respectively. These residues could then potentially be involved in the formation of a {FAD^{•-} TrpH^{•+}} radical-pair. The $\Delta T / T$ changes in Figure IV. 3 a) disappear almost completely on a 100 ps time scale, the decay time associated with $EADS_3$. We can thus associate this 100 ps time constant with an effective geminate recombination of the formed intermolecular radical-pair. Altogether, the experiments on the W_AF mutant prove that the first electron transfer in ErCry4 from Trp_A is efficiently blocked by mutation. At the same time, our findings highlight the role of competing intra- and intermolecular electron transfer processes, involving electron donors outside the conserved tetradic Trp chain, for the radical-pair formation in Cry.

IV.3.1.c Transient Absorption Spectra of ErCry4 W_CF and W_DF

The performed analysis puts us now in an excellent position to explore the electron transfer across the Trp chain in ErCry4 W_CF and W_DF mutants (Figure IV. 3 c) and Figure IV. 3 d)). In both cases, the $\Delta T / T$ spectra at early time delays ($EADS_1$ in Figure IV. 3 g) and Figure IV. 3 h)) are very similar to those discussed before for the W_AF and W_BF mutants, except for minor changes in peak amplitudes. In the case of the W_CF and W_DF samples, the initial dynamics points to a first electron transfer from Trp_A to FAD with close to 100 % efficiency and time constants of $\tau_1 = 0.49$ ps (W_CF) and 0.4 ps (W_DF), respectively. Also, the few-ps decay of $EADS_2$ from the W_CF mutant is seen, now with time constants

of $\tau_2 = 4.1 \text{ ps}$ (W_{CF}) and 2.2 ps (W_{DF}). In contrast to the W_{BF} mutant case, the shape of the spectrum of the Trp radical cation changes slightly when going from $EADS_2$ to $EADS_3$, most dominantly around 500 nm and in the far red region. Since $EADS_2$ is not affected by an extension of the Trp chain, our data do not support the assignment of τ_2 to an electron transfer process. Instead, our observation presents strong arguments in favor of vibrational cooling as suggested earlier [236]. The spectra recorded for both the W_{CF} and the W_{DF} mutants show a third $EADS_3$ component with a spectral lineshape and a decay time ($\tau_3 = 58 \text{ ps}$ for W_{CF} and 26 ps for W_{DF}) that are very similar to those observed for the W_{BF} mutant. In stark contrast to the W_{BF} mutant, however, a fourth $EADS_4$ component now appears after the third relaxation step with an amplitude which is approximately 2/3 of that of $EADS_3$, and with an almost identical lineshape. This finding implies that, even after the third relaxation step, i.e., after about 100 ps, the excited ErCry4 in the sample still contains a sizeable concentration of radical-pairs and that geminate recombination is not yet complete. This observation thus points to a secondary electron transfer step, $\{FAD^{\cdot-}Trp_A H^{+\cdot}\} \xrightarrow{k_2} \{FAD^{\cdot-}Trp_B H^{+\cdot}\}$, in which an electron is transferred from Trp_B to Trp_A with a rate constant $k_2 = 1/\tau_3$. The data in Figure IV. 3 g) and Figure IV. 3 h) indicate that this secondary electron transfer occurs with a yield of $\eta_2 \approx 0.77$ for W_{CF} and 0.71 for W_{DF} . In the case of the W_{CF} mutant, the resulting radical-pair concentration then recombines very slowly with $\tau_r \approx 1.6 \text{ ns}$. In the W_{DF} mutant, both the GSB and the radical-pair absorption decay more quickly than for the other mutants. The analysis in Figure IV. 3 h) reveals the presence of a new decay channel with a decay time $\tau_4 = 144 \text{ ps}$. This relaxation process has little effect on the shape of the $\Delta T / T$ spectra since the spectra from $EADS_3$ to $EADS_5$ differ only in amplitude. We assign the observed decay to the third electron transfer step, $\{FAD^{\cdot-}Trp_B H^{+\cdot}\} \xrightarrow{k_3} \{FAD^{\cdot-}Trp_C H^{+\cdot}\}$, in which an electron is transferred from Trp_C to Trp_B at a rate of $k_3 = 1/\tau_4$ and with a yield of $\eta_3 \approx 0.52$. This yield is significantly lower than that of the second step. The population dynamics of the different neutral and charged radical states in mutant W_{DF} that is predicted by the analysis of the $\Delta T / T$ spectra is summarized in Figure IV. 4 d). This analysis indicates that only a small fraction of about 20–25% of the initially generated radical-pairs is still present after the first three electron transfers along the Trp chain (yellow line in Figure IV. 4 d)). These radical-pairs then undergo geminate recombination on a time scale of $\tau_r = 2.0 \text{ ns}$ ($EADS_5$). Comparative studies of several samples of the same mutant indicate that the number of decay components needed to explain the experimental data do not depend on the specific studied sample. Also, the deduced decay times and yields are quite similar.

IV.3.1.d Transient Absorption Spectra of Wild-type ErCry4

We now compare the results in Figure IV. 3 to a TA study of wild-type ErCry4 under similar experimental conditions. Qualitatively, the $\Delta T / T$ spectra in Figure IV. 5 a) look almost identical to those recorded for the W_DF mutant. Spectra at selected t_w are shown in Figure IV. 5 b). The dynamics at selected probe wavelengths are compared to the results from a global fit analysis presented in Figure IV. 5 c). As in the case of the W_DF mutant, this analysis reveals five distinct *EADS* spectra with features that closely resemble those of the W_DF mutant. Also, the decay times associated to those five components are almost the same as for the W_DF mutant. This strongly indicates that the sequential electron transfer model developed from the mutant spectra can be used to explain the wild type data. As such, we assign the time constant $\tau_2 = 3 \text{ ps}$ to vibrational cooling and identify the decay time of *EADS*₅ with geminate recombination dynamics of the radical-pair with $\tau_r = 2 \text{ ns}$.

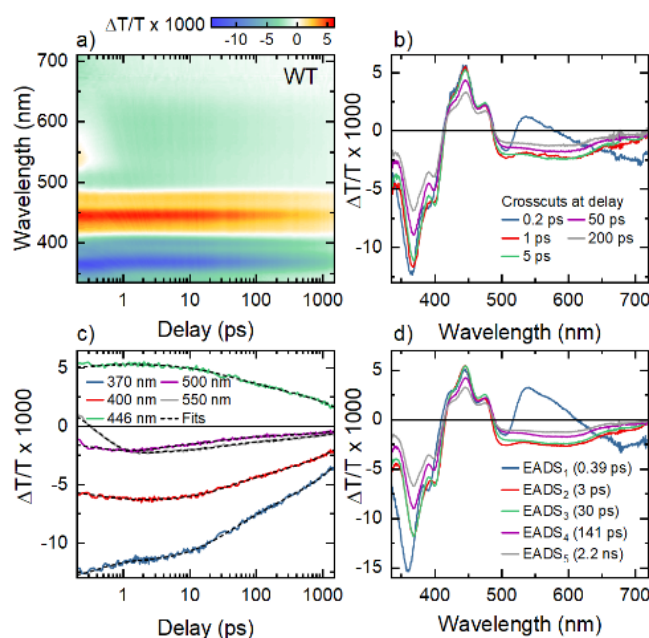


Figure IV. 5 Transient absorption spectroscopy of wild-type ErCry4 proteins. a) Differential transmission $\Delta T / T$ spectra of the wild type protein for delays been 0.2 ps and 1.5 ns (logarithmic time axis). b) $\Delta T / T$ spectra at selected delays. c) Dynamics of the $\Delta T / T$ spectra at selected wavelengths. The results of the global analysis are added as black dashed lines. d) *EADS* spectra as obtained from the global data analysis. The resulting spectra are very similar to those of mutant W_DF. Based on the analysis of the mutant spectra, we assign the components with decay times of 0.39, 30, and 141 ps to the first, second and third sequential electron transfer across the tryptophan chain of the protein. The 3 ps decay component is associated with vibrational cooling of the optically generated radical-pairs, while the 2.2 ns component reflects radical-pair recombination.

Sample	$\mathbf{ET}_1(\eta_1)$	$\mathbf{ET}_2(\eta_2)$	$\mathbf{ET}_3(\eta_3)$
W _B F	0.51 ps (100%)		
W _C F	0.49 ps (100%)	58 ps (77%)	
W _D F	0.40 ps (100%)	26 ps (71%)	144 ps (52%)
WT	0.39 ps (100%)	30 ps (78%)	141 ps (77%)

Table IV. 1 Electron transfer times and yields for the investigated mutants and the wild type protein.

Our experimental results provide clear evidence for three sequential electron transfers in wild type ErCry4, with decay constants of $k_1 = 1/0.39 \text{ ps}^{-1}$, $k_2 = 1/0.30 \text{ ps}^{-1}$, and $k_3 = 1/141 \text{ ps}^{-1}$. The associated yields of the individual steps are $\eta_1 = 1.0$, $\eta_2 = 0.78$, and $\eta_3 = 0.77$. In these measurements, the yield of the third step is somewhat higher than in the case of the W_DF mutant. This points to a radical-pair concentration in the wild type protein being more than half of the initially optically generated concentration. The electron transfer rates and yields deduced for the wild-type protein and all mutants are summarized in Table IV.1

IV.3.2 Quantum Mechanical / Molecular Mechanical Simulations

IV.3.2.a Occupancy of Tryptophan Sites

The measured electron transfer rate constants can now be compared to the theoretical predictions that rely on QM/MM simulations [298, 304]. The entire cryptochrome is simply too large for a purely quantum-mechanical treatment, and therefore hybrid methods should be employed. These simulations were performed for the WT ErCry4 to provide additional atomistic insights into the nature of the process. We note that this is a first attempt to carry out quantum simulations of electron transfer in ErCry4, and to obtain a direct comparison to the experiment. Earlier phenomenological studies [154] helped estimating the kinetics of the charge transfer steps in the protein, however, these studies did not take explicit account for the atomistic dynamics of the environment.

The experimental electron transfer times through the tryptophan tetrad are on the scale of hundreds of picoseconds, which make the non-adiabatic semi-classical electron transfer simulation scheme based on a fragment-molecular-orbital implementation of the DFTB [298, 304, 308, 315, 316] a suitable framework to model the process computationally. For an accurate description of the electron transfer process, an account of motion of the biological scaffold of the protein is essential. Moreover, this essentially classical motion should be coupled to the quantum dynamics of the transferring electron.

The DFTB approach has been used previously to study real time electron transfers in frog and plant cryptochromes [298, 308], and therefore we have now applied it here for modeling ET₂₋₄ steps (see Figure IV. 2 a) in ErCry4. The ErCry4 structure for the electron transfer studies was obtained through homology modeling, equilibrated through extended Molecular Dynamics (MD) simulations, and justified through numerous prior analyses [154, 302, 317]. The prerequisite for the ET₂₋₄ simulations was the {FAD^{•-} Trp_AH^{•+}} radical-pair, which arises after the first electron transfer, ET₁. Here, an electron vacancy (electron hole) is residing at the Trp_A residue and, following the time dependent Schrödinger Equation, it starts to propagate through the tryptophan tetrad, facilitated by the motion of the protein [298]. As the electron hole progresses through the tetrad, it is possible to define its probability to occupy one of the tryptophan residues (occupation); the time evolution of the occupation of each tryptophan then in turn can be used to determine the electron transfer kinetics. Note, that ET₁ was not considered in the computational description since this transfer involves excited flavin and tryptophan, which in turn require a special treatment within DFTB, while ET₂₋₄ only include tryptophan residues, see section IV.2.5 for a thorough description of the DFTB treatment.

The time-dependency of the average occupancies of the tryptophan tetrad is shown in Figure IV. 6 a) (with symbols) for the 1 ns-long simulations and, in Figure IV. 6 b), for shorter simulations, capped at 630 ps, where the electron hole has reached Trp_CH^{•+} or Trp_DH^{•+} with a probability of at least 0.3. The 1 ns-long simulations include all trajectory results, independent of whether the electron transfer along the tryptophan tetrad was completed or not. The averaging in Figure IV. 6 a) and b) has been performed over the independent simulations. The solid lines in Figure IV. 6 a) and b) correspond to the numerical fits to the simulated data which were obtained from the solution of the set of coupled differential Equations,

$$\begin{aligned}
\frac{d[Trp_A]}{dt} &= k_2 [Trp_A], \\
\frac{d[Trp_B]}{dt} &= k_2 [Trp_A] - k_3 [Trp_B], \\
\frac{d[Trp_C]}{dt} &= k_3 [Trp_B] - k_4 [Trp_C], \\
\frac{d[Trp_D]}{dt} &= k_4 [Trp_C].
\end{aligned}
\tag{IV.4}$$

Here $[Trp_m]$ denotes the electron hole occupancy of the m '-th tryptophan and k_n is the transfer rate constant for the n '-th electron transfer. The transfer rate analysis permits us to estimate the characteristic transfer times of each electron transfer process; the results are summarized in Table IV. 2.

The performed analysis shows that an electron transfer between the different tryptophans in ErCry4 is possible. However, Figure IV. 6 a) shows some discrepancies between the simulated data and the fitted curves at longer times, while these are less pronounced in Figure IV. 6 b). The poor fitting of the simulation data in the case of Figure IV. 6 a) is due to the large uncertainty in the average occupation values of the four residues $\text{Trp}_{\text{A-D}}$ in that case. The analysis of the simulations reveals that in a significant fraction of the simulations, the electron transfer was not completed over the timespan of 1 ns. In a series of trajectories, we find that the electron hole at the Trp_{A} residue hardly ever transfers

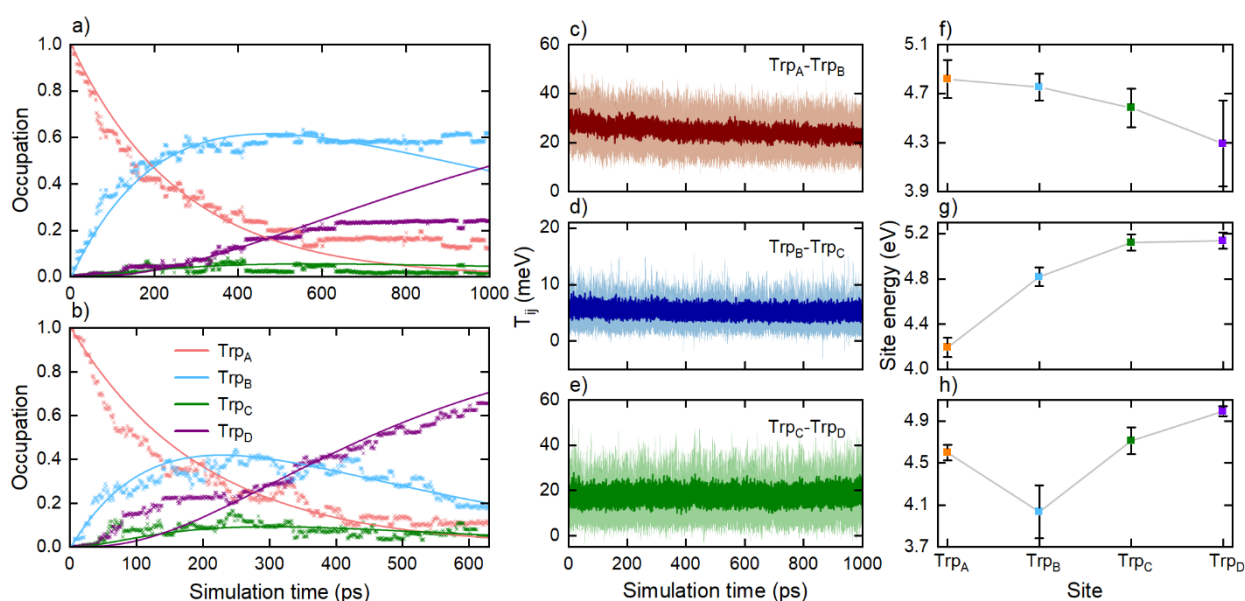


Figure IV. 6 Characterization of electron transfers (ET_2 – ET_4) in the tryptophan tetrad by QM/MM DFTB simulations. a) Average occupation of the four tryptophan sites computed over 50 simulations (points), fitted through Equation (IV.4) (lines). b) Average occupation of the four tryptophan sites (points) computed over 27 simulations where a transfer is considered complete, i.e., the occupation of $\text{Trp}_{\text{C}}\text{H}^{\bullet+}$ or $\text{Trp}_{\text{D}}\text{H}^{\bullet+}$ reaches at least a value of 0.3. The solid lines show a fit to Equation (IV.4). c)–e) Average electronic couplings computed over 50 simulations between two neighboring tryptophan sites as a function of simulation time (dark color) with the corresponding standard deviation (light color). f)–h) Average site energies of the different tryptophans in the electron transfer chain divided into three electron transfer scenarios observed in the simulations: f) shows the average site energies for the completed electron transfers ($N = 27$) (see supporting Video S1 in Timmer et al. [16, 17]). g) The average site energies for the transfers that do not go beyond the first tryptophan Trp_{A} ($N = 13$) (see supporting Video S2 in Timmer et al. [16]), and h) the average site energies for the transfers that stop at Trp_{B} ($N = 60$) (see supporting Video S3 in Timmer et al. [3, 16, 18–20]).

to Trp_{B} . This is a natural effect stemming from the fact that different initial structures support the ET process to different extent, and some do so very slowly. Covering this dependence in its entirety would require a much larger number of individual simulations, associated with a prohibitively large computational effort. The current protocol is a practicable solution that might merely lead to a somewhat, but uniformly overestimated rates of the individual ET steps. To illustrate the influence of those simulations that do not show a sequential electron transfer across the Trp chain on the overall kinetics, we have included in Figure IV. 6 b) the data for the simulations where the occupancy of

Trp_CH^{•+} or Trp_DH^{•+} reaches at least 0.3 at the end of the simulation. One notes a much better correspondence of the average occupancy of the tryptophans and the solution of the kinetic Equation (IV.4) in this case. The results shown in Figure IV. 6 b) show an electron transfer Trp_B→Trp_AH^{•+} on a 200 ps time scale that is followed by an electron transfer from Trp_C→Trp_BH^{•+}. The fourth electron transfer, from Trp_D→Trp_CH^{•+} is predicted on a somewhat faster, < 100 ps, time scale. Thus, the occupancy of Trp_CH^{•+} will necessarily remain low and it will be difficult to clearly distinguish the occupancies of Trp_CH^{•+} and Trp_DH^{•+} experimentally. This agrees well with our experimental observations for the wild-type samples as well as the mutants. The corresponding simulated electron transfer times are presented in Table IV. 2.

IV.3.2.b Marcus Theory Analysis

The results of the DFTB simulations can be qualitatively understood if we consider weak coupling between donor and acceptor sites, and assume the high temperature limit. In this case the electron transfer rate can be estimated, following Marcus-Hopfield theory [318] as

$$K_{ET} = \left\langle \frac{T_{ij}^2}{\hbar} \right\rangle \sqrt{\frac{\pi}{\lambda k_B T}} \exp \left[-\frac{(\hbar \Delta G + \lambda)^2}{4\lambda k_B T} \right]. \quad (\text{IV.5})$$

The rate of the electron transfer process is governed by three parameters: the coupling between the electron donor and acceptor sites, T_{ij} ($i, j = A, B, C, D$); the thermodynamic driving force, ΔG ; and the reorganization energy λ . The driving force is related to the so-called site energy, as demonstrated earlier [298]. The electronic coupling between two different tryptophan sites is defined as $T_{ij} = \langle \phi_i | \hat{H}_0 | \phi_j \rangle$, while the site energies can be identified as the ionization potentials (IP) of the respective tryptophans as $\varepsilon_i = \langle \phi_i | \hat{H}_0 | \phi_i \rangle$. Here the ϕ_i denotes the molecular orbitals of the electrons delocalized at the respective tryptophan residues, while \hat{H}_0 is the Hamiltonian of the system.

Figure IV. 6 c)-e) show the time evolution of the electronic coupling T_{ij} ($i, j = A, B, C, D$), see Equation (IV.5), between the neighboring sites of the tryptophan tetrad. These coupling strengths are the fundamental results of the DFTB calculations and have been extensively discussed previously [298, 308]. In particular, it was shown that despite the simplicity of the DFTB approach, it yields accurate coupling values for charge transfer between tryptophan residues in cryptochromes and photolyases [298, 308, 319], comparable with values obtained using higher order methods. Physically, the electronic couplings determine the probability of electron transfer between the sites, similarly to their appearance in the Marcus equation. It is revealed that the average value of T_{BC} between Trp_B and Trp_C is around 5

meV and while the coupling strength is significantly higher between Trp_C and Trp_D, where it turns out to be 20-30 meV.

Dataset	ET ₂	ET ₃	ET ₄
1 ns (Figure IV. 6 a))	260 ps	960 ps	90 ps
630 ps (Figure IV. 6 b))	200 ps	260 ps	60 ps

Table IV. 2 Estimated electron transfer times obtained from the simulations of electron hole propagation over tryptophan tetrad. Results are shown for the numerical fits of the solution of Equation (IV.5) to the computed data for the 1 ns-long simulation and 630 ps long simulations, averaged over 50 and 27 independent simulations, respectively. In the latter case only those simulations where Trp_CH^{•+} or Trp_DH^{•+} obtained an electron hole occupancy of at least 0.3 were considered. The values have been rounded to the nearest 10 ps.

The average site energies are shown in Figure IV. 6 f)-h) for all studied tryptophan sites. One distinguishes three major scenarios of the DFTB calculations, namely completed electron transfers (Figure IV. 6 f), supporting Video S1 in Timmer et al. [16]), no electron transfer from Trp_BH to Trp_AH^{•+} (Figure IV. 6 g, supporting Video S2 in Timmer et al. [16]), and no electron transfer from Trp_CH to Trp_BH^{•+} (Figure IV. 6 h)), supporting Video S3 in Timmer et al. [16]). The site energies in Figure IV. 6 f)-h) have been averaged over the corresponding simulations. The three outcomes show rather different site energies. Note, that the electronic coupling T_{ij} would contribute only quadratically to the overall electron transfer rate constant, while the energy difference and reorganization energy (site energies) contribute exponentially, see Equation (IV.5) The average site energy difference between Trp_A and Trp_B is -0.05 eV for the cases with completed charge transfers +0.62 eV for the cases where no transfer from Trp_BH to Trp_AH^{•+} was observed; and -0.56 eV for the case where the electron hole is stuck at the Trp_BH^{•+} site. Not surprisingly, there is no electron transfer to Trp_AH^{•+} in Figure IV. 6 g) with a site energy difference of +0.62 eV. The same can be observed in Figure IV. 6 h), where there is no electron transfer as the site energy difference is 0.68 eV for the Trp_C→Trp_BH transition, whereas in Figure IV. 6 f) the site energies decrease for each electron transfer step.

IV.4 Discussion

The ability to express high purity cryptochrome 4 proteins from night-migratory European robins and to replace the tryptophan residues individually by redox-inactive phenylalanine has allowed us to provide new microscopic insight into the light-induced electron transfer dynamics across the tetradic tryptophan chain that connects the flavin chromophore to the surface of this protein. Using ultrafast optical spectroscopy, in connection with a Marcus-Hopfield model for the electron transfer inside the protein, we could unravel several of the primary steps in the photocycle of this photoreceptor which is suggested to play a decisive role in the magnetic compass sensing of migratory songbirds [20, 27, 154].

When replacing the tryptophan amino acid that is located most closely to the FAD chromophore (Trp_A) with a phenylalanine blocker, intermolecular electron transfer along the Trp tetrad is efficiently suppressed and slower intra- and intermolecular transfer paths are revealed. MD simulations suggest that the intermolecular steps likely involve other Trps, outside the tetrad. In all other mutants and in the wild-type protein, Trp_A serves as an efficient donor, transferring an electron to FAD within 0.5 ps after photoexcitation and with a yield of unity. The experiments reveal vibrational cooling dynamics within the manifold of radical-pair states on a few-ps timescale which are insensitive to mutation. They provide evidence for a cascade of sequential electron transfers along the chain in which the second ($\text{Trp}_B \rightarrow \text{Trp}_A$) and third ($\text{Trp}_C \rightarrow \text{Trp}_B$) steps occur with transfer times of 30 ps and 140 ps, respectively, and can be selectively blocked by mutation. In the present work, all pump-probe experiments have been performed at a temperature of 1° C and in a buffer solution at pH8 to avoid photodegradation of the light-sensitive protein. We found that, under these conditions, the protein is photostable for several hours. It is known that under physiological conditions (40-43° C), the pH of most bird cells is 7.3.[233, 320]. The change in the charge states of proteins caused by reducing temperature, principally due to a shift in the acid-base equilibrium of histidine side chains, can be reversed by an increase in pH, suggesting that pH 8 at 1° C should be similar to physiological conditions [176, 233].

Assuming the validity of the Marcus-Hopfield model (Equation (IV.5)), we would expect that the electron transfer times decrease only slightly, by approximately 50%, when increasing the temperature from 1° C, chosen in the present work to 42° C, the body temperature of European robins. As such, we expect that the main conclusions of this work remain valid under physiological conditions. Preliminary results of an experimental study of the temperature dependence of the electron transfer dynamics indeed show that the electron transfer rates and yields change only weakly with temperature over the range from 1° C to 30° C. The temperature dependence will be discussed in more detail in a forthcoming publication.

In the wild-type protein, the yield is found to be quite high (> 75 %) while in the mutation W_DF , in which the terminal Trp_D is replaced, the third electron transfer step has a lower yield, (~ 50%). Our data,

probing the dynamics within the first 1.5 ns after photoexcitation, do not provide clear indication for a fourth transfer step from Trp_D to Trp_C, either due to the lack of a good optical sensor for these distant tryptophans in the present measurements or because this step is either too slow or too fast to be resolved here. A comparison of the TA data from the wild-type protein and the mutant W_DF suggests that the presence of the fourth tryptophan in the chain has very little effect on the dynamics within the first 1.5 ns, except for apparently increasing the concentration of radical -pairs at the end of the measurement window. Such a change in concentration could be explained, e.g., by a transfer time for the fourth electron transfer from Trp_D→Trp_C that is faster than that for the third step and is forming an equilibrium between the associated radical-pairs [154, 291]. The present data indeed point to the formation of such an equilibrium and suggest more refined studies of the functional role of the terminal Trp.

While the time constant that we have deduced for the first and second electron transfers agree well with those recently reported by Kutta et al. for cryptochrome from fruit flies [236], the electron transfer times measured here are somewhat slower than recent predictions [154] on the basis of MD simulations and Moser-Dutton theory. They also appear to be faster than those predicted using DFTB-based hybrid quantum mechanics/molecular mechanics (QM/MM) simulations that have been presented here as a first benchmark test for our experimental work. In the QM/MM simulations, the first ET₁ could not be modeled, remaining an open question for the future until reliable DFTB parameters become available for the excited flavin chromophore. The simulations give atomistic insight into the sequential electron transfer cascade through the tryptophan tetrad with the typical transfer times in the 100 ps range. Here, it is interesting to note that the simulations suggest that for certain ErCry4 configurations the electron transfer through the tetrad simply does not progress and the electron hole stays stuck at Trp_AH^{•+}. In such cases, the calculations suggest an increase in average site energy on going from Trp_AH^{•+} to Trp_BH^{•+} of 0.62 eV. In contrast, when this electron transfer does take place, it is because there is a decrease in the average site energy. The increases in site energy found for some of the simulations cannot be attributed to a single amino acid residue but are a collective effect of the protein environment that, overall, appears slightly different in the various starting configurations used in the QM/MM simulations.

The characteristic electron transfer times for the ET₂ and ET₃ processes obtained in cases when the electron has been transferred through the entire tetrad are in a reasonable, order-of-magnitude agreement between experiment and theory. Following Equation (IV.4) and Table IV. 2, one concludes that the agreement is worse for the ET₂ process and turns out to be much closer for the ET₃ process. It is important to stress that computationally we could also establish the characteristic time for the ET₄ (60 ps) process, that so far has been inaccessible to the experiment; the ET₄ process is expected to happen somewhat faster than the preceding electron transfer steps. This would explain why it is difficult to separate ET₃ and ET₄ experimentally. The theoretical electron transfer times follow from a simple kinetic model, cf. Equation (IV.4), that could reproduce the computed QM/MM average time

dependence of charge occupation of the four tryptophan residues reasonably well. The model did not include the electron back-transfer processes, that are expected to happen significantly slower than the forward electron transfers, consistent with earlier studies [297, 298, 308] and the present measurements.

In the future, the computational methodology could possibly be improved by considering a more sophisticated QM description of the tryptophan tetrad, e.g., going beyond the DFTB model. Another methodological advance could involve polarizable embedding models [321], where account of the changes in the environment due to the propelling electron would be considered. These theories are not yet ready to be applied to the problem studied here but could potentially improve the agreement between experiment and model. Most importantly, we expect quantitatively new insight into the first step of the electron transfer cascade, from Trp_A to the FAD chromophore, which is still beyond the scope of the presently employed charge transfer models.

IV.5 Summary and Outlook

In summary, our results demonstrate a long-distance, sequential FAD-Trp electron transfer chain with time constants ranging from less than 0.5 ps to more than 150 s. This chain results in the formation of a high yield of long-lived radical-pairs upon photoexcitation and thus is a crucial primary step in the radical-pair mechanism. The broad spread of ET time constants is to be contrasted with the ET dynamics in recently investigated flavin-containing non-natural photoenzymes [322]. Taken together, our results provide new microscopic insight into the inner workings of this sequential electron transfer chain. They demonstrate how charge flow and thus radical-pair formation across the tryptophan tetrad in cryptochrome proteins can be sensitively controlled by site-selective mutation of the amino acid structure of the chain. The ability to apply sensitive pump-probe spectroscopies to cryptochromes from night-migratory robins, demonstrated in our work, presents a step forward towards probing not only the flow of charge but also the transport of spins [299] along such chains by all-optical means. More generally, this may be helpful for monitoring dynamical spin correlations in radical-pairs in biomolecules or organic photovoltaic materials.

Chapter V

V.1 Summary and Conclusion

The long-range navigation of migratory birds using the earth's weak magnetic field has been known for over a century. Even though, the primary sensory molecule and the mechanism behind this were unclear for a long time. Numerous controlled behavioral experiments on migratory birds proved that they possess very accurate magnetic compasses, and the mechanism is light-dependent. The experimental results also suggest that migratory birds acquire compass information as visual patterns. So, the compass sensors should be located in an easily light-receivable and vision-altering location. This circumstantial evidence suggests that the primary location will be the retina of birds. The behavioral experiment results also reveal that the magnetic compass carried by the birds is sensitive to the earth's magnetic field intensity, inclination (the angle between the geomagnetic field lines and the earth's surface), and declination (angular deviation between magnetic and geographic poles) angle rather than the polarity of the geomagnetic field [3, 11, 27, 38, 40, 66].

All these observations point out that the primary mechanism behind the magnetic compass is the light-induced radical-pair formation. Radicals, an odd number of electrons in the outer shell of molecules, are magnetically sensitive due to the electron's inherent quantum property spin. Radical-pairs are formed either by breaking the bond between two molecules or by electron transfer between them. The initial spin of the radical-pairs is most probably a singlet state. The spin state of radical-pairs can coherently interconvert between singlet and triplet states by the combined effects of hyperfine and Zeeman effects. The quantum yield of the triplet state of the radical-pair entirely depends on the direction of the external magnetic field and the orientation of the radical-pair. These provide directional effects for magnetoreception in birds [11, 20, 66].

Cryptochromes are the only protein molecules found in vertebrates that can form light-induced radical-pairs. They have many other functions in plants, insects, and animals and are considered the primary sensor molecules for magnetoreception due to their ability to form radical-pairs. Light-induced electron transfer from a chain of three or four tryptophan (Trp) amino-acid residues in cryptochrome to the flavin adenine dinucleotide (FAD) cofactor on a femtosecond (fs) to picosecond (ps) timescales produce a {FAD^{•-} TrpH^{•-}} radical-pair. This radical-pair and its further chemical reactions are sensitive to the geomagnetic field for a nanosecond to microsecond time scale [20].

In this thesis, the light-induced charge transfer process along the Trp chain and the formation of radical-pairs in cryptochrome 4 (ErCry4) molecule from a night-migratory bird European robin were probed using highly sensitive ultrafast spectroscopy techniques. In ErCry4 protein, FAD chromophore is non-

covalently bound inside the protein, and four tryptophan chain residues, W395 (Trp_A), W372 (Trp_B), W318 (Trp_C), and W369 (Trp_D), are connected to it. The FAD chromophore and these four Trp residues play an important role in the photoactivation of the ErCry4 protein. During the photoactivation, light-induced sequential electron transfer creates long-lived spin-correlated radical-pairs responsible for the magnetic sensitivity reported in the ErCry4 [154]. Through these ultrafast experiments with femtosecond (fs) to a picosecond (ps) time resolution, it was tried to find the photophysical properties of cryptochrome protein and the effects of the protein environment on the dynamics and yields of the light-induced charge transfer process in ErCry4. The advantages of fluorescence and transient absorption (TA) spectroscopic techniques were explored and applied to the purified ErCry4 (WT ErCry4) and its four mutant samples W_XF (X = A, B, C, D) in which the Trp residues involved in the electron transfer reaction are site selectively replaced with inactive phenylalanine (F). These mutations block the electron transfer at different positions in the ErCry4 protein. The experimental results are compared with Marcus-Hopfield theory and density functional tight binding (DFTB) based hybrid quantum mechanics/molecular mechanics (QM/MM) models.

The absorption spectra of the WT ErCry4 and four mutants peak at 450 nm with well-resolved vibronic structures. The vibronic structures are the characteristic features of the protein-bound FAD chromophore inside the protein, and these structures will disappear for FAD molecules in solution. The peak at 450 nm can be assigned to $\pi_2 \rightarrow \pi_3$ molecular orbital transition in the isoalloxazine ring of the FAD molecule inside the protein [1].

The photoluminescence (PL) properties of the molecular FAD in buffer solution, WT ErCry4, and its four mutants were characterized using a time-resolved excitation-emission (EE) spectrometer with a <100 ps time resolution, which is developed internally [4]. The EE spectrometer is developed by introducing a passively-stabilized interferometer (TWINS) in the excitation and emission arms of the spectrometer along with a broadband, pulsed supercontinuum source. The introduction of the TWINS interferometer in both arms allows for the separation of even spectrally overlapping incoherent PL from coherent scattering. The acquired emissions from the samples using EE spectrometer are time-resolved and polarization-resolved using a time-correlated single-photon counting detection scheme. The spectral and dynamical information derived from EE spectrometer allows for monitoring the redox state of protein samples. The PL emission from the cryptochrome protein samples is very low. The stacked conformer of FAD molecules is bound to the protein molecules and quenches the fluorescence emission due to the electron transfer from the nearest Trp. The detected weak PL from the protein samples was due to the tiny fraction of free FAD molecules present in the samples, which are their open conformer form. The intensity of the detected PL indicates that more than 97% of FAD molecules are initially bound with cryptochrome protein, and synthesized samples have excellent purity. The developed EE spectrometer has the capability of detecting such shallow fluorescence from the samples. It can also

monitor the photo-induced release of the protein-bound FAD into the surrounded buffer solution due to the photodegradation of protein samples. Only a maximum of 2% increase in free FAD concentration was observed in the protein samples over a 12 hours measurement time. In addition, the higher residual value of the rotation anisotropy data of WT ErCry4 obtained from the EES once again confirms the presence of a perfectly aligned protein-bound chromophore inside the protein. Different from WT ErCry4 and the other three mutant samples, the W_AF mutant in which the Trp_A is replaced with F shows the PL signature of protein-bound FAD, an indication of effective electron transfer to FAD from Trp_A.

The excitation-emission studies of protein samples were an excellent background study of WT ErCry4 and its four mutants before the TA measurements. They gave valuable information about the redox state, protein chromophore binding, and stability of samples prior to TA measurements.

The TA experiments were carried out with 28 fs pump pulses which can be tunable between 250 to 1000 nm, and supercontinuum generated probe pulses that range between 320 and 750 nm [16]. During the experiment, differential transmission $\Delta T / T$ spectra of WT ErCry4, its four mutants, and molecular FAD in buffer solution were recorded for magic angle polarization of pump and probe for delay times up to 1.5 ns. This thesis explains the TA results using a multi-exponential decay model to deduce a minimal set of evolution associated difference spectra (*EADS*). The analysis of experimental results provided evidence for sequential electron transfer along the Trp chain and the formation of radical-pairs within 0.5 ps (Trp_A→FAD), 30 ps (Trp_B→Trp_A), and 140 ps (Trp_C→Trp_B) after photoexcitation, with quantum yields of 1, 0.77, and 0.5, respectively. The experimental results did not provide evidence for fourth electron transfer (Trp_D→Trp_C). However, the yield of the long-lived radical-pairs increased by a factor of two by the presence of the fourth Trp (Trp_D). This suggests that the fourth electron transfer Trp_D→Trp_C is faster than Trp_C→Trp_B, which causes an equilibrium between the associated radical-pairs. Further studies are needed on the functional role of the Trp_D. The TA experiments also revealed vibrational cooling of the optically generated radical-pairs within 3 ps. The studies of W_AF mutant and molecular dynamic simulation provided relevant information about additional intra and intermolecular photo-induced electron transfer that involved adenine moiety of FAD cofactor and two other Trp residues Trp290 and Trp350, which are present at an edge-to-edge distance of 4 Å from adenine and 7.5 Å from flavin moiety respectively.

The deduced electron transfer time from the experiments is slower than the results predicted based on molecular dynamic simulations and Moser-Dutton theory in Xu et al. [154]. But these experimental electron transfer times are found to be faster than simulation results using DFTB based hybrid QM/MM models. This DFTB-based QM/MM model is used for comparison of the experimental results. The simulation results give an atomistic insight into the sequential electron transfer cascade along the Trp chains with transfer times in the 100 ps range. The second ($\text{Trp}_B \rightarrow \text{Trp}_A$) and third ($\text{Trp}_C \rightarrow \text{Trp}_B$) electron transfer times from the simulation are reasonable and have an order-of-magnitude agreement with experimental results. In addition, the simulation could predict the fourth ($\text{Trp}_D \rightarrow \text{Trp}_C$) electron transfer time, which is faster than the third one, so it was inaccessible by the experiment. Unfortunately, the first electron transfer ($\text{Trp}_A \rightarrow \text{FAD}$) could not be calculated using simulation due to the unavailability of reliable DFTB parameters for excited flavin molecules.

The developed and implemented PL and TA spectroscopy techniques, together with DFTB-based QM/MM simulations, provide detailed insight into sequential electron transfer across the Trp chain inside the cryptochrome protein molecules. The spectroscopic results gave the time scale and quantum yield of the first three electron transfer reactions inside the protein, and simulation results could predict the time scale of the fourth electron transfer. The results indicate that the charge separation progress across the Trp chains can be controlled by site-selective mutation of the amino acid structures. These results are important not only for probing and manipulating radical-pair dynamics and charge flow in magnetoreceptive systems but also for transport of spins across this chain.

V.2 Outlook

Even though this thesis has derived the dynamic and yield of charge transfer across Trp, there is no information about the potential energy surface of the electronic state involved in the sequential electron transfer in the ErCry4. This information is critical for quantitative microscopic modeling of charge transfer [188, 222, 223, 323, 324] in cryptochrome, along with time-resolved results derived through this thesis. A broadband two-dimensional electronic spectroscopy (2DES) and time-resolved vibrational spectroscopy (TRVS) [222, 223, 323, 325] can be used to obtain these parameters. The core of

magnetoreception in cryptochrome through the radical-pair mechanism is the light-induced charge transfer and radical-pair formation, and finally, the magnetic sensitivity by coherent interconversion of the spin states of formed radical-pairs. One can sense the quantitative information about coherent intersystem crossing by probing the spin dynamics of the formed radical-pairs. That will prove the cornerstone of the current proposed radical-pair based magnetoreception. The magneto-optical Kerr effect [326] and recently developed pump-push [299] spectroscopy have the competence to confirm the coherent singlet-triplet interconversion. The results gained through this thesis and further extension of optical experiments and theoretical simulation definitely reveal the secrets of magnetoreception through the radical-pair mechanism.

Appendix-A.

A.II

Additional information of Chapter II [4]

A.II.1 TWINS Interferometer

A.II.1.1 TWINS

TWINS (Translating-Wedge-Based Identical Pulses eNcoding System) devices, invented by G. Cerullo and co-workers in 2012, is a common path interferometer that allows to generate highly stable, phase-locked, collinear pulse pairs in the spectral range from the ultraviolet to near-infrared [215]. To create the pulse replicas, the TWINS uses a delay line based on birefringent crystals [216, 217]. Before analyzing the working principle of the TWINS, we briefly recall the main concept of birefringence. When linearly polarized light travels through a uniaxial birefringent material, it experiences a refractive index that depends on its polarization. Specifically, the light component whose polarization is perpendicular to the optical axis of the birefringent crystal experiences the ordinary refractive index (

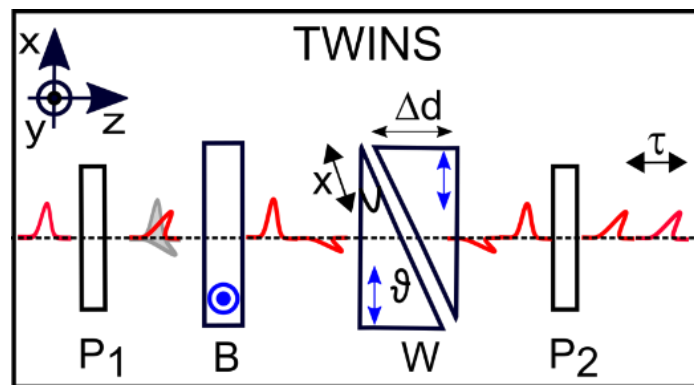


Figure A. II. 1 [4] Schematic representation of TWINS interferometer. The polarizer P_1 is oriented at an angle θ_1 with respect to the x -axis and, and the input electric field polarized according to the angle θ_1 after the polarizer P_1 . The birefringent block B has an optical axis (blue dot) along y -axis induce a fixed time delay between different polarization components of the electric field. The block W consists of a pair of birefringent wedges with an opening angle ϑ that can generate a variable thickness by moving one of the wedges (black arrow). The optical axes of the wedges are along x -axis (blue arrow). The variable thickness generates a variable time delay τ between the polarization components of the electric field. Finally, the polarizer P_2 projects the two electric field replicas into a common polarization according to the angle θ_2 .

$n_o(\omega)$), and the parallel polarization component experiences the extraordinary ($n_e(\omega)$) refractive

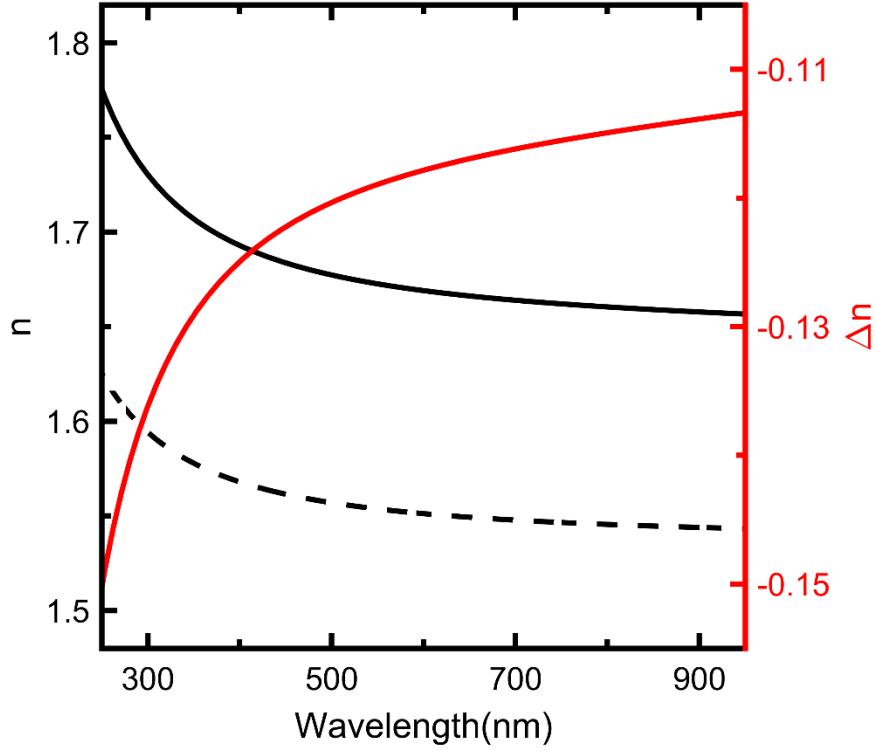


Figure A. II. 2 Ordinary (n_o solid black line) and extra ordinary (n_e dotted black line) refractive index of alpha BBO (α -BBO) crystal. The birefringence is shown in the red line. For α -BBO, $n_o > n_e$ [15].

index, where ω is angular optical frequency. This difference in refractive index causes a relative time

delay, $\frac{n_o(\omega) - n_e(\omega)}{c_0} d$ between the two polarization components, which depends on the thickness d

of the material and the speed of light in vacuum c_0 . By changing the thickness of the birefringent material, a frequency-dependent relative delay between the two polarization components of the passing light can be introduced. The schematic diagram of a TWINS interferometer is shown in Figure A. II. 1. The TWINS interferometer consists of two polarizers P_1 and P_2 and two main birefringence blocks made of alpha barium borate (α -BBO), one plate with fixed thickness B and one with variable thickness W . The latter is made up of two wedges. α -BBO crystals are uniaxial negative birefringence material. In

a negative uniaxial birefringence crystal, the extraordinary ray's phase velocity, $v_{pe} = \frac{c}{n_e}$, is greater

than that of an ordinary ray, $v_{po} = \frac{c}{n_o}$. The refractive indexes n_o and n_e of α -BBO crystal are indicated

in the solid and dotted black line in Figure A. II. 2. The birefringence Δn of the crystal is plotted as a red curve in Figure A. II. 2 for the wavelength range 400 to 1000 nm [15].

Consider a monochromatic plane wave $\vec{E}_{in}(z,t) = \vec{E}_{in} \exp(-i\omega t + ik_0 z)$ incident on a TWINS with amplitude $\vec{E}_{in} = (E_{in,x}, E_{in,y}, 0)$, frequency ω and k vector $\vec{k} = k_0 e \vec{z}$. The incident field $\vec{E}_{in}(z,t)$ passes initially through the polarizer P_1 , which is oriented at an angle θ_1 with respect to the x -axis. It then propagates through the birefringent plate B (Figure A. II. 1), an $\alpha - BBO$ crystal with the optical axis along the y direction. The two polarization components in the incident electric field experience n_o and n_e refractive index in block B according to its propagation direction and that causes a constant delay between them. The field then passes through a second birefringent block W with variable thickness. The block W consists of two $\alpha - BBO$ wedges and the optical axes of the wedges are along the x -axis. One of the wedges is placed in a translation stage so that the movement of the translation stage varies the effective thickness in the light path. The geometry of the wedge is shown in Figure A. II. 3. The polarization component of transmitting electric field that experiences n_o refractive index in block B transmits with a phase velocity v_{pe} in block W , and it advances the other component after the wedge, as shown in Figure A. II. 1. Finally, before the field exits from the TWINS, it passes the second polarizer P_2 , which is oriented at an angle to the x -axis. The interference of the pulse replicas after the TWINS interferometer is ensured by the second polarizer P_2 by projecting the two time delayed pulses onto the same polarization states.

Here Jones formalism [327] is used to understand the effect of different optical components on the amplitude and phase of the transmitted light \vec{E}_T after the TWINS in parallel approximation formalism. The possible components of the field in the propagation direction are ignored here, and the amplitude of the incident field becomes $\vec{E}_{in} = \begin{pmatrix} E_{in,x} \\ E_{in,y} \end{pmatrix}$. The Jones matrix for a linear polarizer can be written as,

$$P_i = \begin{pmatrix} \cos^2(\theta_i) & \sin(\theta_i)\cos(\theta_i) \\ \sin(\theta_i)\cos(\theta_i) & \sin^2(\theta_i) \end{pmatrix} = \begin{pmatrix} \cos(\theta_i) \\ \sin(\theta_i) \end{pmatrix} \begin{pmatrix} \cos(\theta_i) & \sin(\theta_i) \end{pmatrix}, i = 1, 2.. \quad (\text{A.II.1})$$

In block B , the y -axis component of the passing electric field experiences a refractive index n_e and the x -axis component propagates with a phase velocity, v_{po} . In W the x and y -axis components of the propagating electric fields have phase velocities v_{pe} and v_{po} since the optical axes of the wedges are oriented along the x -axis. The Jones formalism for B and W crystals are given in Equation (A.II.2) by considering their thicknesses as d , and $d + \Delta d$, respectively,

$$\begin{aligned}
B &= \begin{pmatrix} e^{ik_0 n_o d} & 0 \\ 0 & e^{ik_0 n_e d} \end{pmatrix} \\
W &= \begin{pmatrix} e^{ik_0 n_e (d+\Delta d)} & 0 \\ 0 & e^{ik_0 n_o (d+\Delta d)} \end{pmatrix}.
\end{aligned} \tag{A.II.2}$$

The reflection losses in the entrance and exit surfaces of birefringent materials are ignored in the case of an ideal TWINS. If the free-space propagation is also neglected, the electric field after the TWINS

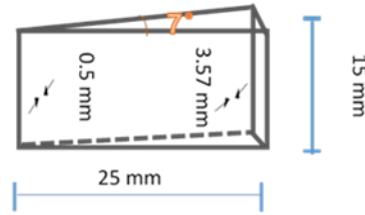


Figure A. II. 3 Geometry of α -BBO wedge.

can be described as, $\vec{E}_T = P_2 \cdot W \cdot B \cdot P_1 \cdot \vec{E}_{in}$:

$$\vec{E}_T = P_2 \cdot W \cdot B \cdot P_1 \cdot \vec{E}_{in} \tag{A.II.3}$$

$$\vec{E}_T = \begin{pmatrix} \cos(\theta_2) \\ \sin(\theta_2) \end{pmatrix} \cdot \left(\cot(\theta_2) \cot(\theta_1) e^{ik_0[(n_e - n_o)\Delta d]} + 1 \right) \cdot e^{ik_0 n_o (d+\Delta d) + ik_0 n_e d} \cdot \sin(\theta_1) \sin(\theta_2) \cdot \left(\cos(\theta_1) E_{in,x} + \sin(\theta_1) E_{in,y} \right) \tag{A.II.4}$$

There are five different terms present in \vec{E}_T . The first term determines the polarization of the exiting field from the TWINS, and the second polarizer, P_2 controls it. The next term is the most interesting one, representing the splitting of the incident electric field into two replicas and its amplitude is given by the orientation angles of polarizers P_1 and P_2 . The maximum amplitude ratio for a perfect TWINS is one, which leads to the condition $\cot(\theta_2) \cot(\theta_1) = 1, \cot(\theta_2) = \tan(\theta_1), \theta_1 + \theta_2 = \frac{\pi}{2}$. The third term is a constant phase acquired on both polarization components of electric field while passing through the TWINS. Finally, the last term sets the amplitude of the exiting light from the TWINS. It is given by the components of incoming electric field which are parallel to the polarizer P_1 . The exiting field's throughput is fixed by the term $\sin(\theta_1) \sin(\theta_2)$ which depends on the angles of the two polarizers P_1 and P_2 . In the case of an ideal TWINS, this throughput is maximized when

$\sin(\theta_1)\sin(\theta_2) = \sin\left(\frac{\pi}{2} - \theta_2\right)\sin(\theta_2) = \sin(2\theta_2) = \frac{1}{2}$, i.e. $\theta_1 = \theta_2 = \frac{\pi}{4}$ are the optimum TWINS polarizer angles. Then the Equation (A.II.4) becomes,

$$\begin{aligned}\vec{E}_T &= \left(e^{ik_0\Delta n\Delta d} + 1\right) \frac{1}{4} \begin{pmatrix} 1 \\ 1 \end{pmatrix} e^{ik_0n_o(d+\Delta d)+ik_0n_e d} \left(E_{in,x} + E_{in,y}\right) \\ \vec{E}_T &= \left(e^{ik_0\Delta n\sin(\mathcal{G})x} + 1\right) \vec{E}_0,\end{aligned}\tag{A.II.5}$$

where $\Delta n = (n_e - n_o)$ and from Figure A. II. 1 $\Delta d = \sin(\mathcal{G})x$, \mathcal{G} is wedge opening angle. A frequency and position dependent phase shift $\Delta\varphi(\omega, x)$ is experienced between orthogonal polarization components of the ultrashort pulses while traveling through the TWINS,

$$\Delta\varphi(\omega, x) = \frac{\omega}{c_0} \Delta n \sin(\mathcal{G})x,\tag{A.II.6}$$

with wave number $\tilde{k} = k_0\Delta n(\omega)\sin \mathcal{G}x$. This splits the incident field into two pulse replica with equal amplitude \vec{E}_0 . In an ideal TWINS the phase shift $\Delta\varphi$ depends only on the wedge position x . However practically the TWINS are not perfect. The polarizer's angles θ_1 and θ_2 may not be optimum in real situations, creating pulse replicas of the incident light with unequal amplitude E_0 and cE_0 , $c = \cot(\theta_1)\cot(\theta_2)$. Moreover, the translation stage for the wedge may be aligned at a slight angle to the optical axis of the block W. In addition to that, the block B also may not be perfectly orthogonal to the incident light. Due to all these reasons an off axis transmission of light through the birefringent materials [328] creates a thickness independent phase offset $\tilde{\varphi}(\omega)$ in the transmitted light. Then the Equation (A.II.6) becomes,

$$\Delta\varphi(x, \omega) = \Delta\tilde{\varphi}(\omega) + \frac{\omega}{c_0} \Delta n \sin(\mathcal{G})x.\tag{A.II.7}$$

The amplitude \vec{E}_T of the electric field after the TWINS interferometer is,

$$\begin{aligned}\vec{E}_T &= \left(1 + \cot(\theta_1)\cot(\theta_2)e^{i\left(\Delta\tilde{\varphi}(\omega) + \frac{\omega}{c_0}\Delta n\sin(\mathcal{G})x\right)}\right) \begin{pmatrix} \cos(\theta_2) \\ \sin(\theta_2) \end{pmatrix} e^{ik_0n_o(d+\Delta d)+ik_0n_e d} \left(\cos(\theta_1)E_{in,x} + \sin(\theta_1)E_{in,y}\right) \\ \vec{E}_T &= \left(1 + ce^{i\Delta\varphi(x, \omega)}\right) \vec{E}_0\end{aligned}\tag{A.II.8}$$

A real TWINS interferometer creates two-pulse replicas of the incident light with amplitude \vec{E}_0 and $c\vec{E}_0$. The variable time delay between the pulses is then,

$$\tau = \frac{\Delta n(\omega) \sin(\vartheta)x}{c_0}. \quad (\text{A.II.9})$$

x is the positioning of the wedges. So in our real TWINS interferometer, the two linear polarizers (P_1 and P_2 , M42 \times 0.75 # 52-57 Edmond optics) are oriented at an angle of 45° with respect to the optical axis. The B block has a thickness of 3mm. Each wedge in block W has a dimension of $25 \times 15 \text{ mm}$ and thickness from 0.5 to 3.5 mm. The wedge has an opening angle, $\vartheta = 7^\circ$. If the wedge moved for 1 mm,

then it produces a time delay, $\tau = \frac{(1.5552 - 1.6748) \sin(7^\circ) 1 \text{ mm}}{c_0} = -48.6 \text{ fs}$ between the pulse replicas

at 525 nm. For a wedge length of 25 mm, the TWINS can generate a maximum delay of 1.2 ps between the pulse pairs for light at a wavelength of 525 nm.

The TWINS interferometer has many advantages over any other conventional interferometer. The relative time delay between two pulse replicas is exceptionally stable, locked, and reproducible since both pulse pair follow the same optical path. It is easy to produce even minimal time delays with precision between the pulse pairs using TWINS. In addition to that, TWINS interferometers are unresponsive to any mechanical fluctuations [6, 216]. These advantages make the TWINS interferometer suitable for different linear and nonlinear experiments such as Fourier transform-based absorbance [6, 216], excitation and emission spectroscopy [208, 217], time-and frequency-resolved fluorescence spectroscopy [218], hyper-spectral imaging [208, 219], pump-probe [6, 216, 220], two-dimensional electronic spectroscopy [4, 6, 133, 217, 220-223, 252, 270], and stimulated Raman Scattering microscopy [224].

A.II.1.2 TWINS Calibration

It is necessary to calibrate the TWINS interferometer to explore its advantages. The calibration process finds the relation between the TWINS wave number axis \tilde{k} and optical frequency ω . In this procedure, light from supercontinuum sources is getting through the TWINS interferometer, and a spectrometer records the interferogram between two pulse replicas after the TWINS, at different stage positions [4, 217, 221]. These results in a spectrally resolved linear autocorrelation of pulse replicas from the TWINS, as shown in Figure A. II. 4 (b). The intensity of the electric field after the TWINS for a position x can be found from Equation (A.II.8) as,

$$I(x, \omega) = \left| 1 + c e^{i\Delta\varphi(x, \omega)} \right|^2 \left| \vec{E}_0 \right|^2$$

$$I(x, \omega) = (1 + c^2)I_0 + 2c \cos(\Delta\tilde{\varphi}(\omega) + i\tilde{k}(\omega)x)I_0, \quad (\text{A.II.10})$$

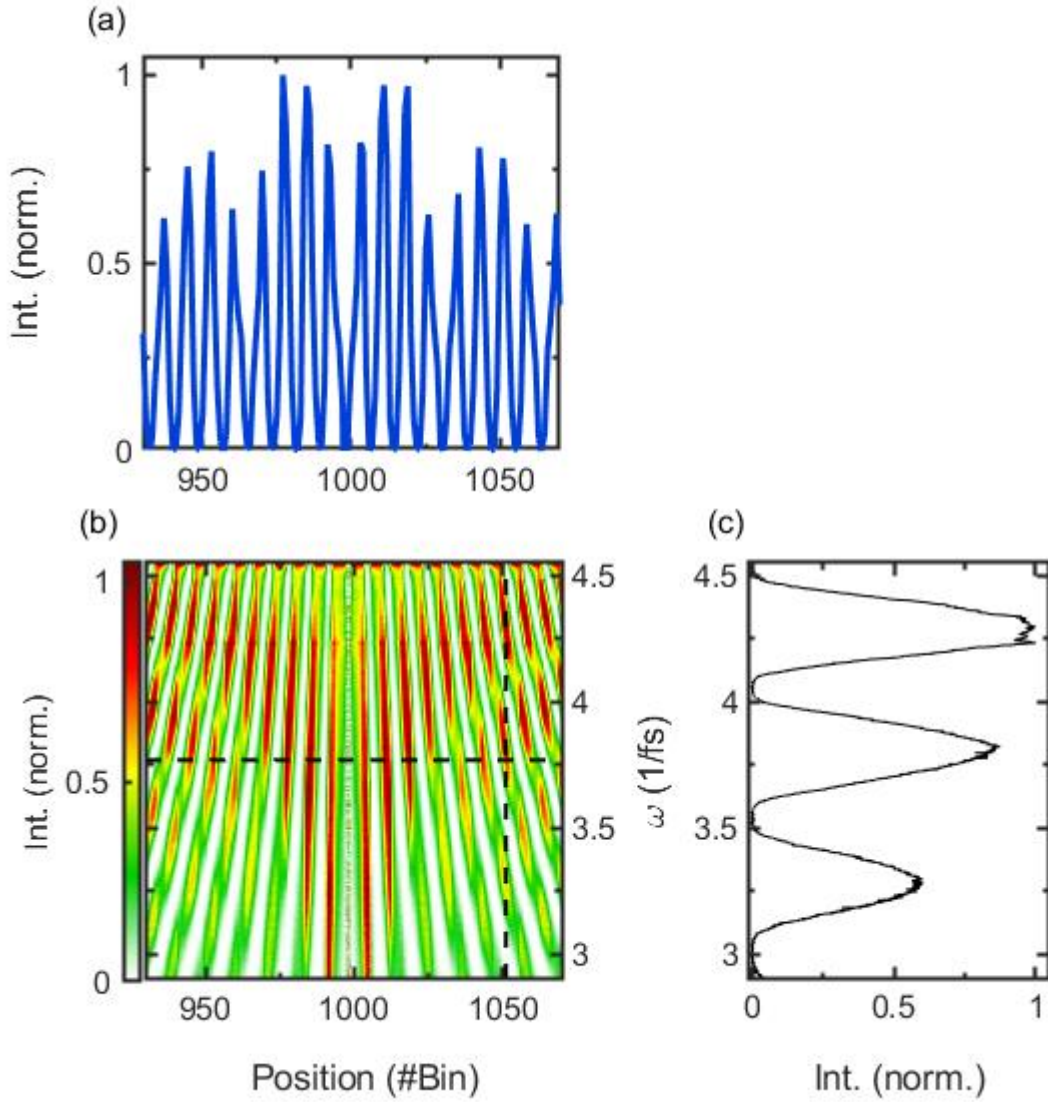


Figure A. II. 4 TWINS calibration. (b) A two-dimensional linear autocorrelation as a function position (bin) and frequency (ω) of supercontinuum white light sources were recorded during TWINS calibration. (a) Interferogram for $\omega = 3.77(\frac{1}{fs})$ (dashed horizontal black line in (b)) and (c) spectral interferogram at bin position 1050 (dashed vertical line in (b)).

where $I_0(\omega) = |\vec{E}_0|^2$. The first two terms in Equation (A.II.10) are constant, contributing to the background of the interferogram recorded by the spectrometer. Then the isolated background-free

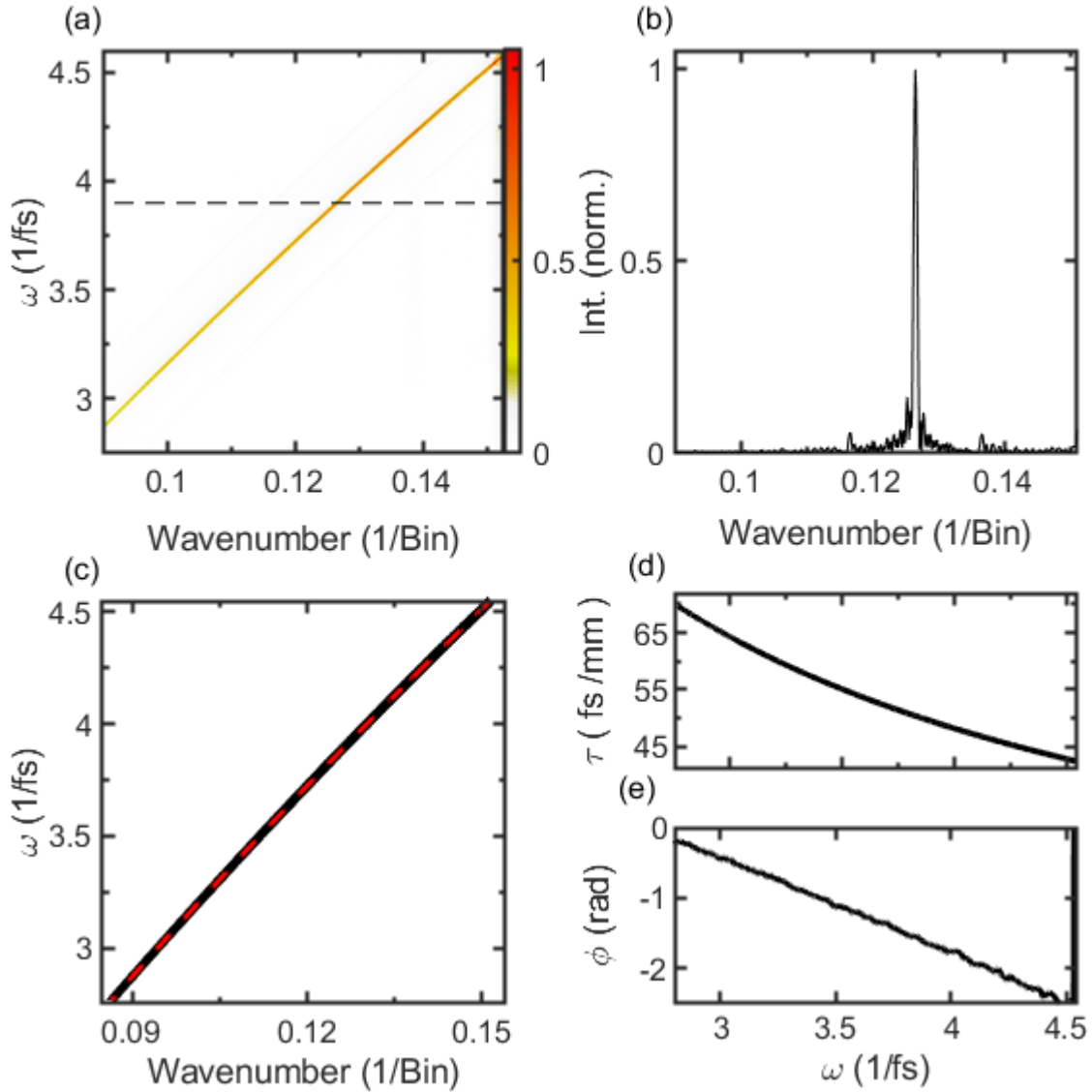


Figure A. II. 5 A 2D map as a function of spatial frequency (1/bin) and frequency (ω) calculated from Fourier transform of Figure A. II. 4 (b) along with positions. (b) Crosscut of (a) at frequency $\omega = 3.85$ ($\frac{1}{fs}$) (horizontal dashed black line) gives peaks at $\tilde{k}(\omega)$ in wavenumber axis. (c) The black solid line curve obtained by collecting $\tilde{k}(\omega)$ for all ω from (a). The red dotted line is the calibration curve $k^c(\omega)$. (d) The delay τ induced for each optical frequency ω for one millimeter movement of TWINS stage. (e) The position independent constant phase ϕ induced by TWINS interferometer for each ω due to the off axis transmission of light through the birefringence material.

fringes are,

$$I^c(x, \omega) = 2c \cos(\Delta\tilde{\varphi}(\omega) + i\tilde{k}(\omega)x)I_0(\omega). \quad (\text{A.II.11})$$

The crosscuts of Figure A. II. 4(b) at $\omega = 3.77(1/fs)$, and $x = 1065$ is shown in Figure A. II. 4 (a) ($I^c(x, \omega = 3.77)$) and 4 (c) ($I^c(x = 1065, \omega)$) respectively. The $I^c(x, \omega)$ is modulating according to the phase $\Delta\varphi$ induced in the each position, and it has a period of oscillation $\frac{2\pi}{\tau(x, \omega)}$. The contrast of the

interference fringes is $C = 1 - \frac{I_{\min}}{I_{\max}}$, I_{\min} and I_{\max} are minimum and maximum intensities of $I^c(x, \omega)$.

Here TWINS has a contrast of greater than 99.5% (Figure A. II. 4 (a) and (c)). The Fourier transform of fringes, $\tilde{I}^c(k, \omega)$ along x (Figure A. II. 5 (a)) is giving peaks at $\tilde{k}(\omega)$ in positive wave number axis for each ω as shown in Figure A. II. 5 (b) ($\omega = 3.85(1/fs)$),

$$\begin{aligned}\tilde{I}^c(k, \omega) &= \int_{-\infty}^{\infty} I^c(x, \omega) e^{-ikx} dx = \int_{-\infty}^{\infty} 2c \cos(\Delta\tilde{\varphi}(\omega) + i\tilde{k}(\omega)x) I_0(\omega) e^{-ikx} dx, \\ \tilde{I}^c(k, \omega) &= 2ce^{i\Delta\tilde{\varphi}(\omega)} \int_{-\infty}^{\infty} (e^{i\tilde{k}(\omega)x} + e^{-i\tilde{k}(\omega)x}) e^{-ikx} dx, \\ \tilde{I}^c(k, \omega) &= 2ce^{i\Delta\tilde{\varphi}(\omega)} \begin{pmatrix} \delta(k - \tilde{k}(\omega)) \\ +\delta(k + \tilde{k}(\omega)) \end{pmatrix}, \\ \tilde{I}^c(k, \omega) &= 2ce^{i\Delta\tilde{\varphi}(\omega)} \delta(k - \tilde{k}(\omega)), \tilde{k}(\omega) > 0.\end{aligned}\tag{A.II.12}$$

By collecting peaks position in $\tilde{k}(\omega)$ for all incidents ω , a calibration curve $\omega^c(k)$

$$\omega^c(k) = \omega^1 + \omega^2 \tilde{k}(\omega) + \omega^3 \tilde{k}(\omega)^2 + \omega^4 \tilde{k}(\omega)^3 + \omega^5 \tilde{k}(\omega)^4\tag{A.II.13}$$

and its inverse, $k^c(\omega)$, (Figure A. II. 5 (c)) can be obtained to calibrate the frequency axis of TWINS.

The wavenumber axis $\tilde{k}(\omega)$ can be related to $k^c(\omega)$ using the step size δx of the translation stage in

calibration scan as $2\pi\tilde{k}(\omega) = \frac{2\pi}{\delta x} k^c(\omega)$. A time delay $\tau = 50fs$ induced by TWINS interferometer at

$\omega = 3.86(1/fs)$ for 1 mm movement of translation stage. For all other input ω the TWINS induced τ

is shown in Figure A. II. 5 (d). Moreover, the absolute phase $\Delta\tilde{\varphi}(\omega)$ (Figure A. II. 5 (e)) and amplitude

cI_0 can be extracted from $\tilde{I}^c(k, \omega)$. The relative amplitude c of each replica is;

$$c = \frac{1}{2} (1 \pm \sqrt{1 - C}).\tag{A.II.14}$$

The two side peaks in Figure A. II. 5 (b) are due to the inaccurate movement of the translation stage that causes a mismatch between TWINS' expected positions and actual positions. This inaccuracy in position causes a frequency modulation in the interferogram and results in side peaks in Fourier transform, as seen in Figure A. II. 5 (b). This position mismatch can be calculated from the calibration scan. For that $\tilde{I}^c(k, \omega)$ with and without side peaks simulated for all ω Fourier transformed them back to the interferogram. The zero-crossing positions of both interferogram are noted separately, and the difference between these positions gives the mismatch between expected and actual positions (Figure A. II. 6).

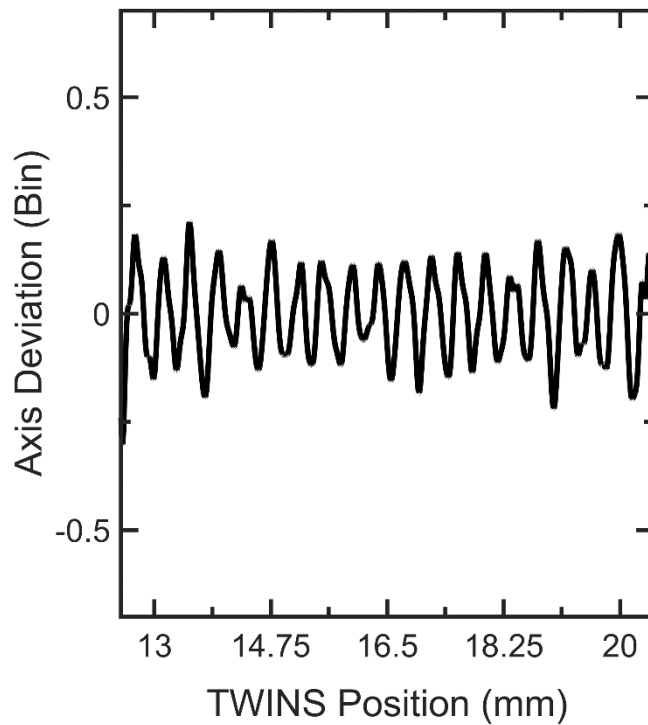


Figure A. II. 6 TWINS position mismatch. The deviations in the TWINS position due to the inaccurate movement of the translation stage.

A.II.1.3 TWINS Spectrometer

TWINS interferometer and the Fourier spectroscopy can be combined and then can form a Fourier transform spectrometer in visible to infrared spectral range with high spectral resolution, frequency accuracy and large through put [4, 6, 216, 217]. For that a photodiode is placed after the TWINS and that records $\bar{I}(x)$, intensity of the transmitted light from TWINS for each of its position, a first-order field autocorrelation of incident light. The Fourier transform of $\bar{I}(x)$ gives the intensity spectrum,

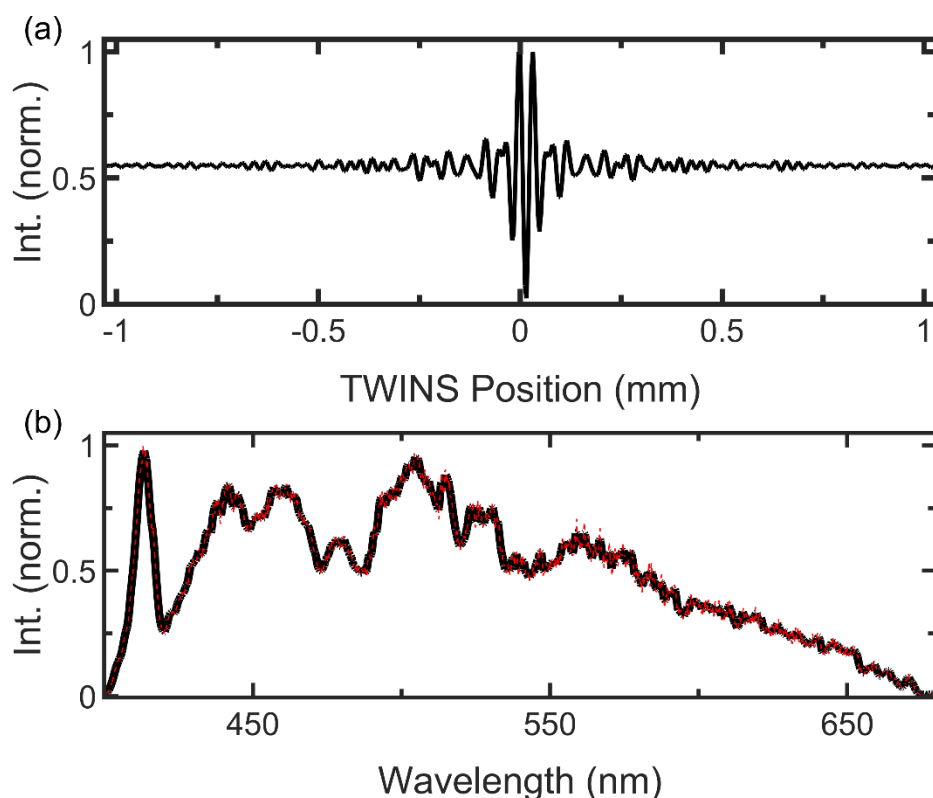


Figure A. II. 7 TWINS spectrometer. (a) A first order field autocorrelation $\bar{I}(x)$ of white light recorded using a photodiode by placing detector behind the TWINS and moving the TWINS stage for 8 mm. (b) Retrieved white light spectrum (dotted red line) by Fourier transforming (a) into wavenumber axis k and transforming k into frequency ω using calibration curve $k^c(\omega)$. The spectrum of the white light recorded using spectrometer shown in the black dotted line.

$I_0(\omega)$ of the incident light. According to the Plancherel's theorem $\bar{I}(x)$ is a spectral integration of $I(x, \omega)$ and that can be written as,

$$\begin{aligned} \bar{I}(x) &= I^{BG} + I'(x) \\ \bar{I}(x) &= (1 + c^2) \int_{-\infty}^{\infty} I_0(\omega) d\omega + 2c \int_{-\infty}^{\infty} \cos(\Delta\tilde{\varphi}(\omega) + i\tilde{k}(\omega)x) I_0 d\omega. \end{aligned} \quad (\text{A.II.15})$$

The first term in Equation (A.II.15) is a background and that should be subtracted during data analysis.

The Fourier transform of interference term $I'(x)$ gives positive side bands ($k > 0$) spectrum $\tilde{I}(k)$.

$$\begin{aligned}\bar{I}(x) &= I^{BG} + I'(x) \\ \bar{I}(x) &= (1 + c^2) \int_{-\infty}^{\infty} I_0(\omega) d\omega + 2c \int_{-\infty}^{\infty} \cos(\Delta\tilde{\varphi}(\omega) + ik(\omega)x) I_0 d\omega.\end{aligned}\tag{A.II.16}$$

The incident spectrum $I_0(\omega)$ can be obtained by converting the k axis into frequency axis (ω) using the calibration curve $k^c(\omega)$,

$$I_0(\omega) = \frac{1}{c} \tilde{I}(k^c(\omega)) \frac{\delta k^c}{\delta \omega}(\omega) e^{-i\Delta\tilde{\varphi}(\omega)}.\tag{A.II.17}$$

The transformation to wavelength axis [234] gives the desired spectrum of incident light;

$$I_0(\lambda) = \frac{2\pi c_0}{\lambda^2} I_0\left(\frac{2\pi c_0}{\lambda}\right)\tag{A.II.18}$$

The white light spectrum recorded using TWINS interferometer is shown in Figure A. II. 7 in dotted red line.

The resolution of the spectrometer can be varied by adjusting the wedge movement distance in the TWINS. It is clear that from the Figure A. II. 5 (d), TWINS interferometer induced maximum delay

$\tau^{\max} \approx 50 \text{ fs}$ for 1 mm movement in the frequency range $3 - 4.59 \left(\frac{1}{\text{fs}}\right)$ (400-700 nm). This gives an

average spectral resolution of $\Delta\lambda = \frac{\lambda^2}{c\tau^{\max}} \approx 6.5 \text{ nm}$ for this spectral range [6, 216, 218]. The step size

δx for the translation stage is chosen in such a way, that satisfies Nyquist sampling theorem;

$$B < \frac{1}{2\tau^{\max} \delta x},\tag{A.II.19}$$

to record at least two data points per in the spatial oscillation period, where B is the maximum spectral frequency present in the incident light. By considering our spectral range 400-700 nm a maximum step size of 10 μm can be chosen for TWINS translation stage.

A.II.2 BI-TWINS

A.II.2.1 BI-TWINS Signal

As discussed in the earlier section, two TWINS (BI-TWINS) interferometers were used in our experimental setup. It was assumed that the excitation light $I_0(\omega)$ after passing through the excitation TWINS, may either coherently scatter towards the detector or may be absorbed by the sample and emit the incoherent photoluminescence (PL). The coherent spectrum $I_0^{sc}(\omega)$ can be described as;

$$I_0^{sc}(\omega) = t_s(\omega)I_0(\omega) \quad (\text{A.II.20})$$

Then the incoherent emission from the sample can be described using the absorption spectrum $\alpha(\omega)$, a normalized emission spectrum $I_{FL}(\omega)$ and the quantum efficiency QE of the sample,

$$I_0^{fl}(\omega_{ex}, \omega_d) = QE \cdot I_{FL}(\omega_d) \alpha(\omega_{ex}) I_0(\omega_{ex}). \quad (\text{A.II.21})$$

These two kinds of emissions can be identified using the BI-TWINS setup. Here the excitation and detection TWINS have their own calibration curve $k_{ex/det}^d(\omega)$ and phase offset $\Delta\tilde{\varphi}_{ex/det}(\omega)$ and amplitude ratios $c_{ex/det}$ (see section A.II.1.2 TWINS Calibration). During the experiment, the excitation TWINS creates spectrum $I_{ex}(x_{ex}, \omega_{ex})$ when the white light $I_0(\omega)$ passes through it (Equation (A.II.10)) and the light interact with the sample. Then the sample either coherently scatters the excitation spectrum to the detection arm,

$$I_{ex}^{sc}(x_{ex}, \omega_{det}) = t_s(\omega_{det}) \cdot I_{ex}(x_{ex}, \omega_{det}) \quad (\text{A.II.22})$$

or emits incoherently,

$$I_{ex}^{fl}(x_{ex}, \omega_{det}) = QE \cdot I_{FL}(\omega_{det}) \int_0^{\infty} \alpha(\omega_{ex}) I_{ex}(x_{ex}, \omega_{det}) d\omega_{ex}. \quad (\text{A.II.23})$$

The emitted light passes through the detection TWINS and is recorded with temporally and spectrally integrating photodiode. An EE interferogram $\bar{I}_d(x_{ex}, x_{det})$ is recorded using the photodiode and by scanning both excitation (x_{ex}) and detection (x_{det}) TWINS motor positions. The recorded EE interferogram $\bar{I}_d(x_{ex}, x_{det})$ can be calculated from $I_{ex}^{sc}(x_{ex}, \omega_{det})$ using Equation (A.II.10) (section A.II.1.2) and integrating over all frequencies (Equation (A.II.15)),

$$\bar{I}_d^{sc/fl}(x_{ex}, x_{det}) = I_{BG}^{sc/fl} + I_{det}^{sc/fl}(x_{det}) + I_{ex}^{sc/fl}(x_{ex}) + I^{sc/fl}(x_{ex}, x_{det}). \quad (\text{A.II.24})$$

The first term $I_{BG}^{sc/fl}$ is a constant background created by excitation and detection TWINS.

$$\bar{I}_d^{sc/fl}(x_{ex}, x_{det}) = I_{BG}^{sc/fl} + I_{det}^{sc/fl}(x_{det}) + I_{ex}^{sc/fl}(x_{ex}) + I^{sc/fl}(x_{ex}, x_{det}). \quad (\text{A.II.25})$$

The second term $I_{det}^{sc/fl}(x_{det})$ only depends on the detection TWINS position, and it is the field autocorrelation of the emitted light $I_0^{sc/fl}(\omega_{det})$ using the detection TWINS:

$$I_{det}^{sc/fl}(x_{det}) = 2c_{det}(1 + c_{ex}^2) \int_{-\infty}^{\infty} \cos(\Delta\varphi_{det}(x_{det}, \omega_{det})) I_0^{sc/fl}(\omega_{det}) d\omega_{det}. \quad (\text{A.II.26})$$

The Equation (A.II.26) appears as a vertical stripe in the EE interferogram (simulated: Figure II. 4 (c) and (d), Figure A. II. 8 (a), measured: Figure II. 5 (a)). Equation (A.II.24) also contains a third term, $I_{ex}^{sc/fl}(x_{ex})$, which depends only on excitation TWINS position, x_{ex} . The x_{ex} position dependency appears as horizontal stripes in the EE interferogram (simulated: Figure II. 4 (c) and (d), Figure A. II. 8 (a), measured: Figure II. 5 (a)).

$$I_{ex}^{fl}(x_{ex}) = 2c_{ex}(1 + c_{det}^2) \int_{-\infty}^{\infty} \cos(\Delta\varphi_{ex}(x_{ex}, \omega_{ex})) I^{PLE}(\omega_{ex}) d\omega_{ex}. \quad (\text{A.II.27})$$

The Equation (A.II.27) indicates the photoluminescence excitation (PLE) spectrum of the sample, where $I^{PLE}(\omega_{ex}) = \alpha(\omega_{ex}) I_0(\omega_{ex}) QE \int_{-\infty}^{\infty} I_{FL}(\omega_{det}) d\omega_{det}$ (simulated: Figure II. 4 (d), Figure A. II. 8 (a), measured: Figure II. 5 (a)). Here $I^{PLE}(\omega_{ex})$ is generated by the remaining white light being after absorbed by the sample, the output of the excitation TWINS. The scatter component also creates a similar component I_{ex}^{sc} ,

$$I_{ex}^{sc} = 2c_{ex}(1 + c_{det}^2) \int_{-\infty}^{\infty} \cos(\Delta\varphi_{ex}(x_{ex}, \omega_{ex})) I_0^{sc}(\omega_{ex}) d\omega_{ex}. \quad (\text{A.II.28})$$

It is clear that from Equations (A.II.26) and (A.II.27), $I_{det}^{sc/fl}(x_{det})$ and $I_{ex}^{fl}(x_{ex})$ can be measured individually by placing a single TWINS in the detection, or excitation arm respectively.

The fourth term $I^{sc/fl}(x_{ex}, x_{det})$ has a dependency on excitation and detection TWINS, and so it is very important and interesting. Moreover, the shape of the fourth component for coherent and incoherent emission is different in the map. In the case of incoherent emissions, the fourth component can be

written as the product of the autocorrelation components ($I_{\text{det}}^{\text{fl}}(x_{\text{det}})$ and $I_{\text{ex}}^{\text{fl}}(x_{\text{ex}})$) measured by the excitation and detection TWINS, separately which is normalized by the constant background $I_{\text{BG}}^{\text{fl}}$,

$$I^{\text{fl}}(x_{\text{ex}}, x_{\text{det}}) = \frac{1}{I_{\text{BG}}^{\text{fl}}} I_{\text{det}}^{\text{fl}}(x_{\text{det}}) I_{\text{ex}}^{\text{fl}}(x_{\text{ex}}). \quad (\text{A.II.29})$$

$I^{\text{fl}}(x_{\text{ex}}, x_{\text{det}})$ creates a checkerboard pattern in the center of the EE interferogram (simulated: Figure II. 4 (d), Figure A. II. 8 (a) and (b), measured: Figure II. 5 (a), (c), and (d), Figure II. 7 (a) and (b)). The size of the pattern in the map is determined by the envelope of the autocorrelation by both TWINS. A two-dimensional FT of $I^{\text{fl}}(x_{\text{ex}}, x_{\text{det}})$ and transformation of the corresponding wavenumber axis using Equations(A.II.17) and (A.II.18) gives incoherent EE spectrum $I^{\text{fl}}(x_{\text{ex}}, x_{\text{det}})$. The retrieved $I_0^{\text{fl}}(\omega_{\text{ex}}, \omega_{\text{det}})$ is the product of the fluorescence spectrum along the detection axis and its PLE spectrum along the excitation axis. This spectrum can be transformed to the wavelength domain, $I_0^{\text{fl}}(\lambda_{\text{ex}}, \lambda_{\text{det}})$ using Equation (A.II.18).

The coherent contribution of the fourth component can be written as;

$$I^{\text{sc}}(x_{\text{ex}}, x_{\text{det}}) = 4c_{\text{ex}}c_{\text{det}} \int_{-\infty}^{\infty} \cos(\Delta\varphi_{\text{ex}}(x_{\text{ex}})) \cos(\Delta\varphi_{\text{d}}(x_{\text{det}})) I_0^{\text{sc}} d\omega_{\text{det}}. \quad (\text{A.II.30})$$

Here $\Delta\varphi_{\text{ex}}$, $\Delta\varphi_{\text{det}}$, and I_0^{sc} are dependent on ω_{det} , but for clarity, it is omitted here. In the EE map, $I^{\text{sc}}(x_{\text{ex}}, x_{\text{det}})$ causes diagonal stripes-like patterns (simulated: Figure II. 4 (c), Figure A. II. 8 (a), measured: Figure II. 5 (c)). In the case of monochromatic waves, the coherent map is characterized by a checkerboard pattern in the entire map. Since a broadband source is used, there will be a superposition of checkerboard pattern with a different periodicity which will constructively interfere along the diagonals and result in diagonal stripes. These diagonals do not overlap with incoherent PL except in the center of the map (measured: Figure II. 5(c), simulated: Figure A. II. 8 (a) and (b)). The stripe-like pattern along the diagonal of the EE map is the exclusive property of the coherent emission that can be used to identify and separate coherent and incoherent signal contribution in the BI-TWINS. We can rewrite $I^{\text{sc}}(x_{\text{ex}}, x_{\text{det}})$:

$$I^{\text{sc}}(x_{\text{ex}}, x_{\text{det}}) = I_+^{\text{sc}}(x_{\text{ex}}, x_{\text{det}}) + I_-^{\text{sc}}(x_{\text{ex}}, x_{\text{det}}) \quad (\text{A.II.31})$$

There are two similar components $I_+^{\text{sc}}(x_{\text{ex}}, x_{\text{det}})$ (falling diagonal) and $I_-^{\text{sc}}(x_{\text{ex}}, x_{\text{det}})$ (rising diagonal) with an interference pattern that emerges along the map diagonals. Then,

$$I_{\pm}^{sc}(x_{ex}, x_{det}) = 2c_{ex}c_{det} \int_{-\infty}^{\infty} \cos(\Delta\tilde{\varphi}_{ex} \pm \Delta\tilde{\varphi}_{det} + k_{ex}^c x_{ex} \pm k_{det}^c x_{det}) I_0^{sc} d\omega_{det} \quad (\text{A.II.32})$$

By knowing the calibration curves k_{ex}^c and k_{det}^c , we can determine the coherent light scattering spectrum $I_0^{sc}(\omega)$ from the Fourier transform of Equation (A.II.32). The retrieval of the scattering spectrum $I_0^{sc}(\omega)$ and separation of both components are described in detail in the next section.

A.II.2.2 Separation Method

As discussed in the previous section, the BI-TWINS map $I(x_{ex}, x_{det})$ consists of unique features of coherent (diagonal) and incoherent (center) emission (Figure A. II. 8 (a) and (b)).

$$I(x_{ex}, x_{det}) = I^{sc}(x_{ex}, x_{det}) + I^fl(x_{ex}, x_{det}) \quad (\text{A.II.33})$$

To separate $I(x_{ex}, x_{det})$ and $I^fl(x_{ex}, x_{det})$, firstly subtract the constant background (equation (A.II.25)), vertical (equation (A.II.26)), and horizontal (equation (A.II.27)) components from the BI-TWINS map (Figure A. II. 8 (a)). The remaining diagonals are basically constant along the corresponding diagonal and they should only depend on the distance between rising and falling diagonals, i.e. $I_{\pm}^{sc}(x_{ex}, x_{det}) = I_{\pm}^{sc}(x_{ex} \pm x_{det})$. But this is possible only when the excitation and detection TWINS are identical, and both of them are described by the same calibration curve $k_{det}^c(\omega) = k_{ex}^c(\omega)$. But this is not feasible in a practical situation since the wavelength depend time delay introduced by the two TWINS is not identical due to the manufacturing tolerance. The conversion of axes to common excitation or detection axis is one of the solution for this, but that causes changes in measured data and introduces any artifacts. Considering all these facts, it is better to transform the x_{ex} axis to a new axis, \hat{x}_{ex} which is described using the calibration curve $k_c^{det}(\omega)$. For this, data is transformed into the Fourier domain.

$$\tilde{I}(k_{ex}, x_{det}) = \int_{-\infty}^{\infty} I(x_{ex}, x_{det}) \cdot e^{-ik_{ex}x_{ex}} dx_{ex}. \quad (\text{A.II.34})$$

Then the k_{ex} axis is substituted by a new \hat{k}_{ex} axis such that $\omega_{ex}^c(k_{ex}) = \omega_{det}^c(\hat{k}_{ex})$:

$$\hat{\tilde{I}}(\hat{k}_{ex}, x_{det}) = \tilde{I}\left(k_{ex}^c\left(\omega_{det}^c\left(\hat{k}_{ex}\right)\right), x_{det}\right) \cdot \frac{\partial k_{ex}^c}{\partial \omega}\left(\omega_{det}^c\left(\hat{k}_{ex}\right)\right) \frac{\partial \omega_{det}^c}{\partial k}\left(\hat{k}_{ex}\right). \quad (\text{A.II.35})$$

The transformed interferogram is retrieved via inverse Fourier transform of $\hat{\tilde{I}}(\hat{k}_{ex}, x_{det})$:

$$\hat{I}(\hat{x}_{ex}, x_{det}) = \frac{1}{2\pi} \int_{-\infty}^{\infty} \hat{I}(\hat{k}_{ex}, x_{det}) \cdot e^{+i\hat{x}_{ex}\hat{k}_{ex}} d\hat{k}_{ex}. \quad (\text{A.II.36})$$

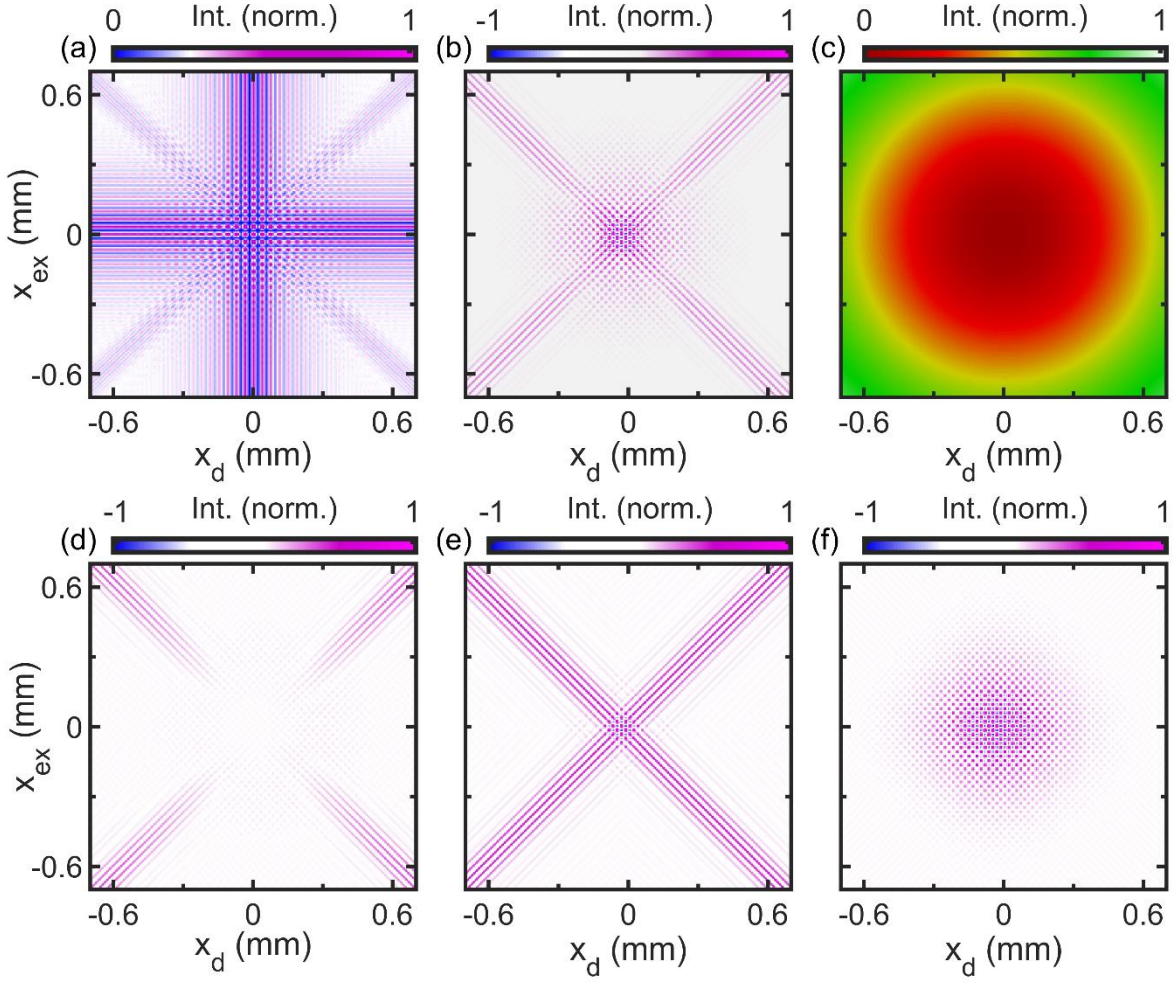


Figure A. II. 8 Separation of coherent and incoherent scattering. (a) A simulated excitation and emission interference map for coherent and incoherent scattering from a fictitious sample (Figure II. 4 (b)). The diagonal stripes are from the coherent scattering and vertical and horizontal stripes have contributed from both coherent and incoherent emission. (b) Simulated map with contributions from coherent (diagonals) and incoherent (center) emission. This map was generated after subtraction of the background signal discussed in the Equations (A.II.25)–(A.II.28). The excitation axis x_{ex} also changed to the new axis \hat{x}_{ex} (see section A.II.2.2 Separation Method). An Invert Gaussian-shaped weight function (c) is used to suppress the incoherent contribution. (d) Map (b) multiplied with (c). (e) and (f) Isolated coherent and incoherent scattering from the BI-TWINS map (b).

The background-subtracted and excitation axis corrected BI-twins map is shown in Figure A. II. 8 (b). On the new axis, the diagonal patterns can be simplified as;

$$\hat{I}_{\pm}^{sc}(x_{\pm}) = 2c_{ex}c_{det} \int_{-\infty}^{\infty} \cos(\Delta\phi_{\pm}(\omega_{det}) + k_{det}^c(\omega_{det})x_{\pm}) I_0^{sc} d\omega_{det}. \quad (\text{A.II.37})$$

Here $\hat{I}_{\pm}^{sc}(x_{\pm})$ have the same functional form of the vertical coherent background term $I_{\text{det}}^{sc/fl}(x_{\text{det}})$ (equation (A.II.26)) in a coordinate system (x_+, x_-) , but it rotates by 45° . Moreover, it is clear that the $\hat{I}_{\pm}^{sc}(x_{\pm})$ pattern depends only on the distances $x_{\pm} = \hat{x}_{ex} \pm x_d$ from the diagonals and on the phase offset $\Delta\phi(\omega_{\text{det}}) = \Delta\phi_{ex}(\omega_{\text{det}}) \pm \Delta\phi_{\text{det}}(\omega_{\text{det}})$.

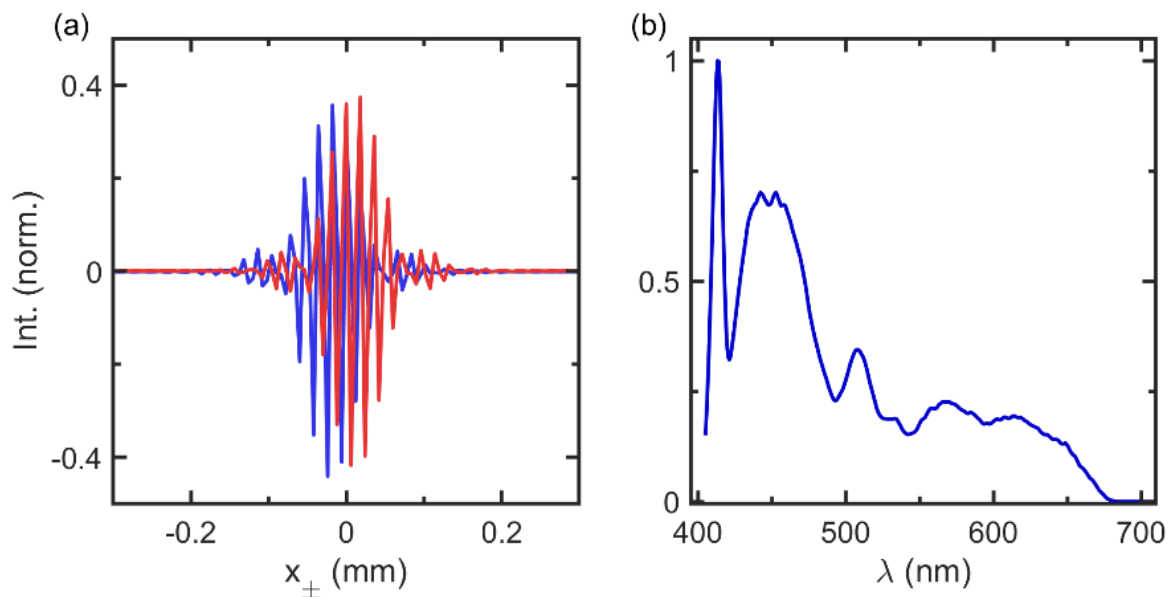


Figure A. II. 9 Cross sections of the residual coherent contribution $\hat{I}_{\pm}^{sc}(x_{\pm})$ along the axes x_{\pm} orthogonal to the rising (blue line) and falling (red line) diagonals, respectively. The \hat{I}_{+}^{sc} and \hat{I}_{-}^{sc} only differ in their spectral offset. (b) Spectrum of the whitelight source after filtering recorded by PD₁.

The next step in the separation process is a reconstruction of the falling and rising diagonals by averaging the map along the x_{\pm} coordinate axes. Before the averaging process, it is necessary to suppress the incoherent contribution in the center of the BI-TWINS interferogram. This is done by multiplying the map (Figure A. II. 8 (b)) with a weight function, an inverted Gaussian shape with an appropriately selected width (Figure A. II. 8 (c)). Figure A. II. 8 (d) shows the map successfully suppressing incoherent contribution. Then a weighted average is performed along the diagonals of Figure A. II. 8 (d) and reconstructed the original diagonal map of coherent emission $\hat{I}^{sc}(\hat{x}_{ex}, x_d) = \hat{I}_{+}^{sc}(\hat{x}_{ex} + x_d) + \hat{I}_{-}^{sc}(\hat{x}_{ex} - x_d)$ (Figure A. II. 8 (e)). The resulting diagonal cross sections $\hat{I}_{\pm}^{sc}(x_{\pm})$ are displayed in Figure A. II. 9 (a). Fringe spacing and contrast are identical as $\hat{I}_{+}^{sc}(x_{+})$ and $\hat{I}_{-}^{sc}(x_{-})$ only different in their spectral phase offset (Equation). A direct Fourier transform of $\hat{I}_{\pm}^{sc}(x_{\pm})$

and axis calibration (A.II.1.2) provide a coherent light scattering spectrum $I_0^{sc}(\omega_d)$. Using Equation (A.II.18) this spectrum can be expressed as a function of wavelength, $I_0^{sc}(\lambda_d)$.

In the final step of the separation, $\hat{I}^{sc}(\hat{x}_{ex}, x_d)$ (Figure A. II. 8 (e)) subtract from $\hat{I}(\hat{x}_{ex}, x_d)$ (Figure A. II. 8 (b)) to obtain the incoherent fluorescence contribution $\hat{I}^{fl}(\hat{x}_{ex}, x_d)$ (Figure A. II. 8(f)). A two-dimensional Fourier transform and axis calibration of $\hat{I}^{sc}(\hat{x}_{ex}, x_d)$ and $\hat{I}^{fl}(\hat{x}_{ex}, x_d)$ provides isolated coherent $I_0^{sc}(\lambda_{ex}, \lambda_d)$ (Figure II. 4 (e)) and incoherent ($I_0^{fl}(\lambda_{ex}, \lambda_d)$) (Figure II. 4 (f)) EE spectrum, respectively.

A.III

Additional information of Chapter III

A.III.1 ErCry4 Protein Sample Preparation Protocol for Spectroscopic Experiments

A.III.1.1 Protocol for washing BME from ErCry 4 sample

The ErCry4 samples are always stored in the buffer and 2-mercaptoethanol (BME) (10 mM) mixture at lower concentrations in an aliquot. The buffer solution contains 20 mM Tris, 250 mM NaCl, and 20% Glycerol. One aliquot contains a 200 μ L ErCry4 sample (5-6 mg/mL) which has 6.2 μ M FAD (4.87 mg/L). Usually, we use 2-3 aliquots (2-3 mg).

For washing out the BME from a protein sample, the steps given below are followed:

1. Add 400 μ L ErCry 4 sample to an Amicon Ultra-0.5 Centrifugal Filter Unit.
2. Centrifuge the sample at 4° C, 14,000 rpm for 3 minutes.
3. Check the volume of the sample in the filter. It should be at 200 μ L.
 - a. If the total volume of the sample is above 200 μ L, centrifuge it at the same conditions for 1 minute.
 - b. If the total volume of the sample is below 200 μ L, add supernatant from the column to the filter and make it 200 μ L.
4. Mix the sample in the filter by pipetting twice to thrice.
5. Discard the remaining supernatant from the column.
 - a. If there is a remaining sample, add the rest to the filter and repeat steps 2-5.
6. Add 200 μ L of buffer into the filter and repeat steps 2-5 for nine additional times.

There will be ~10 μ M BME present in the sample after BME washing.

A.III.1.2 Protocol for concentrating ErCry 4 sample

The FAD_{ox}, FADH[•], and FADH⁻ all have a molar absorbance coefficient of 6,000 cm⁻¹M⁻¹ at 393 nm [2, 17]. So at 393 nm FAD in ErCry4 has an absorbance of 0.06 for 80 μ M and 0.15 for 200 μ M in a 0.15 cm path length cuvette. After washing out BME from the sample, it can be concentrated to the desired concentration by following these steps:

1. Centrifuge the BME-washed sample (~ 200 μ L) in Amicon Ultra-0.5 Centrifugal Filter Unit at 4° C, 14000 rpm for 2.30 minutes (the same filter from BME washing can be used).

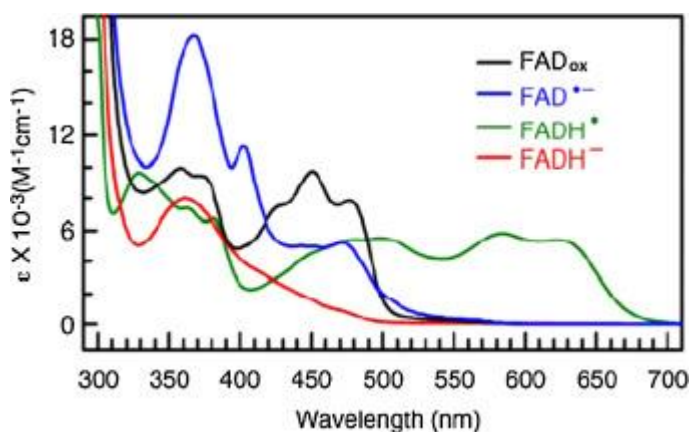


Figure.A.III.1 Molar absorption coefficient ($\epsilon(M^{-1}cm^{-1})$) of different redox states of FAD [2].

2. Check the volume of the sample in the filter unit.
3. Repeat steps 1-2 until the sample volume in the filter becomes 100 μ L (if started with 400 μ L sample) or below 150 μ L (if started with 600 μ L sample).
4. Check the absorbance of the sample at 393 nm and calculate the FAD concentration.
 - a. If the concentration is too low, centrifuge the sample again in the same conditions as in step 1 for 90 seconds and recheck the absorbance.
 - b. If the concentration is too high, dilute the sample with buffer solution without BME.
5. Repeat step 4 until the desired concentration is reached.

A.III.1.3 Protocol for oxidizing ErCry 4 sample

The absorption coefficient of FAD_{ox} at 472 nm is $9,053\text{ cm}^{-1}M^{-1}$ [2, 17]. For successful oxidation of the sample, follow the steps below:

1. Measure the exact volume of the concentrated sample and transfer the sample to a new fresh aliquot
2. Add 1-1.2 mM PFC to the sample (20 mM PFC in buffer solution already prepared and kept in the fridge).
3. Centrifuge the sample for one hour.
4. Check the absorbance of the sample (Normally, a small contribution from $FADH^{\bullet}$ is visible).
5. Add another 2 mM PFC to the sample
6. Then centrifuge the sample for one hour.
7. Measure the absorbance spectrum
 - a. If the absorbance spectrum again shows the contribution from $FADH^{\bullet}$, add another 2 mM PFC to the sample and centrifuge for one hour.
8. Repeat step 7 until the contribution of $FADH^{\bullet}$ in the sample vanishes.

9. Check the absorbance at 472 nm to estimate the concentration of FAD_{ox} in the sample.

Please try to keep the protein sample always at least below 4° C.

A.III.2 Undersampling

According to the Nyquist sampling theorem, a band-limited continuous signal can be perfectly sampled and reconstructed if it is sampled (f_s) over twice the highest frequency (f_H) of the signal. Here our excitation laser light has a spectral range from 400 to 680 nm ($7.55 \times 10^{14} - 4.41 \times 10^{14}$ Hz). So the Nyquist sampling frequency f_s should be greater than 1.5×10^{15} Hz ($2F_H$). The pulse delay generated by the TWINS interferometer for 1mm movement of the wedge position is calculated as ≈ 50 fs (

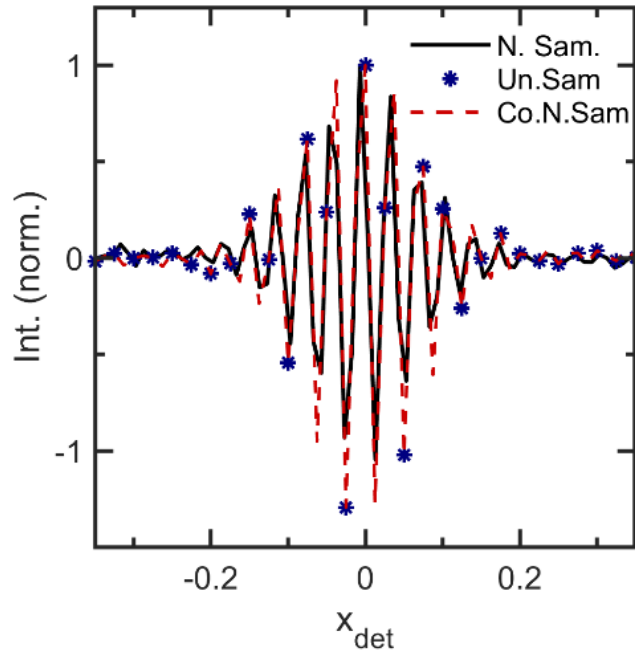


Figure.A.III. 2 Interference structures of molecular FAD emission recorded using the detection TWINS in the BI-TWINS spectrometer under Nyquist sampling condition (black solid line) and undersampled condition (blue ‘*’ sign). The undersampled interference patterns converted to Nyquist sampling condition and exactly matching with interference pattern recorded under Nyquist sampling condition (red dashed line).

2×10^{13} Hz) (Equation (A.II.9)). This leads to the condition that the TWINS interferometer has to be moved in a step size maximum of 12.5 μm to fulfill the Nyquist sampling. The interference pattern of molecular FAD emission recorded using detection TWINS in the BI-TWINS spectrometer in Nyquist sampling condition is shown in Figure.A.III. 2 (sold black line). This interference pattern contains almost 20 interference fringes in total. But following the undersampling condition, f_s can be reduced

below Nyquist frequency. The undersampling frequency $f_{s/un}$ can be calculated as, $\frac{2f_H}{n} \leq f_{s/un} \leq \frac{2f_L}{n-1}$

. The value n should be $1 \leq n \leq \frac{f_H}{f_H - f_L}$ and in our case $n = 2$. So the $f_{s/un}$ is calculated as 8×10^{14} Hz

for our situation. The calculated undersampling frequency $f_{s/un}$ corresponds to a TWINS step size of 25 μm . The interference pattern of molecular FAD emission recorded in the undersampling condition is shown in Figure.A.III. 2 (blue “*” sign). There are only eight fringes in the undersampled interference pattern. It is possible to obtain an emission spectrum of molecular FAD by applying FT, and a corresponding calibration scan of detection TWINS on undersampled interference patterns with the same noise level as Nyquist sampled patterns [224]. Using the undersampled step size in the BI-TWINS spectrometer, the size of the intensity map is reduced to 121×121 pixels, and the measurement time for a single map to 70 minutes. So the undersampling condition minimizes the size of data and measurement time without the depletion of resolution and quality. In addition, the reduction of measurement time always preserves the delicate and precious samples; the method mainly conserves the biological samples from photodegradation due to continuous optical excitation.

It is also possible to convert the undersampled data to Nyquist sampled condition, for which the data recorded in the undersampled condition are converted into the Fourier domain and zero-padded accordingly. After that, the zero-padded data are converted into the pixel domain. In Figure.A.III. 2, red dashed line shows the interference pattern that converted to the Nyquist sampling from the undersampling condition. The measured interference pattern (solid black line) excellently matches the converted Nyquist sampling data (Figure.A.III. 2, red dash line). The BI-TWINS intensity map that is recorded in the undersampling condition can also be converted to Nyquist sampled data map, then it results in an intensity map with size 242×242 pixels.

Interference structures of molecular FAD emission recorded using the detection TWINS in the BI-TWINS spectrometer under Nyquist sampling condition (black solid line) and undersampled condition (blue “*” sign). The undersampled interference patterns converted to Nyquist sampling condition and exactly matching with interference pattern recorded under Nyquist sampling condition (red dashed line).

A.IV

Additional information of Chapter IV [16]

A.IV.1 Linearity and Sample Stability

To ensure that TA experiments are performed in a linear pump-power regime, the dependence of $\Delta T / T$ signal strength on pump pulse energy was recorded for a wild type sample. The spot sizes of pump and probe at their intersection were set to $\sim 50 \times 50 \mu\text{m}^2$.

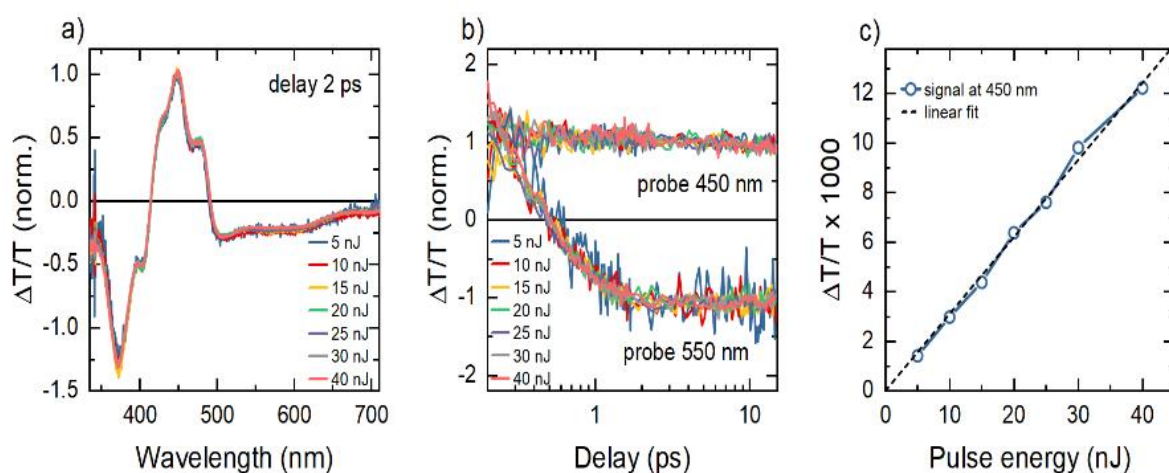


Figure A. IV. 1 Effect of the pump pulse energy on $\Delta T / T$ signals for wild-type ErCry4 protein. a) Normalized differential spectra at a delay of 2 ps and b) normalized dynamics at 450 and 550 nm recorded for pump pulse energy ranging from 5 to 40 nJ. c) Differential transmission signal averaged over the delays from 5 to 15 ps at 450 nm as a function of the pump pulse energy (blue circles) together with a linear fit through the origin. This linear relationship of signal strength and pump pulse energy shows that the experiments are performed well within the linear pump-power regime.

Figure A. IV. 1 a) shows that the shape of the $\Delta T / T$ spectra at a fixed delay of 2 ps, normalized to their maximum at 450 nm, does not change with pump energy in the range between 5 and 40 nJ. Also the dynamics at selected delays do not change when varying the pump energy in this range. As seen in Figure A. IV. 1 c), no deviation from a linear pump-power dependence can be observed. This ensures that all reported TA measurements in this manuscript, recorded at a pump energy of 20 nJ, are well within the linear pump-power regime, not exceeding the $\chi^{(3)}$ regime. To test for possible sample degradation during the nonlinear measurements, we have investigated the time evolution of the differential transmission spectrum of a $W_B F$ mutant at a fixed delay of 2 ps. No visible change in $\Delta T / T$ is seen during the course of the 6.5 hours measurement. The experimental conditions were the same as

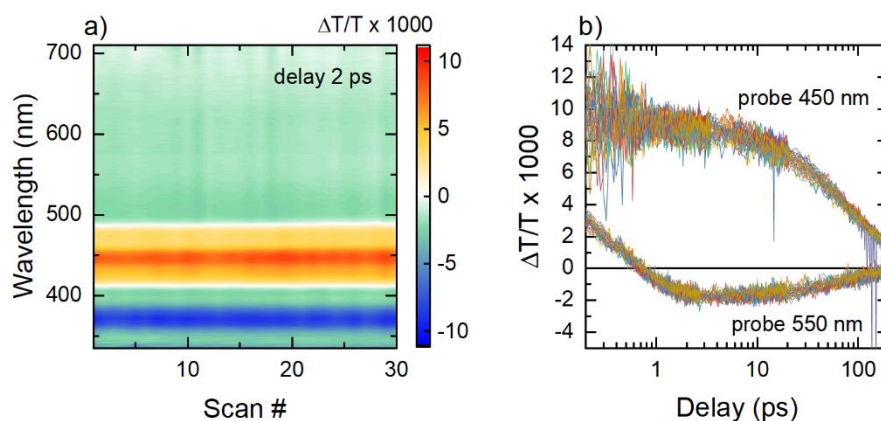


Figure A. IV. 2 Stability of the differential transmission spectra over 30 delay scans, for a measurement of the $W_B F$ mutant, lasting ~ 6.5 hours. The measurement is performed for parallel pump/probe polarization using 20 nJ pump pulses at 450 nm. a) Raw differential transmission spectra at a delay of 2 ps for all 30 scans show no visible change during the entire measurement. b) The dynamics of all scans at 450 and 550 nm further indicate no significant sample degradation during the measurement. Fluctuations at 450 nm within the first ps arise from interferences between the probe and scattered pump pulse, remaining after scattering correction.

for the data shown in Figure IV. 4 and Figure IV. 5 in the Result section Chapter IV . In Figure A. IV. 2 b), the dynamics of the $\Delta T / T$ signal are displayed at selected probe wavelengths of 450 and 550 nm for all 30 scans shown in Figure A. IV. 2. Also here, we find no change of signal over the span of the measurement time, indicating negligible amounts sample degradation during the 6.5 hour measurement period, longer than any measurement reported in the main manuscript.

A.IV.2 Potassium Ferricyanide Oxidizer

In all experiments that are shown in the Result section of Chapter III and Chapter IV , potassium ferricyanide (PFC) has been added as an oxidizing agent to counteract photoreduction of the sample during the measurement [154]. Figure A. IV. 3 a) shows the linear absorption spectrum of 1 mM PFC in Tris buffer (20% glycerol, 200 mM NaCl, pH 8.0). The main absorption band around ~ 420 nm has some overlap with the 450 nm pump pulse spectrum.

The addition of ~ 1.5 mM PFC during sample preparation will oxidize a partially reduced sample. This oxidation may partially or even fully deplete the PFC concentration. In the latter case, additional PFC has been added until the sample shows no residual absorption of reduced FAD. A reduced sample shows a broad $FADH^{\cdot -}$ absorption band in the range of 500 to 700 nm, in contrast to a fully reduced sample only containing FAD_{ox} . The amount of PFC remaining in the now fully oxidized sample is then determined using linear absorption measurements. The remaining amount of PFC, which counteracts photo-reduction during the experiments is found to range from ~ 1.7 to 2.6 mM in the investigated samples at the start of the measurement.

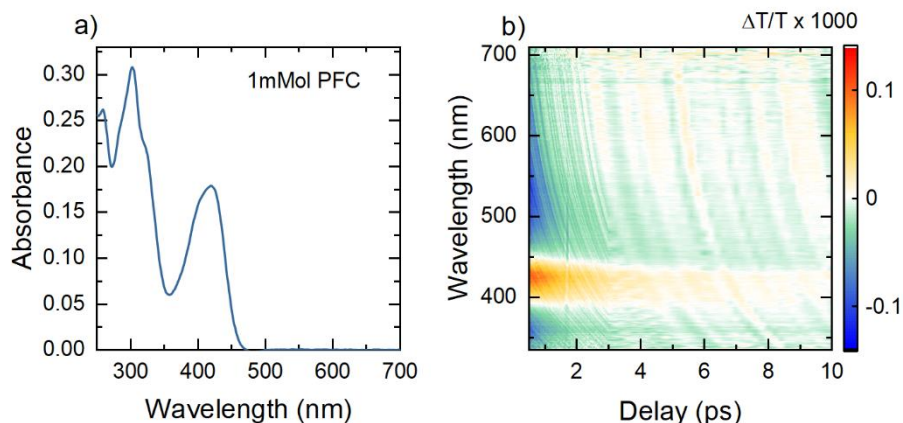


Figure A. IV. 3 Linear absorption and nonlinear differential transmission spectra of PFC oxidizer. a) Linear absorption spectrum of 1 mM PFC in Tris buffer. b) Probe-chirp-corrected $\Delta T/T$ map of 1 mM PFC in buffer recorded under the same experimental conditions as for the ErCry4 measurements. Note that the differential transmission signal is $< 10^{-4}$.

A TA measurement of 1 mM PFC in buffer under the same experimental conditions as the ErCry4 measurements is shown in Figure A. IV. 3 b). Here, only a very weak differential transmission signal on the order of 0.01% can be observed, decaying within a few ps. This makes possible PFC contributions to the nonlinear signal of the protein measurements negligible.

A.IV.3 FAD in Buffer

A TA measurement of a 200 μM solution of molecular FAD dissolved in a buffer containing 1 mM PFC is shown in Figure A. IV. 4. The sample was measured under the same experimental conditions as used for the ErCry4 measurements. A global analysis of the data results in four *DADS* spectra that are displayed in Figure A. IV. 4 d). The spectral shapes of these *DADS* spectra and their associated decay times closely follow those reported by Brazard et al. [22]. Here, the long-lived 3.2 ns component (3.0 ns in [22]) can be assigned to the relaxation of the open conformer of optically excited FAD, in which the distance between the electron-donating adenine moiety and the electron-accepting isoalloxazine group is so large that an intramolecular electron transfer is efficiently suppressed. The *DADS* spectrum with a much shorter decay time of 6.6 ps (5.4 ps in [22]) is assigned to monitor the intramolecular electron transfer between adenine and isoalloxazine in the closed conformer of FAD. Additional *DADS* spectra with decay times of 1.7 and 35 ps (1 ps and 31 ps in [22], respectively) are attributed to solvation dynamics and to the decay of the FAD dimer, respectively. No effect of PFC on dynamics and spectral shapes can be observed.

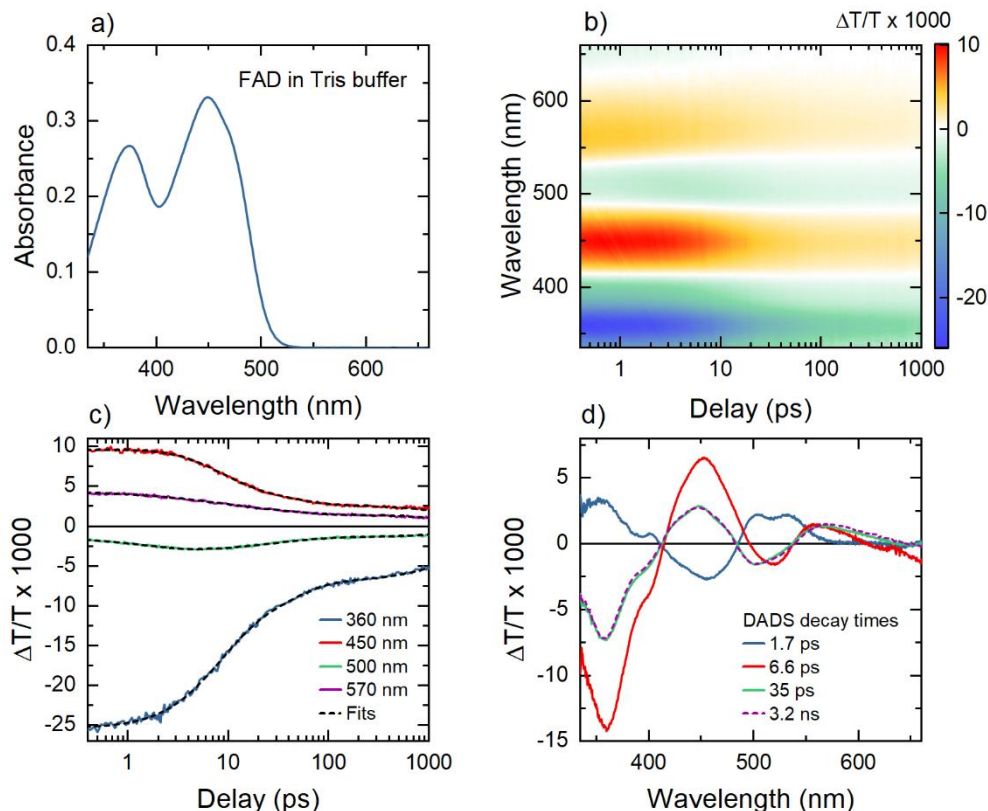


Figure A. IV. 4 Linear absorption and nonlinear differential transmission of molecular FAD in buffer solution. a) Linear absorption spectrum of 0.2 mM FAD in Tris buffer (20% glycerol, 200 mM NaCl, pH 8.0). b) Probe-chirp-corrected $\Delta T/T$ map of 200 μM FAD in Tris buffer containing 2 mM PFC, measured under the same experimental conditions as the ErCry4 measurements. c) Dynamics of the differential transmission signal for selected wavelengths. The result of the global analysis of the data is superimposed as dashed black lines. d) The four DADS spectra that are obtained from a global analysis of the data and their associated decay times. Spectra and decay times are very similar to those reported in [22] for a sample with a 0.23 mM concentration. No effects of the PFC oxidizer on the dynamics and on the spectra can be observed.

A.IV.4 Data Preparation and Analysis

For each ErCry4 measurement, a measurement of the differential transmission signal of a plain buffer solution was performed. This measurement shows, within ± 100 fs around time zero and at all probe wavelengths, a well-known and strong coherent scattering contribution that arises from the cross-phase modulation between the chirped few-ps probe pulse and the short pump pulse [329]. This coherent scattering signal can be employed to measure the wavelength-dependent zero point of the delay, $t_w = 0$. For this, the method described in [280] was used to fit the solvent signal. Based on this fit, the origin of the time delay axis was corrected for each TA measurement. Afterward, the coherent solvent

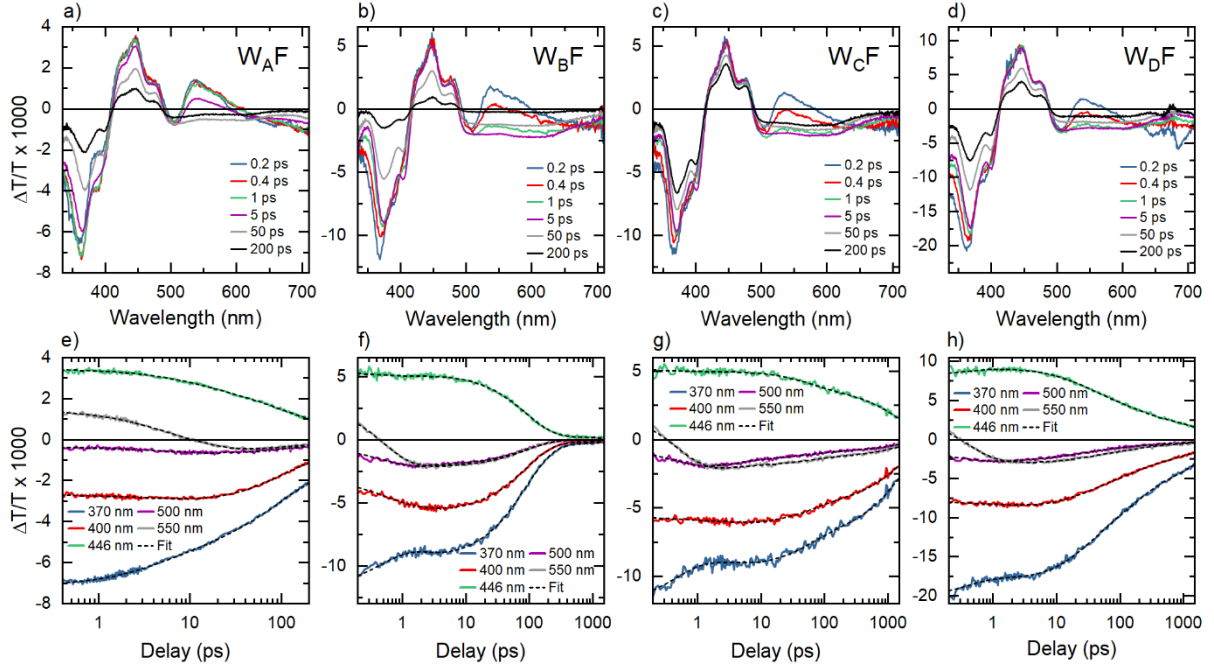


Figure A. IV. 5 a)-d): Differential transmission spectra of all four investigated ErCry4 mutants at selected delays. The spectra are cross-sections through the data presented in Figure IV. 3 in the Result section, Chapter IV. e)-h): Dynamics at selected wavelengths for the four mutants (solid lines). The fits obtained from the global analysis (black dashed lines) show excellent agreement with the experimental data.

contribution, as obtained from the reference measurement, has been subtracted from the protein measurement. To avoid any spurious, residual solvent contribution in the measurements discussed in this chapter, the TA data for delays below 200 fs were discarded from the data analysis.

To investigate the ErCry4 wild type and mutant datasets, a global analysis was performed using a Matlab-based toolbox [301]. To obtain decay associated difference spectra (*DADS*), only monoexponential decays were used as mathematical model functions. Each *DADS* component, $DADS_i(\lambda)$, $i = 1, \dots, n$, represents the spectral amplitude of the signal contribution that is decaying with a time constant τ_i . In this way, the global fit will reproduce the complete, experimentally measured data set by a sum over all $DADS_i(\lambda)$ spectra multiplied by an exponential decay with decay time τ_i

$$\frac{\Delta T}{T}(\lambda, t_w) = \sum_{i=1}^n DADS_i(\lambda) e^{-\frac{t_w}{\tau_i}}. \quad (\text{A.IV.1})$$

The i -th term of this sum, $DADS_i \exp(-t_w / \tau_i)$, is the time-dependent differential transmission spectrum associated with the relaxation component i . This representation in terms of independent

components with monotonically increasing decay times accurately describes the dynamics expected from a sequential rate equation model.

The *DADS* spectra that result from the global analysis for all mutants and the wild-type are shown in Figure A. IV. 6. The datasets were modeled using the smallest number of decays necessary to fully

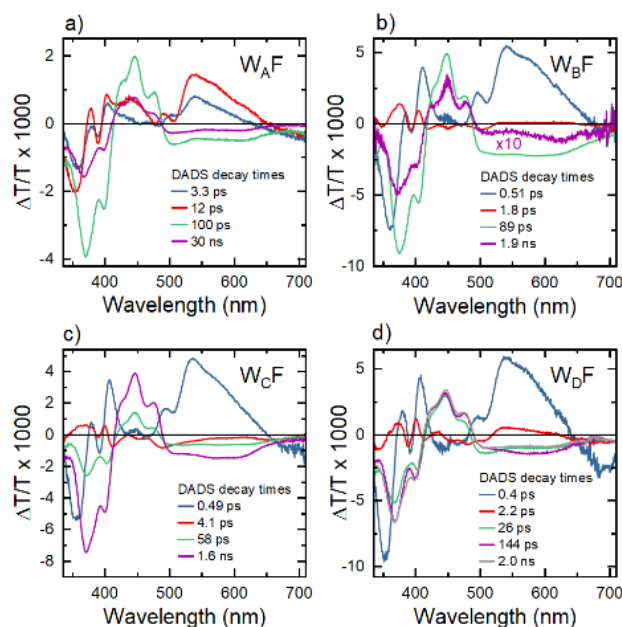


Figure A. IV. 6 *DADS* spectra resulting from a global analysis of the differential transmission maps recorded for the four ErCry4 mutants (Figure IV. 3). The global analysis results in a minimal number of physically meaningful decay components with different differential transmission spectra and associated decay times that are depicted in the individual subpanels. These *DADS* spectra are then used to calculate the *EADS* spectra of the four mutants that are shown in Figure IV. 3 e)-h) in section Results of Chapter IV .

describe the dynamics of the data at all wavelengths. The correctness of this number was judged by the appearance of temporally and spectrally flat and unstructured residuals. For wild type ErCry4 and the W_DF mutant five and for the W_AF, W_BF and W_CF mutants four exponential decays were needed to represent the measured data. Figure A. IV. 5 e)-h) shows the fits resulting from the global analysis compared to the experimental data dynamics at selected wavelengths. A convincing agreement between fit and data validates the *DADS* obtained by the global analysis.

These *DADS* spectra may either reflect the exponential decay or the rise of a certain spectral component in the data. As such, their physical interpretation may sometimes be challenging when spectral components that rise in time overlap with decaying components. This is indeed the case for the present samples where some spectral signatures of the rise in radical-pair concentration overlap with decaying signals from oxidized flavin. The physical interpretation of the spectra may be facilitated by transforming them into evolution-associated difference spectra (*EADS*) that are defined [162] as

$$EADS_k(\lambda) = \sum_{i=k}^n DADS_i(k) \quad (\text{A.IV.2})$$

The first spectrum, $EADS_1$, represents the sum over all $DADS$ spectra and, thus, the differential transmission spectrum at delay zero, $\Delta T / T(\lambda, t_w = 0)$. The k -th spectrum, $EADS_k, k > 1$, then gives a differential transmission spectrum which is the difference between $\Delta T / T(t_w = 0)$ and the sum of the first $k - 1$ $DADS$ spectra. Provided that the decay constants are sufficiently different, this approximately represents the shape of the differential transmission at a delay shortly after these $k - 1$ relaxation steps have been completed.

The $EADS$ spectra are then used to extract spectra for different electronic states of FAD (FAD_{ox} , FAD_{ox}^* and $FAD^{\bullet-}$), as well as for the different tryptophans (Trp_A , Trp_B , and Trp_C). The absorption spectra of the excited flavin, $A_{FAD_{ox}^*}$, and the third radical-pair A_{RP3} were obtained by removing the measured absorbance $A_{FAD_{ox}}$ from $EADS_1$ and $EADS_5$, which were converted from differential transmission $\Delta T / T$ to differential absorbance ΔA using

$$A_{FAD_{ox}^*}(\lambda) = \log_{10}(1 - EADS_1(\lambda)) + nA_{FAD_{ox}}, \quad (\text{A.IV.3})$$

and

$$A_{RP3}(\lambda) = A_{FAD^{\bullet-}}(\lambda) + A_{Trp_C H^{\bullet+}}(\lambda) = \log_{10}(1 - EADS_5(\lambda)) + nA_{FAD_{ox}^*}. \quad (\text{A.IV.4})$$

The scaling factor n is chosen as 0.025 such that the obtained spectra are flat and unstructured at the peaks around 450 nm, similar to procedures described in [183, 236].

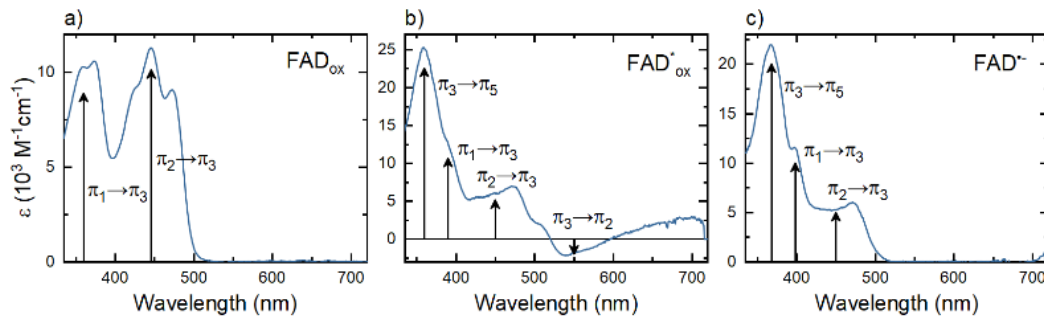


Figure A. IV. 7 Spectral assignment of the differential transmission spectra of a) FAD_{ox} , b) FAD_{ox}^* , and c) $FAD^{\bullet-}$ as obtained from the W_{DF} dataset. The assignment is based on quantum-chemical calculations recently reported by Schwinn et al. [1]. The corresponding intramolecular transitions for FAD_{ox} and $FAD^{\bullet-}$ are marked with black arrows. The molecular orbitals that are involved in the FAD_{ox}^* absorption are assumed to be the same as those for $FAD^{\bullet-}$. An additional stimulated emission peak ($\pi_3 \rightarrow \pi_2$) appears in FAD_{ox}^* at around 550 nm.

Literature spectra of TrpH⁺ show mainly absorption above ~500 nm and below ~380 nm [314], while FAD^{•-} only absorbs at wavelengths below ~500 nm [1, 2]. Thus, to disentangle the absorbance spectrum A_{RP3} into its components $A_{FAD^{•-}}$ and $A_{Trp_cH^{•+}}$, a sum of 11 Gaussian spectra is fitted to A_{RP3} , where 4 Gaussians represent the plateau for wavelengths above ~500 nm, taken as the TrpcH⁺ absorbance. After subtracting $A_{Trp_cH^{•+}}$ from A_{RP3} , the remaining FAD^{•-} absorbance is used to extract the Trp_BH^{•+} and Trp_AH^{•+} spectra from $EADS_4$ and $EADS_2$, respectively.

Absorbance is converted to molar extinction ϵ using the experimentally measured FAD_{ox} absorbance and a reference value of 11300 M⁻¹cm⁻¹ for the molar extinction of FAD_{ox} at a wavelength of 450 nm [22, 162, 236]. This approach results in the species spectra depicted in Figure IV. 4 c), which are very similar to those reported by Kutta et al. [236].

A.IV.5 Additional Simulation Data

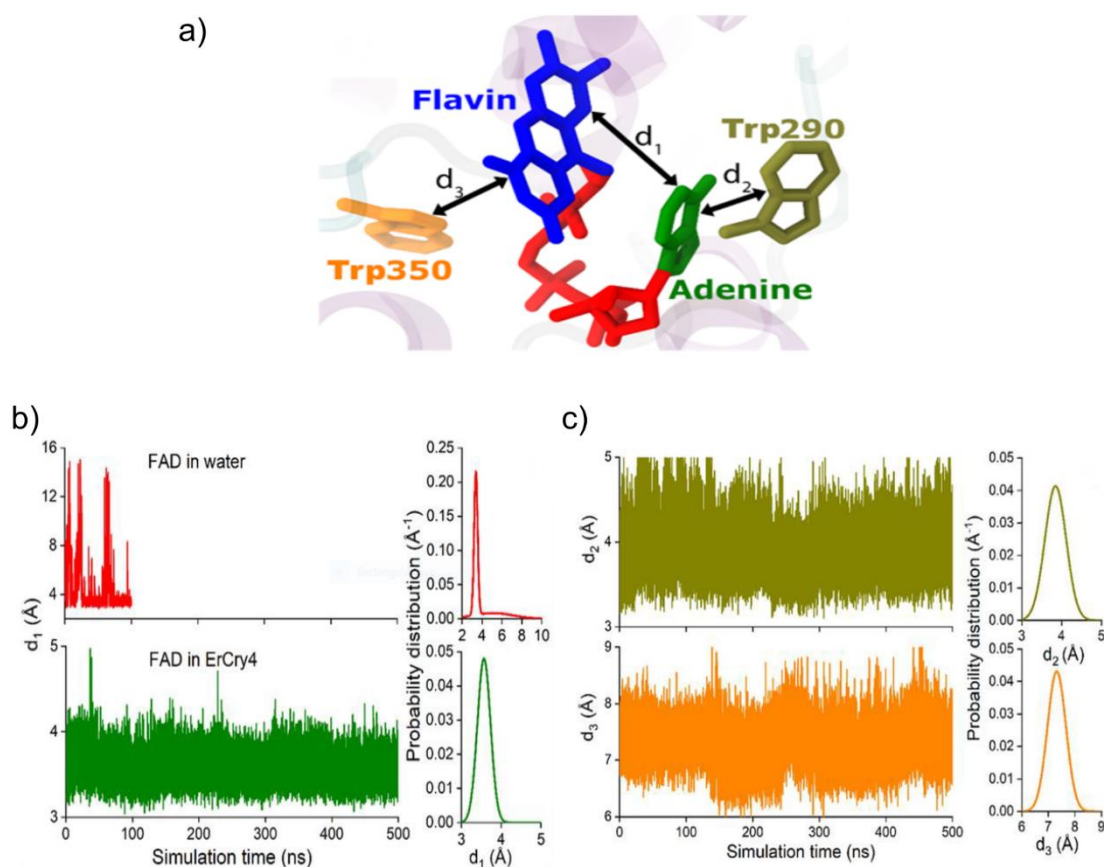


Figure V. 1 a) Flavin adenine dinucleotide (FAD) cofactor with the indicated internal edge-to-edge distances between the flavin and adenine (d_1) cofactors, the edge-to-edge distance between adenine and Trp290 residue (d_2) and the edge-to-edge distance between the flavin and the Trp350 residue (d_3). b) Flavin-adenine edge-to-edge distance for solvated FAD in water and embedded in ErCry4 respectively with the corresponding probability density distributions. (c) Edge-to-edge distances between adenine and the Trp290 residue (d_2) and flavin and the Trp350 residue (d_3) in ErCry4, see Figure A. IV. 6. Time evolution of the two distances as well as the probability density distribution of the distances are shown.

References

1. Schwinn, K., N. Ferré, and M. Huix-Rotllant, *UV-visible absorption spectrum of FAD and its reduced forms embedded in a cryptochrome protein*. *Physical Chemistry Chemical Physics*, 2020. **22**(22): p. 12447-12455.
2. Kao, Y.-T., et al., *Ultrafast Dynamics of Flavins in Five Redox States*. *Journal of the American Chemical Society*, 2008. **130**(39): p. 13132-13139.
3. Xu, J., *Experimental validation of the radical pair mechanism in cryptochrome 4 proteins for avian magnetoreception*, in *Fakultät für Mathematik und Naturwissenschaften 2022*, Carl von Ossietzky Universität: Oldenburg.
4. Lünemann, D.C., et al., *Distinguishing between coherent and incoherent signals in excitation-emission spectroscopy*. *Optics Express*, 2021. **29**(15): p. 24326-24337.
5. Kapusta, P., et al., *Time-resolved fluorescence anisotropy measurements made simple*. *Journal of Fluorescence*, 2003. **13**(2): p. 179-183.
6. Oriana, A., et al., *Scanning Fourier transform spectrometer in the visible range based on birefringent wedges*. *Journal of the Optical Society of America a-Optics Image Science and Vision*, 2016. **33**(7): p. 1415-1420.
7. <https://i.pinimg.com/originals/dc/26/07/dc260757d20e6b96122d675b68bfd354.jpg>.
8. Bartölke, R., et al., *The secrets of cryptochromes: photoreceptors, clock proteins, and magnetic sensors*. *Neuroforum*, 2021. **27**(3): p. 151-157.
9. Zoltowski, B.D., et al., *Chemical and structural analysis of a photoactive vertebrate cryptochrome from pigeon*. *Proceedings of the National Academy of Sciences*, 2019. **116**(39): p. 19449-19457.
10. Heelis, P.F., *The photophysical and photochemical properties of flavins (isoalloxazines)*. *Chemical Society Reviews*, 1982.
11. Ritz, T., S. Adem, and K. Schulten, *A model for photoreceptor-based magnetoreception in birds*. *Biophysical journal*, 2000. **78**(2): p. 707-718.
12. Kao, Y.-T., et al., *Ultrafast Dynamics and Anionic Active States of the Flavin Cofactor in Cryptochrome and Photolyase*. *Journal of the American Chemical Society*, 2008. **130**(24): p. 7695-7701.
13. Liu, B., et al., *Searching for a photocycle of the cryptochrome photoreceptors*. *Current opinion in plant biology*, 2010. **13**(5): p. 578-586.
14. Chaves, I., et al., *The cryptochromes: blue light photoreceptors in plants and animals*. *Annual review of plant biology*, 2011. **62**(1): p. 335-364.
15. Tamošauskas, G., et al., *Transmittance and phase matching of BBO crystal in the 3– 5 μ m range and its application for the characterization of mid-infrared laser pulses*. *Optical Materials Express*, 2018. **8**(6): p. 1410-1418.
16. Timmer, D., et al., *Tracking the Electron Transfer Cascade in European Robin Cryptochrome 4 Mutants*. *Journal of the American Chemical Society*, 2023. **145** (21): p. 11566-11578.

17. Dodson, C.A., P.J. Hore, and M.I. Wallace, *A radical sense of direction: signalling and mechanism in cryptochrome magnetoreception*. Trends in Biochemical Sciences, 2013. **38**(9): p. 435-446.
18. Islam, S.D., et al., *Fluorescence quenching of flavin adenine dinucleotide in aqueous solution by pH dependent isomerisation and photo-induced electron transfer*. Chemical physics, 2003. **295**(2): p. 137-149.
19. Abhigyan Sengupta; Rahul V. Khade, P.H., *pH dependent dynamic behavior of flavin mononucleotide (FMN) and flavinadenine dinucleotide (FAD) in femtosecond to nanosecond time scale*. Journal of Photochemistry and Photobiology A:Chemistry, 2011. **221**: p. 105-112.
20. Hore, P.J. and H. Mouritsen, *The Radical-Pair Mechanism of Magnetoreception*. Annual Review of Biophysics, 2016. **45**(1): p. 299-344.
21. Maeda, K., et al., *Magnetically sensitive light-induced reactions in cryptochrome are consistent with its proposed role as a magnetoreceptor*. Proceedings of the National Academy of Sciences, 2012. **109**(13): p. 4774-4779.
22. Brazard, J., et al., *New insights into the ultrafast photophysics of oxidized and reduced FAD in solution*. J Phys Chem A, 2011. **115**(15): p. 3251-62.
23. Leenders, R., et al., *Flavin dynamics in reduced flavodoxins: A time-resolved polarized fluorescence study*. European journal of biochemistry, 1993. **211**(1-2): p. 37-45.
24. Gill Jr, R.E., et al., *Extreme endurance flights by landbirds crossing the Pacific Ocean: ecological corridor rather than barrier?* Proceedings of the Royal Society B: Biological Sciences, 2009. **276**(1656): p. 447-457.
25. Egevang, C., et al., *Tracking of Arctic terns *Sterna paradisaea* reveals longest animal migration*. Proceedings of the National Academy of Sciences, 2010. **107**(5): p. 2078-2081.
26. Jouventin, P. and H. Weimerskirch, *Satellite tracking of wandering albatrosses*. Nature, 1990. **343**(6260): p. 746-748.
27. Mouritsen, H., *Long-distance navigation and magnetoreception in migratory animals*. Nature, 2018. **558**(7708): p. 50-59.
28. Berthold, P., *A comprehensive theory for the evolution, control and adaptability of avian migration*. Ostrich, 1999. **70**(1): p. 1-11.
29. Mouritsen, H., *Spatiotemporal orientation strategies of long-distance migrants*, in *Avian migration*. 2003, Springer. p. 493-513.
30. Brower, L., *Monarch butterfly orientation: missing pieces of a magnificent puzzle*. The Journal of experimental biology, 1996. **199**(1): p. 93-103.
31. Warrant, E., et al., *The Australian Bogong moth *Agrotis infusa*: a long-distance nocturnal navigator*. Frontiers in behavioral neuroscience, 2016. **10**: p. 77.
32. Gerlach, G., et al., *Smelling home can prevent dispersal of reef fish larvae*. Proceedings of the national academy of sciences, 2007. **104**(3): p. 858-863.
33. Putman, N.F., et al., *Evidence for geomagnetic imprinting as a homing mechanism in Pacific salmon*. Current Biology, 2013. **23**(4): p. 312-316.
34. Lohmann, K.J., et al., *Regional magnetic fields as navigational markers for sea turtles*. Science, 2001. **294**(5541): p. 364-366.

35. Wiltschko, W. and R. Wiltschko, *Migratory orientation of European robins is affected by the wavelength of light as well as by a magnetic pulse*. Journal of Comparative Physiology A, 1995. **177**(3): p. 363-369.
36. Holland, R., *True navigation in birds: from quantum physics to global migration*. Journal of Zoology, 2014. **293**(1): p. 1-15.
37. Wiltschko, W., et al., *Red light disrupts magnetic orientation of migratory birds*. Nature, 1993. **364**(6437): p. 525-527.
38. Wiltschko, W., *The influence of magnetic total intensity and inclination on directions preferred by migrating European robins (Erithacus rubecula)*. NASA, Washington Animal Orientation and Navigation, 1972.
39. Lefeldt, N., et al., *Migratory blackcaps tested in Emlen funnels can orient at 85 degrees but not at 88 degrees magnetic inclination*. Journal of Experimental Biology, 2015. **218**(2): p. 206-211.
40. Wiltschko, W., *Über den Einfluß statischer Magnetfelder auf die Zugorientierung der Rotkehlchen (Erithacus rubecula)*. Zeitschrift für Tierpsychologie, 1968. **25**(5): p. 537-558.
41. Lohmann, K.J., C.M. Lohmann, and N.F. Putman, *Magnetic maps in animals: nature's GPS*. Journal of Experimental Biology, 2007. **210**(21): p. 3697-3705.
42. Chernetsov, N., et al., *Migratory Eurasian reed warblers can use magnetic declination to solve the longitude problem*. Current Biology, 2017. **27**(17): p. 2647-2651. e2.
43. Wiltschko, W. and R. Wiltschko, *Light-dependent magnetoreception in birds: the behaviour of European robins, Erithacus rubecula, under monochromatic light of various wavelengths and intensities*. Journal of Experimental Biology, 2001. **204**(19): p. 3295-3302.
44. Gagliardo, A., et al., *Oceanic navigation in Cory's shearwaters: evidence for a crucial role of olfactory cues for homing after displacement*. Journal of Experimental Biology, 2013. **216**(15): p. 2798-2805.
45. Mouritsen, H., D. Heyers, and O. Güntürkün, *The neural basis of long-distance navigation in birds*. Annu. Rev. Physiol, 2016. **78**(133-154): p. 610.
46. Bett, N.N. and S.G. Hinch, *Olfactory navigation during spawning migrations: a review and introduction of the Hierarchical Navigation Hypothesis*. Biological Reviews, 2016. **91**(3): p. 728-759.
47. Geva-Sagiv, M., et al., *Spatial cognition in bats and rats: from sensory acquisition to multiscale maps and navigation*. Nature Reviews Neuroscience, 2015. **16**(2): p. 94-108.
48. Sarel, A., et al., *Vectorial representation of spatial goals in the hippocampus of bats*. Science, 2017. **355**(6321): p. 176-180.
49. Kalmijn, A.J., *The detection of electric fields from inanimate and animate sources other than electric organs*, in *Electroreceptors and other specialized receptors in lower Vertebrates*. 1974, Springer. p. 147-200.
50. Kalmijn, A.J., *Electric and magnetic field detection in elasmobranch fishes*. Science, 1982. **218**(4575): p. 916-918.
51. Meyer, C.G., K.N. Holland, and Y.P. Papastamatiou, *Sharks can detect changes in the geomagnetic field*. Journal of the Royal Society Interface, 2005. **2**(2): p. 129-130.
52. Viguiier, C., *Le sens de l'orientation et ses organes chez les animaux et chez l'homme*. Revue Philosophique de la France et de l'Etranger, 1882: p. 1-36.

53. Kano, F., et al., *Head-mounted sensors reveal visual attention of free-flying homing pigeons*. Journal of Experimental Biology, 2018. **221**(17).
54. Nimpf, S., et al., *A putative mechanism for magnetoreception by electromagnetic induction in the pigeon inner ear*. Current Biology, 2019. **29**(23): p. 4052-4059. e4.
55. Bazylinski, D.A. and R.B. Frankel, *Magnetosome formation in prokaryotes*. Nature Reviews Microbiology, 2004. **2**(3): p. 217-230.
56. Uebe, R. and D. Schüler, *Magnetosome biogenesis in magnetotactic bacteria*. Nature Reviews Microbiology, 2016. **14**(10): p. 621-637.
57. Blakemore, R., *Magnetotactic bacteria*. Science, 1975. **190**(4212): p. 377-379.
58. Kirschvink, J.L., M.M. Walker, and C.E. Diebel, *Magnetite-based magnetoreception*. Current opinion in neurobiology, 2001. **11**(4): p. 462-467.
59. Shaw, J., et al., *Magnetic particle-mediated magnetoreception*. Journal of The Royal Society Interface, 2015. **12**(110): p. 20150499.
60. Eder, S.H., et al., *Magnetic characterization of isolated candidate vertebrate magnetoreceptor cells*. Proceedings of the National Academy of Sciences, 2012. **109**(30): p. 12022-12027.
61. Fleissner, G., et al., *Ultrastructural analysis of a putative magnetoreceptor in the beak of homing pigeons*. Journal of Comparative Neurology, 2003. **458**(4): p. 350-360.
62. Beason, R., N. Dussourd, and M. Deutschlander, *Behavioural evidence for the use of magnetic material in magnetoreception by a migratory bird*. The Journal of experimental biology, 1995. **198**(1): p. 141-146.
63. Davila, A.F., et al., *Magnetic pulse affects a putative magnetoreceptor mechanism*. Biophysical Journal, 2005. **89**(1): p. 56-63.
64. Holland, R.A. and B. Helm, *A strong magnetic pulse affects the precision of departure direction of naturally migrating adult but not juvenile birds*. Journal of The Royal Society Interface, 2013. **10**(81): p. 20121047.
65. Zapka, M., et al., *Visual but not trigeminal mediation of magnetic compass information in a migratory bird*. Nature, 2009. **461**(7268): p. 1274-1277.
66. Schulten, K., C.E. Swenberg, and A. Weller, *A biomagnetic sensory mechanism based on magnetic field modulated coherent electron spin motion*. Zeitschrift für Physikalische Chemie, 1978. **111**(1): p. 1-5.
67. Alken, P., et al., *International geomagnetic reference field: the thirteenth generation*. Earth, Planets and Space, 2021. **73**(1): p. 1-25.
68. Nava, J.J.G., P.E. Ambrosio, and D.S. Dominguez, *Cytoprotective Effect of 120 Hz Electromagnetic Fields on Early Hepatocarcinogenesis: Experimental and Theoretical Findings*, in *Vitamin E in Health and Disease*. 2018, IntechOpen.
69. Hore, P.J., K.L. Ivanov, and M.R. Wasielewski, *Spin chemistry*. J Chem Phys, 2020. **152**(12): p. 120401.
70. Woodward, J., *Radical pairs in solution*. Progress in Reaction Kinetics and Mechanism, 2002. **27**(3): p. 165-207.
71. Rodgers, C.T., *Magnetic field effects in chemical systems*. Pure and Applied Chemistry, 2009. **81**(1): p. 19-43.
72. Zhang, Y., et al., *Recent advances in magnetic field-enhanced electrocatalysis*. ACS Applied Energy Materials, 2020. **3**(11): p. 10303-10316.

73. Beretta, G., et al., *The effects of electric, magnetic and electromagnetic fields on microorganisms in the perspective of bioremediation*. Reviews in Environmental Science and Bio/Technology, 2019. **18**(1): p. 29-75.
74. Zadeh-Haghighi, H. and C. Simon, *Magnetic field effects in biology from the perspective of the radical pair mechanism*. Journal of the Royal Society Interface, 2022. **19**(193): p. 20220325.
75. Smith, J., et al., *Radical pairs may play a role in xenon-induced general anesthesia*. Scientific Reports, 2021. **11**(1): p. 1-13.
76. Gould, I.R., N.J. Turro, and M.B. Zimmt, *Magnetic field and magnetic isotope effects on the products of organic reactions*. Advances in physical organic chemistry, 1984. **20**: p. 1-53.
77. Gerson, F. and W. Huber, *Electron spin resonance spectroscopy of organic radicals*. 2003: John Wiley & Sons.
78. Demtröder, W., *Atoms, molecules and photons*. Vol. 3. 2010: Springer.
79. Sakurai, J.J. and E.D. Commins, *Modern quantum mechanics, revised edition*. 1995, American Association of Physics Teachers.
80. Dikanov, S., A. Shubin, and V. Parmon, *Modulation effects in the electron spin echo resulting from hyperfine interaction with a nucleus of an arbitrary spin*. Journal of Magnetic Resonance (1969), 1981. **42**(3): p. 474-487.
81. Schulten, C., *Swenberg, and A. Weller*. Z. Phys. Chem, 1978. **111**: p. 1.
82. Zeeman, P., *VII. Doublets and triplets in the spectrum produced by external magnetic forces*. The London, Edinburgh, and Dublin Philosophical Magazine and Journal of Science, 1897. **44**(266): p. 55-60.
83. Efimova, O. and P. Hore, *Role of exchange and dipolar interactions in the radical pair model of the avian magnetic compass*. Biophysical Journal, 2008. **94**(5): p. 1565-1574.
84. HAMEKA, H., *1 SPIN-ORBIT COUPLING AND INTERSYSTEM CROSSING*. The Triplet State, 1967: p. 1.
85. Khudyakov, I., *Yu. A Sereberennikov, NJ Turro*. Chem. Rev, 1993. **93**: p. 537.
86. Illas, F., et al., *Magnetic coupling in biradicals, binuclear complexes and wide-gap insulators: a survey of ab initio wave function and density functional theory approaches*. Theoretical Chemistry Accounts, 2000. **104**(3): p. 265-272.
87. Brocklehurst, B. and K.A. McLauchlan, *Free radical mechanism for the effects of environmental electromagnetic fields on biological systems*. International journal of radiation biology, 1996. **69**(1): p. 3-24.
88. McLauchlan, K.A. and U. Steiner, *Invited article: The spin-correlated radical pair as a reaction intermediate*. Molecular Physics, 1991. **73**(2): p. 241-263.
89. Lewis, A., *Spin Dynamics in Radical Pairs*. 2018: Springer.
90. Weller, A., F. Nolting, and H. Staerk, *A quantitative interpretation of the magnetic field effect on hyperfine-coupling-induced triplet formation from radical ion pairs*. Chemical Physics Letters, 1983. **96**(1): p. 24-27.
91. Steiner, U.E. and T. Ulrich, *Magnetic field effects in chemical kinetics and related phenomena*. Chemical Reviews, 1989. **89**(1): p. 51-147.
92. Timmel, C.R., et al., *Effects of weak magnetic fields on free radical recombination reactions*. Molecular Physics, 1998. **95**(1): p. 71-89.

93. Miura, T., *Studies on coherent and incoherent spin dynamics that control the magnetic field effect on photogenerated radical pairs*. Molecular Physics, 2020. **118**(6): p. e1643510.
94. Miura, T., K. Maeda, and T. Arai, *The spin mixing process of a radical pair in low magnetic field observed by transient absorption detected nanosecond pulsed magnetic field effect*. The Journal of Physical Chemistry A, 2006. **110**(12): p. 4151-4156.
95. Hiscock, H.G., et al., *The quantum needle of the avian magnetic compass*. Proceedings of the National Academy of Sciences, 2016. **113**(17): p. 4634-4639.
96. Lau, J.C., C.T. Rodgers, and P. Hore, *Compass magnetoreception in birds arising from photo-induced radical pairs in rotationally disordered cryptochromes*. Journal of The Royal Society Interface, 2012. **9**(77): p. 3329-3337.
97. Solov'Yov, I.A., H. Mouritsen, and K. Schulten, *Acuity of a cryptochrome and vision-based magnetoreception system in birds*. Biophysical journal, 2010. **99**(1): p. 40-49.
98. Wiltschko, W. and R. Wiltschko, *Bird orientation under different sky sectors*. Zeitschrift für Tierpsychologie, 1974. **35**(5): p. 536-542.
99. Mouritsen, H., *The magnetic senses*, in *Neurosciences-From Molecule to Behavior: a university textbook*. 2013, Springer. p. 427-443.
100. Mouritsen, H., et al., *Cryptochromes and neuronal-activity markers colocalize in the retina of migratory birds during magnetic orientation*. Proceedings of the National Academy of Sciences, 2004. **101**(39): p. 14294-14299.
101. Liedvogel, M., et al., *Chemical magnetoreception: bird cryptochrome 1a is excited by blue light and forms long-lived radical-pairs*. PloS one, 2007. **2**(10): p. e1106.
102. Biskup, T., et al., *Direct observation of a photoinduced radical pair in a cryptochrome blue-light photoreceptor*. Angewandte Chemie International Edition, 2009. **48**(2): p. 404-407.
103. Branden, C.I. and J. Tooze, *Introduction to protein structure*. 2012: Garland Science.
104. Gutteridge, A. and J.M. Thornton, *Understanding nature's catalytic toolkit*. Trends in biochemical sciences, 2005. **30**(11): p. 622-629.
105. Lodish, U.H., et al., *Molecular Cell Biology*. 2008: W. H. Freeman.
106. Murray, R.K., D.K. Granner, and V.W. Rodwell, *Harper's illustrated biochemistry*. 2010.
107. Nelson, D.L. and M.M. Cox, *Lehninger Principles of Biochemistry*. 2017. New York Worth, New York, 2005.
108. Ahmad, M. and A.R. Cashmore, *HY4 gene of A. thaliana encodes a protein with characteristics of a blue-light photoreceptor*. Nature, 1993. **366**(6451): p. 162-166.
109. Gressel, J., *Blue light photoreception*. Photochemistry and photobiology, 1979. **30**(6): p. 749-754.
110. Yang, Z., et al., *Cryptochromes orchestrate transcription regulation of diverse blue light responses in plants*. Photochemistry and photobiology, 2017. **93**(1): p. 112-127.
111. Sancar, A., *Cryptochrome: the second photoactive pigment in the eye and its role in circadian photoreception*. Annual review of biochemistry, 2000. **69**(1): p. 31-67.
112. Park, H.-W., et al., *Crystal structure of DNA photolyase from Escherichia coli*. Science, 1995. **268**(5219): p. 1866-1872.
113. Tamada, T., et al., *Crystal structure of DNA photolyase from Anacystis nidulans*. Nature structural biology, 1997. **4**(11): p. 887-891.

114. Liedvogel, M. and H. Mouritsen, *Cryptochromes—a potential magnetoreceptor: what do we know and what do we want to know?* Journal of the Royal Society Interface, 2010. **7**(suppl_2): p. S147-S162.
115. Yang, H.-Q., et al., *The C termini of Arabidopsis cryptochromes mediate a constitutive light response.* Cell, 2000. **103**(5): p. 815-827.
116. Deisenhofer, J., *DNA photolyases and cryptochromes.* Mutation Research/DNA Repair, 2000. **460**(3-4): p. 143-149.
117. Kavakli, I.H., et al., *The photolyase/cryptochrome family of proteins as DNA repair enzymes and transcriptional repressors.* Photochemistry and photobiology, 2017. **93**(1): p. 93-103.
118. Loontjens, F.G., et al., *Binding characteristics of Hoechst 33258 with calf thymus DNA, poly [d (AT)] and d (CCGGAATTCCGG): multiple stoichiometries and determination of tight binding with a wide spectrum of site affinities.* Biochemistry, 1990. **29**(38): p. 9029-9039.
119. Lin, C., et al., *Expression of an Arabidopsis cryptochrome gene in transgenic tobacco results in hypersensitivity to blue, UV-A, and green light.* Proceedings of the National Academy of Sciences, 1995. **92**(18): p. 8423-8427.
120. Selby, C.P. and A. Sancar, *A cryptochrome/photolyase class of enzymes with single-stranded DNA-specific photolyase activity.* Proceedings of the National Academy of Sciences, 2006. **103**(47): p. 17696-17700.
121. Müller, M. and T. Carell, *Structural biology of DNA photolyases and cryptochromes.* Current opinion in structural biology, 2009. **19**(3): p. 277-285.
122. Brudler, R., et al., *Identification of a new cryptochrome class: structure, function, and evolution.* Molecular cell, 2003. **11**(1): p. 59-67.
123. Daiyasu, H., et al., *Identification of cryptochrome DASH from vertebrates.* Genes to Cells, 2004. **9**(5): p. 479-495.
124. Facella, P., et al., *CRY-DASH gene expression is under the control of the circadian clock machinery in tomato.* FEBS letters, 2006. **580**(19): p. 4618-4624.
125. Li, Q.H. and H.Q. Yang, *Cryptochrome signaling in plants.* Photochemistry and Photobiology, 2007. **83**(1): p. 94-101.
126. El-Din El-Assal, S., et al., *The role of cryptochrome 2 in flowering in Arabidopsis.* Plant Physiology, 2003. **133**(4): p. 1504-1516.
127. Emery, P., et al., *CRY, a Drosophila clock and light-regulated cryptochrome, is a major contributor to circadian rhythm resetting and photosensitivity.* Cell, 1998. **95**(5): p. 669-679.
128. Takahashi, J.S., *Molecular components of the circadian clock in mammals.* Diabetes, Obesity and Metabolism, 2015. **17**: p. 6-11.
129. Vanderstraeten, J., P. Gailly, and E.P. Malkemper, *Light entrainment of retinal biorhythms: cryptochrome 2 as candidate photoreceptor in mammals.* Cellular and Molecular Life Sciences, 2020. **77**(5): p. 875-884.
130. Van Der Horst, G.T., et al., *Mammalian Cry1 and Cry2 are essential for maintenance of circadian rhythms.* Nature, 1999. **398**(6728): p. 627-630.
131. Bolte, P., et al., *Cryptochrome 1a localisation in light- and dark-adapted retinæ of several migratory and non-migratory bird species: no signs of light-dependent activation.* Ethology Ecology & Evolution, 2021. **33**(3): p. 248-272.

132. Nießner, C., et al., *Avian ultraviolet/violet cones identified as probable magnetoreceptors*. PLoS one, 2011. **6**(5): p. e20091.
133. Nießner, C., et al., *Seasonally changing cryptochrome 1b expression in the retinal ganglion cells of a migrating passerine bird*. PLoS One, 2016. **11**(3): p. e0150377.
134. Bolte, P., et al., *Localisation of the putative magnetoreceptive protein cryptochrome 1b in the retinae of migratory birds and homing pigeons*. PLoS One, 2016. **11**(3): p. e0147819.
135. Okamura, H., et al., *Photic induction of mPer1 and mPer2 in cry-deficient mice lacking a biological clock*. Science, 1999. **286**(5449): p. 2531-2534.
136. Quinn, T.P., *Evidence for celestial and magnetic compass orientation in lake migrating sockeye salmon fry*. Journal of Comparative Physiology, 1980. **137**(3): p. 243-248.
137. Phillips, J.B. and S.C. Borland, *Behavioural evidence for use of a light-dependent magnetoreception mechanism by a vertebrate*. Nature, 1992. **359**(6391): p. 142-144.
138. Putman, N.F., et al., *Longitude perception and bicoordinate magnetic maps in sea turtles*. Current Biology, 2011. **21**(6): p. 463-466.
139. Mouritsen, H., *Magnetoreception in birds and its use for long-distance migration*, in *Sturkie's avian physiology*. 2022, Elsevier. p. 233-256.
140. Shakhparonov, V.V. and S.V. Ogurtsov, *Marsh frogs, Pelophylax ridibundus, determine migratory direction by magnetic field*. Journal of Comparative Physiology A, 2017. **203**(1): p. 35-43.
141. Günther, A., et al., *Double-Cone Localization and Seasonal Expression Pattern Suggest a Role in Magnetoreception for European Robin Cryptochrome 4*. Current Biology, 2018. **28**(2): p. 211-223.e4.
142. Einwich, A., et al., *A novel isoform of cryptochrome 4 (Cry4b) is expressed in the retina of a night-migratory songbird*. Scientific reports, 2020. **10**(1): p. 1-9.
143. Bouly, J.-P., et al., *Cryptochrome blue light photoreceptors are activated through interconversion of flavin redox states*. Journal of Biological Chemistry, 2007. **282**(13): p. 9383-9391.
144. Hoang, N., et al., *Human and Drosophila cryptochromes are light activated by flavin photoreduction in living cells*. PLoS biology, 2008. **6**(7): p. e160.
145. Salomon, M., et al., *Photochemical and mutational analysis of the FMN-binding domains of the plant blue light receptor, phototropin*. Biochemistry, 2000. **39**(31): p. 9401-9410.
146. Iseki, M., et al., *A blue-light-activated adenylyl cyclase mediates photoavoidance in Euglena gracilis*. Nature, 2002. **415**(6875): p. 1047-1051.
147. Chosrowjan, H., et al., *The stacked flavin adenine dinucleotide conformation in water is fluorescent on picosecond timescale*. Chemical Physics Letters, 2003. **378**(3-4): p. 354-358.
148. Galbán, J., et al., *The intrinsic fluorescence of FAD and its application in analytical chemistry: a review*. Methods and Applications in Fluorescence, 2016. **4**(4): p. 042005.
149. Shafiqul D.M. Islam, T.S., Alfons Penzkofer, Peter Hegemann, *Fluorescence quenching of flavin adenine dinucleotide in aqueous solution by pH dependent isomerisation and photo-induced electron transfer*. Chemical Physics Letters, 2003. **295**.
150. Hitomi, K., et al., *Eukaryotic Class II Cyclobutane Pyrimidine Dimer Photolyase Structure Reveals Basis for Improved Ultraviolet Tolerance in Plants**. Journal of Biological Chemistry, 2012. **287**(15): p. 12060-12069.

151. Hitomi, K., et al., *Functional motifs in the (6-4) photolyase crystal structure make a comparative framework for DNA repair photolyases and clock cryptochromes*. Proceedings of the National Academy of Sciences, 2009. **106**(17): p. 6962-6967.
152. Ozturk, N., et al., *Animal type 1 cryptochromes: analysis of the redox state of the flavin cofactor by site-directed mutagenesis*. Journal of Biological Chemistry, 2008. **283**(6): p. 3256-3263.
153. Immeln, D., et al., *Primary Events in the Blue Light Sensor Plant Cryptochrome: Intraprotein Electron and Proton Transfer Revealed by Femtosecond Spectroscopy*. Journal of the American Chemical Society, 2012. **134**(30): p. 12536-12546.
154. Xu, J., et al., *Magnetic sensitivity of cryptochrome 4 from a migratory songbird*. Nature, 2021. **594**(7864): p. 535-540.
155. Hush, N. and A.S. Cheung, *Ionization potentials and donor properties of nucleic acid bases and related compounds*. Chemical Physics Letters, 1975. **34**(1): p. 11-13.
156. Amouyal, E., A. Bernas, and D. Grand, *On the photoionization energy threshold of tryptophan in aqueous solutions*. 1979, Wiley Online Library. p. 1071-1077.
157. Müller, F., *Chemistry and biochemistry of flavoenzymes*. Vol. 3. 1991: CRC Press.
158. Li, Y.F., P.F. Heelis, and A. Sancar, *Active site of DNA photolyase: tryptophan-306 is the intrinsic hydrogen atom donor essential for flavin radical photoreduction and DNA repair in vitro*. Biochemistry, 1991. **30**(25): p. 6322-6329.
159. Byrdin, M., et al., *Quantum yield measurements of short-lived photoactivation intermediates in DNA photolyase: toward a detailed understanding of the triple tryptophan electron transfer chain*. The Journal of Physical Chemistry A, 2010. **114**(9): p. 3207-3214.
160. Zhong, D. and A.H. Zewail, *Femtosecond dynamics of flavoproteins: charge separation and recombination in riboflavine (vitamin B2)-binding protein and in glucose oxidase enzyme*. Proceedings of the National Academy of Sciences, 2001. **98**(21): p. 11867-11872.
161. Martin, R., et al., *Ultrafast flavin photoreduction in an oxidized animal (6-4) photolyase through an unconventional tryptophan tetrad*. Physical Chemistry Chemical Physics, 2017. **19**(36): p. 24493-24504.
162. Lacomat, F., et al., *Ultrafast oxidation of a tyrosine by proton-coupled electron transfer promotes light activation of an animal-like cryptochrome*. Journal of the American Chemical Society, 2019. **141**(34): p. 13394-13409.
163. Müller, P., et al., *Discovery and functional analysis of a 4th electron-transferring tryptophan conserved exclusively in animal cryptochromes and (6-4) photolyases*. Chemical Communications, 2015. **51**(85): p. 15502-15505.
164. Brazard, J., et al., *Spectro- Temporal Characterization of the Photoactivation Mechanism of Two New Oxidized Cryptochrome/Photolyase Photoreceptors*. Journal of the American Chemical Society, 2010. **132**(13): p. 4935-4945.
165. Miles, D.W., et al., *Vicinal effects on the optical activity of some adenine nucleosides*. The Journal of Physical Chemistry, 1968. **72**(5): p. 1483-1491.
166. Ahmad, M., et al., *Magnetic intensity affects cryptochrome-dependent responses in Arabidopsis thaliana*. Planta, 2007. **225**(3): p. 615-624.
167. Yoshii, T., M. Ahmad, and C. Helfrich-Förster, *Cryptochrome mediates light-dependent magnetosensitivity of Drosophila's circadian clock*. PLoS biology, 2009. **7**(4): p. e1000086.
168. Harris, S.-R., et al., *Effect of magnetic fields on cryptochrome-dependent responses in Arabidopsis thaliana*. Journal of the Royal Society Interface, 2009. **6**(41): p. 1193-1205.

169. Fedele, G., et al., *Genetic analysis of circadian responses to low frequency electromagnetic fields in Drosophila melanogaster*. PLoS genetics, 2014. **10**(12): p. e1004804.
170. Foley, L.E., R.J. Gegear, and S.M. Reppert, *Human cryptochrome exhibits light-dependent magnetosensitivity*. Nature communications, 2011. **2**(1): p. 1-3.
171. Fedele, G., et al., *An electromagnetic field disrupts negative geotaxis in Drosophila via a CRY-dependent pathway*. Nature communications, 2014. **5**(1): p. 1-6.
172. Gegear, R.J., et al., *Animal cryptochromes mediate magnetoreception by an unconventional photochemical mechanism*. Nature, 2010. **463**(7282): p. 804-807.
173. Marley, R., et al., *Cryptochrome-dependent magnetic field effect on seizure response in Drosophila larvae*. Scientific reports, 2014. **4**(1): p. 1-4.
174. Henbest, K.B., et al., *Magnetic-field effect on the photoactivation reaction of Escherichia coli DNA photolyase*. Proceedings of the National Academy of Sciences, 2008. **105**(38): p. 14395-14399.
175. Sheppard, D.M., et al., *Millitesla magnetic field effects on the photocycle of an animal cryptochrome*. Scientific reports, 2017. **7**(1): p. 1-7.
176. Weber, S., et al., *Origin of light-induced spin-correlated radical pairs in cryptochrome*. The Journal of Physical Chemistry B, 2010. **114**(45): p. 14745-14754.
177. Möller, A., et al., *Retinal cryptochrome in a migratory passerine bird: a possible transducer for the avian magnetic compass*. Naturwissenschaften, 2004. **91**(12): p. 585-588.
178. Hill, E. and T. Ritz, *Can disordered radical pair systems provide a basis for a magnetic compass in animals?* Journal of the Royal Society Interface, 2010. **7**(suppl_2): p. S265-S271.
179. Lau, J.C., et al., *Effects of disorder and motion in a radical pair magnetoreceptor*. Journal of The Royal Society Interface, 2010. **7**(suppl_2): p. S257-S264.
180. Rodgers, C.T. and P.J. Hore, *Chemical magnetoreception in birds: the radical pair mechanism*. Proceedings of the National Academy of Sciences, 2009. **106**(2): p. 353-360.
181. Ozturk, N., et al., *Comparative photochemistry of animal type 1 and type 4 cryptochromes*. Biochemistry, 2009. **48**(36): p. 8585-8593.
182. Qin, S., et al., *A magnetic protein biocompass*. Nature materials, 2016. **15**(2): p. 217-226.
183. Kutta, R.J., et al., *Vertebrate cryptochromes are vestigial flavoproteins*. Scientific reports, 2017. **7**(1): p. 1-11.
184. Pooam, M., et al., *Magnetic sensitivity mediated by the Arabidopsis blue-light receptor cryptochrome occurs during flavin reoxidation in the dark*. Planta, 2019. **249**(2): p. 319-332.
185. Wiltshko, R., et al., *Light-dependent magnetoreception in birds: the crucial step occurs in the dark*. Journal of The Royal Society Interface, 2016. **13**(118): p. 20151010.
186. Müller, P. and M. Ahmad, *Light-activated cryptochrome reacts with molecular oxygen to form a flavin-superoxide radical pair consistent with magnetoreception*. Journal of Biological Chemistry, 2011. **286**(24): p. 21033-21040.
187. Vasa, P., et al., *Real-time observation of ultrafast Rabi oscillations between excitons and plasmons in metal nanostructures with J-aggregates*. Nature Photonics, 2013. **7**(2): p. 128-132.
188. Falke, S.M., et al., *Coherent ultrafast charge transfer in an organic photovoltaic blend*. Science, 2014. **344**(6187): p. 1001-1005.

189. Glauber, R.J., *Coherent and incoherent states of the radiation field*. Physical Review, 1963. **131**(6): p. 2766.
190. Loudon, R., *The quantum theory of light*. 2000: OUP Oxford.
191. Höffges, J., et al., *Heterodyne measurement of the fluorescent radiation of a single trapped ion*. Optics Communications, 1997. **133**(1-6): p. 170-174.
192. Hartschuh, A., et al., *Simultaneous fluorescence and Raman scattering from single carbon nanotubes*. Science, 2003. **301**(5638): p. 1354-1356.
193. Beversluis, M.R., A. Bouhelier, and L. Novotny, *Continuum generation from single gold nanostructures through near-field mediated intraband transitions*. Physical Review B, 2003. **68**(11): p. 115433.
194. Hegarty, J., et al., *Resonant Rayleigh scattering from an inhomogeneously broadened transition: A new probe of the homogeneous linewidth*. Physical Review Letters, 1982. **49**(13): p. 930.
195. Wang, H., et al., *Spontaneous emission of excitons in GaAs quantum wells: The role of momentum scattering*. Physical review letters, 1995. **74**(15): p. 3065.
196. Haacke, S., et al., *Resonant femtosecond emission from quantum well excitons: The role of Rayleigh scattering and luminescence*. Physical review letters, 1997. **78**(11): p. 2228.
197. Woerner, M. and J. Shah, *Resonant secondary emission from two-dimensional excitons: Femtosecond time evolution of the coherence properties*. Physical review letters, 1998. **81**(19): p. 4208.
198. Müller, M. and A. Zumbusch, *Coherent anti-Stokes Raman scattering microscopy*. ChemPhysChem, 2007. **8**(15): p. 2156-2170.
199. Freudiger, C.W., et al., *Label-free biomedical imaging with high sensitivity by stimulated Raman scattering microscopy*. Science, 2008. **322**(5909): p. 1857-1861.
200. Saar, B.G., et al., *Video-rate molecular imaging in vivo with stimulated Raman scattering*. science, 2010. **330**(6009): p. 1368-1370.
201. Yi, J.-M., et al., *Doubly resonant plasmonic hot spot–exciton coupling enhances second harmonic generation from Au/ZnO hybrid porous nanosponges*. ACS Photonics, 2019. **6**(11): p. 2779-2787.
202. Andersen, C.M. and R. Bro, *Practical aspects of PARAFAC modeling of fluorescence excitation-emission data*. Journal of Chemometrics: A Journal of the Chemometrics Society, 2003. **17**(4): p. 200-215.
203. Zepp, R.G., W.M. Sheldon, and M.A. Moran, *Dissolved organic fluorophores in southeastern US coastal waters: correction method for eliminating Rayleigh and Raman scattering peaks in excitation–emission matrices*. Marine chemistry, 2004. **89**(1-4): p. 15-36.
204. Rinnan, Å. and C.M. Andersen, *Handling of first-order Rayleigh scatter in PARAFAC modelling of fluorescence excitation–emission data*. Chemometrics and intelligent laboratory systems, 2005. **76**(1): p. 91-99.
205. Głowacz, K., et al., *Excitation-emission matrix fluorescence spectroscopy for cell viability testing in UV-treated cell culture*. RSC advances, 2022. **12**(13): p. 7652-7660.
206. Bahram, M., et al., *Handling of Rayleigh and Raman scatter for PARAFAC modeling of fluorescence data using interpolation*. Journal of Chemometrics: A Journal of the Chemometrics Society, 2006. **20**(3-4): p. 99-105.

207. Peng, L., et al., *Fourier fluorescence spectrometer for excitation emission matrix measurement*. Optics Express, 2008. **16**(14): p. 10493-10500.
208. Thyrgaug, E., et al., *Single-molecule excitation–emission spectroscopy*. Proceedings of the National Academy of Sciences, 2019. **116**(10): p. 4064-4069.
209. Lakowicz, J.R., *Principles of fluorescence spectroscopy*. 2006: Springer.
210. Li, H., W. Zheng, and Z. Huang, *Rapid near-infrared fluorescence excitation-emission matrix spectroscopy for multifluorophore characterization using an acousto-optic tunable filter technique*. Journal of Biomedical Optics, 2010. **15**(2): p. 027010.
211. Lepetit, L., G. Chériaux, and M. Joffre, *Linear techniques of phase measurement by femtosecond spectral interferometry for applications in spectroscopy*. JOSA B, 1995. **12**(12): p. 2467-2474.
212. Gurioli, M., et al., *Coherent vs incoherent emission from semiconductor structures after resonant femtosecond excitation*. Physical review letters, 1997. **78**(16): p. 3205.
213. Shah, J., *Ultrafast luminescence spectroscopy using sum frequency generation*. IEEE Journal of Quantum Electronics, 1988. **24**(2): p. 276-288.
214. Schmidt, S., et al., *Distinguishing between ultrafast optical harmonic generation and multiphoton-induced luminescence from ZnO thin films by frequency-resolved interferometric autocorrelation microscopy*. Optics Express, 2010. **18**(24): p. 25016-25028.
215. Brida, D., C. Manzoni, and G. Cerullo, *Phase-locked pulses for two-dimensional spectroscopy by a birefringent delay line*. Optics Letters, 2012. **37**(15): p. 3027-3029.
216. Preda, F., et al., *Linear and Nonlinear Spectroscopy by a Common-Path Birefringent Interferometer*. Ieee Journal of Selected Topics in Quantum Electronics, 2017. **23**(3).
217. Perri, A., et al., *Excitation-emission Fourier-transform spectroscopy based on a birefringent interferometer*. Optics Express, 2017. **25**(12): p. A483-A490.
218. Perri, A., et al., *Time- and frequency-resolved fluorescence with a single TCSPC detector via a Fourier-transform approach*. Optics Express, 2018. **26**(3): p. 2270-2279.
219. Perri, A., et al., *Hyperspectral imaging with a TWINS birefringent interferometer*. Optics Express, 2019. **27**(11): p. 15956-15967.
220. Preda, F., et al., *Broadband pump-probe spectroscopy at 20-MHz modulation frequency*. Optics Letters, 2016. **41**(13): p. 2970-2973.
221. Rehault, J., et al., *Two-dimensional electronic spectroscopy with birefringent wedges*. Review of Scientific Instruments, 2014. **85**(12).
222. De Sio, A., et al., *Intermolecular conical intersections in molecular aggregates*. Nature Nanotechnology, 2021. **16**(1): p. 63-68.
223. De Sio, A., et al., *Tracking the coherent generation of polaron pairs in conjugated polymers*. Nature communications, 2016. **7**(1): p. 1-8.
224. Réhault, J., et al., *Broadband stimulated Raman scattering with Fourier-transform detection*. Optics Express, 2015. **23**(19): p. 25235-25246.
225. Zhang, X.-X., et al., *Femtosecond broadband fluorescence upconversion spectroscopy: Improved setup and photometric correction*. Review of Scientific Instruments, 2011. **82**(6): p. 063108.
226. Schmidt, B., et al., *A broadband Kerr shutter for femtosecond fluorescence spectroscopy*. Applied Physics B, 2003. **76**(8): p. 809-814.

227. Chen, K., et al., *Transient grating photoluminescence spectroscopy: an ultrafast method of gating broadband spectra*. The journal of physical chemistry letters, 2014. **5**(10): p. 1732-1737.
228. Campillo, A. and S. Shapiro, *Picosecond streak camera fluorometry-A review*. IEEE Journal of Quantum Electronics, 1983. **19**(4): p. 585-603.
229. Gobets, B., et al., *Time-resolved fluorescence emission measurements of photosystem I particles of various cyanobacteria: a unified compartmental model*. Biophysical journal, 2001. **81**(1): p. 407-424.
230. DV, O., *Connor and D. Phillips*. Time-Correlated Single Photon Counting, 1984: p. 37-54.
231. Rivolta, I., et al., *Cellular uptake of coumarin-6 as a model drug loaded in solid lipid nanoparticles*. Journal of Physiology and Pharmacology, 2011. **62**(1): p. 45.
232. Abdel-Mottaleb, M., et al. *Photophysics and dynamics of coumarin laser dyes and their analytical implications*. in *Proceedings of the Indian Academy of Sciences-Chemical Sciences*. 1992. Springer.
233. Reeves, R.B., *The Interaction of Body Temperature and Acid-Base Balance in Ectothermic Vertebrates*. Annual Review of Physiology, 1977. **39**(1): p. 559-586.
234. Mooney, J. and P. Kambhampati, *Get the Basics Right: Jacobian Conversion of Wavelength and Energy Scales for Quantitative Analysis of Emission Spectra*. The Journal of Physical Chemistry Letters, 2013. **4**(19): p. 3316-3318.
235. Shirdel, J., et al., *Absorption and fluorescence spectroscopic characterisation of the circadian blue-light photoreceptor cryptochrome from Drosophila melanogaster (dCry)*. Chemical Physics, 2008. **352**(1): p. 35-47.
236. Kutta, R.J., N. Archipowa, and N.S. Scrutton, *The sacrificial inactivation of the blue-light photosensor cryptochrome from Drosophila melanogaster*. Physical Chemistry Chemical Physics, 2018. **20**(45): p. 28767-28776.
237. Condon, E., *A theory of intensity distribution in band systems*. Physical Review, 1926. **28**(6): p. 1182.
238. Franck, J. and E. Dymond, *Elementary processes of photochemical reactions*. Transactions of the Faraday Society, 1926. **21**(February): p. 536-542.
239. Kattinig, D.R., I.A. Solov'yov, and P. Hore, *Electron spin relaxation in cryptochrome-based magnetoreception*. Physical Chemistry Chemical Physics, 2016. **18**(18): p. 12443-12456.
240. O'Connor, D., *Time-correlated single photon counting*. 2012: Academic press.
241. Debye, P., *Polar Molecules*. 419 FOURTH AVENUE, AT 29TH STREET, NEW YORK, UR Chemical Catalog Company. 1929, Inc.
242. Einstein, A., *Investigations on the Theory of the Brownian Movement*. 1956: Courier Corporation.
243. Kollmann, H., et al., *Probing the Ca²⁺ switch of the neuronal Ca²⁺ sensor GCAP2 by time-resolved fluorescence spectroscopy*. ACS chemical biology, 2012. **7**(6): p. 1006-1014.
244. Robin, J.r., et al., *Differential nanosecond protein dynamics in homologous calcium sensors*. ACS Chemical Biology, 2015. **10**(10): p. 2344-2352.
245. Schröder, G.F., U. Alexiev, and H. Grubmüller, *Simulation of fluorescence anisotropy experiments: probing protein dynamics*. Biophysical journal, 2005. **89**(6): p. 3757-3770.
246. James, T.L., G.B. Matson, and I.D. Kuntz, *Protein rotational correlation times determined in aqueous solution by carbon-13 rotating frame spin-lattice relaxation in the presence of an off-*

- resonance radiofrequency field*. Journal of the American Chemical Society, 1978. **100**(11): p. 3590-3594.
247. Yang, Z., et al., *Miniaturization of optical spectrometers*. Science, 2021. **371**(6528): p. eabe0722.
248. DeCoster, B., et al., *Low-lying electronic states of carotenoids*. Biochimica et Biophysica Acta (BBA)-Bioenergetics, 1992. **1102**(1): p. 107-114.
249. Reilly, N.J., T.W. Schmidt, and S.H. Kable, *Two-Dimensional Fluorescence (Excitation/Emission) Spectroscopy as a Probe of Complex Chemical Environments*. The Journal of Physical Chemistry A, 2006. **110**(45): p. 12355-12359.
250. Li, L., et al., *New advances in fluorescence excitation-emission matrix spectroscopy for the characterization of dissolved organic matter in drinking water treatment: a review*. Chemical Engineering Journal, 2020. **381**: p. 122676.
251. Seredyńska-Sobecka, B., et al., *Monitoring organic loading to swimming pools by fluorescence excitation–emission matrix with parallel factor analysis (PARAFAC)*. water research, 2011. **45**(6): p. 2306-2314.
252. Elcoroaristizabal, S., et al., *Fluorescence excitation–emission matrix spectroscopy as a tool for determining quality of sparkling wines*. Food chemistry, 2016. **206**: p. 284-290.
253. Islam, K., et al., *Autofluorescence excitation-emission matrices as a quantitative tool for the assessment of meat quality*. Journal of Biophotonics, 2020. **13**(1): p. e201900237.
254. Gascooke, J.R., U.N. Alexander, and W.D. Lawrance, *Two dimensional laser induced fluorescence spectroscopy: a powerful technique for elucidating rovibronic structure in electronic transitions of polyatomic molecules*. J Chem Phys, 2011. **134**(18): p. 184301.
255. Andrade-Eiroa, Á., M. Canle, and V. Cerdá, *Environmental applications of excitation-emission spectrofluorimetry: an in-depth review II*. Applied Spectroscopy Reviews, 2013. **48**(2): p. 77-141.
256. Coble, P.G., *Characterization of marine and terrestrial DOM in seawater using excitation-emission matrix spectroscopy*. Marine chemistry, 1996. **51**(4): p. 325-346.
257. DaCosta, R.S., H. Andersson, and B.C. Wilson, *Molecular fluorescence excitation-emission matrices relevant to tissue spectroscopy*. Photochem Photobiol, 2003. **78**(4): p. 384-92.
258. Stevens, P., J. Mather, and W. Brune, *Measurement of tropospheric OH and HO₂ by laser-induced fluorescence at low pressure*. Journal of Geophysical Research: Atmospheres, 1994. **99**(D2): p. 3543-3557.
259. Gratien, A., et al., *UV and IR absorption cross-sections of HCHO, HCDO, and DCDO*. The Journal of Physical Chemistry A, 2007. **111**(45): p. 11506-11513.
260. Anzai, H., et al., *Fourier transform two-dimensional fluorescence excitation spectrometer by using tandem Fabry-Pérot interferometer*. Review of Scientific Instruments, 2015. **86**(1): p. 014101.
261. Piatkowski, L., E. Gellings, and N.F. Van Hulst, *Broadband single-molecule excitation spectroscopy*. Nature communications, 2016. **7**(1): p. 1-9.
262. Martinez, M., M.-A. Pitarque, and R. van Eldik, *Outer-sphere redox reactions in sterically hindered pentaam (m) inecobalt (III) complexes. A temperature and pressure dependence kinetic study*. Journal of the Chemical Society, Dalton Transactions, 1994(21): p. 3159-3163.

263. Mondal, P., K. Schwinn, and M. Huix-Rotllant, *Impact of the redox state of flavin chromophores on the UV-vis spectra, redox and acidity constants and electron affinities*. Journal of Photochemistry and Photobiology A: Chemistry, 2020. **387**: p. 112164.
264. Abraham, H. and J. Lemoine, *Disparition instantanée du phénomène de Kerr*. Compt. Rend.(Paris), 1899. **129**: p. 206-208.
265. Schrieffer, C., et al., *Ultrasensitive ultraviolet-visible 20 fs absorption spectroscopy of low vapor pressure molecules in the gas phase*. Review of Scientific Instruments, 2008. **79**(1): p. 013107.
266. Hamm, P. and M. Zanni, *Concepts and methods of 2D infrared spectroscopy*. 2011: Cambridge University Press.
267. Siders, C.W., et al., *Detection of nonthermal melting by ultrafast X-ray diffraction*. Science, 1999. **286**(5443): p. 1340-1342.
268. Rousse, A., et al., *Non-thermal melting in semiconductors measured at femtosecond resolution*. Nature, 2001. **410**(6824): p. 65-68.
269. Kuehn, W., et al., *Strong correlation of electronic and lattice excitations in GaAs/AlGaAs semiconductor quantum wells revealed by two-dimensional terahertz spectroscopy*. Physical Review Letters, 2011. **107**(6): p. 067401.
270. Somma, C., et al., *Two-phonon quantum coherences in indium antimonide studied by nonlinear two-dimensional terahertz spectroscopy*. Physical Review Letters, 2016. **116**(17): p. 177401.
271. Baum, P., D.-S. Yang, and A.H. Zewail, *4D visualization of transitional structures in phase transformations by electron diffraction*. science, 2007. **318**(5851): p. 788-792.
272. Van Der Veen, R.M., et al. *Single-nanoparticle phase transitions visualized by ultrafast electron microscopy*. in *International Conference on Ultrafast Phenomena*. 2014. Optica Publishing Group.
273. Gulde, M., et al., *Ultrafast low-energy electron diffraction in transmission resolves polymer/graphene superstructure dynamics*. Science, 2014. **345**(6193): p. 200-204.
274. Polli, D., et al., *Conical intersection dynamics of the primary photoisomerization event in vision*. Nature, 2010. **467**(7314): p. 440-443.
275. Klimov, V.I., et al., *Single-exciton optical gain in semiconductor nanocrystals*. Nature, 2007. **447**(7143): p. 441-446.
276. Gélinas, S., et al., *Ultrafast long-range charge separation in organic semiconductor photovoltaic diodes*. Science, 2014. **343**(6170): p. 512-516.
277. Mukamel, S., *Principles of nonlinear optical spectroscopy*. 1999: Oxford University Press on Demand.
278. Maiuri, M., M. Garavelli, and G. Cerullo, *Ultrafast Spectroscopy: State of the Art and Open Challenges*. Journal of the American Chemical Society, 2020. **142**(1): p. 3-15.
279. Zewail, A.H., *Femtochemistry: Atomic-scale dynamics of the chemical bond*. The Journal of Physical Chemistry A, 2000. **104**(24): p. 5660-5694.
280. Baudisch, B., *Time resolved broadband spectroscopy from UV to NIR*. 2018, lmu.
281. Griffin Jr, E.A., D. Staknis, and C.J. Weitz, *Light-independent role of CRY1 and CRY2 in the mammalian circadian clock*. Science, 1999. **286**(5440): p. 768-771.
282. Hsu, D.S., et al., *Putative human blue-light photoreceptors hCRY1 and hCRY2 are flavoproteins*. Biochemistry, 1996. **35**(44): p. 13871-13877.

283. Zhu, H., et al., *Cryptochromes define a novel circadian clock mechanism in monarch butterflies that may underlie sun compass navigation*. PLoS biology, 2008. **6**(1): p. e4.
284. Stanewsky, R., et al., *The cryb mutation identifies cryptochrome as a circadian photoreceptor in Drosophila*. Cell, 1998. **95**(5): p. 681-692.
285. Somers, D.E., P.F. Devlin, and S.A. Kay, *Phytochromes and cryptochromes in the entrainment of the Arabidopsis circadian clock*. Science, 1998. **282**(5393): p. 1488-1490.
286. Lin, C., et al., *Enhancement of blue-light sensitivity of Arabidopsis seedlings by a blue light receptor cryptochrome 2*. Proceedings of the National Academy of Sciences, 1998. **95**(5): p. 2686-2690.
287. Guo, H., et al., *Regulation of flowering time by Arabidopsis photoreceptors*. Science, 1998. **279**(5355): p. 1360-1363.
288. Solov'yov, I.A., D.E. Chandler, and K. Schulten, *Magnetic field effects in Arabidopsis thaliana cryptochrome-1*. Biophysical journal, 2007. **92**(8): p. 2711-2726.
289. Pinzon-Rodriguez, A., S. Bensch, and R. Muheim, *Expression patterns of cryptochrome genes in avian retina suggest involvement of Cry4 in light-dependent magnetoreception*. Journal of The Royal Society Interface, 2018. **15**(140): p. 20180058.
290. Kattinig, D.R., et al., *Electron spin relaxation can enhance the performance of a cryptochrome-based magnetic compass sensor*. New Journal of Physics, 2016. **18**(6): p. 063007.
291. Wong, S.Y., et al., w. Journal of the Royal Society Interface, 2021. **18**(184): p. 20210601.
292. Lukacs, A., et al., *Electron hopping through the 15 Å triple tryptophan molecular wire in DNA photolyase occurs within 30 ps*. Journal of the American Chemical Society, 2008. **130**(44): p. 14394-14395.
293. Paulus, B., et al., *Spectroscopic characterization of radicals and radical pairs in fruit fly cryptochrome-protonated and nonprotonated flavin radical-states*. The FEBS journal, 2015. **282**(16): p. 3175-3189.
294. Solov'yov, I.A., D.E. Chandler, and K. Schulten, *Exploring the possibilities for radical pair effects in cryptochrome*. Plant signaling & behavior, 2008. **3**(9): p. 676-677.
295. Brazard, J., et al., *Primary photoprocesses involved in the sensory protein for the photophobic response of Blepharisma japonicum*. The Journal of Physical Chemistry B, 2008. **112**(47): p. 15182-15194.
296. Liu, Z., et al., *Determining complete electron flow in the cofactor photoreduction of oxidized photolyase*. Proceedings of the National Academy of Sciences, 2013. **110**(32): p. 12966-12971.
297. Solov'yov, I.A., et al., *Decrypting cryptochrome: revealing the molecular identity of the photoactivation reaction*. Journal of the American Chemical Society, 2012. **134**(43): p. 18046-18052.
298. Lüdemann, G., et al., *Solvent driving force ensures fast formation of a persistent and well-separated radical pair in plant cryptochrome*. Journal of the American Chemical Society, 2015. **137**(3): p. 1147-1156.
299. Mims, D., et al., *Readout of spin quantum beats in a charge-separated radical pair by pump-push spectroscopy*. Science, 2021. **374**(6574): p. 1470-1474.
300. Sweetser, J.N., D.N. Fittinghoff, and R. Trebino, *Transient-grating frequency-resolved optical gating*. Optics letters, 1997. **22**(8): p. 519-521.

301. Rabe, M., *Spectram: A MATLAB® and GNU octave toolbox for transition model guided deconvolution of dynamic spectroscopic data*. Journal of Open Research Software, 2020. **8**.
302. Hanić, M., et al., *Computational Reconstruction and Analysis of Structural Models of Avian Cryptochrome 4*. The Journal of Physical Chemistry B, 2022. **126**(25): p. 4623-4635.
303. Hess, B., et al., *LINCS: a linear constraint solver for molecular simulations*. Journal of computational chemistry, 1997. **18**(12): p. 1463-1472.
304. Hess, B., et al., *GROMACS 4: algorithms for highly efficient, load-balanced, and scalable molecular simulation*. Journal of chemical theory and computation, 2008. **4**(3): p. 435-447.
305. Paul Bauer, B.H., & Erik Lindahl, *GROMACS 2022.3 Manual (2022.3)*. Zenodo. 2022.
306. Wang, J., et al., *Development and testing of a general amber force field*. J Comput Chem, 2004. **25**(9): p. 1157-74.
307. Lindorff-Larsen, K., et al., *Improved side-chain torsion potentials for the Amber ff99SB protein force field*. Proteins, 2010. **78**(8): p. 1950-8.
308. Sjulstok, E., et al., *Molecular insights into variable electron transfer in amphibian cryptochrome*. Biophysical journal, 2018. **114**(11): p. 2563-2572.
309. Pariser, R. and R.G. Parr, *A semi-empirical theory of the electronic spectra and electronic structure of complex unsaturated molecules. II*. The Journal of Chemical Physics, 1953. **21**(5): p. 767-776.
310. Pople, J.A., *Electron interaction in unsaturated hydrocarbons*. Transactions of the Faraday Society, 1953. **49**: p. 1375-1385.
311. Kubar, T. and M. Elstner, *Coarse-grained time-dependent density functional simulation of charge transfer in complex systems: application to hole transfer in DNA*. The Journal of Physical Chemistry B, 2010. **114**(34): p. 11221-11240.
312. Kubař, T. and M. Elstner, *Efficient algorithms for the simulation of non-adiabatic electron transfer in complex molecular systems: application to DNA*. Physical Chemistry Chemical Physics, 2013. **15**(16): p. 5794-5813.
313. van Stokkum, I.H., D.S. Larsen, and R. Van Grondelle, *Global and target analysis of time-resolved spectra*. Biochimica et Biophysica Acta (BBA)-Bioenergetics, 2004. **1657**(2-3): p. 82-104.
314. Solar, S., et al., *Oxidation of tryptophan and N-methylindole by N3. cntdot., Br2.-, and (SCN) 2.-radicals in light-and heavy-water solutions: a pulse radiolysis study*. The Journal of Physical Chemistry, 1991. **95**(9): p. 3639-3643.
315. Kubař, T. and M. Elstner, *A hybrid approach to simulation of electron transfer in complex molecular systems*. Journal of The Royal Society Interface, 2013. **10**(87): p. 20130415.
316. Kubar, T. and M. Elstner, *What governs the charge transfer in DNA? The role of DNA conformation and environment*. The Journal of Physical Chemistry B, 2008. **112**(29): p. 8788-8798.
317. Hanić, M., et al., *On the energetic differences of avian cryptochromes 4 from selected species*. The European Physical Journal D, 2022. **76**(10): p. 1-14.
318. Marcus, R.A. and N. Sutin, *Electron transfers in chemistry and biology*. Biochimica et Biophysica Acta (BBA)-Reviews on Bioenergetics, 1985. **811**(3): p. 265-322.
319. Holub, D., et al., *Functional role of an unusual tyrosine residue in the electron transfer chain of a prokaryotic (6–4) photolyase*. Chemical science, 2018. **9**(5): p. 1259-1272.

320. Roos, A. and W.F. Boron, *Intracellular pH*. *Physiological reviews*, 1981. **61**(2): p. 296-434.
321. Reinholdt, P., et al., *Polarizable density embedding for large biomolecular systems*. *Journal of Chemical Theory and Computation*, 2020. **16**(10): p. 5999-6006.
322. Kudisch, B., et al., *Active-site environmental factors customize the photophysics of photoenzymatic Old Yellow Enzymes*. *The Journal of Physical Chemistry B*, 2020. **124**(49): p. 11236-11249.
323. Nguyen, X.T., et al., *Ultrafast charge carrier relaxation in inorganic halide perovskite single crystals probed by two-dimensional electronic spectroscopy*. *The Journal of Physical Chemistry Letters*, 2019. **10**(18): p. 5414-5421.
324. Andrea Rozzi, C., et al., *Quantum coherence controls the charge separation in a prototypical artificial light-harvesting system*. *Nature communications*, 2013. **4**(1): p. 1-7.
325. De Sio, A. and C. Lienau, *Vibronic coupling in organic semiconductors for photovoltaics*. *Physical Chemistry Chemical Physics*, 2017. **19**(29): p. 18813-18830.
326. Rave, W., R. Schäfer, and A. Hubert, *Quantitative observation of magnetic domains with the magneto-optical Kerr effect*. *Journal of Magnetism and Magnetic Materials*, 1987. **65**(1): p. 7-14.
327. HENRY HURWITZ, J., R. CLARK JONES, *A New Calculus for the Treatment of Optical Systems II. Proof of Three General Equivalence Theorems*. *Optical Society of America*, 1941. **31**(7): p. 493-499.
328. Yeh, P., *Extended Jones matrix method*. *Optical Society of America*, 1982. **72**(4): p. 507-512.
329. Ekvall, K., et al., *Cross phase modulation artifact in liquid phase transient absorption spectroscopy*. *Journal of applied physics*, 2000. **87**(5): p. 2340-2352.

Publication Related to This Thesis

- **Distinguishing Between Coherent and Incoherent Signals in Excitation-Emission Spectroscopy**

Optics Express Vol. 29, Issue 15, pp. 24326-24337 (2021)

Daniel C. Lünemann*, **Anitta R. Thomas***, Jingjing Xu, Rabea Bartölke, Henrik Mouritsen, Antonietta De Sio, and Christoph Lienau

<https://doi.org/10.1364/OE.428850>

*Both authors contributed equally to this chapter. Anitta Rose Thomas and Daniel C. Lünemann planned and performed the experiments. Both analyzed data and wrote the paper together. Anitta Rose Thomas prepared the samples for the experiments. Christoph Lienau and Antonietta De Sio supervised the project.

- **Tracking the Electron Transfer Cascade in European Robin Cryptochrome 4 Mutants**

J. Am. Chem. Soc., 145, 21, 11566–11578 (2023)

Daniel Timmer, Anders Frederiksen, Daniel C. Lünemann, **Anitta R. Thomas**, Jingjing Xu, Rabea Bartölke, Jessica Schmidt, Antonietta De Sio, Iliia A. Solovyov, Henrik Mouritsen, and Christoph Lienau

ja-2023-00442v.R1

Anitta Rose Thomas and Daniel C. Lünemann performed and analyzed the photoluminescence experiments. A.R.T prepared the samples for the experiments. Daniel Timmer performed and analyzed the transient absorption experiments Rabea Bartölke., Jessica Schmidt. and Jingjing Xu. developed the Cry4 expression protocols and expressed and purified the protein samples. Iliia A. Solovyov. and Anders Frederiksen performed the computational modeling. Christoph Lienau, Antonietta De Sio, Iliia A. Solovyov and Henrik Mouritsen. planned and supervised the project. Christoph Lienau wrote the paper with input from all other authors.

Acknowledgment

I sincerely thank Prof. Dr. Christoph Lienau for his scientific supervision throughout my doctoral studies. His immense support allowed me a great deal to complete this thesis successfully. The intense scientific discussion on experimental data, critical questions, and comments gave me more insight into the physical concepts in physics that contributed remarkably to this work.

I thank Prof. Dr. Mathias Wollenhaupt for the evaluation of my doctoral thesis.

I thank Prof. Dr. Karl-Wilhelm Koch for being my third reviewer.

I thankfully remember Dr. Antonietta De Sio for her valuable suggestions, discussions, and support all over my doctoral period.

I thank Daniel C. Lünemann for his friendly and constructive companionship in the lab. Without his support and our productive discussions, we could not have completed many scientific projects in this thesis.

I especially remember Daniel Timmer and Xuan Trung Nguyen for their scientific collaboration and valuable suggestions.

I am thankful to our collaborative partners, Jingjing Xu, Rabea Bartölke, Jessica Schmidt, and Prof. Dr. Henrik Mouritsen from Institut für Biologie und Umweltwissenschaften, University of Oldenburg. Their time-bound production of protein samples and training on sample purification helped me handle the precious protein samples successfully.

I am thankful to our theoretical collaborative partners, Anders Frederiksen and Prof. Dr. Ilia A. Solov'yova from Institut für Physik, University of Oldenburg and Tomáš Kubař and Marcus Elstner from the Department for Theoretical Chemical Biology, Institute for Physical Chemistry, Karlsruhe Institute of Technology.

I would like to thank Raimond Angermann for his technical support and friendly nature.

I thankfully remember Margret Warns Her kind advice helps me adapt to German culture.

I thank all my colleagues in the Ultrafast Nano-Optics working group during my doctoral studies, PD Dr. Petra Groß, Dr. Vladimir Smirnov, Thomas Quenzel, Moritz Gittinger, Dr. Jens Brauer, Jinxin Zhan, Prof. Dr. Martin Silies, Dr. Jinhui Zhong, Dr. Jan Vogelsang, Germann Hergert, Andreas Wüste, Sven Stephan, Kathrin Winte, Dr. Juemin Yi, Tom Jehle, and Bernd Schwenker.

I thank the Research Training Group (RTG) Molecular basis of sensory biology (DFG, GRK 1885), SFB1372 Magnetoreception and navigation in vertebrates and the German Academic Exchange Service (DAAD) for giving me an excellent chance to work on this project and their financial support. I thankfully remember all the supports from Dr. Petra Hülper (former RTG coordinator), Dr. Kristin Tietje, and Tina Schlüter.

I thank my former professor, Dr. Reji Philip, RRI, Bangalore, India, for his encouragement and motivation. My previous colleagues and friends, Dr. Pranitha Sankar, Dr. Jijil J J, Nidhin Prasannan, Sarayoo Sasidharan, Dr. Anoop KK, Dr. Sreekanth Perumbilavil, and Muhamad Shafi Ollakkan.

I am grateful to my mentor and teacher Prof. Alex Shinu Scaria for his support and personal guidance.

I thank my family, my real strength. Papa, Mummy, and my brothers Tony and Tom; are always there for me. I may not complete this doctoral study without my man Akhil Joseph. Last but not least, I thank my thesis co-author, our baby boy Edward Joseph.

I thank Chennai Publishing Services (CPS) Pvt Ltd for proofreading my thesis.

I thank all the nearest and dearest.

Declaration of Independence

I hereby confirm that I have written this thesis independently and used only the mentioned and allowed sources. Furthermore, I assure that I have followed the general principles of scientific work and publication guidelines of the good scientific practice of the Carl von Ossietzky University Oldenburg.

Oldenburg, 25.09.2023

.....

Anitta Rose Thomas